**Title**
Interplay of Galactic Winds and Circumgalactic Media



**Author**
Fielding, Drummond

**Publication Date**
2018

Peer reviewed|Thesis/dissertation

**Interplay of Galactic Winds and Circumgalactic Media**

by

Drummond B. Fielding

A dissertation submitted in partial satisfaction of the

requirements for the degree of

Doctor of Philosophy

in

Astrophysics

in the

Graduate Division

of the

University of California, Berkeley

Committee in charge:

Professor Eliot Quataert, Chair
Associate Professor Mariska Kriek
Associate Professor Daniel Kasen

Summer 2018

**Interplay of Galactic Winds and Circumgalactic Media**

## Abstract

Interplay of Galactic Winds and Circumgalactic Media

by

Drummond B. Fielding

Doctor of Philosophy in Astrophysics

University of California, Berkeley

Professor Eliot Quataert, Chair

The flow of gas through the circumgalactic medium (CGM) regulates galaxy growth over cosmic time. Observations have recently revealed a complex multi-phase structure in the CGM that has challenged many of the established theories and highlights significant gaps in our understanding of this critical aspect of galaxy formation. The spatial scales relevant to the CGM span a huge range with its structure and evolution determined by small-scale processes—such as the launching of galactic winds by clustered supernovae and thermal instability in the hydrostatic halo—and large-scale processes—such as cosmological accretion. I will describe my efforts to use controlled numerical simulations to understand the details and interplay of these multi-scale processes in order to develop a coherent picture of the CGM that is consistent with observations.

To my parents, Lynne Buschman and Brian Fielding

Your unwavering support and encouragement to seek beauty and follow my curiosity got me where I am today.

# Contents

# List of Figures

# List of Tables

# Acknowledgments

I have been truly fortunate to have had an incredible cast of people to interact and work with during my time at UC Berkeley and it is my pleasure to have the opportunity to thank them all.

First, I am deeply grateful to my advisor, Eliot Quataert, for his persistent encouragement, insight, and compassion. I could not have asked for a better mentor. I was given the freedom to explore independently while simultaneously being challenged and stimulated by his seemingly endless fount of creativity and understanding. I have learned and grown immensely while working with him. I have much to aspire to as a scientist and even more so as a human.

I thank Chris McKee for advising me through my first project in graduate school. I learned how to see to the core of the matter at hand from his penetrating questions.

Mike McCourt and Davide Martizzi and deserve a big thanks for helping me get off my feet as a fledgeling graduate student. Much of what has become my thesis work grew out of projects they began. Their advice, lessons, and encouragement were instrumental in bringing all of my projects to fruition.

I thank my eternal cubical-mate and brother in cheese Sean Ressler, who made my afternoons vastly more enjoyable with endless stories, references, and the occasional profound scientific discussion. Likewise, I thank my other cubical mates Chris J. White, Daniel Lecoanet, and Kareem El-Badry for putting up with me and Sean and for being both challenging sounding boards and sources of scientific inspiration.

I thank Sasha Tchekhovskoy and Mariska Kriek for impeccable career advice and countless useful discussions throughout my time at Berkeley.

My friends Lucas Brambrink, Danny Goldstein, and Philipp Moesta have all been indispensable to my successes. I thank Lucas for always being available, for teaching me to run, for spearheading countless backpacking trips, and for motivating me by his genuine excitement and interest. I thank Danny for looking out for me throughout graduate school and for always being willing to talk and think deeply. And I thank Philipp Moesta for all of the excellent conversations over coffee and hard fought squash matches.

Finally, I would like to thank my parents and my sister for their love and support, and for giving me someone to call and talk to on six years worth of bike rides to and from campus.

# Chapter 1

# Introduction

The growth of galaxies over cosmic time is regulated by flows of gas into and out of their interstellar media (ISM). This thesis is about how gas is ejected from galaxies' ISM in the form of galactic winds and how these winds interact with the reservoir of gas surrounding galaxies, known as the circumgalactic medium (CGM). I study these processes using controlled hydrodynamic simulations. The philosophy behind my technique is to isolate specific phenomena by idealizing distinct aspects of galaxy evolution to answer well-posed questions in a reliable and readily interpretable manner. This approach sacrifices a degree of realism in order to provide clear physical intuition for how the relevant mechanisms work.

This introduction begins with a brief overview of the relevant observations and theory, followed by summary of my work that will also serve as a guide to the remaining chapters, and ends with a discussion of related work that I have contributed to, is in progress, or have completed.

## 1.1 Background

In the established Cold Dark Matter theory of structure formation, as the universe evolves matter over-densities seeded soon after the big bang collapse to form dark matter halos. As the halos grow, baryonic matter is accreted along with dark matter. The baryonic component interacts with the existing circumgalactic material and the kinetic energy gained during infall is thermalized in an accretion shock. The characteristic temperature of this accretion shock heated CGM gas is given by the virial theorem and depends on the depth of the dark matter halo's gravitational potential well:

$$T_{\rm vir} = \frac{\mu m_p}{2k_{\rm B}} \frac{G{\rm M}_{\rm halo}}{r_{\rm vir}} = 5\times10^5\ {\rm K}\ \left(\frac{{\rm M}_{\rm halo}}{10^{12}\,{\rm M}_\odot}\right)^{2/3} (1+z), \tag{1.1}$$

where I have taken $\mu = 0.62$ as is appropriate for an ionized third solar metallicity plasma. Here $r_{\rm vir}$ is the size of a dark matter halo and is defined to be the radius where the average density of the halo exceeds some threshold. Throughout this thesis I will adopt the "200m" approximation of $r_{\rm vir}$ in which $\bar{\rho}_{\rm halo}(r_{200,m}) = 200\,\rho_m$, where the mean matter density of the universe is given by

$\rho_m = \frac{3\,H_0^2\Omega_m\,(1+z)^3}{8\pi G}$. The virial radius can, therefore, be expressed as

$$r_{\rm vir} \approx r_{200,m} = \left(\frac{G{\rm M_{halo}}}{100 H_0^2 \Omega_m\,(1+z)^3}\right)^{1/3} = 320\ {\rm kpc}\ \left(\frac{\rm M_{halo}}{10^{12}\,{\rm M_\odot}}\right)^{1/3} (1+z)^{-1}, \tag{1.2}$$

where, in the second equality, I have adopted $H_0 = 70$ km/s/Mpc, and $\Omega_m = 0.27$, as I will throughout.

The evolution of the post-shock gas depends on how efficiently it can cool. The efficiency of cooling can be assessed by comparing the cooling time

$$t_{\rm cool} = \frac{\gamma}{\gamma - 1}\frac{k_{\rm B}T}{n\Lambda(T)}, \tag{1.3}$$

where $\Lambda(T)$ is the cooling curve defined such that $\dot{E} = n^2\Lambda(T)$, to the dynamical time

$$t_{\rm dyn} = \frac{r_{\rm vir}}{v_{\rm vir}} = \sqrt{\frac{r_{\rm vir}^3}{G{\rm M_{halo}}}} = \frac{1}{10 H_0\sqrt{\Omega_m(1+z)^3}}, \tag{1.4}$$

which is roughly the time over which the CGM reaches hydrostatic equilibrium. If the accretion shock heated gas radiates away its energy more rapidly than the system can adjust it will cool and fall to the center of the halo.

Fig. 1.1 shows the temperature dependence of a third solar metallicity cooling curve $\Lambda(T)$. At high temperatures ($T \gtrsim 10^7$ K) the gas is almost entirely ionized and can only cool via bremsstrahlung. At intermediate temperatures ($T \sim 10^5 - 10^6$ K) the metals are partially ionized and the gas can cool efficiently via line cooling. The cooling curve drops again at low temperatures ($T \lesssim 10^4$ K) as the gas becomes mostly neutral. The peak of the cooling curve is at $T \sim 2-3\times10^5$ K, which corresponds to the virial temperature of ${\rm M_{halo}} \sim 10^{11.5}\,{\rm M_\odot}$ halo using equation 1.1. This critical halo mass $M_{\rm crit} \approx 10^{11.5} - 10^{12}\ {\rm M_\odot}$ separates the evolution of halos. Above $M_{\rm crit}$, $t_{\rm cool}$ of the virialized gas is longer than $t_{\rm dyn}$, so the CGM forms a quasi-static hot halo. On the other hand, in halos less massive than $M_{\rm crit}$ the CGM gas can efficiently cool, accrete onto the central galaxy, and build a significant mass of stars (Rees & Ostriker, 1977; Silk, 1977; Binney, 1977). This critical halo mass is also roughly independent of redshift (Birnboim & Dekel, 2003), which can be seen by the fact that $T_{\rm vir} \propto (1+z)$, $n \propto (1+z)^{-3}$, and $\Lambda \propto T^{-1/2}$ between $10^5 - 10^7$ K, so $t_{\rm cool} \propto (1+z)^{3/2}$ and since $t_{\rm dyn} \propto (1+z)^{3/2}$, the ratio $t_{\rm cool}/t_{\rm dyn}$ has no redshift dependence.

A natural prediction of this basic theory for the cooling of accretion shock heated gas is that galaxies residing in lower mass halos with ${\rm M_{halo}} < {\rm M_{crit}}$ should contain nearly all of their share of the cosmic baryon budget in stars and ISM. Observed galaxies, however, contain only a small fraction of the halo's expected baryons (e.g., Behroozi et al., 2013). Fig. 1.2 shows the ratio of the stellar mass to the dark matter halo's baryon budget, $M_{\rm baryon} = f_{\rm b}{\rm M_{halo}}$, as a function of halo mass for lower mass halos, where $f_{\rm b} = \Omega_{\rm b}/\Omega_{\rm m} \approx 0.16$ (Planck Collaboration et al., 2016). The dark matter mass is not directly observable, so the association of a galaxy to a halo is done by using the abundance matching technique. Fig. 1.2 demonstrates that at most 20 percent of a halo's

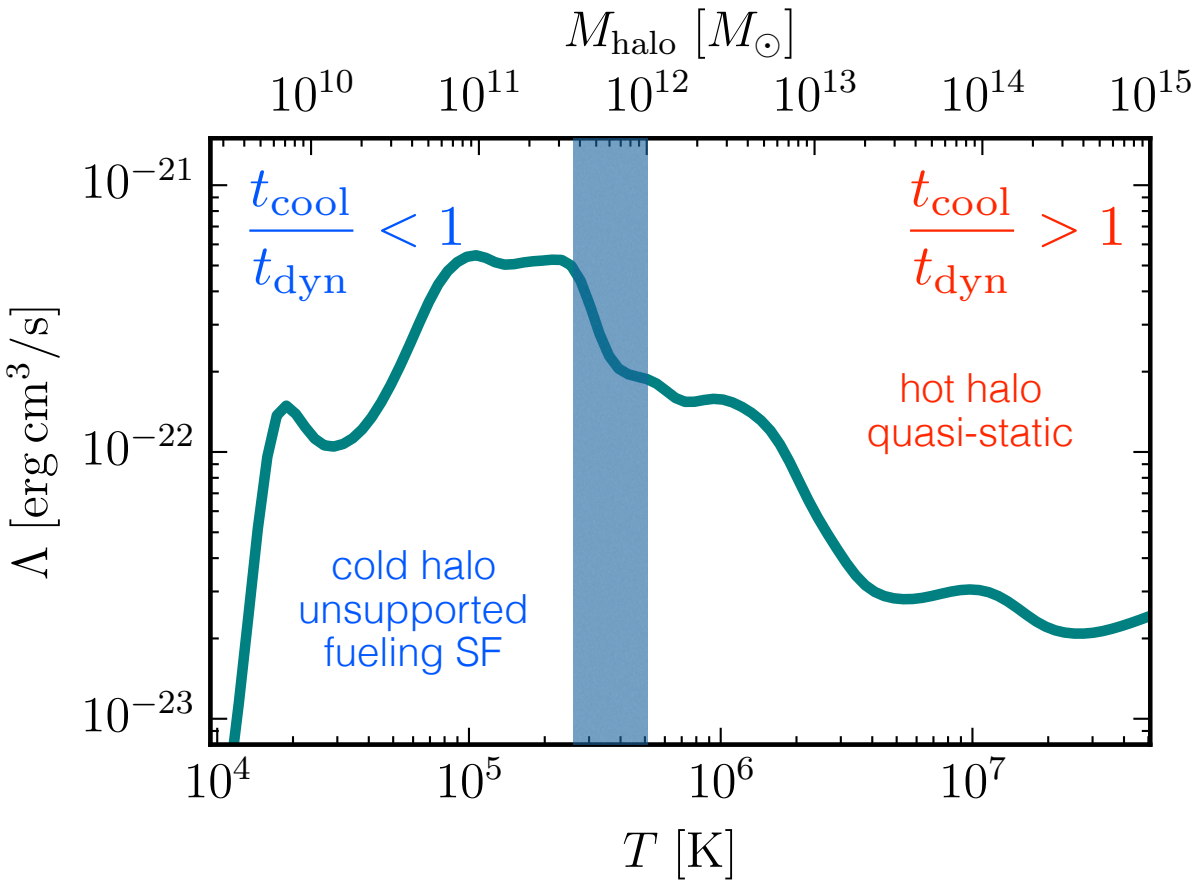


Figure 1.1: The third solar cooling curve temperature dependence from Wiersma et al. (2009), defined in such a way that the volumetric energy loss is given by $n_H^2\Lambda(T)$. The top horizontal axis shows the corresponding halo mass assuming the gas is at $T_{\rm vir}$ as defined in equation 1.1. The vertical blue shaded region ranging from $T \sim 2.5-5\times10^5$ and $\rm M_{halo} = 10^{11.5}-10^{12}\,M_\odot$ represents the approximate division between accretion shock heated gas cooling rapidly ($t_{\rm cool}/t_{\rm dyn} < 1$) on the low $T$ and low $\rm M_{halo}$ end or slowly cooling ($t_{\rm cool}/t_{\rm dyn} > 1$) on the high $T$ and high $\rm M_{halo}$ end. The slowly cooling halos are expected to be filled with a hot, quasi-static CGM, while in the rapidly cooling halos the CGM should dissipate its energy rapidly, accrete onto the central galaxy and provide fuel for high levels of star formation.

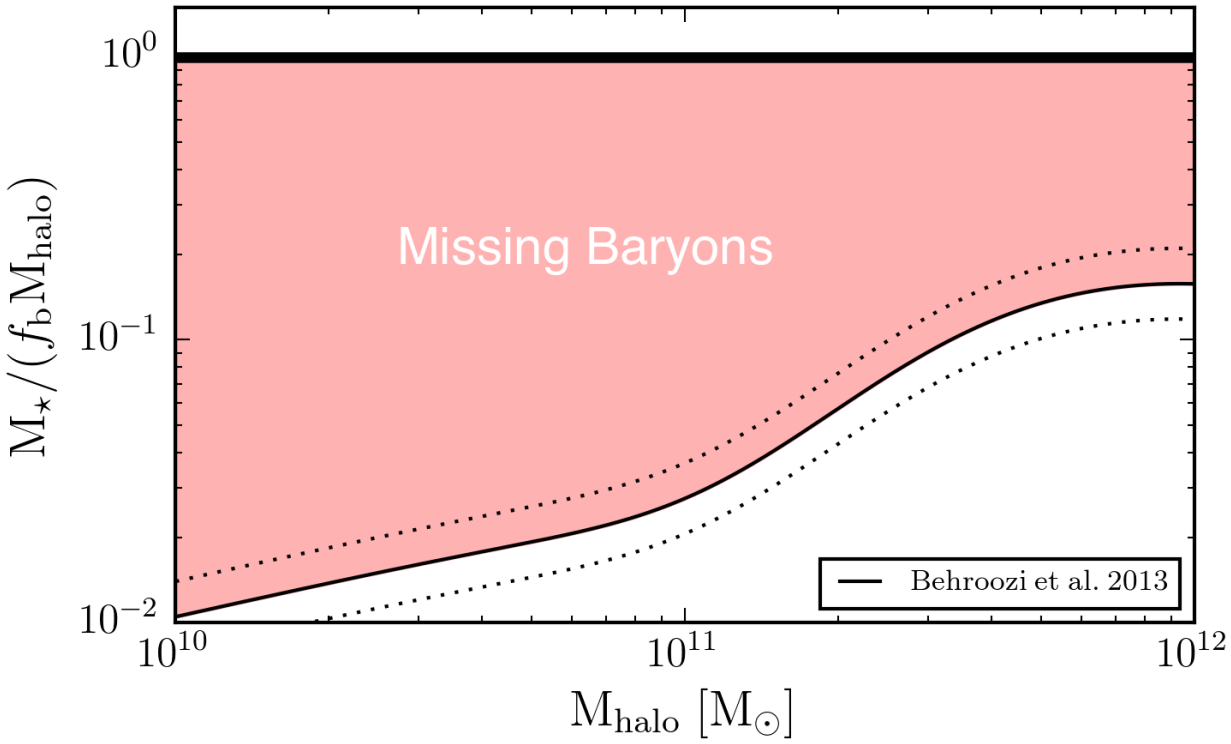


Figure 1.2: If baryons trace dark matter exactly then each halo should have $M_{\rm baryon} = f_{\rm b} M_{\rm halo}$. The thin black line shows the fraction of $M_{\rm baryon}$ in stars as a function of halo mass—known as the stellar mass to halo mass relationship—at $z = 0$ calculated using the abundance matching technique where the dotted lines trace the one sigma uncertainty (Behroozi et al., 2013). If accretion shock heated gas in lower mass halos $M_{\rm halo} \lesssim 10^{12}\,M_\odot$ cools efficiently then the this ratio should be ~1. However the maximum fraction of baryons in stars is $\sim 0.2$. The pink shaded region shows the fraction of baryonic mass that cannot be accounted for by stars alone.

baryons have been turned into stars, which occurs in halos with $M_{\rm halo} \sim 10^{12}\,M_\odot \sim M_{\rm crit}$, and that $10^{11}\,M_\odot$ halos have only ~2 percent of their baryons in stars. Gas in the ISM is readily observable and is insufficient to account for the missing baryons with gas fractions at most order unity (e.g., McGaugh, 2012; Genzel et al., 2015).

Finding these "missing baryons" and understanding why galaxies in low mass halos are not more efficient at forming stars are among the major questions in galaxy formation. There are three possibilities: the baryons may have never been accreted onto the halo in the first place; the baryons may have cooled and accreted onto the galaxy and then been ejected back out in the form of a wind; or the baryons may be in the halo and have been prevented from accreting. It is likely that some combination of all three possibilities takes place in the real universe. All three cases implicate galactic winds as a major driver of galaxy evolution and motivate looking to the CGM to find the missing baryons and understand the fueling of star formation.

Further evidence for the importance of the combined role of galactic winds and accretion from the CGM comes from the fact that the galaxies residing in lower mass halos form stars at a rate such that the gas in their ISM should be depleted in roughly 1 Gyr (e.g., Bigiel et al., 2011; Tacconi et al., 2018). This depletion time is much shorter than the time necessary to build up the amount of mass in stars that is observed in these galaxies. This therefore implies that there must be an external supply of gas to the ISM that enables ongoing star formation. This fuel must come from the CGM. The ability of gas to cool out of the CGM and to accrete onto the galaxy is, therefore, critical to determining how rapidly galaxies grow. This cooling is modulated by the winds the galaxy drives, which can prevent accretion by reheating the CGM.

From a theoretical standpoint, cosmological simulations have been remarkably useful in elucidating the importance of feedback in reproducing the observed properties of galaxies' stellar populations and ISM. In these simulations the feedback is generally from massive stars and accreting super-massive black holes—with stellar feedback being dominant in lower mass halos and black hole feedback being dominant in more massive halos. Without efficient feedback cosmological simulations over-predict the stellar mass of galaxies residing in lower mass halos (e.g., Schaye et al., 2010). However, with properly tuned sub-grid feedback models that are sufficiently powerful the cutting edge cosmological simulations are able to reliably reproduce the stellar mass to halo mass relation at a range of redshifts (e.g., Crain et al., 2015; Vogelsberger et al., 2014). Although these simulations have clearly demonstrated the integral role of galactic winds driven by energetic feedback in reproducing the bulk galaxy properties, the wide range of successful models employed in different simulations negates their predictive power. More constraining observations and/or predictive theories are necessary to break this feedback model degeneracy.

It is now clear that in order to understand what is fueling and halting star formation and where the bulk of the universe's baryons are we have to look not just at the material in galaxies, but around them. Unfortunately, this has historically been hard to do because this gas is generically exceedingly faint and diffuse relative to galaxies themselves. Nevertheless, there is a growing body of observations of the CGM and a phenomenological picture of the flows of gas into and out of galaxies is beginning to take shape. These observations are typically done in absorption using bright background sources such as quasars or the interstellar light itself. Observations in emission are harder to come by, but they have the potential to provide valuable constraints. Emission measurements of the winds from nearby galaxies, such as M82, have been instrumental in constraining the multiphase nature of the winds and the relative mass and energy flux in different phases (e.g., Strickland & Heckman, 2009a). There have only been a few CGM emission observations (e.g., Hayes et al., 2016), although new instruments such as *MUSE* and *Keck Cosmic Web Imager* will enable the CGM to be observed in emission at high redshift $z > 2$ (Martin et al., 2010). Describing the full range of galactic wind and CGM observations is beyond the scope of this introduction, so I will summarize some of the most salient properties.

Galactic winds are seen to emanate from galaxies across a wide range in star formation rates and redshifts (Rubin et al., 2014). Precisely determining the mass and energy carried by the wind is challenging, but there is good evidence that both scale with the star formation rate of the galaxy (e.g., Martin, 1999a; Heckman et al., 2015). The observed properties indicate that the mass outflow rates of the winds relative to the star formation rate (known as the mass loading factor) are order

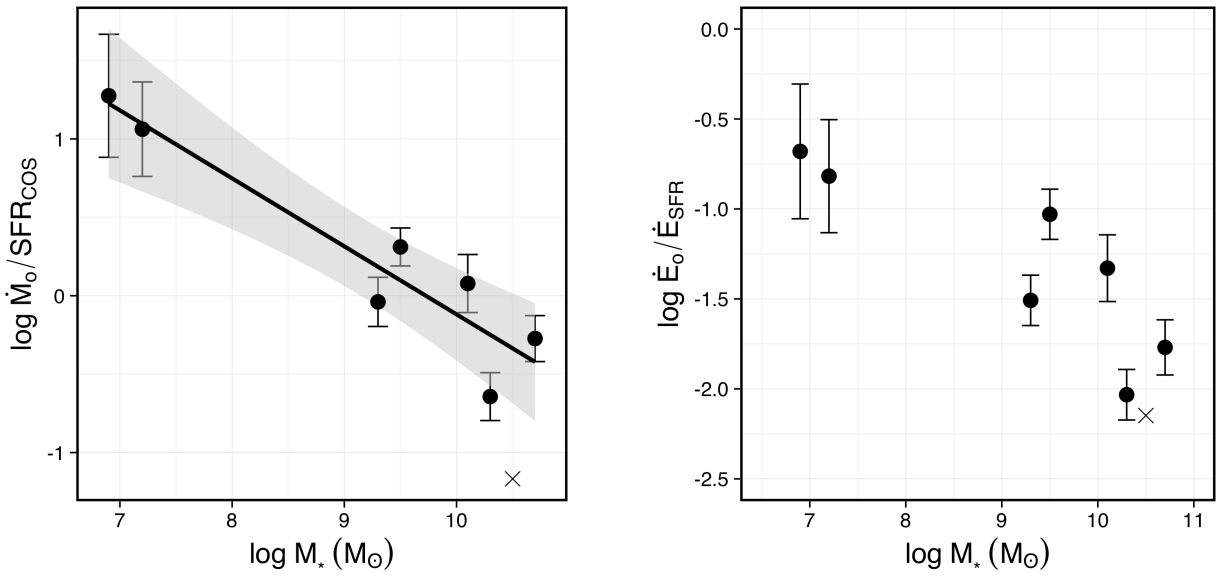


Figure 1.3: The observed mass loading (left; ratio of mass outflow rate to star formation rate) and energy loading (right; ratio of energy outflow rate to energy injection rate from star formation) versus galaxy stellar mass, adapted from Chisholm et al. (2017). Observations like these concretely demonstrate that powerful winds are common and they provide a challenge to theorists to explain how these winds are launched and why they behave as they do.

unity and that the winds carry a significant fraction of the energy (known as the energy loading factor) injected into the ISM from the SNe associated with the star formation. For example, Fig. 1.3 shows among the most reliable measurements to date of the mass loading and energy loading factor from seven nearby star-forming galaxies using ultraviolet absorption lines (Chisholm et al., 2017). Understanding exactly how these winds are driven and why their properties scale the way they do remains an unsolved problem and has motivated much of my thesis work.

Observations of the CGM primarily rely on measuring the absorption in spectra of background galaxies (e.g., Rudie et al., 2012) or quasars (e.g., Chen et al., 1998). The strongest and most constraining absorption comes from lines in the rest-frame UV, which precludes making local universe observations from the ground, although $z \sim 2$ ground based observations have proved fruitful. Low-redshift CGM observations have been revolutionized since the installment of the *Cosmic Origins Spectrograph* on the *Hubble Space Telescope* because of its UV sensitivity. In addition to measuring the absorption a major challenge to these observations is to find the galaxy associated with the absorbers. To date there have been several surveys that have measured CGM absorption and host galaxy properties for low redshift ($z \sim 0.2$) systems (e.g., COS-halos Tumlinson et al. 2013; COS-dwarfs Bordoloi et al. 2014; COS-GASS Borthakur et al. 2015), and there are many more extensive surveys currently underway. These surveys have found large neutral hydrogen and metal absorption by gas at a broad range of ionization states and therefore temperatures out to many hundreds of kpc from the nearest galaxy. The properties of this enriched CGM material correlates

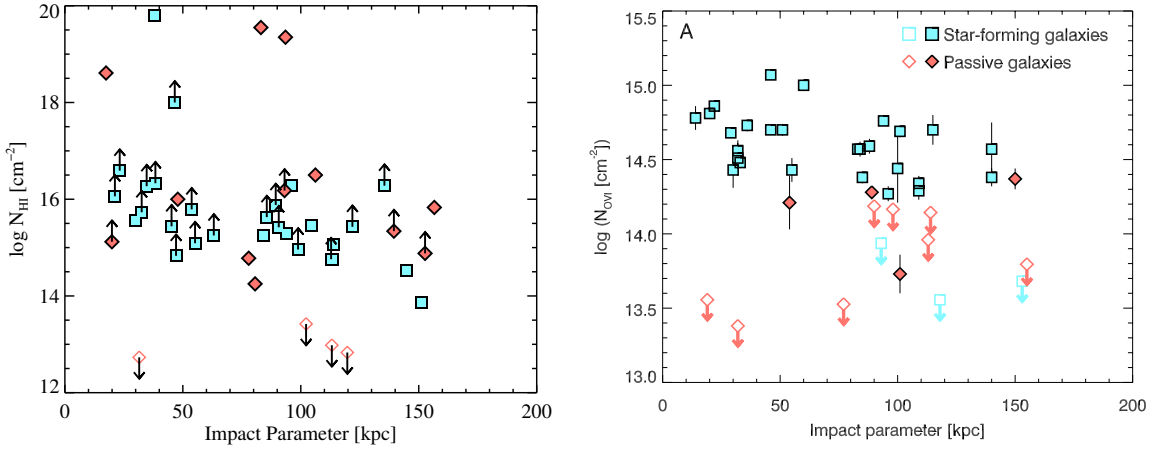


Figure 1.4: Observed circumgalactic H I (left; adapted from Tumlinson et al. 2013) and O VI (right; adapted from Tumlinson et al. 2011) column densities versus impact parameter. The large column densities, high covering fractions, and star formation rate dependence (or lack thereof) have proved very challenging to explain theoretically. Simple modeling based on these observations indicate cooling flow rates $\gg$ the observed star formation rates (McQuinn & Werk, 2018), and cold gas masses larger than the ISM and stellar mass combined (Werk et al., 2014). A more detailed understanding of the enrichment and heating of the CGM as well as more sophisticated modeling of the observations is needed to bring the observations and theory into agreement, but already these observations are proving to be an essential probe of the fundamental physics governing galaxy formation.

with many properties of the host galaxy such as star formation rate, mass, distance, environment, and redshift. For example, Fig. 1.4 shows the COS-halos measurements of neutral hydrogen (H I) and five-times ionized oxygen (O VI) column densities as a function of impact parameter (distance of galaxy to quasar line of sight) for star forming and quiescent galaxies. Intriguingly, the H I, which traces cold gas, does not correlate with star formation rate, while the O VI, which traces gas at $\sim 3 \times 10^5$ K, has a strong star formation rate dependence. These observations have the potential to be incredibly constraining on the properties of the CGM and therefore galaxy formation in general. Existing models are over-simplified, but have begun to make predictions about the physical state of the CGM based on these observations. A straightforward cooling flow model for the O VI, assuming its collisionally ionized, implies that cooling mass fluxes may be as high as 100 $M_\odot$/yr (McQuinn & Werk, 2018). Photoionization models that assume the absorption by neutral and singly or doubly ionized species comes from gas all at the same density and temperature indicate that the CGM of roughly Milky Way mass galaxies contains as much as $10^{11} M_\odot$ in cold ($T \sim 10^4$ K) gas (Werk et al., 2014) with metallicities ranging from tenth solar to super solar (Prochaska et al., 2017). These inferred properties need to be refined by taking into account the multiphase nature of the CGM (see §1.3.2 below on work that is currently underway), but they provide a

useful demonstration of the power of CGM observations to probe the flows of gas into and out of galaxies. Moreover, cosmological simulations have mostly under predicted the observed CGM properties (e.g., Hummels et al., 2013) highlighting the ability of CGM observations to constrain the wide range of feedback models.

Theoretically the launching of galactic winds, and the subsequent enrichment, heating, and stirring the CGM is poorly understood. There are a plethora of plausible galactic wind driving mechanisms from the energy injected by supernova to the radiation pressure from massive stars to the cosmic rays generated in supernova remnants. On the other hand there is a dearth of viable theories for how so much gas spanning more than a factor of 100 in temperature coexists seemingly all throughout the CGM of both star forming and quiescent galaxies. This thesis aims to help explain how galactic winds are launched—specifically, how energetic they are and how much mass they carry—and how these galactic winds interact with the surrounding CGM to regulate the flow of gas into the galaxy. In the following section I will summarize the three main projects that comprise my efforts in this endeavor.

## 1.2 Thesis Summary and Guide to Chapters

I begin in Chapter 2 by describing my research on the large-scale interaction of galactic winds and the CGM. The aim of this work is to understand how accretion from the IGM and winds launched from the central galaxy shape the CGM over a range of dark matter halo masses. This work made use of an idealized numerical setup that was designed to focus the majority of the computational expense on the diffuse gas in CGM rather than the galaxy itself, as is the case in cosmological simulations. This enabled us to achieve unprecedented spatial resolution in the CGM at a fraction of the computational cost. To achieve this goal, the center of the halo, where the galaxy would be, is excised from the computational domain. The galaxy is modeled in these simulations with a simple star formation and galactic wind model in which a fraction of the accreted material is assumed to turn into stars and the remainder is ejected back out into the CGM at a specified velocity. The inexpensive nature of these simulations allowed us to adopt a wide range of galactic wind model parameters and systematically study how the CGM responds to changes in the feedback model. We find that at higher halo masses $\sim 10^{12}\,M_\odot$ the CGM is predominantly quasi-static and thermal pressure supported, with feedback and cooling setting the phase structure and evolution in the central $\sim 20$ % of the halo. On the other hand, at lower halo masses $\sim 10^{11}\,M_\odot$ the accretion shock heated gas cools rapidly and the CGM is instead populated by wind material interacting directly with IGM inflows. In the lower mass halos the CGM material is predominantly supported by non-thermal pressure, and its properties depend sensitively on the feedback model parameters. I explore the possibility of exploiting the feedback model sensitivity of CGM properties to use CGM observations to constrain the properties of galactic winds. However, although we found that the overall dynamics were well converged with spatial resolution the details of the phase structure, which the observations are most sensitive to, were not. As I will discuss briefly in the next section, this finding has motivated projects currently underway and planned for the near future to understand how the details of the phase structure impact the observations in order to use

the observations to better constrain the global CGM properties.

Chapters 3 and 4 cover my work on understanding how SNe launch galactic winds. In chapter I address the importance of geometry when it comes to simulations of galactic winds launched by SNe. Previous works, including a study led by Davide Martizzi that I was the second author on—which I will describe in the following section—found using local box simulations of small patches of the ISM that SNe alone fail to drive powerful galactic winds. However, I show that in global simulations that include an entire galactic disk as well as the surrounding medium SNe alone can in fact launch powerful winds. The reason for the discrepancy between the winds launched in global simulations relative to local simulations is that local simulations adopt periodic boundary conditions in the horizontal directions. These boundary conditions artificially collimate the wind and prevent it from expanding and converting its enthalpy to kinetic energy. The collimated wind instead remains slow and hot, radiates away its energy, and falls back to the galaxy before escaping into the surrounding medium. In our global simulations, which had ISM conditions and SNe injection models very similar to what was used in the local simulations, the winds expand and accelerate without losing much energy to cooling and escape far out into the halo. Furthermore, I demonstrate that by clustering the SNe the strength of the winds is increased dramatically up to the levels thought to be necessary to explain observations. I take this as evidence that SNe can be the primary driver of galactic winds although additional processes may increase their efficacy. This is a key step towards developing an ab initio understanding of the launching of galactic winds.

In chapter 4 I build upon the work presented in chapter 3 by studying in greater detail how the clustering of SNe enhances their ability to launch powerful galactic winds. In this work we present arguments that the spatial and temporal clustering of SNe is expected because most massive stars that eventually become core-collapse SNe form in clusters that survive for longer than the lifetime of these stars. We then show analytically that clustered SNe should collectively drive a super-bubble in the ISM. This super-bubble will continue to expand until it reaches pressure equilibrium with the surrounding ISM. Above a critical cluster mass, however, the super-bubble will reach the scale height of the galactic disk and breakout prior reaching equilibrium and prior to the cessation of SNe. Previous related works simulated clustered SNe-driven super-bubble expansion, but they only considered the pre-breakout evolution. In this chapter, I show that the energetics change dramatically once the super-bubble breaks out by simulating the pre- and post-breakout evolution of clustered SNe. While the super-bubble is confined within the disk 90 to >99 % of the energy injected by SNe is radiated away. In the simulations of star clusters that are more massive than the critical value, which we show corresponds to a star formation efficiency of $\sim 3$ %, the super-bubble breaks out. Post-breakout the amount of energy injected by SNe that is lost to radiative cooling falls to $\lesssim 80$ %, leaving behind a sizable fraction to drive a powerful wind. We show how the wind properties change with cluster mass and gas surface density, as well as how the energy and mass is partitioned in phase space. The amount of mass and energy carried by the winds in these simulations is commensurate with observationally inferred values and brings us one step closer to developing a self-consistent model for galactic winds. Although these simulations are idealized they will immediately be useful in improving galactic wind models used in cosmological and global halo simulations. Moreover, the controlled numerical setup ideally suited to be used in future studies to test the impact of additional physical processes such as magnetic fields, conduction, and

cosmic rays.

## 1.3 Related Works

### 1.3.1 Contributing Author

Of the four (published) projects I contributed to while completing my thesis the most relevant to the rest of this thesis is Martizzi et al. (2016a), which I was the second author of. In this work we numerically simulated the ISM turbulence and galactic wind properties that result from detonating (unclustered) SNe in a stratified patch. My primary contribution to this work was in regard to winds that were launched. I developed a set of "tall box" numerical simulations that enabled us to study the long range propagation of the galactic winds up to 5 kpc above the disk midplane, where as our fiducial simulations only extended up to 0.5 kpc above the disk midplane. These tall box simulations demonstrated one of the main findings of this work: nearly all of the mass and energy carried by the winds just above the disk scale height does not make it beyond a few kpc from the disk. We determined that the failure of the winds to carry any significant mass or energy out into the surround medium was a geometric effect. Because these simulations simulated only a portion of a larger galaxy we adopted periodic boundary conditions in the disk midplane direction. As a result of this the resulting winds could not expand without running into mirror copies of itself. This artificial collimation caused the wind to evolve following a plane-parallel geometry rather than a spherical geometry. We demonstrated analytically that a plane parallel wind does not undergo a transition from subsonic to supersonic (except in the case of catastrophic cooling), whereas a spherical wind has such a transition (Parker, 1965). The implication of this is that most of the energy of the wind remains in thermal energy, which is subject to radiative losses, rather than being converted to kinetic energy and escaping out into the halo. This finding motivated the work that I will describe in Chapter 3.

### 1.3.2 Ongoing Work

At the time of writing, I am in the process of working on a semi-analytic model for the phase structure of the CGM and its implications for observations. Currently, the state-of-the-art technique for modeling CGM absorption line observations is to assume that all of the ions tracing low temperature come from material in the same phase and to find the density that best matches all the ions under the assumption that they are in photoionization equilibrium with the UV background (e.g., Werk et al., 2014; Prochaska et al., 2017). However, by assuming a delta function distribution for the cold phase the fit to the observations is more often than not quite poor. I am currently developing a physically motivated semi-analytic description of the CGM phase distribution that accounts for the true *multi*phase nature of the gas. The processes that regulate the phase structure are uncertain particularly at low temperatures where cooling, conduction, and turbulent mixing are all expected to be relevant. By parameterizing the phase-structure and then generating mock observations I will be able to quantify the sensitivity of observations and the inferred physical properties

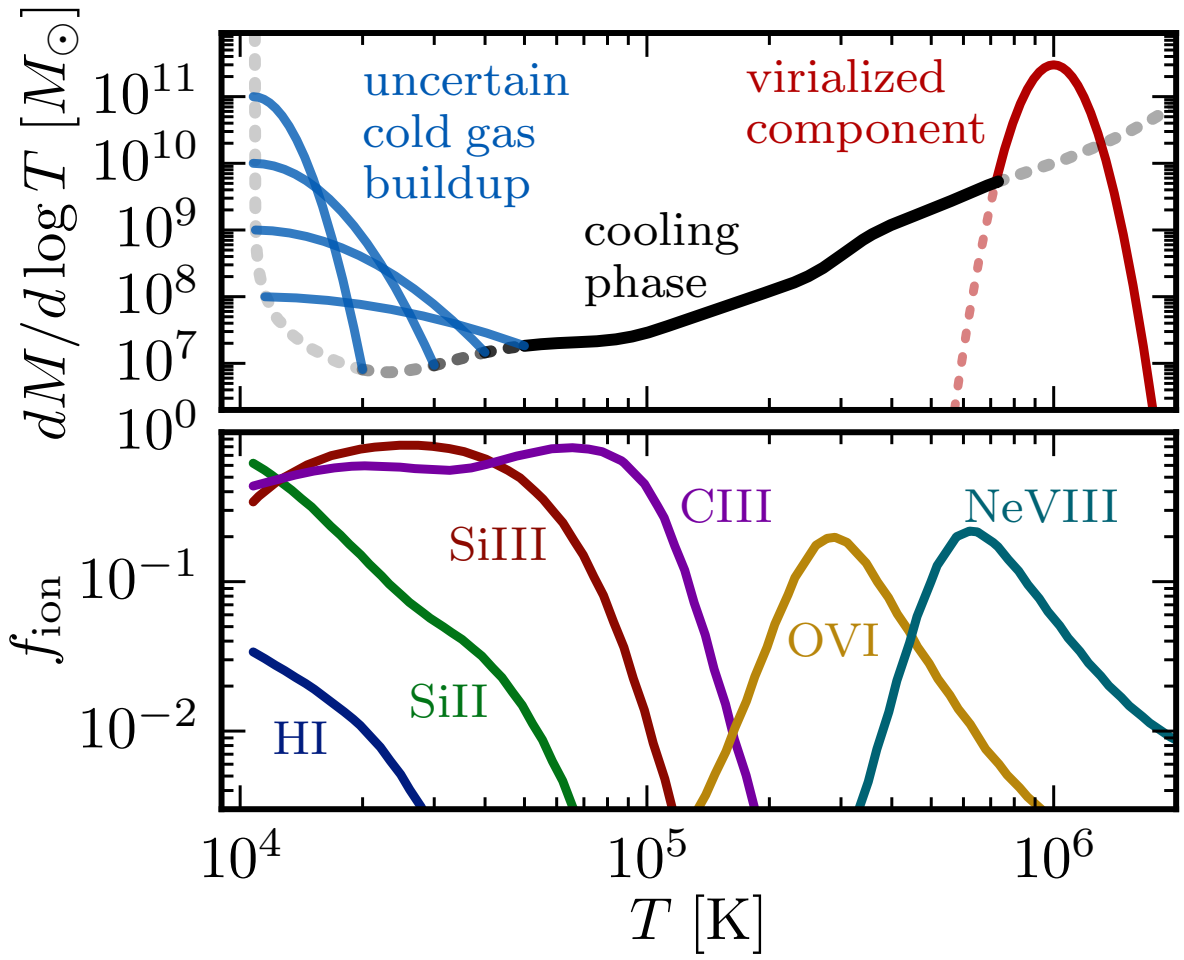


Figure 1.5: Example CGM phase distribution (top) and fractional abundance of commonly observed ions at a characteristic CGM pressure $P/k_{\rm B}$ = 100 K cm$^{-3}$ (bottom). Small changes to the poorly constrained, highly sensitive low temperature phase structure can have a major impact on the integrated ion column densities.

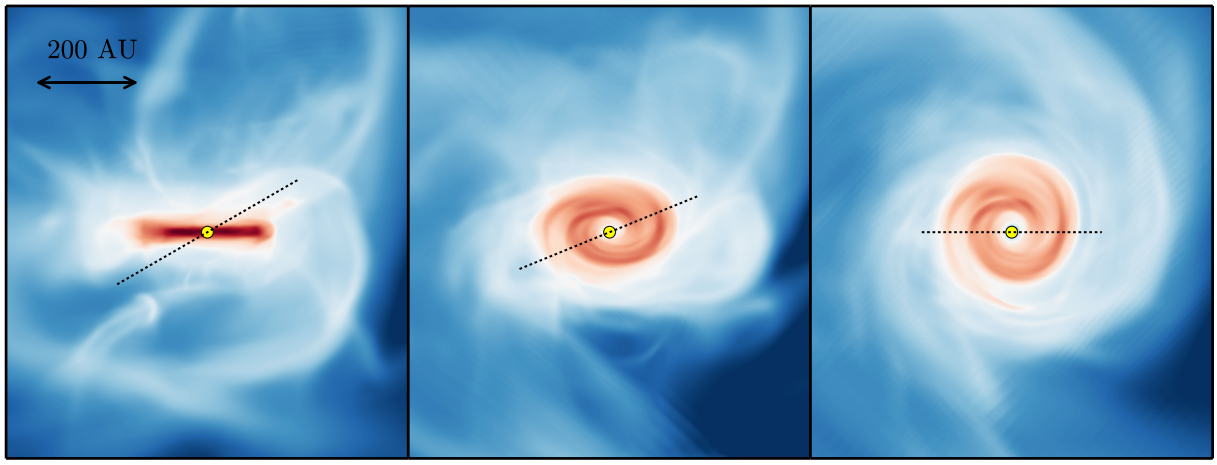


Figure 1.6: An example of a misaligned protostar-protostellar disk system from a turbulent magnetohydrodynamic star formation simuation viewed edge-on (left), at an intermediate angle (center) and face-on (right) (Fielding et al., 2015). Each image is density projection, 800 AU on a side. The dashed line indicates the direction of the stellar spin axis, and its length is the scaled according to the projection of the image. The small yellow dot in the center of each image shows the location of the star particle.

(i.e. cold gas mass, metallicity, and absorbing cloud size) to the details of the phase structure. In Fig. 1.5 I show a schematic representation of the semi-analytic phase-structure distribution and the temperature dependence of several commonly observed ions. This demonstrates that ion ratios, which are used in the standard photoionization modeling to find the density, are very sensitive to the exact shape of the phase distribution and only by understanding this sensitivity can we make reliable inferences from the observations.

This is part of a larger effort I plan to pursue over the coming years to understand how the global CGM properties set the details of the phase structure and are thereby encoded in the observations. In doing so I aim to tap into the power of absorption line CGM studies to constrain the fundamental phsyics governing galaxy evolution.

### 1.3.3 Past Projects

In the first two years of graduate school I led a paper unrelated to this thesis, but that adopted a similar approach (Fielding et al., 2015). In this paper we studied the relative angular momenta of a protostar and its protoplanetary disk using idealized (magneto)hydrodynamical simulations. The motivation for this work is the observed misalignment between the orbital angular momentum vector of some Hot Jupiters and the spin axis of their host stars. We sought to explain this so-called spin-orbit misalignment as a natural by product of turbulence in the natal environment of stars. The crux of the physical scenario we proposed is that the spin axis of a star reflects the integrated

accreted angular momentum, but the disk's angular momentum is continually shed and replaced, and is therefore dominated by the most recently accreted material. In a turbulent medium the most recently accreted material is not expected to be related to all of the previously accrete material so the angular momenta of the disk and star should be misaligned. If this misalignment persists then the planets that form in the disk will be misaligned as observed. To test this scenario we ran a series of idealized hydrodynamic and magnetohydrodynamic simulations of star formation in a turbulent medium. Fig. 1.6 shows an example of a misaligned disk-star system in one of our simulations. We found a distribution of misalignments that is broadly consistent with observations.

# List of publications

### First Author Publications

- Drummond Fielding, Eliot Quataert, & Davide Martizzi. *Clustered Supernovae Drive Powerful Galactic Winds after Super-Bubble Breakout*. (submitted)
- Drummond Fielding, Eliot Quataert, Davide Martizzi, & Claude-André Faucher-Giguère. *How Supernovae Launch Galactic Winds*, MNRAS, letters, 470, 39 (2017).
- Drummond Fielding, Eliot Quataert, Michael McCourt, & Todd Thompson. *The Impact of Star Formation Feedback on the Circumgalactic Medium*, MNRAS, 466, 3810 (2017).
- Drummond Fielding, Christopher McKee, Aristotle Socrates, Andrew Cunningham, & Richard I. Klein. *The Turbulent Origin of Spin-Orbit Misalignment in Planetary Systems*, MNRAS, 450, 3306 (2015).

### Contributing Author Publications

- Davide Martizzi, Claude-André Faucher-Giguère, Eliot Quataert, & Drummond Fielding. *Simulations of Jet Heating in Galaxy Clusters: Successes and Numerical Challenges*, (in press), arXiv:1805.06461
- Jonathan Stern, Claude-André Faucher-Giguère, Joseph Hennawi, Zachary Hafen, Sean Johnson, & Drummond Fielding. *Does Circumgalactic OVI Trace Low-Pressure Gas Beyond the Accretion Shock? Clues from HI and Low-Ion Absorption, Line Kinematics, and Dust Extinction*, (in press), arXiv:1803.05446
- Davide Martizzi, Drummond Fielding, Claude-André Faucher-Giguère, & Eliot Quataert. *Supernova Feedback in a Vertically Stratified Medium: Interstellar Turbulence and Galactic Winds*, MNRAS, 459, 2311 (2016).
- Stella S. R. Offner, Michael M. Dunham, Katherine I. Lee, Héctor G. Arce, & Drummond Fielding. *The Turbulent Origin of Outflow and Spin Misalignment in Multiple Star Systems*, ApJ, 827L, 110 (2016).

# Chapter 2

# The Impact of Star Formation Feedback on the Circumgalactic Medium

An earlier version of this article was previously published as Fielding D., Quataert E., McCourt M., and Thompson T. A., 2017, MNRAS, 466, 3810

## 2.1 Abstract

We use idealized three-dimensional hydrodynamic simulations to study the dynamics and thermal structure of the circumgalactic medium (CGM). Our simulations quantify the role of cooling, galactic winds driven by stellar feedback, and cosmological gas accretion in setting the properties of the CGM in dark matter haloes ranging from $10^{11} - 10^{12}\,\mathrm{M}_\odot$. Our simulations support a conceptual picture in which the properties of the CGM, and the key physics governing it, change markedly with halo mass near $\sim 10^{11.5}\,\mathrm{M}_\odot$.As in calculations without stellar feedback, we find that above a critical halo mass of $\sim 10^{11.5}\,\mathrm{M}_\odot$ the halo gas is supported by thermal pressure created in the virial shock. The thermal properties of the halo gas at small radii (near any central galaxy) are regulated by feedback triggered when $t_{\rm cool}/t_{\rm ff} \lesssim 10$ in the hot halo gas. Below the critical halo mass, however, there is no thermally supported halo and self-regulation at $t_{\rm cool}/t_{\rm ff} \sim 10$ does not apply. Instead, the halo gas properties are determined by the interaction between cosmological gas inflow and outflowing galactic winds. The halo gas is not in hydrostatic equilibrium, but is largely supported against gravity by bulk flows (turbulence and coherent inflow/outflow). Its phase structure depends sensitively on both the energy per unit mass and the mass-loading factor of the galaxy outflows. This sensitivity may allow measurements of the thermal state of the CGM in lower mass haloes to constrain the nature of galactic wind feedback. Our idealized simulations can account for some of the properties of the multiphase halo gas inferred from quasar absorption line observations, including the presence of significant mass at a wide range of temperatures, and the characteristic O VI and C IV column densities and kinematics. However, we under-predict the neutral hydrogen content of the $z \sim 0$ CGM.

## 2.2 Introduction

The classic paradigm in galaxy formation is that dark matter haloes are initially filled with hot gas heated to the virial temperature by an accretion shock. This virialized gas settles into rough hydrostatic equilibrium in the dark matter potential. In sufficiently massive haloes the virialized gas cannot cool on a Hubble time and the galactic accretion rate is set by the cooling rate of the halo gas. However, the shock heated gas cools quickly and rapidly loses pressure support in less massive haloes. The critical transition between rapid and slow cooling occurs at dark matter halo masses on the order of $\sim 10^{11.5}$ $M_\odot$, relatively independent of redshift (Rees & Ostriker, 1977; Silk, 1977; Binney, 1977).

Using analytic calculations and spherically symmetric simulations Birnboim & Dekel (2003) sharpened the understanding of galaxy growth in haloes below $\sim 10^{11.5}$ $M_\odot$ by showing that inflowing gas does not form an accretion shock near the virial radius when the cooling time of the post-shock gas $t_{\rm cool}$ is less than the free fall time $t_{\rm ff}$. Their calculations, however, neglected feedback processes.

Cosmological simulations have subsequently borne out these ideas with greater realism (e.g., Kereš et al., 2005; Dekel et al., 2009). These simulations have verified the existence of a critical halo mass $\sim 10^{11.5}$ $M_\odot$ below which accretion proceeds via 'cold streams' that penetrate directly to small radii. In more massive haloes the classic picture remains appropriate with gas shock heated to the virial temperature. The exact transition between cold and hot accretion remains somewhat uncertain, however, with different numerical techniques providing somewhat different answers (Kereš et al., 2012; Nelson et al., 2013).

The transition in how galaxies acquire their gas appears to be key for understanding many properties of galaxies. Notably, this critical halo mass corresponds to the stellar mass where galaxies transition from being predominantly blue and star forming to red and quiescent (e.g., Yang et al., 2009), and to roughly the peak in the stellar-to-halo mass ratio (e.g., Behroozi et al., 2010).

In parallel to this improved understanding of halo and galaxy accretion, there has been rapid advancement in our understanding of the properties and dynamics of halo gas. For cluster and group mass haloes ($\geq 10^{13}$ $M_\odot$) thermal instability triggered feedback regulation (e.g., McCourt et al., 2012; Sharma et al., 2012a,b; Li et al., 2015) has proved successful in explaining some of the properties of both the cool and hot intracluster (intragroup) medium (Voit & Donahue, 2015). Simultaneously, quasar absorption line observations have begun to provide detailed quantitative constraints on the mass, metal content, and phase structure of gas in galaxy mass dark matter haloes (e.g., Steidel et al., 2010; Tumlinson et al., 2011; Rudie et al., 2012; Werk et al., 2014; Borthakur et al., 2015).

In this paper, we adopt an idealized approach to studying the gaseous haloes of galaxies, the circumgalactic medium, i.e., CGM. The interplay of cooling, galactic winds driven by stellar feedback, and cosmological accretion of gas shape the CGM and determine its dynamics and thermal structure. Our aim in this paper is in part to assess the impact of stellar feedback on what has become the established understanding of the dark matter halo mass dependence of virial shock stability. Furthermore, we seek to determine how the phase structure of halo gas changes with halo mass and feedback parameterization. These topics are, of course, also addressed by fully cos-

mological simulations focused on the CGM that incorporate stellar feedback (e.g., van de Voort & Schaye, 2012; Shen et al., 2013; Ford et al., 2013; Nelson et al., 2015; Faucher-Giguère et al., 2015, 2016; van de Voort et al., 2016). Here we adopt a complementary approach and use idealized three dimensional hydrodynamic simulations that sacrifice some degree of realism, but provide more control and better physical insight into the dominant processes.

In this initial study we make several important simplifications. The most readily apparent relative to cosmological simulations is that we do not consider filamentary accretion and instead feed gas into our haloes quasi-spherically. This choice was made because of the computational subtleties in resolving instabilities between inflow filaments and halo gas (Kereš et al., 2012; Nelson et al., 2013; Lecoanet et al., 2015), which is in some sense a distinct (albeit important) set of questions from those we address here. Additionally, we make the fairly standard simplification of solving the ideal hydrodynamics equations only. Magnetic fields, (anisotropic) conduction (Balbus, 2001; Quataert, 2008; McCourt et al., 2011), viscosity (Kunz, 2011; Parrish et al., 2012), and cosmic rays (Booth et al., 2013) may be important for properly modeling the CGM. In future studies we plan to relax these assumptions while maintaining the controlled and idealized nature of our simulations.

The structure of this paper is as follows. We describe our computational set-up in Section 2.3. In Section 2.4 we present the results of our simulations, focusing on the halo mass dependence of the CGM properties, how the CGM changes as we modify the feedback physics, and a comparison of our results to observations of the $z \sim 0$ CGM. In Section 3.5 we conclude with a summary of our results and discuss the implications and future directions of our work.

## 2.3 Method

We study the long term evolution of gas in galactic haloes – in particular, how the evolution changes with halo mass and with feedback efficiency/strength. The numerical experiment we designed models the relevant physical processes while remaining simple enough for us to readily determine what causes the resulting behavior. Our model for the galactic halo takes into account the gravitational potential of the dark matter, optically thin radiative cooling, ongoing cosmological accretion, and galactic feedback that is triggered when gas is accreted on to the central galaxy. We ran 3-dimensional hydrodynamic simulations with an ideal gas equation of state using the ATHENA code (Stone et al., 2008; Gardiner & Stone, 2008), which integrates the standard fluid equations. We make use of the static mesh refinement capabilities of ATHENA to reach high resolution in the central regions of the haloes.

At the scales we are interested in, dark matter dominates the gravitational potential, so we do not include any baryonic contribution to the gravitational potential in our calculations. We treat the dark matter as a static potential that follows an NFW profile (Navarro et al., 1997). We adopt the common '200m' definition of the mass and $r_{\rm vir}$ of the halo. They are defined such that the mean density of the halo is 200 times $\bar{\rho}_m$, the mean matter density of the Universe: $\mathrm{M_{halo}} = \mathrm{M_{200}}_m = 200\bar{\rho}_m(4\pi/3)r_{\rm vir}^3$. We assume a $\Lambda$CDM cosmology with $(\Omega_m, \Omega_\Lambda, H_\circ) = (0.27, 0.73, 70$ km/s/Mpc).

We restrict our attention to the $z = 0$ universe. However, our results are generally applicable to a wide range of redshifts because the dynamics are not expected to change much with redshift at fixed halo mass (Dekel & Birnboim, 2006). This is due to the very weak redshift dependence of $t_{\rm cool}/t_{\rm ff}$ at the accretion shock of a halo. We have confirmed this in our setup with a small set of simulations, but we leave a detailed investigation of the redshift dependence to a future work.

In keeping with the idealized nature of these calculations we keep the metallicity of the gas fixed at one-third solar, including the cosmologically inflowing gas and the galactic wind gas, which are likely less and more metal enriched, respectively. All gas is assumed to be in photoionization equilibrium (PIE) with the meta-galactic UV/X-ray background (Haardt & Madau, 2001). We note, however, that the assumption of ionization equilibrium may not always be valid (Oppenheimer et al., 2016). We adopt the PIE cooling (and heating) rates tabulated by Wiersma et al. (2009). The difference between the PIE cooling rate and the collisional ionization equilibrium (CIE) cooling rate (e.g., Sutherland & Dopita, 1993) is significant at the typical, low densities of the haloes we consider. Additionally, we do not allow gas to cool below $T = 10^4$ K. This temperature floor is somewhat redundant given the low temperature photoionization heating, but ensures that unresolved dense clumps do not become under-pressurized and overly massive.

We include cosmological accretion of gas by feeding in cold gas at the turn-around radius, $r_{\rm ta} = 2r_{\rm vir}$, which is the outer boundary of our computational domain. This accretion is quasi-spherical ($\delta\rho/\rho \sim 0.3$ perturbations are introduced to break spherical symmetry, the details of the perturbations are discussed below); as we discuss in Section 3.5, other accretion geometries, such as filaments, will be considered in future work. The accretion rate at the turn around radius, $\dot{\rm M}_{\rm ta}$, is calibrated to match the mean rates measured by McBride et al. (2009) in the large, dark matter only, Millennium Simulation (Springel et al., 2005) – scaled appropriately by the cosmic baryon fraction $f_{\rm b} = 0.17$. Explicitly, we use $\dot{\rm M}_{\rm ta} = 7\,{\rm M}_\odot\,{\rm yr}^{-1}({\rm M}_{\rm halo}/10^{12}{\rm M}_\odot)$.

We use a physically motivated mechanical galactic feedback model that depends on the wind velocity $v_{\rm wind}$ and the mass loading factor of the wind $\eta$, which is defined such that

$$\dot{\rm M}_\star\eta = \dot{\rm M}_{\rm out},\ \dot{\rm M}_{\rm in}\frac{\eta}{\eta+1} = \dot{\rm M}_{\rm out}. \tag{2.1}$$

We do not simulate star formation so the star formation rate in equation (2.1) instead represents the rate at which gas is excised from the inner edge of the domain.

We are not interested in studying the actual galaxy itself, so we model it as a small sphere that behaves as a sink and a source. The galaxy has a radius $r_{\rm gal} = 0.025r_{\rm vir} = 8.0\,{\rm kpc}\,({\rm M}_{\rm halo}/10^{12}{\rm M}_\odot)^{1/3}$. When there is an inward mass flux $\dot{\rm M}_{\rm in}$ on to the galaxy, feedback is triggered and a corresponding outward mass flux – given by equation (2.1) – is injected into a thin shell just outside of the galaxy. Additionally, $\dot{\rm M}_\star = \dot{\rm M}_{\rm in}(\eta+1)^{-1}$ is removed from the domain. The feedback is ejected

Table 2.1: Simulation parameters

| $M_{halo}$ [a] | $r_{vir}$ [b] | $v_{vir}$ [c] | $\dot{M}_{ta}$ [d] | $\eta$ | $\left(\frac{v_{wind}}{v_{esc}}\right)^2$ | $\epsilon_\star$ ($\times 10^{-6}$) | label |
|---|---|---|---|---|---|---|---|
| $10^{11}$ | 148 | 54 | 0.7 | 5 | 1 | 1.0 | fiducial high $\eta$ |
| | | | | 5 | 3 | 3.0 | strong high $\eta$ |
| | | | | 0.3 | 4.5 | 0.3 | fiducial low $\eta$ |
| | | | | 0.3 | 9 | 0.6 | strong low $\eta$ |
| $10^{11.5}$ | 217 | 79 | 2.2 | 3 | 2 | 2.6 | fiducial high $\eta$ |
| | | | | 0.3 | 6.75 | 0.9 | fiducial low $\eta$ |
| $10^{12}$ | 319 | 116 | 7.0 | 2 | 3 | 5.4 | fiducial high $\eta$ |
| | | | | 0.3 | 9 | 2.4 | fiducial low $\eta$ |

[a] in units of $M_\odot$; [b] in units of kpc; [c] in units of km s$^{-1}$; [d] in units of $M_\odot$ yr$^{-1}$. For each halo mass, we ran simulations with both high and low mass-loading $\eta$ and corresponding lower or higher $v_{wind}$, respectively. For each choice of $\eta$ for the $10^{11}$ $M_\odot$ halo we adopted a fiducial (smaller) and a 'strong' (larger) $v_{wind}$. Note that $v_{esc} \approx 3.5\, v_{vir}$ at $r_{gal}$, where the wind is launched, which can be used to determine $v_{wind}$. We make use of static mesh refinement in these simulations to increase the resolution in the centers of haloes. The fiducial spatial resolution is 57 cells per $r_{vir}$ ($\Delta x = 5.6$ kpc $M_{12}^{1/3}$, where $M_{12} = M_{halo}(10^{12} M_\odot)^{-1}$), 114 cells per $r_{vir}$ ($\Delta x = 2.8$ kpc $M_{12}^{1/3}$), and 228 cells per $r_{vir}$ ($\Delta x = 1.4$ kpc $M_{12}^{1/3}$), for $r > 1.125 r_{vir}$, $1.125 r_{vir} > r > 0.5625 r_{vir}$, and $r < 0.5625 r_{vir}$, respectively. In Appendix 2.A we sensitivity of our results on spatial resolution and find our results are well converged.

isotropically[1] with a velocity $v_{wind}$ that is proportional to the local escape speed $v_{esc}$.[2] The energetic efficiency of feedback can be expressed with our feedback parameters, $\eta$ and $v_{wind}$, as follows:

$$\begin{aligned} \epsilon_\star &= \frac{\dot{E}_{out}}{\dot{M}_\star c^2} = \frac{\frac{1}{2}\dot{M}_{out} v_{wind}^2}{\dot{M}_\star c^2} = \frac{\eta}{2}\left(\frac{v_{wind}}{c}\right)^2 \\ &= 2.7 \times 10^{-6} \left(\frac{\eta}{3}\right)\left(\frac{v_{wind}}{v_{esc}}\right)^2 \left(\frac{v_{esc}}{400\,\mathrm{km\,s^{-1}}}\right)^2 . \end{aligned} \tag{2.2}$$

The feedback model parameters are listed in Table 2.1. For each halo mass we ran a simulation with a high and low mass loading factor. The mass loading factors, $\eta$, were chosen to bracket the expected range for star formation feedback as suggested by observations (Martin, 1999a; Veilleux

[1] On time scales of a few Gyr, we find little difference if the gas is ejected isotropically or is confined to fixed opening angles $\sim 60°$; however over the course of $\sim 5-10$ Gyr if the direction of the conical outflows is kept fixed the outflows excavate a cavity and blow out along the axis. This may not be realistic because the orientation of a galaxy's outflow will change as its dark matter halo's angular momentum changes over the course of a Hubble time (Book et al., 2011; Bett & Frenk, 2012). Although we adopt an isotropic outflow, instantaneously the outflow often resembles the familiar biconical form as it follows the path of least resistance.

[2] Our fiducial feedback model has no thermal energy input. When included, thermal energy makes little difference. For the radii at which we inject energy neglecting thermal energy is likely a valid approximation since any hot outflow will have swept up and incorporated a substantial amount of cold gas and adiabatically cooled as it expanded (Thompson et al., 2016a).

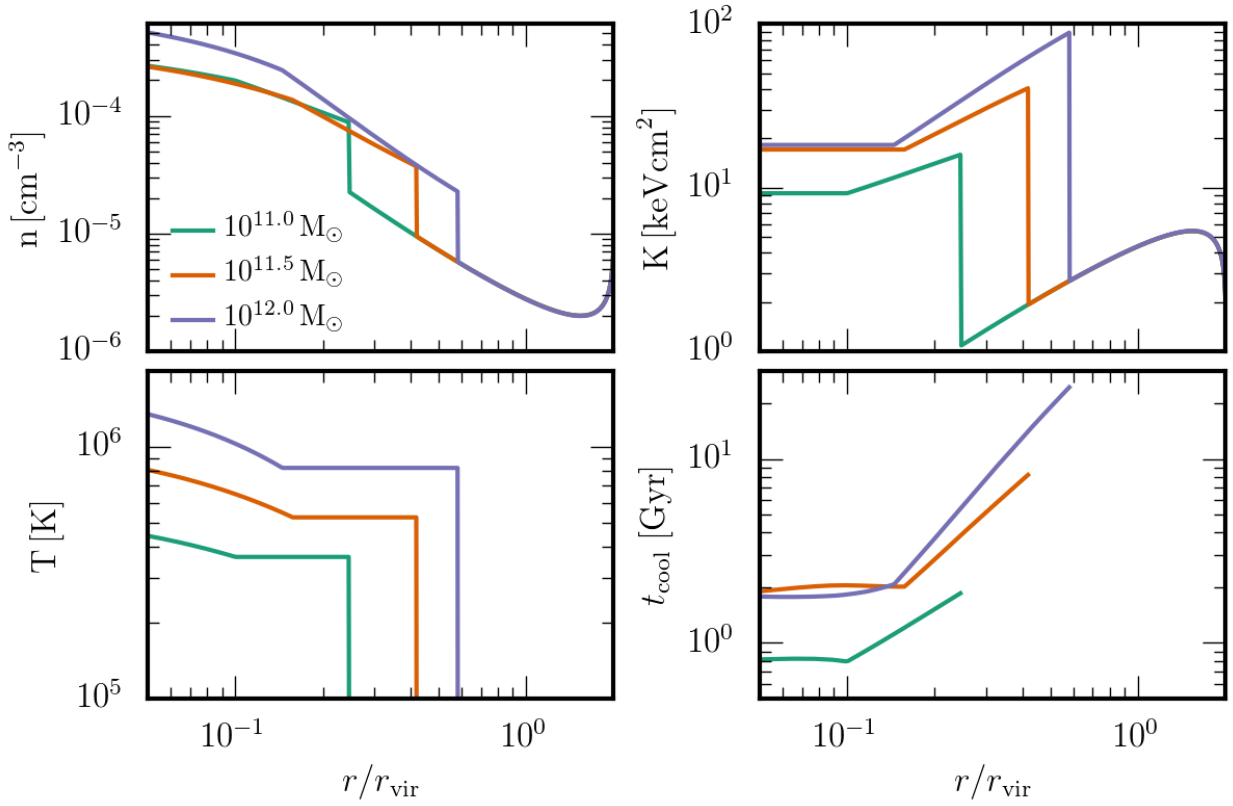


Figure 2.1: Initial conditions (density $n$, entropy $K = k_B T n^{-2/3}$, temperature $T$, and cooling time $t_{\rm cool}$) for $M_{\rm halo} = 10^{11}$, $10^{11.5}$, and $10^{12}$ $M_\odot$ haloes in teal, orange, and purple, respectively. Initial radii for the isentropic cores are $r_{\rm core}/r_{\rm vir} = 0.1$, 0.16, and 0.15, and the initial shock radii are $r_{\rm sh}/r_{\rm vir} = 0.25$, 0.42, and 0.58, respectively. Note that the cooling time is not well defined for regions with $T < 10^4$ K because we impose a floor to our cooling function at $10^4$ K.

et al., 2005a; Heckman et al., 2015) and cosmological simulations (Muratov et al., 2015). Likewise the wind velocities span the range of expected velocities of ~100s $-10^3$ km s$^{-1}$. In Table 2.1 each $v_{\rm wind}$ is listed relative to the escape velocity (of the dark matter halo) at $r_{\rm gal}$ – where the wind is launched – that is defined as

$$v_{\rm esc} = \sqrt{-2\Phi_{\rm NFW}(r_{\rm gal})} \approx 3.5 v_{\rm vir}. \tag{2.3}$$

For each choice of $\eta$ in the $10^{11}$ $M_\odot$ haloes we adopted a model with a fiducial $v_{\rm wind}$ and one with a higher $v_{\rm wind}$; we refer to the latter as the 'strong' $v_{\rm wind}$ models. These additional models allow us to better study the response of the CGM to the choice of wind model at this halo mass. As we discuss below, the CGM properties are particularly sensitive to changes in feedback in lower mass haloes ~ $10^{11}$ $M_\odot$.

For reference, we can approximate a standard feedback efficiency by assuming that there is one supernova for every 100 $M_\odot$ of stars formed and each supernova supplies $10^{51}$ ergs of energy. The corresponding feedback efficiency is $\epsilon_{\star,\rm ref} = 10^{51}{\rm ergs}/100 M_\odot c^2 = 5.6 \times 10^{-6}$. Table 2.1 shows that all of our feedback models have $\epsilon_\star \leq 5.6 \times 10^{-6}$. Note that we adopt more efficient feedback models in more massive haloes. This is necessary for feedback to have a non-negligible impact on the CGM in these haloes.

The fiducial initial conditions of the three halo masses we consider, $M_{\rm halo} = 10^{11}, 10^{11.5}$, and $10^{12}$ $M_\odot$, are shown in Figure 2.1. Gas is initialized in a hot virialized halo in hydrostatic equilibrium out to a virial shock radius $r_{\rm sh}$. Beyond the shock and out to $r_{\rm ta}$, the gas is cold ($T_{\rm IGM} = 10^4$ K – the exact temperature of the intergalactic gas does not change the outcome as long as the virial shock is strong, i.e., so long as $T_{\rm IGM} \ll T_{\rm vir}$) and freely falling with its density set to preserve $\dot{M}_{\rm ta}$. The density and temperature of the gas at the virial shock obey the usual shock jump conditions. Within the shock the gas is isothermal at the shock temperature until the core radius, $r_{\rm core}$, where the gas switches to constant entropy. For the larger mass haloes we consider, there are constraints on properties of the core (e.g., theory: Maller & Bullock 2004; Sharma et al. 2012b and observations: Fang et al. 2013; Voit & Donahue 2015), so we choose a consistent value for $r_{\rm core}$ – extrapolating for halo masses with no constraint. For increasing halo mass ($10^{11}, 10^{11.5}$, and $10^{12}$ $M_\odot$) the initial radii for the isentropic cores are $r_{\rm core}/r_{\rm vir} = 0.1$, 0.16, and 0.15, and the initial shock radii are $r_{\rm sh}/r_{\rm vir} = 0.25$, 0.42, and 0.58. The corresponding initial gas fractions within $r_{\rm vir}$ are $f_{\rm gas} = 0.013, 0.017$, and 0.026. For comparison, the time average baryon[3] fractions within $r_{\rm vir}$ are $\sim$0.05 – 0.1, reflecting the new equilibrium reached after several dynamical times ($t_{\rm dyn} = (GM/r_{\rm vir})^{-1/2} = (10H_\circ)^{-1} = 1.4$ Gyr).

We introduce isobaric density perturbations throughout the domain that break the spherical symmetry. The amplitude of the perturbations satisfy $\delta\rho/\rho = 0.3$ and have a power spectrum that goes as $k^{-1/2}$ for $1 \leq \frac{kL_{\rm box}}{2\pi} \leq 100$, where $k$ is the wave number of the perturbation and $L_{\rm box}$ is the size of our domain. The results are insensitive to the details of how the perturbations are introduced. We do not add any angular momentum to gas in our domain. We assume that the disk circularizes on small scales ($\lesssim 0.05 r_{\rm vir}$) (e.g., Mo et al., 1998) comparable to where gas is removed and injected, so angular momentum is not essential on the scales we study here.

To ensure that our results do not depend sensitively on our initial conditions we ran simulations with no initial shock. In this case, a thermal pressure supported gaseous halo never develops in the lower mass $10^{11}$ $M_\odot$ halo because at the 'galaxy' radius the accretion shock's cooling time is shorter than all other relevant time-scales.[4] Alternatively, in higher mass haloes ($\gtrsim 10^{11.5}$ $M_\odot$) an accretion shock at the 'galaxy' radius has a sufficiently long cooling time to allow a virialized halo to develop. For all halo masses within a few dynamical times the behavior of simulations with and without initial shocks are very similar.

In our simulations we use static mesh refinement in the center of the domain to achieve high spatial resolution in the halo cores. The base level resolution is 57 cells per $r_{\rm vir}$, and our fiducial

[3]Here we define the baryon fraction to be gas between $r_{\rm gal}$ and $r_{\rm vir}$ and gas excised from the domain at small radii ('stars').

[4]The perturbations we impose break spherical symmetry and ensure that there is a shock at small radii.

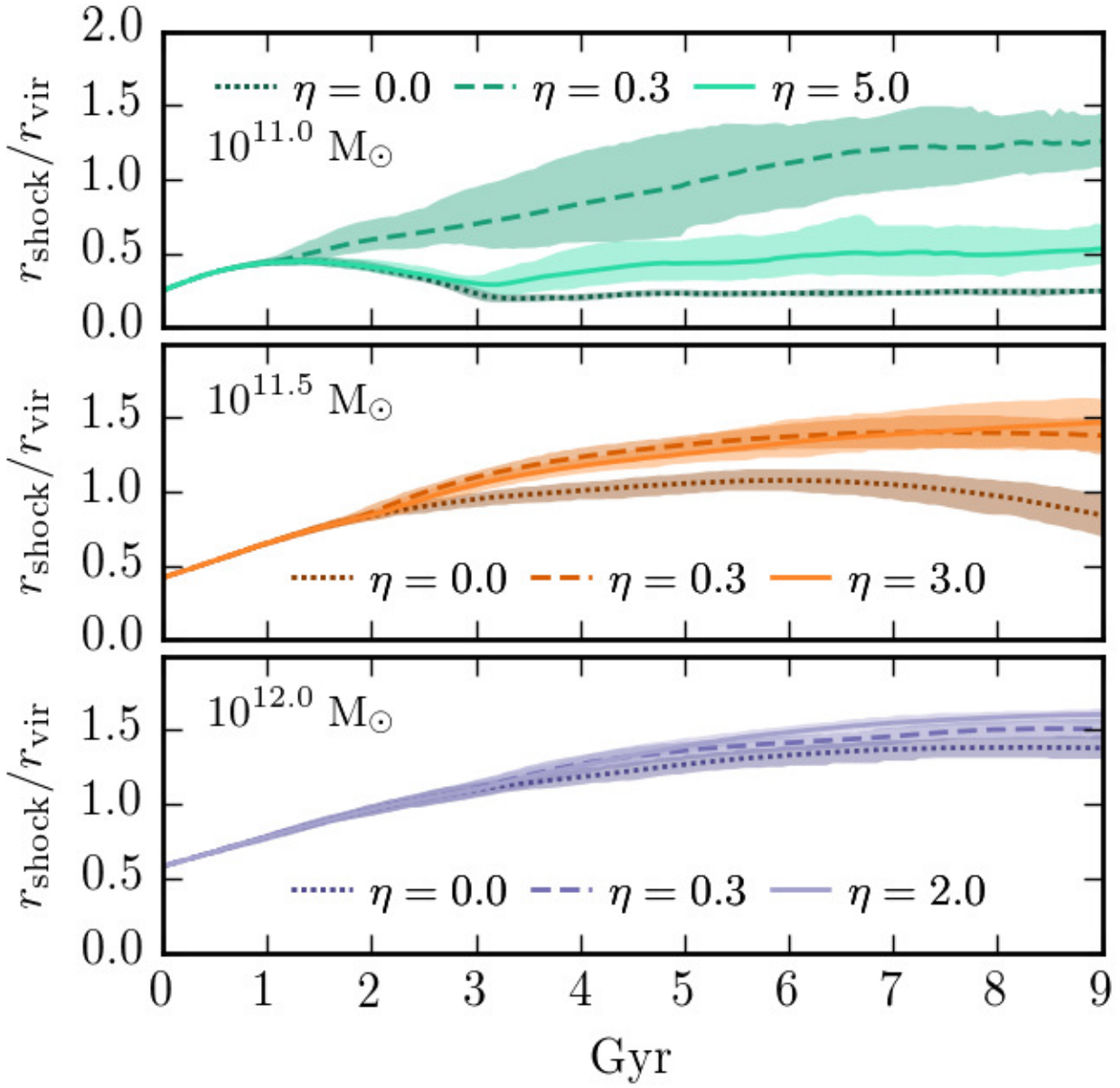


Figure 2.2: The shock radius evolution normalized by the virial radius for simulations with the feedback models listed in Table 2.1 ($\eta > 0$) and with no feedback ($\eta = 0$). The 'strong' feedback models for the $10^{11}$ M$_\odot$ halo are omitted for clarity. In both of these simulations the shock radius steadily increases reaching $2r_{\rm vir}$ by 6 Gyr. The shaded regions show the 1 $\sigma$ quantiles of the shock radii measured at different angles. The initial virial shocks in the higher mass haloes, $\geq 10^{11.5}$ M$_\odot$, gradually grow over time. Alternatively, in the $10^{11}$ M$_\odot$ haloes the initial virial shocks quickly become unstable to cooling and collapse, after which, in the simulations with feedback, incoming gas shocks directly on the outgoing galactic wind – this is highly aspherical and leads to a range of shock radii for the remainder of the simulation. The shock in the $10^{11}$ M$_\odot$ haloes is best interpreted as a 'wind shock' produced when inflowing gas meets outflowing galactic wind material. By contrast at higher masses, the shock is a canonical virial shock between inflow and a roughly hydrostatic halo. The impact of feedback on the longevity of the virial shock decreases with halo mass.

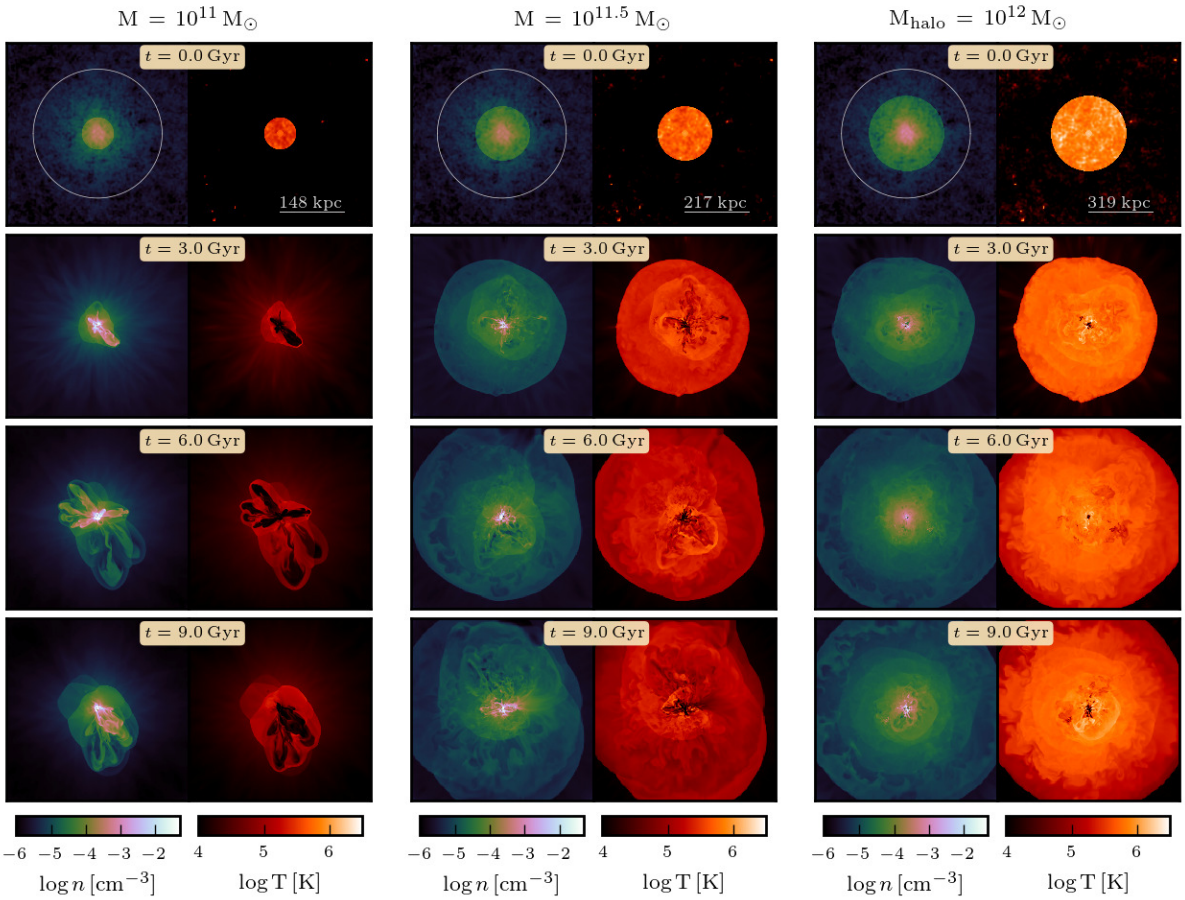


Figure 2.3: Number density and temperature slices at four times through the center of $10^{11}$, $10^{11.5}$, and $10^{12}$ $M_\odot$ haloes for the fiducial $\eta = 5$, 3, and 2 simulations, respectively (Table 2.1). The width of each image is 2.8 $r_{\rm vir}$. The circles and lines in the upper panels have a radius and length of $r_{\rm vir}$, respectively. In the $10^{11}$ $M_\odot$ halo the initial virial shock quickly collapses and the halo gas transitions to a less spherically symmetric configuration, supported by turbulent motions and ram pressure driven by stellar feedback. In the $10^{12}$ $M_\odot$ halo, the virial shock grows and feedback only affects gas in the core. The effects of changes to the feedback model can be seen in Figure 2.4, which shows the $10^{11}$ $M_\odot$ halo with a low $\eta$, higher $v_{\rm wind}$ feedback model.

resolution runs have two additional refined levels, which brings the spatial resolution to $\Delta x = r_{\rm vir}/228 = 1.4$ kpc $(M_{\rm halo}/10^{12}M_\odot)^{1/3}$. In Appendix 2.A we discuss our convergence study. We ran these simulations using as many as four levels of refinement and found our primary results well converged. Note, however, that we find a resolution dependence to the inherently non-linear process of cold clump condensation via thermal instability in more massive haloes. This is because the size of the fragments should be set by thermal conduction (which we do not include) to be approximately the Field length $\lambda_F$ (the maximum length scale over which conduction dominates cooling), which is $\lambda_F \lesssim 10$ pc $\ll \Delta x$ for $10^{-4}$ cm$^{-3}$ gas at $10^4$ K. This resolution dependence may have important implications for cosmological simulations, which may have difficulty resolving the thermal instability in halo gas.

## 2.4 Results

We now present the results of our $10^{11}$ to $10^{12}$ $M_\odot$ halo simulations that use both the high $\eta$ and the low $\eta$ feedback models as listed in Table 2.1. Simulations of $10^{13}$ $M_\odot$ haloes were similar to $10^{12}$ $M_\odot$ except for requiring a factor of ~2-3 more efficient feedback to suppress runaway cooling. We focus our attention on how the different feedback models change (or do not change) the resulting CGM structure and the central galaxies' growth. We find that in haloes with $M_{\rm halo} \gtrsim 10^{11.5}$ $M_\odot$ the CGM properties are relatively insensitive to the choice of feedback model for a wide range of feedback parameters. However, in lower mass haloes, $\lesssim 10^{11.5}$ $M_\odot$, the properties of halo gas depend more sensitively on differences in galactic wind properties.

The cooling rate of astrophysical plasmas ensures that (absent feedback) there is a critical halo mass, $\sim 10^{11.5}-10^{12}M_\odot$, which delineates different physical regimes of circumgalactic gas. Above this critical halo mass gaseous haloes can be thermally supported, but at lower halo masses they cannot (Silk, 1977; Rees & Ostriker, 1977; Binney, 1977; Birnboim & Dekel, 2003). This is due primarily to the fact that the cooling rate peaks around $10^{5.5}$ K, which is the virial temperature $T_{\rm vir}$ of a halo at $\sim 10^{11.5} - 10^{12}$ $M_\odot$, so the cooling time of the virialized gas is shorter relative to its free-fall time than it is in more massive haloes. Here we show that in the presence of galactic feedback the picture remains similar, but with the modification that in low mass haloes gas can instead be supported by the ram pressure and turbulence generated from vigorous feedback rather than by thermal pressure. The impact of feedback on either side of the critical halo mass is reflected in the evolution, galactic accretion history, phase structure, and pressure support of the CGM.

Figure 2.2 shows the accretion shock radius evolution in the simulations with both feedback models at all halo masses. For comparison we also show the shock radius evolution in simulations without any feedback, i.e., $\eta = 0$. To account for the lack of spherical symmetry, we measure the shock radius along 48 equally spaced rays emanating from the galaxy and plot the mean and the $1\sigma$ range. In the more massive haloes $\gtrsim 10^{11.5}$ $M_\odot$ the virialized gas remains stable for the duration of the simulations and the shock steadily grows with time. Feedback has a minor impact on the growth of the virial halo in the $10^{12}$ $M_\odot$ halo.

Going to lower masses the impact of feedback increases. Without feedback the virial shock of

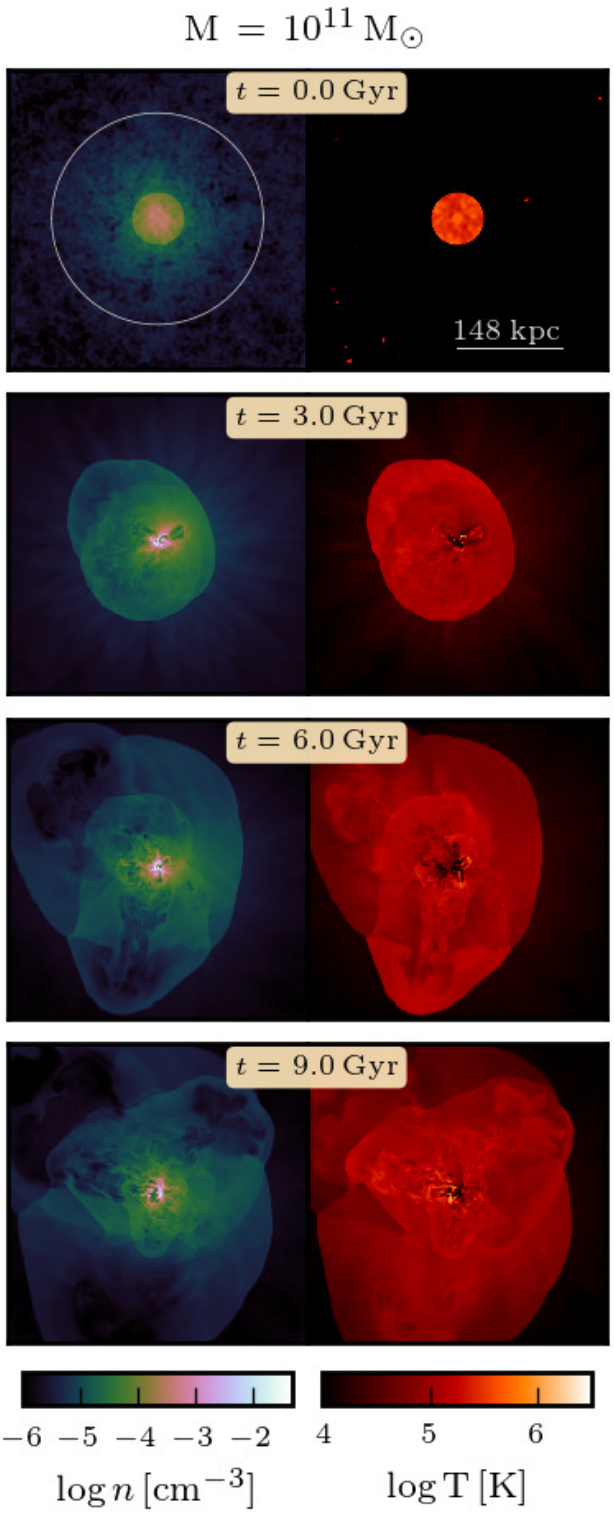


Figure 2.4: Number density and temperature slices at four times through the center of the $10^{11}$ $M_\odot$ halo with feedback having a higher energy per unit mass (the $\eta = 0.3$ and $v_{\rm wind} = \sqrt{4.5}v_{\rm esc}$ model in Table 2.1). The width of each image is 2.8 $r_{\rm vir}$. The circles and lines in the upper panels have a radius and length of $r_{\rm vir}$, respectively. The lower mass loading and higher wind velocity of this feedback model relative to the high $\eta$ model yield a much hotter and less dense gaseous halo (compare with Figure 2.3). We omit the analogous plots for the $10^{11.5}$ and $10^{12}$ $M_\odot$ haloes because in these cases there is visually little difference between the low $\eta$ feedback model and the high $\eta$ feedback model shown in Fig. 2.3.

the $10^{11.5}$ $M_\odot$ halo begins to collapse after $\sim$ 6 Gyr[5], but with feedback the virial shock radius is relatively insensitive to the choice of feedback parameters. In the $10^{11}$ $M_\odot$ haloes the initial virial shock quickly collapses, which is the same with or without feedback. The fact that after the initial collapse there is any shocked gas beyond $r_{\rm gal}$ is because feedback is driving gas out into the halo, which halts the progression of the inflowing gas. The wider range of shock radii at a given time relative to more massive systems is indicative of the transition from a canonical accretion shock, where inflowing gas hits a roughly hydrostatic, spherical atmosphere, to a 'wind' shock, where the inflowing material directly impacts outflowing wind ejecta. At this low halo mass the choice of feedback parameters makes a large difference for the resulting shock evolution. The low $\eta$ model, which has larger wind velocities and wind shock temperatures, is much more effective in halting the advance of large scale accreting gas. Moreover, in both of the 'strong' feedback models (with yet larger $v_{\rm wind}$, not shown in Figure 2.2), feedback is so efficient that the shock radius expands in certain directions to the outer boundary of the domain thereby entirely halting the inflow of gas and even launching gas beyond $r_{\rm ta}$.

Figure 2.3 shows density and temperature slices at several different times for haloes with masses of $10^{11}$, $10^{11.5}$, and $10^{12}$ $M_\odot$ with the (fiducial) high $\eta$ feedback efficiency model. In these images the rapid cooling of the initial virialized gas in the $10^{11}$ $M_\odot$ halo is readily apparent. After the virial shock collapse, inflowing gas at this halo mass directly interacts with gas expelled by the galactic wind producing a wind shock. The resulting wind shocks cool quickly because the shock temperature $T_{\rm shock} \sim T_{\rm vir}$ (since $v_{\rm wind} \sim v_{\rm esc}(r_{\rm gal}) \sim v_{\rm vir}$) and the cooling rate is very high at the virial temperatures for these halo masses – which is why the initial pressure supported gas collapsed quickly in the first place. These rapidly cooling shocks result in highly anisotropic outflows even though the galactic wind is ejected isotropically. This anisotropy is reflected in the large spread at late times in the measured shock radius in Figure 2.2. The outflows change direction on Gyr time-scales and inflowing gas that does not make it all the way to the galaxy is delayed for at most a few dynamical times.

Figure 2.3 demonstrates that the behavior is strikingly different in the only slightly more massive haloes. The gas in these higher mass haloes ($10^{11.5}$ and $10^{12}$ $M_\odot$) never experiences the dramatic total loss of thermal pressure support. In this case, inflowing gas from large radii is incorporated into the virialized halo via a virial shock and remains far from the central galaxy for many Gyr. However, cooling does occur in these haloes, but it is primarily in their cores. This cooling leads to inflow and subsequent feedback that in turn stabilizes the halo core against additional cooling.

As demonstrated in the shock radius evolution (Figure 2.2), the difference between feedback models is negligible in the higher mass haloes, but in the $10^{11}$ $M_\odot$ haloes the difference can be large. In Figure 2.4 we show density and temperature slices at several different times of the $10^{11}$ $M_\odot$ halo with the fiducial low $\eta$ feedback model ($\eta = 0.3$ and $v_{\rm wind} = \sqrt{4.5} v_{\rm esc}$; see Table 2.1). Relative to the fiducial high $\eta$ model, the halo is filled with much more hot, $> 10^5$ K, and diffuse, $< 10^{-4}$ cm$^{-3}$, gas. This halo gas remains suspended at large radii, $\sim r_{\rm vir}$, for much longer than the halo gas in

[5]In reality, over 6 Gyr this halo may have grown considerably, leading to a deeper potential, higher shock temperature, and less prominent cooling, so this turnover may be an artifact of our non-evolving dark matter potential.

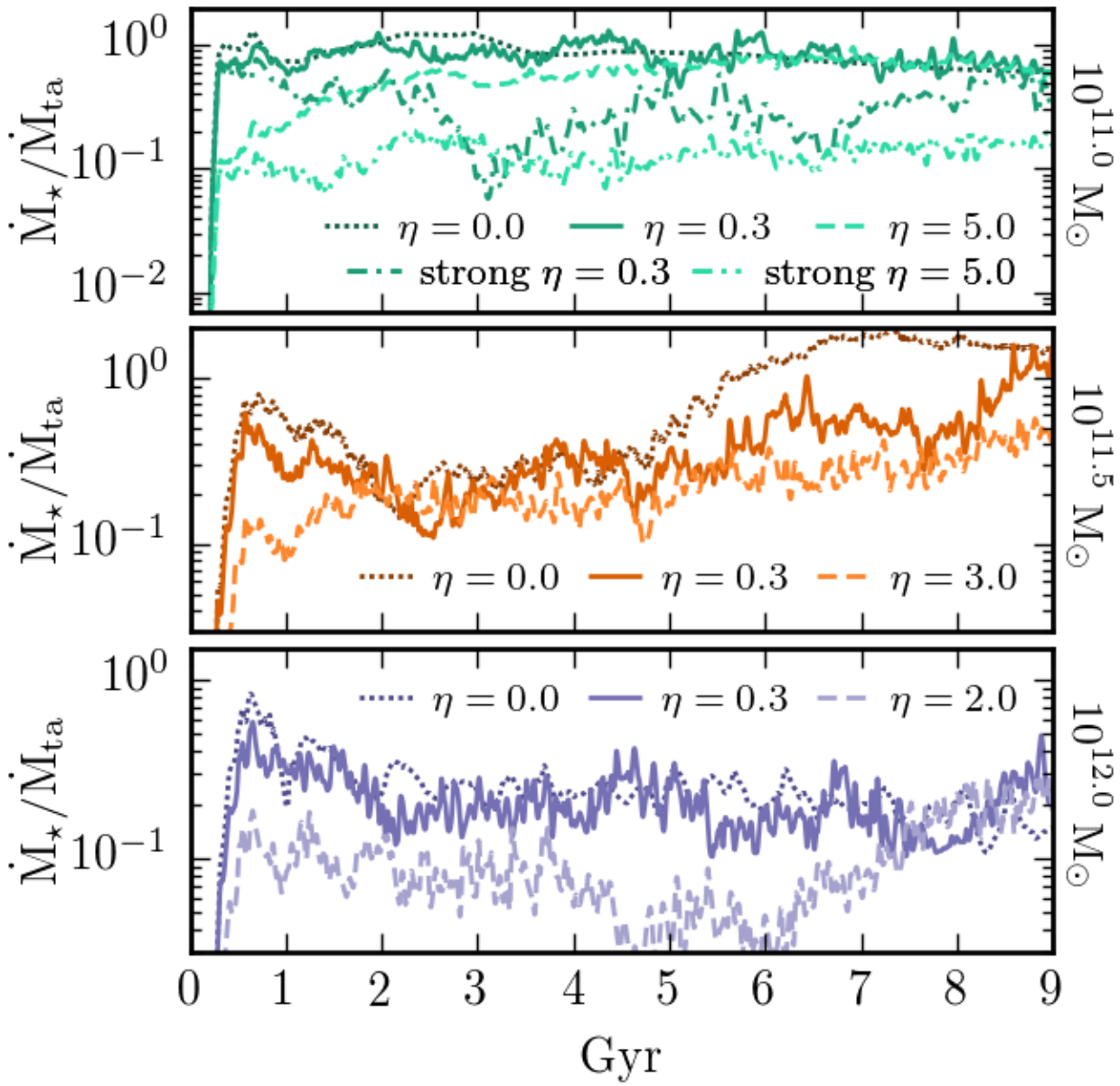


Figure 2.5: Star formation rate evolution for $10^{11}$, $10^{11.5}$, and $10^{12}$ M$_\odot$ haloes, from top to bottom. We show results from no feedback ($\eta = 0$), and a range of feedback parameters (see Table 2.1). Here the star formation rate is defined to be $\dot{M}_\star = \dot{M}_{in}/(1+\eta)$, where $\dot{M}_{in}$ is the inflow rate at $r_{gal}$; $\dot{M}_\star$ is also the rate at which gas is removed from the domain at each time step.

the high $\eta$ model due to its longer cooling time. Visually, the halo gas in the low $\eta$ $10^{11}$ $M_\odot$ simulation in Figure 2.4 resembles the virialized haloes at higher masses in Figure 2.3. However, as we discuss below (see Figure 2.11 and corresponding text), the halo gas in the low $\eta$ $10^{11}$ $M_\odot$ simulation in Figure 2.4 is not a standard thermally supported halo, but is instead supported to a large extent by bulk motions driven by the galactic wind.

Figure 2.5 shows the star formation rate normalized by the cosmological accretion rate that is fed into the haloes at the turn around radius, $\dot{M}_{ta}$, for simulations with and without feedback. Recall that we are defining the star formation rate as $\dot{M}_\star = \dot{M}_{in}(\eta + 1)^{-1}$ where $\dot{M}_{in}$ is the amount of gas that enters the 'galaxy,' which we model as a sphere of radius $r_{gal} = 0.025 r_{vir}$ at the center of the halo. In the $10^{11}$ $M_\odot$ haloes with the fiducial feedback models even though the galactic winds do arrest some of the inflowing gas, the star formation rate of the galaxy is approximately the same whether or not there is feedback and reaches $\dot{M}_\star \sim \dot{M}_{ta}$. With the strong feedback models, however, the powerful wind shock cuts the galactic gas supply, dropping $\dot{M}_\star$ by an order of magnitude. In the higher mass haloes the stable virial shock at large radii prevents most of the inflowing gas from reaching the galaxy. However, cooling in the halo cores leads to appreciable accretion on to the galaxy. In some cases, feedback at these halo masses suppresses the resulting star formation by up to a factor of $\sim 3 - 10$ by reheating the cores.

### 2.4.1 Phase structure and dynamics of halo gas

Figure 2.6 compares the radial profiles of spherically averaged number density and temperature averaged from 3 to 9 Gyr. The $10^{11}$ $M_\odot$ haloes with the strong feedback models are omitted for clarity[6]. As expected, for all masses the low $\eta$ feedback model (with higher $v_{wind}$) results in lower central densities and higher temperatures. The difference between the CGM structure that results from adopting either the low or the high $\eta$ feedback model becomes larger at lower halo masses. Additionally, lower mass haloes are more centrally concentrated. The $10^{11}$ $M_\odot$ halo has a density profile power law index $\lesssim -2$ – similar to or steeper than the underlying NFW profile – and the $10^{12}$ $M_\odot$ halo has a density profile power law index $\sim -1.5$. The density profiles of the $10^{12}$ $M_\odot$ haloes in Figure 2.6 are in good agreement with what is inferred in the Milky Way from OVII and OVIII emission (Miller & Bregman, 2015).

None of our haloes demonstrate a clear density core. Such cores are often used in phenomenological modeling of halo gas (e.g., Maller & Bullock, 2004; Sharma et al., 2012b; Voit et al., 2015). Previous studies with a similar approach to ours that focused on slightly more massive haloes ($\gtrsim 10^{13.5}$ $M_\odot$) found distinct density cores in their haloes at a radius of $\lesssim 0.05 r_{vir}$ (Sharma et al., 2012a). The lack of cores in our haloes may be a consequence of insufficient resolution close to the inner edge of our domain ($r_{gal} = 0.025 r_{vir}$), or the limited region of the $\eta - v_{wind}$ parameter space covered by our models. In particular, the feedback in our simulations, which is in the form of a galactic wind, tends to produce a roughly $r^{-2}$ density profile due to either inflow or outflow

[6]The profiles of the strong feedback $10^{11}$ $M_\odot$ haloes are similar to the fiducial feedback model $10^{11}$ $M_\odot$ haloes, but with slightly lower densities and higher temperatures.

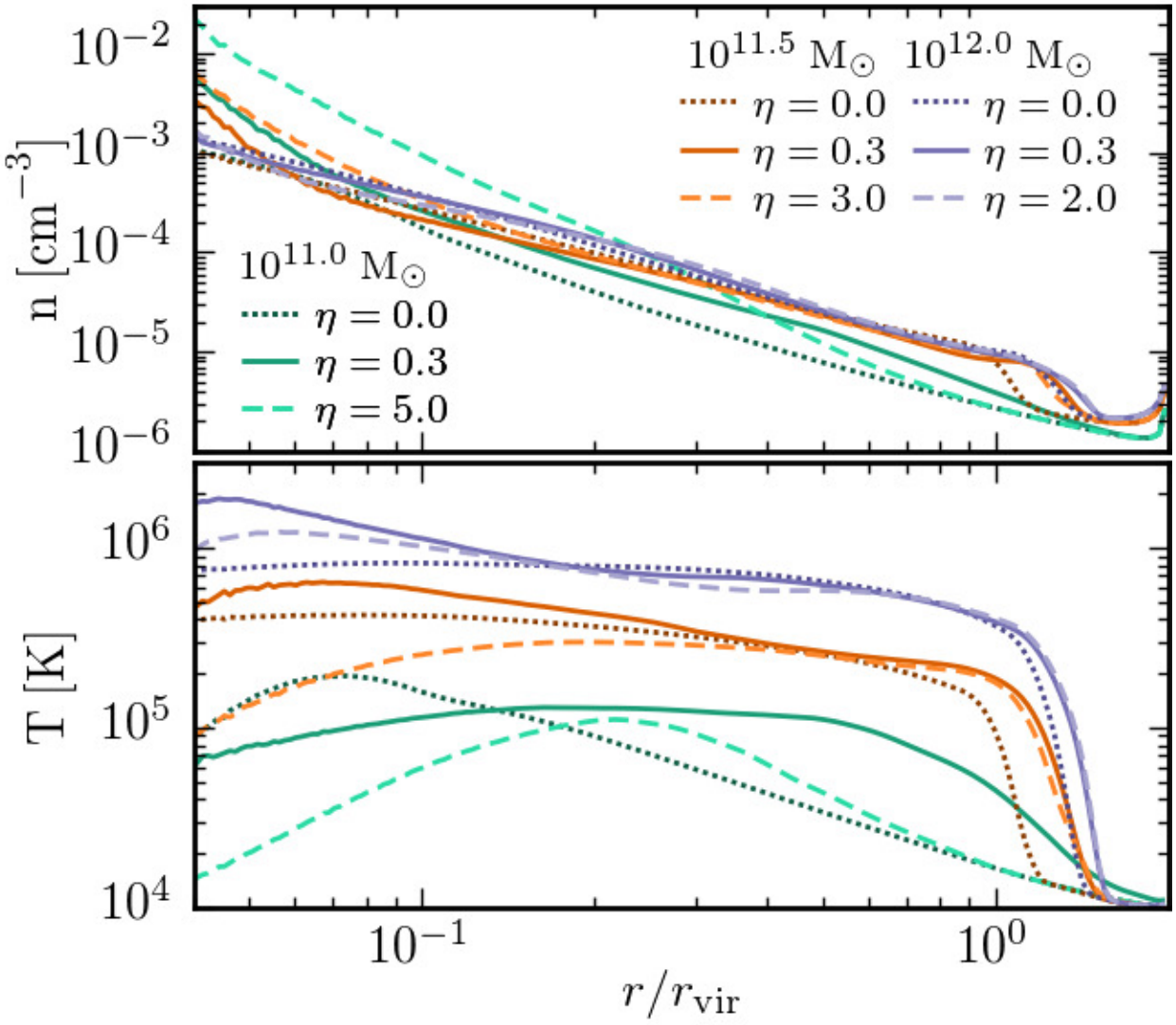


Figure 2.6: Radial profiles of the number density (top) and temperature (bottom) averaged from 3 to 9 Gyr for all halo masses with and without ($\eta = 0$) feedback. The $10^{11}$ M$_\odot$ haloes with the strong feedback models (Table 2.1) are omitted for clarity; their profiles are similar to but slightly more diffuse and hotter than the $10^{11}$ M$_\odot$ halo profiles shown. The radial range spans $\sim 2r_{\rm gal}$ to $r_{\rm ta} = 2r_{\rm vir}$. The impact of the feedback model becomes increasingly important in setting the structure of the CGM as halo mass decreases.

at small radii. Yet lower $\eta$ and higher $v_{\rm wind}$, or thermal feedback – as was used in Sharma et al. (2012a) – may be required to produce a significant density core.

Figures 2.7 and 2.8 show a different way of quantifying the thermal structure of the halo gas, via $d{\rm M}/d\log{\rm T}$, the mass contained in a given logarithmic bin in temperature. The radial range extends from $2r_{\rm gal}$ out to the outer boundary of the domain $2r_{\rm vir}$. Quantifying the amount of mass in different temperature regimes is directly related to many of the best observational constraints we have on the structure of the CGM. X-ray emission and absorption are sensitive to gas at $\geq 10^6$ K (e.g., Milky Way: Gupta et al. 2012; Miller et al. 2016, other galaxies: Forman et al. 1985; O'Sullivan et al. 2001; Mulchaey & Jeltema 2010; Anderson & Bregman 2011). In addition, UV absorption lines in the spectra of background quasars in dark matter haloes at these masses can be used to measure the amount of mass in different temperature regimes $\sim 10^4 - 10^{5.5}$ K (e.g., Steidel et al., 2010; Tumlinson et al., 2011; Rudie et al., 2012; Werk et al., 2014; Borthakur et al., 2015). Figure 2.7 shows the phase structure evolution for the (fiducial) high $\eta$ feedback models and for comparison Figure 2.8 shows the same quantity for the $10^{11}$ M$_\odot$ halo with the fiducial low $\eta$ feedback model (the difference between the feedback models in the two higher mass haloes is minor so they are not shown). The phase structure in the $10^{11}$ M$_\odot$ haloes with the strong feedback models (see Table 2.1) are similar to that shown in Figure 2.8.

With the fiducial high $\eta$ feedback model the vast majority of the mass resides at ${\rm T} \lesssim 10^{4.5}$ K in the $10^{11}$ M$_\odot$ halo, whereas with the low $\eta$ feedback model the wind is able to populate the intermediate temperature range, $\sim 10^{4.5} - 10^{5.5}$ K, with significant amount of gas. This is because of the longer cooling times of the wind shock heated gas with the larger $v_{\rm wind}$ in the low $\eta$ model. In the $10^{11.5}$ and $10^{12}$ M$_\odot$ haloes the majority of the mass is at the virial temperature $\sim 10^{5.5} - 10^6$ K. Cooling of the accretion shock heated gas, the formation of dense clumps by thermal instability, and cooling of galactic wind shocks eventually fill the intermediate temperature range. The origin of the intermediate temperature halo gas thus differs dramatically in haloes above and below $10^{11.5}$ M$_\odot$. Moreover, below $10^{11.5}$ M$_\odot$ the amount of gas in a given temperature regime – particularly the cool/warm $\sim 10^{4.5} - 10^{5.5}$ K regime is more sensitive to the feedback model. Alternatively, in the haloes with long lived thermal pressure support, $\gtrsim 10^{11.5}$ M$_\odot$, the amount of gas in a given temperature regime depends more on the mass of the halo and less (although non-negligibly) on the feedback physics.

The inhomogeneous density structure of our haloes can be seen in Figure 2.9 which shows the time averaged (from 3 to 9 Gyr), mass weighted density probability distribution function in radial bins extending from $2r_{\rm gal}$ to $1.25r_{\rm vir}$. Changing the range of times for the averaging makes essentially no difference, as long as a few dynamical times have elapsed, which allows any initial transients to pass (this is true for all of the time averaged plots we show despite the lack of a true equilibrium in Figures 2.7 and 2.8). The $10^{11}$ M$_\odot$ haloes with the strong feedback models are similar to the fiducial low $\eta$ model, so they are omitted. The $10^{11}$ M$_\odot$ haloes have significant amounts of mass in a broad range of densities extending from $\sim 10^{-6}$ cm$^{-3}$ – predominantly at large radii $\sim r_{\rm vir}$ – to $\gtrsim 10^{-2}$ cm$^{-3}$ – mostly in the halo cores. In a given radial bin the width of the density distribution spans more than an order of magnitude, and even relatively close to the galaxy, $\sim 0.5r_{\rm vir}$, there is an appreciable amount of gas at the low densities ($\sim 10^{-5}$ cm$^{-3}$) where photoionization dominates over collisional ionization. Going to higher masses the width of density

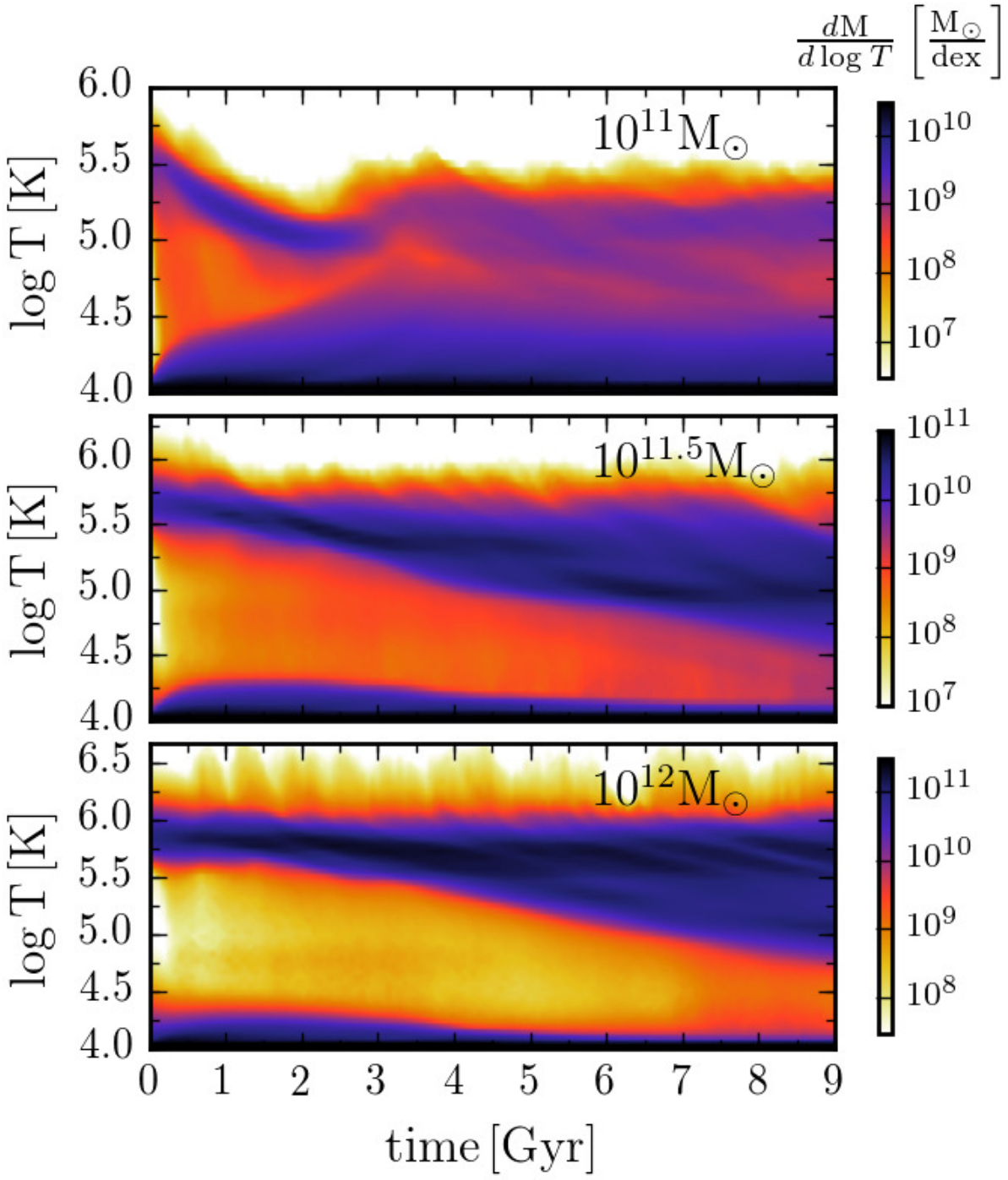


Figure 2.7: The amount of mass per logarithmic temperature bin over time between 2 $r_{\rm gal}$ and 2 $r_{\rm vir}$ is shown for the fiducial high $\eta$ feedback model simulations of all three halo masses. The two higher mass haloes cool slowly leading to modest amounts of $< 10^{5.5}$ K gas that cools out of a hotter ambient background. The $10^{11}$ $\mathrm{M}_\odot$ halo, on the other hand, cools quickly and all of the $\gtrsim 10^5$ K gas is a result of the galactic wind shocking on gas accreted from large scales. Figure 2.8 shows that in $\sim 10^{11}$ $\mathrm{M}_\odot$ haloes feedback with a larger energy per unit mass (lower $\eta$; Table 2.1) leads to a much broader phase distribution in the CGM.

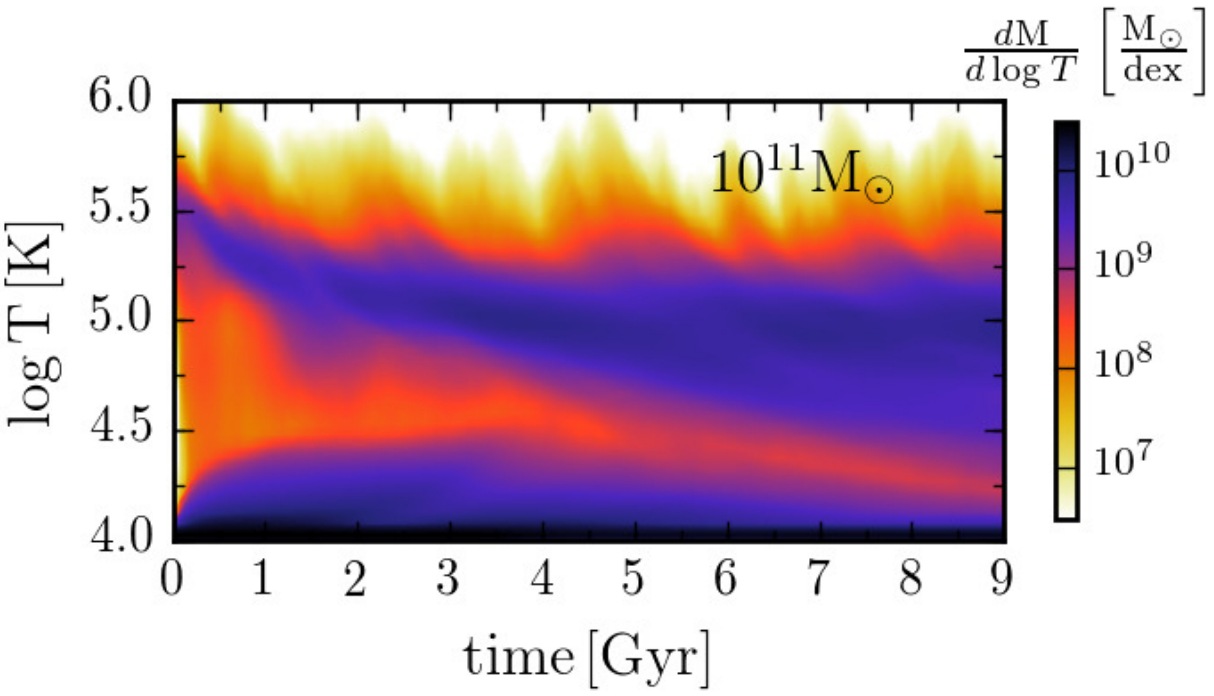


Figure 2.8: Amount of mass per logarithmic bin in $T$ for the $10^{11}$ $M_\odot$ halo with the fiducial low $\eta$ feedback model (Table 2.1). The lower mass loading and higher wind velocity of this feedback model lead to a substantial amount of warm gas ($10^5 - 10^6$ K); compare with Figure 2.7. The gas in this temperature regime is a result of galactic wind shocks and the resulting rapid cooling, not an accretion shock on to a static halo as is the case in $\gtrsim 10^{11.5}$ $M_\odot$ haloes.

distribution at a given radius shrinks, as do the differences that result from the different feedback models; this is also reflected in the density profiles shown in Figure 2.6.

Figure 2.10 shows the time averaged (from 3 to 9 Gyrs) density profiles for gas in three temperature bins, which are delineated relative to the haloes' virial temperatures. We also reproduce the density profiles for all of the gas as shown in Figure 2.6. For reference, the virial temperature is $T_{\rm vir} = 1.1\times10^5$K, $2.3\times10^5$K, and $5.1\times10^5$K for the $10^{11}$, $10^{11.5}$, and $10^{12}$ $M_\odot$ haloes, respectively. For each halo the super-virial temperature bin is populated by gas that has been shock heated when the wind material interacts with the ambient CGM. The density of this hot gas in $\leq$ $10^{11.5}$ $M_\odot$ haloes is sensitive to the feedback parameters. The low $\eta$ models have higher wind shock temperatures because of their higher $v_{\rm wind}$ and they also have lower wind densities by definition. This results in more volume filled by the super-virial gas. In addition, in the low $\eta$ models this hot gas extends to larger radii, but has lower density, than in the high $\eta$ models[7]. Observations of gas in this super-virial temperature range would therefore be very useful in constraining the properties of galactic winds; however, to date, most CGM observations are sensitive to gas at $T < 10^{5.5}$K $\lesssim T_{\rm vir}$.

[7]Note that this is true in the 'strong' $10^{11}$ $M_\odot$ haloes, but at densities below those shown in Figure 2.10.

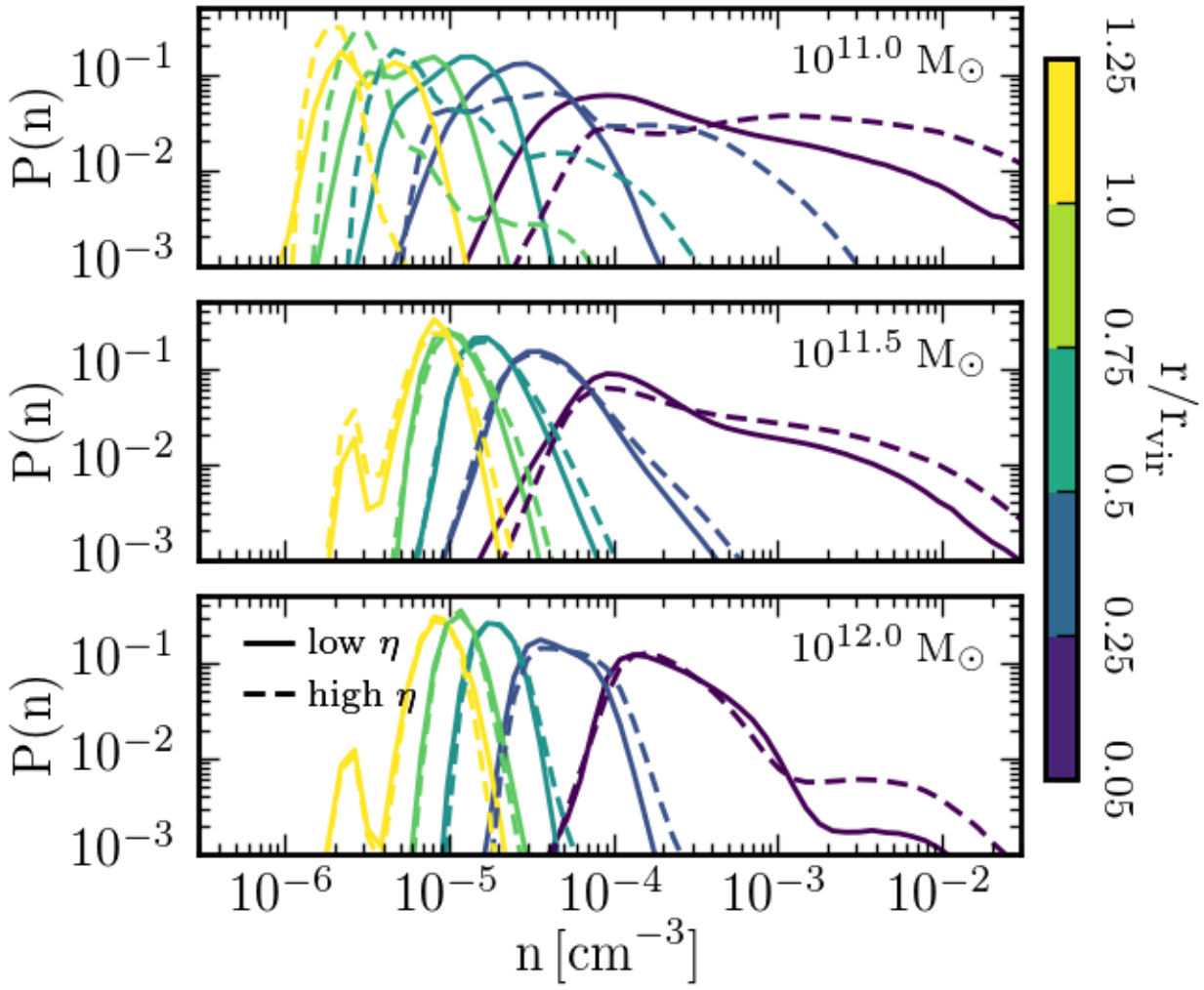


Figure 2.9: The time averaged (from 3 to 9 Gyr), mass weighted density probability distribution function in radial bins. The yellow line corresponds to 1.25 to 1 $r_{vir}$, the green line to 1 to 0.75 $r_{vir}$, the teal line to 0.75 to 0.5 $r_{vir}$, the blue line to 0.5 to 0.25 $r_{vir}$, and the purple line to 0.25 to 0.05 $r_{vir}$ = 2 $r_{gal}$. Halo mass increases from top to bottom, and the low and high $\eta$ feedback models are plotted with solid and dashed lines, respectively. The $10^{11}$ M$_\odot$ haloes with the strong feedback models are omitted because they are similar to the fiducial low $\eta$ model shown here. The peak around $2 \times 10^{-6}$ cm$^{-3}$ corresponds to undisturbed cosmologically accreted gas. The $10^{11}$ M$_\odot$ halo gas has a broader range of densities at a given radius, due to the larger impact of stellar feedback on the CGM.

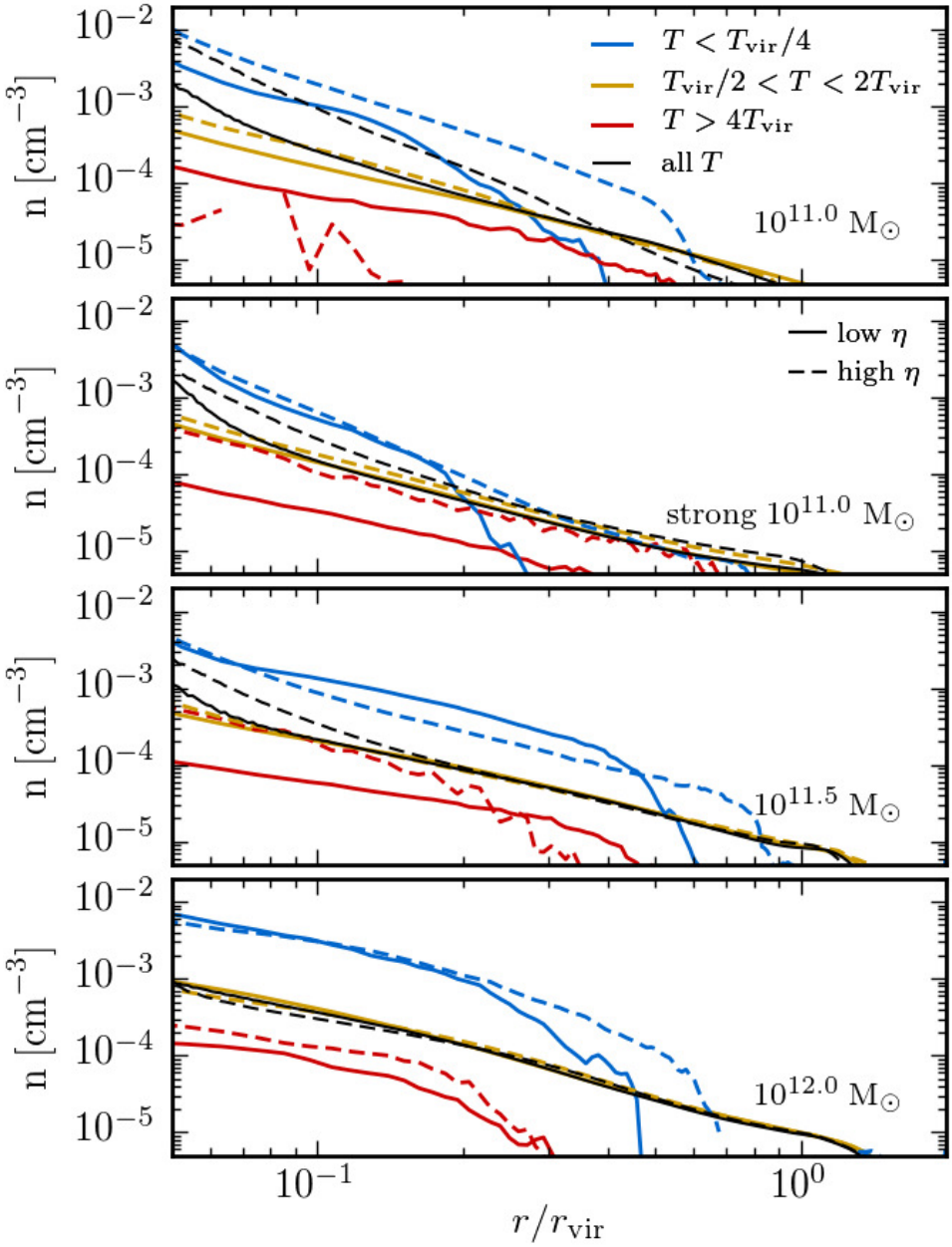


Figure 2.10: The time averaged (from 3 to 9 Gyr) number density profiles of gas in three temperature bins. The hot gas with $T > 4T_{\rm vir}$, virialized gas with $T_{\rm vir}/2 < T < 2T_{\rm vir}$, and cold gas with $T < T_{\rm vir}/4$ are shown in red, gold, and blue, respectively. For reference, the black lines show the number density profiles for gas at all temperatures – same as in Figure 2.6. The solid (dashed) lines correspond to the low (high) $\eta$ feedback models.

Fortunately, the cold gas properties also change in key ways with halo mass and feedback model, which should allow existing and future observations of the cold CGM to constrain galactic wind properties. Focusing on the density profiles of the cold gas in Figure 2.10 (blue line; $T < T_{\rm vir}/4$) it is clear that in all cases the high $\eta$ model result in cold gas out to larger radii. We can gain even more insight and constraining power by comparing the cold gas profiles of the more massive haloes ($10^{12}$ M$_\odot$) that have almost entirely virialized hydrostatic haloes to those of the lower mass haloes ($10^{11}$ M$_\odot$) that have more rapid cooling and more vigorous winds and turbulence. In the high mass haloes the cold gas has very high central densities ($\sim 10^{-2}$ cm$^{-3}$) that decreases slowly with radius until it reaches a sharp cut off at a few $\times 0.1 r_{\rm vir}$. By contrast, in the lower mass haloes the cold gas typically has a slightly lower central density ($\sim 3 \times 10^{-3}$ cm$^{-3}$) that decreases more quickly with radius. In the intermediate halo mass of $10^{11.5}$ M$_\odot$ the cold gas profile with the low $\eta$ feedback model resembles that of the higher mass haloes, while the high $\eta$ feedback model results in a profile that resembles that of the lower mass haloes. Physically, the difference between these profiles is due to the degree of pressure confinement. In the higher mass haloes the cold gas is predominantly surrounded by much hotter, confining gas that drives its density up (see Figure 2.12 for an example density and temperature maps that show these pressure confined cold clumps). This is true for both the cold gas launched by the wind and for cold gas that forms as a result of thermally instability. It is worth noting that this cold gas is under-pressurized relative to the virialized gas by a factor of $\sim 2-3$; however, these cold clumps are only marginally resolved in our simulations so we avoid drawing too strong conclusions from this fact (see Figure 2.A.1).

In contrast to the higher mass haloes, in the lower mass haloes the rapid cooling of virialized gas diminishes the pressure confining medium while continually driving gas down to low temperatures. This populates the low temperature regime without forcing the densities of the cold gas up. Additionally, the rapid cooling even at large radii and the vigorous feedback triggered by the accretion of cold gas drives cold gas out to large radii.

The different contributions to the total pressure support in our simulated haloes are shown in Figure 2.11. We plot the density-weighted radial (from $r_{\rm gal}$ to $r_{\rm vir}$) and time (from 3 to 9 Gyr) averaged sound speed $c_s$, radial velocity $v_r$ (here we adopt $v_r > 0$ for gas flowing toward the center), and velocity dispersion $\sigma = \sqrt{\langle v(r)\rangle^2 - \langle v(r)^2\rangle}$ (all normalized by the halo virial velocity $v_{\rm vir} = \sqrt{G{\rm M}_{\rm halo}/r_{\rm vir}}$. To convert to a velocity in km s$^{-1}$, the halo virial velocities $v_{\rm vir}$ are given in Table 2.1). The sound speed traces the thermal pressure, the velocity dispersion traces turbulent support, and the radial velocity gives a measure of how under ($v_r/v_{\rm vir} > 0$) or over ($v_r/v_{\rm vir} < 0$) pressurized the halo gas is relative to hydrostatic equilibrium. Figure 2.11 quantifies the strong dependence of the halo gas dynamics on the halo mass. In the $10^{12}$ M$_\odot$ haloes changes to feedback make little difference to the pressure support. The gas in these haloes is almost entirely thermal pressure supported ($c_s \sim v_{\rm vir}$) and close to hydrostatic equilibrium ($v_r/v_{\rm vir} \sim 0$). Going to lower masses, the halo gas is farther from hydrostatic equilibrium, the contribution from thermal pressure support decreases, and the contribution of turbulent pressure support increases. Moreover, as we have seen with other CGM properties, the sensitivity of the different pressure contributions to the feedback model increases as halo mass decreases. These trends support the interpretation that the differences in cold gas profiles shown in Figure 2.10 are due to more virialized, pressure confining

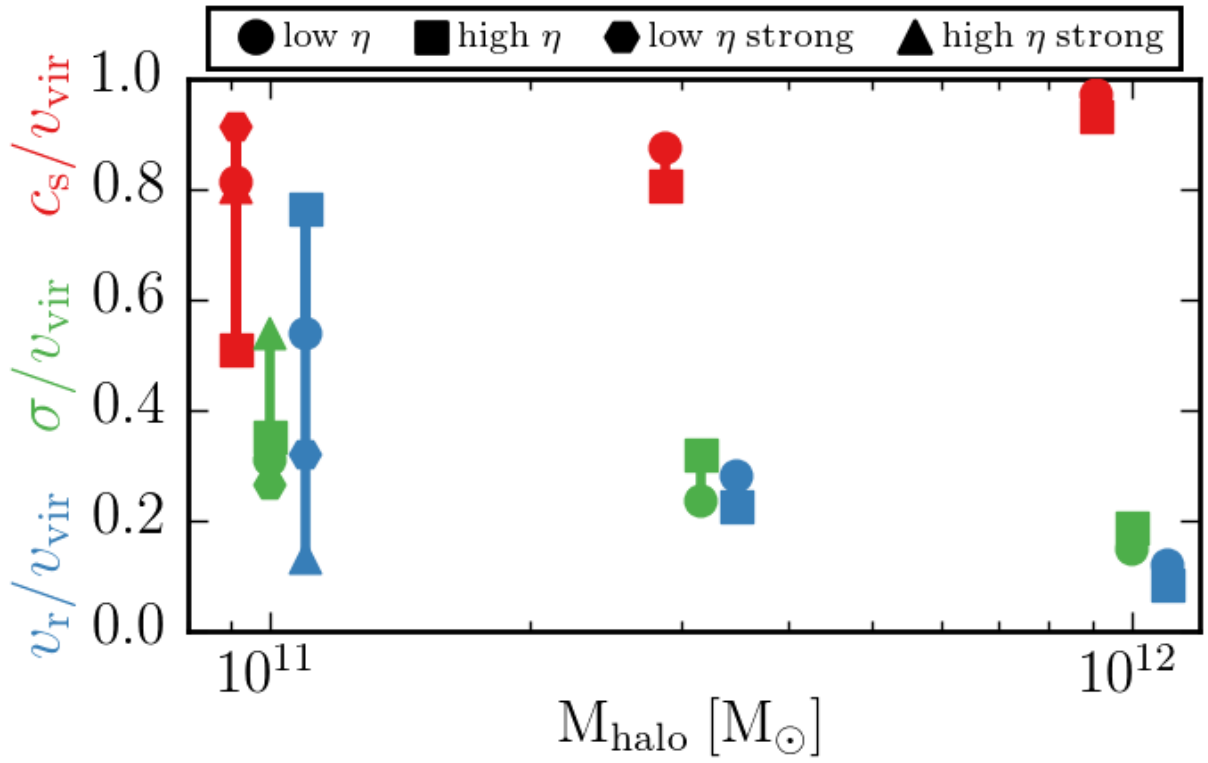


Figure 2.11: Time and mass-weighted radial average of the sound speed (red; shifted to the left by 0.1 dex), velocity dispersion (green), and radial velocity (blue, positive indicates inward motion; shifted to the right by 0.1 dex) normalized by the halo's virial velocity (Table 2.1). The averaging is done from 3 to 9 Gyrs. Large $c_s/v_{\rm vir}$ indicates the haloes gas is thermally supported, large and positive $v_r/v_{\rm vir}$ indicates the halo gas is primarily freely falling in and under pressurized relative to hydrostatic equilibrium, and large $\sigma/v_{\rm vir}$ indicates turbulent support. The $10^{12}$ $M_\odot$ halo gas is primarily thermal pressure supported, while in lower mass haloes bulk flows (turbulence, inflows, and outflows) are increasingly important.

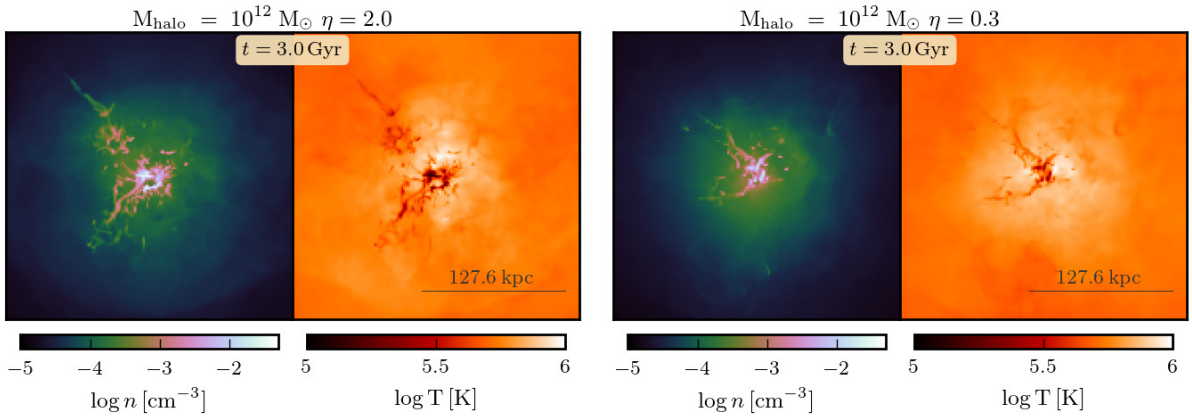


Figure 2.12: The line-of-sight density weighted average number density and temperature in the centers of the two $10^{12}$ $M_\odot$ haloes after 3 Gyr of evolution. Cold, dense clumps are evident within $\sim$ 100 kpc of the central galaxy. The left (right) two images are from the high (low) $\eta$ feedback simulations. The images are $0.8r_{vir}$ = 255 kpc across.

gas in higher mass haloes, and more energy in bulk flows to support cold gas at large radii in lower mass haloes.

### 2.4.2 Thermal instability in the cores of massive haloes

In the more massive haloes ($\gtrsim 10^{11.5}$ $M_\odot$) feedback does little to modify the bulk of the CGM out near $r_{vir}$. However, in their cores the cooling times can be significantly shorter than both a Hubble time and the duration of the simulation. This short cooling time leads to significant inflowing gas and star formation. As is shown Figure 2.5 the resulting galactic wind can in some cases lower the star formation rate by a factor of a few up to an order of magnitude. An analogous scenario occurs in group and cluster mass haloes ($M_{halo} \gtrsim 10^{13.5} M_\odot$). In these systems central cooling times imply large star formation rates that are inconsistent with observations and point to a heating source that is capable of preventing a cooling flow (e.g., McNamara & Nulsen 2007). At this higher halo mass the central heating source is usually assumed to be an active galactic nucleus (AGN), fueled by gas cooling out of the hot halo. The net inflow of cool gas is significantly larger when the hot halo gas is thermally unstable, which requires $t_{cool}/t_{ff} \lesssim 10$ (McCourt et al., 2012; Sharma et al., 2012a; Li et al., 2015). When this condition is satisfied the cold phase rains out on to the central galaxy and triggers enough feedback to reheat the ambient medium and extend the cooling time before the full cooling flow develops. Gas continues to rain out until the feedback drives $t_{cool}/t_{ff} > 10$. Much of the work to date on this global feedback regulation of hot haloes has focused on more massive systems than we consider here and in the regime of the $\eta$-$v_{wind}$ parameter space appropriate for AGN feedback – lower $\eta$ and higher $v_{wind}$. This same sort of thermal instability regulation may occur in the halo mass range we consider. Indeed, Figure 2.12,

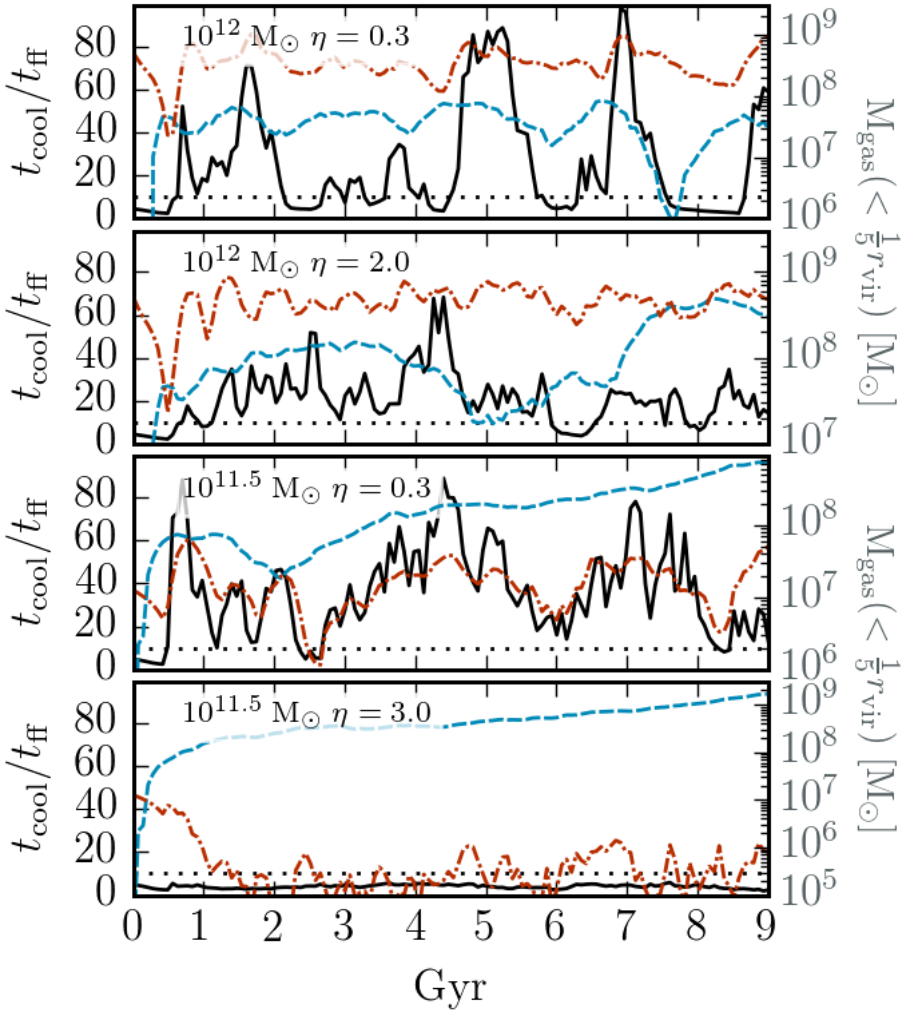


Figure 2.13: Spherical shell averaged $t_{\rm cool}/t_{\rm ff}$ evolution at $r = 3r_{\rm gal} = 0.075\ r_{\rm vir}$ for the $10^{12}$ M$_\odot$ halo simulation with the low $\eta$ (top) and high $\eta$ (upper middle) feedback model, and for the $10^{11.5}$ M$_\odot$ halo simulation with the low $\eta$ (lower middle) and high $\eta$ (bottom) feedback model. We measure $t_{\rm cool}$ in the hot gas ($> T_{\rm vir}$) only. A thin dotted line is drawn at $t_{\rm cool}/t_{\rm ff} = 10$, the value below which thermal instability is predicted to lead to multiphase gas and large accretion rates of cold gas. Additionally, in each panel we plot the amount of cold ($< 10^{4.5}$ K, blue dashed line) and hot ($> 10^6$ K, red dot-dashed line) gas contained within $0.2\ r_{\rm vir}$. In the top three panels the core gas spends most of its time with $t_{\rm cool}/t_{\rm ff} > 10$ with occasional forays down to $t_{\rm cool}/t_{\rm ff} \lesssim 10$. By contrast, in the $10^{11.5}$ M$_\odot$ halo with high $\eta$, $t_{\rm cool}/t_{\rm ff} < 10$ at all times. In the $10^{12}$ M$_\odot$ halo with low $\eta$ (top) changes to the cold gas mass correlate particularly well with $t_{\rm cool}/t_{\rm ff}$, a signature of thermal instability.

which shows the presence of cold, dense clumps in the cores of the $10^{12}$ $M_\odot$ simulations, seems to demonstrate this thermal instability triggered precipitation.

To quantitatively assess the role of thermal instability Figure 2.13 shows the time evolution of $t_{\rm cool}/t_{\rm ff}$ for the hot gas with $T > T_{\rm vir}$ at $3r_{\rm gal} = 0.075r_{\rm vir}$ in the $10^{11.5}$ and $10^{12}$ $M_\odot$ halo simulations with both feedback models (We omit the $10^{11}$ $M_\odot$ haloes because they are similar to the high $\eta$ $10^{11.5}$ $M_\odot$ halo in that the hot gas cooling time is always less than its free fall time). Also shown is the amount of cold ($< 10^{4.5}$ K, blue dashed line) and hot ($> 10^6$ K, red dot-dashed line) gas contained within $0.2r_{\rm vir}$. In all but the high $\eta$ feedback $10^{11.5}$ $M_\odot$ halo, $t_{\rm cool}/t_{\rm ff} > 10$ most of the time with occasional dips below $\sim 10$. Distinguishing cold clump condensation due to thermal instability and cooling triggered by wind shocks (or other sources of cold gas) is non-trivial (which may explain the similarity in Figure 2.12 and the difference in Figure 2.13). Note, however, that the cold gas content in the low $\eta$ feedback model $10^{12}$ $M_\odot$ halo only rises when $t_{\rm cool}/t_{\rm ff} < 10$, and that these increases precede an increase in hot gas. These are strong indicators of the same type of thermal instability regulation as is seen in simulations of high mass haloes. In the other simulations that have $t_{\rm cool}/t_{\rm ff} > 10$ (the high $\eta$ $10^{12}$ $M_\odot$ and the low $\eta$ $10^{11.5}$ $M_\odot$ haloes) this correlation is less obvious, so definitively determining if thermal instability triggered feedback plays any role is more difficult. The haloes that do not show the clear signs of thermal instability have more vigorous turbulence in their cores (see Figure 2.11). Rapid turbulent mixing relative to the thermal instability growth time-scale can render the instability ineffective (Parrish et al., 2010; Ruszkowski & Oh, 2010). The increased turbulence is tied to the fact that the feedback is primarily kinetic rather than thermal. In the simulations of thermal instability triggered feedback in more massive haloes the feedback models have relatively high energy per unit mass or are purely thermal (e.g., Sharma et al., 2012a; Gaspari et al., 2012; Li et al., 2015). The absence of clear signatures of thermal instability triggered feedback in our haloes with more turbulent supported cores may indicate the need for thermal feedback for this regulation to work.

The hot gas in the cores of the $10^{11}$ $M_\odot$ haloes and in the high $\eta$ $10^{11.5}$ $M_\odot$ halo never has $t_{\rm cool}/t_{\rm ff} \gtrsim 10$ (for much of the time $t_{\rm cool} \lesssim t_{\rm ff}$), which demonstrates that thermal instability triggered feedback is not a dominant process. Therefore, models of the impact of thermal instability on galaxy formation should not be extended to lower mass haloes, $\lesssim 10^{12}$ $M_\odot$ (Voit et al., 2015).

### 2.4.3 Connection to Quasar Absorption Observations

Here we briefly present additional analysis of our simulations for comparison to quasar absorption observations of the $z \sim 0$ CGM (e.g., Tumlinson et al., 2013; Danforth et al., 2016). These studies have enabled measurements of the column density of low-ionization state metals and neutral hydrogen at $T \sim 10^4$ K (Werk et al., 2014), medium ionization state gas at $T \sim 10^5$ K (Bordoloi et al., 2014), and higher ionization state gas at temperatures up to $\sim 10^{5.5}$ K (Tumlinson et al., 2011). Additionally, the velocity offset of the halo gas relative to its host galaxy gives a measure of the line-of-sight velocity.

The simplifications inherent to our idealized setup make detailed comparisons between our results and observations suspect. However, a rough comparison can be fruitful, particularly for understanding the trends with changes in halo mass and feedback models. The gas fractions of our

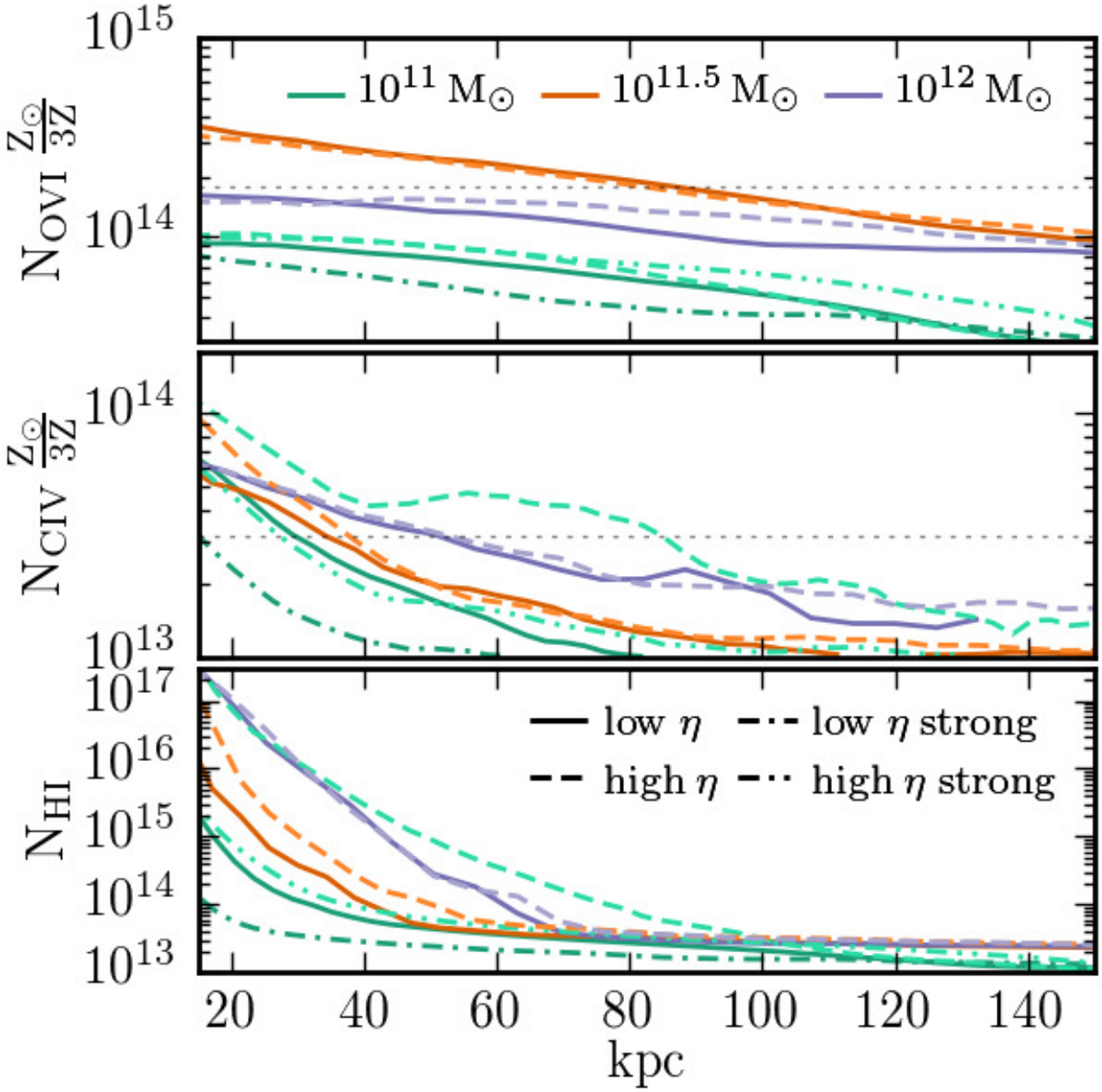


Figure 2.14: O VI (top), C IV (middle), and H I (bottom) column density profiles in units of $cm^{-2}$ for all of our simulated haloes, time averaged from 3 to 9 Gyrs. Our simulations assume a fixed third solar metallicity everywhere so the inferred O VI and C IV column densities can be roughly (not exact because cooling changes) scaled up or down proportional to the metallicity. The thin dotted lines in the top two panels demarcate the low end of the observed column densities – the average measurements are ~0.3-0.5 dex higher – detected by the COS-haloes team (O VI; Tumlinson et al. 2011) and the COS-Dwarfs team (C IV; Bordoloi et al. 2014). The maximum impact parameters of these O VI and C IV detections are 150 and 100 kpc, respectively. The H I column densities in our haloes are several orders of magnitudes lower than are observed (Tumlinson et al., 2013), which may be due physics missing from our simulations.

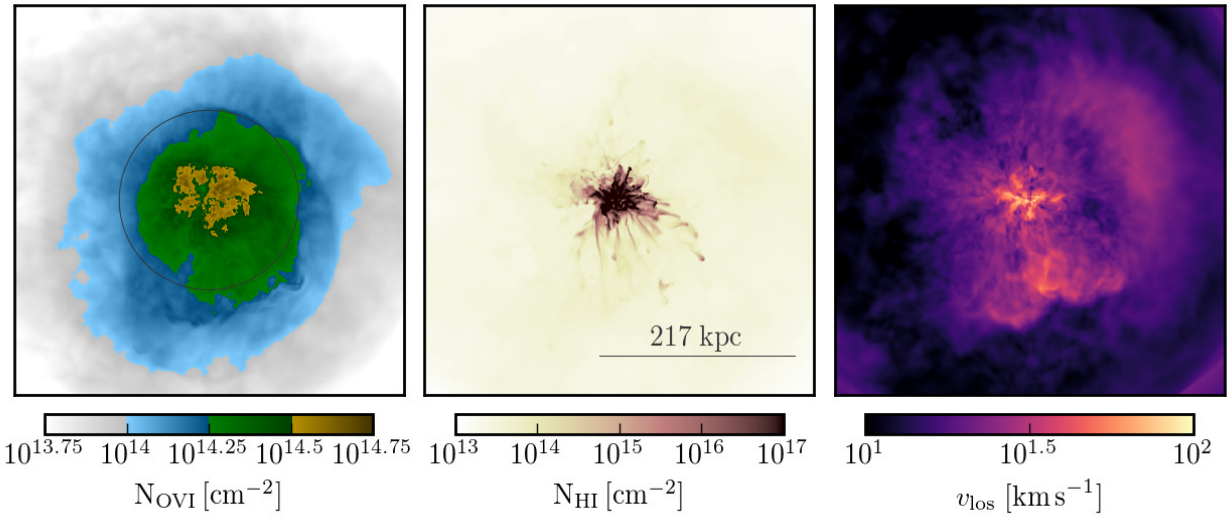


Figure 2.15: Maps of the O VI (left) and H I (middle) column density, and density weighted average line-of-sight velocity (right) from the $10^{11.5}$ $M_\odot$ halo with the high $\eta$ feedback model after 6 Gyr of evolution. The circle in the left panel has a radius of 100 kpc, and the line in the middle panel is $r_{vir}$ long. All three images are $2r_{vir}$ = 434 kpc across.

simulated haloes at late times range from $\sim$ 0.15 ($10^{11}$ $M_\odot$) to $\sim$ 0.25 ($10^{12}$ $M_\odot$) of the cosmic baryon fraction, only a factor of $\lesssim 2$ below what is found at $z = 0$ in cosmological simulations with stellar feedback (e.g., van de Voort et al., 2016). To compare our halo gas properties to observations in more detail, Figure 2.14 shows the O VI, C IV and H I column densities averaged from 3 to 9 Gyrs in all of our simulated haloes with feedback. The ionization state of the oxygen and carbon, which depends on temperature and density, is calibrated to ionization equilibrium models calculated using CLOUDY (Ferland et al. 1998). The neutral hydrogen fraction is approximated using an analytic fit to full radiative transfer simulations (Rahmati et al., 2013). Figure 2.15 shows an O VI and an H I column density map, as well as a density weighted line-of-sight velocity map for the high $\eta$ $10^{11.5}$ $M_\odot$ halo. Note that our simulations have a fixed third solar metallicity throughout the domain. For this reason, we explicitly add the metallicity dependence to the average O VI and C IV column density profiles shown in Figure 2.14.

The O VI column density profiles shown in the top panel of Figure 2.14 are similar to those measured by Tumlinson et al. (2011) who found that star forming galaxies presumed to be $\sim$ $10^{12}$ $M_\odot$ haloes have $N_{O\,VI} > 10^{14.25}$ cm$^{-2}$ out to $\lesssim$ 150 kpc. Additionally, the observed covering fraction of O VI gas is $\sim$0.8 – 1, which is in excellent agreement with our $10^{11.5}$ and $10^{12}$ $M_\odot$ haloes. The O VI column density map in the left panel of Figure 2.15 demonstrates this high cover fraction. We find that the O VI column density peaks in haloes with mass $\sim$ $10^{11.5}$ $M_\odot$. A recent study that accounted for non-equilibrium ionization found that the observed star formation rate dependence of the halo O VI content may be primarily driven by a halo mass dependence, similar to what we

find, albeit peaking at slightly higher halo masses of $\sim 10^{12}$ $M_\odot$ (Oppenheimer et al., 2016).

Figure 2.14 shows that the $\sim 10^{11.5}$ $M_\odot$ haloes' O VI column densities have essentially no dependence on the feedback model. This is because the fraction of collisionally ionized oxygen in the O VI state peaks at $T \approx 10^{5.5}$K, which is $\sim T_{\rm vir}$ at this halo mass. Therefore, in $\sim 10^{11.5}$ $M_\odot$ haloes O VI traces the virialized gas, and, as we have shown, changes to the feedback model have little impact on the amount and structure of virialized gas at these halo masses. In the higher mass haloes, on the other hand, O VI instead traces gas that is somewhat cooler than the virialized gas, so it is gas that has cooled out of the hotter medium or has been launched out of the galaxy by the wind. O VI in $\sim 10^{11}$ $M_\odot$ haloes traces gas that is above $T_{\rm vir}$, so it's presence is entirely due to feedback, which explains why the O VI column density depends more sensitively on feedback at this halo mass.

The fraction of carbon in the C IV ionization state peaks at $\sim 10^5$K. The C IV column density profiles shown in the middle panel of Figure 2.14 are similar to what was measured by Bordoloi et al. (2014) who found that $10^{11} - 10^{11.5}$ $M_\odot$ haloes have $N_{\rm C\,IV} > 10^{13.5}$ cm$^{-2}$ out to $\lesssim 100$ kpc. As with the O VI, the C IV column densities of our haloes are on the low end of the observations, but given the simplifications of our simulations and the assumption of constant metallicity the agreement is encouraging. The most striking feature of the C IV column profiles is the large differences between the profiles of the $10^{11}$ $M_\odot$ haloes with different feedback models. This is expected from the large difference in the resulting CGM phase structure which is shown in the top panel of Figure 2.7 and Figure 2.8. Therefore, C IV can be used to constrain the nature of galactic winds. Indeed, Bordoloi et al. (2014) demonstrated the efficacy of this technique by comparing their observations to simulations that use two different feedback models. Our results in Figure 2.14 qualitatively favor models with large mass loading $\eta$ and modest wind speeds.

Observations of H I around $z \sim 0$ $L^*$ ($M_{\rm halo} \approx 10^{12}$ $M_\odot$) galaxies find typical column densities of $\gtrsim 10^{16.5}$ cm$^{-2}$ at $\sim$ 75kpc (Thom et al., 2012; Werk et al., 2014), and $\sim 10^{14.5}$ cm$^{-2}$ at $\sim$ 150 kpc (Prochaska et al., 2011). The H I content of our simulations, shown in Figures 2.14 and 2.15 (middle panel), are below the observed values by an order of magnitude or more. This discrepancy is similar to what has been found in cosmological simulations (e.g., Hummels et al., 2013). Note that the $N_{\rm H\,I}$ of the $10^{11}$ $M_\odot$ haloes in the central $\sim$ 60kpc varies by up to two orders of magnitude depending on the feedback model. Matching the observed column densities of cooler gas $\lesssim 3\times10^4$ K that is traced by H I with hydrodynamic simulations is challenging because of the stringent spatial resolution requirements necessary to resolve this phase. Observations of the cold CGM at higher redshift, $z \sim 1-2$, imply clump sizes ($\ell \sim N/n$) on the order of $\lesssim$ 10pc (e.g. Prochaska & Hennawi, 2009; Hennawi et al., 2015). There are some claims, however, that the $z \sim 0$ COS-haloes observations point to much larger cold clump sizes of $\sim$ 10kpc (Werk et al., 2014). This result is based on the assumption that all of the absorbers are at the same density. The best fit cold clump size in an alternative model, which assumes small, high density clouds are hierarchically nested within successively larger and less dense clouds, is on the order of 6 pc (Stern et al., 2016). The $\sim$kpc resolution of our simulations at $r_{\rm vir}$, which is better resolution than in the CGM of most cosmological simulations, is likely sufficient to resolve the warm gas traced by O VI gas, but may be insufficient to fully capture the colder H I gas.

The right panel of Figure 2.15 show a typical example of the density weighted line-of-sight

velocity in our simulations. The snapshot comes from the $10^{11.5}$ $M_\odot$ halo with the high $\eta$ feedback model after 6 Gyr of evolution. In practice, we measure the density weighted mean of the absolute value of the line-of-sight velocity, which avoids cancellation and is comparable to the observed measurements of CGM absorption feature velocity offsets relative to their host galaxy. The line-of-sight velocities in our haloes peak near the center at $\sim 100$ km s$^{-1}$ and drop to $\lesssim 10$ km s$^{-1}$ near $r_{\rm vir}$. This is reasonably consistent with observations (e.g., for O VI, see Figure 2B of Tumlinson et al. 2011).

## 2.5 Discussion

We have carried out a suite of idealized three-dimensional hydrodynamic simulations of the baryonic content of dark matter haloes with masses ranging from $10^{11}$ to $10^{12}$ $M_\odot$ that include the effects of cooling, galactic winds driven by stellar feedback, and cosmological gas accretion. For each halo mass we consider, we adopted feedback models that have mass-loading factors, $\eta$, which bracket the expected range for star formation feedback ($\eta$ is the ratio of the galactic wind outflow rate to star formation rate; see equation (2.1)). This provides a controlled setup for understanding the impact of stellar feedback on the CGM.

The standard paradigm in galaxy formation (Rees & Ostriker, 1977; Silk, 1977; Binney, 1977; Birnboim & Dekel, 2003), which omitted feedback, identified a critical halo mass ($\sim 10^{11.5}$ $M_\odot$ relatively independent of $z$), above which the virial shock heated halo gas cools slowly and remains thermally supported for many dynamical times. Alternatively, in haloes below this critical mass the virial shock heated gas cools rapidly and thermal pressure alone is insufficient to support the gas. With our idealized simulations we have added the additional ingredient of stellar feedback without the complexity inherent to cosmological simulations that have also addressed this question. We show that feedback does not significantly alter the critical mass that delineates haloes with and without thermal pressure supported gaseous haloes (e.g., Figure 2.11).

Our simulations demonstrate that the impact of feedback on the thermal structure and dynamics of the CGM differs above and below the critical halo mass. In more massive haloes, $\gtrsim 10^{11.5}$ $M_\odot$, the state of the halo gas at large radii $\sim r_{\rm vir}$ is relatively insensitive to the choice of feedback model. At small radii, near the central galaxy, halo gas is regulated by feedback. Feedback is triggered by accretion of cold gas which condenses out of the hotter ambient medium. With the low $\eta$ (i.e., high energy per unit mass) feedback model this condensation is correlated with epochs when $t_{\rm cool}/t_{\rm ff} \lesssim 10$, which is indicative of the condensation being triggered by thermal instability (Figure 2.13). The resulting heating stabilizes the hot gas against further condensation and reduces the star formation rate by a factor of $2-10$ relative to haloes without feedback (see Figure 2.5). Above a certain minimum level of feedback (the actual value depends on the specific feedback parameterization) changes to the feedback efficiency have a minor impact on the global properties of the halo gas, the main difference being that less efficient feedback heats the CGM less effectively so the haloes spend more time with $t_{\rm cool}/t_{\rm ff} \lesssim 1-10$ (see Figure 2.13). This is in accordance with the findings of similar studies targeting the group and cluster regime (e.g., Sharma et al., 2012a).

Below the critical halo mass, $\sim 10^{11.5}$ $M_\odot$, turbulence and bulk flows play a larger role in

supporting halo gas (Figure 2.11). In this regime, feedback and its interaction with inflowing gas determines the properties of the CGM. Gas in these haloes is out of hydrostatic equilibrium. Changes to the feedback efficiency lead to dramatic differences in the phase structure of the CGM (Figures 2.7 and 2.8). If the galactic wind is heavily mass loaded then much of the mass in the CGM is in the form of dense, cold, outgoing clumps surrounded by relatively sparse inflowing cold gas. The density and velocity of the wind ejecta in this case cause the wind shock cooling times to be very short leading to a paucity of warm, $\gtrsim 10^5$ K, gas. Alternatively, winds with mass loading $< 1$ with a similar total energy lead to a CGM structure that is very different: a multiphase medium with appreciable mass between $\sim 10^4$ K and $10^6$ K (compare Figure 2.8 with the top panel of Figure 2.7) that is supported in part by turbulence and is threaded by dense gas flowing inwards along narrow channels (Figures 2.4 and 2.11). These two feedback models bracket the expected range of wind mass loading (e.g. Martin, 1999a; Veilleux et al., 2005a; Heckman et al., 2015; Muratov et al., 2015), and wind velocities (e.g., Heckman et al., 2000; Martin, 2005; Weiner et al., 2009; Rubin et al., 2011).

An important difference between the CGM of different mass haloes is that the $t_{\rm cool}/t_{\rm ff}$ regulation of hot halo gas that successfully explains much of the structure and evolution of massive haloes ($> 10^{12}$ M$_\odot$) breaks down for halo masses $\lesssim 10^{12}$ M$_\odot$ (see Figure 2.13). Therefore, the attempts of Voit et al. (2015) to explain galaxy properties using this model should also break down at these lower halo masses.

In Section 2.4.3 we present a comparison of our simulations to some of the key results that have come out of quasar sight-line observations of the CGM in the $z \sim 0$ universe (e.g., Tumlinson et al., 2011; Thom et al., 2012; Werk et al., 2014; Borthakur et al., 2015; Danforth et al., 2016). In particular, we show the O VI, C IV and H I content of our haloes, as well as a representative example of the density weighted line-of-sight velocity (Figures 2.14 and 2.15). The idealized nature of our simulations prevents us from making too detailed of a comparison to the observations. Bearing this in mind, the O VI, C IV column densities of our haloes are close to the observed values (Tumlinson et al., 2011; Bordoloi et al., 2014). Likewise, the density weighted line-of-sight velocities of our halo gas ($\sim 100$ km s$^{-1}$) are similar to velocity offsets of the CGM absorption features relative to their host galaxy in background quasar spectra (e.g., Tumlinson et al., 2011; Thom et al., 2012). Interestingly, we find a non-monotonic dependence of $N_{\rm O\,VI}$ on halo mass, with the column densities peaking at $\sim 10^{11.5}$ M$_\odot$ haloes. Several cosmological simulations have tried to reproduce these $N_{\rm O\,VI}$ observations with varying degrees of success (e.g., Tepper-García et al., 2011; Hummels et al., 2013; Ford et al., 2015; Suresh et al., 2015). The inclusion of additional physics, such as cosmic rays (Salem et al., 2016) and non-equilibrium ionization (Oppenheimer et al., 2016), has improved the correspondence with the $N_{\rm O\,VI}$ observations. The results from the latter study indicate a possible strong dependence of the O VI column density on halo mass, which is also seen in our simulations. It is also worth noting that different feedback models lead to different $N_{\rm O\,VI}$ and $N_{\rm C\,IV}$ profiles, particularly at lower halo masses, which may enable observations of the CGM to constrain the nature of galactic winds. This is particularly promising in lower mass haloes, as probed e.g. by the COS-Dwarfs sample (Bordoloi et al., 2014).

The H I content of our haloes (Figure 2.14) are well below the observed values (e.g., Prochaska et al., 2011; Werk et al., 2014). Although the neutral hydrogen column densities are under-

predicted, the total hydrogen column densities in our simulations agree well with values implied by photoionization models of the COS-haloes observations (Werk et al., 2014). This implies that our haloes have roughly the right amount of total gas, but not enough gas that is dense enough for self-shielding to allow the neutral fraction to reach an appreciable value. At $z = 0$ the density above which self-shielding becomes important is $n_{\rm SSh} \approx 3 \times 10^{-3}{\rm cm}^{-3}$ (Rahmati et al., 2013). Figure 2.9 shows that in our simulations the characteristic density is $n \sim 3 \times 10^{-5}{\rm cm}^{-3}$ (at radii where neutral hydrogen is observed $\gtrsim 0.5 r_{\rm vir}$), which is well below $n_{\rm SSh}$. There are a few plausible explanations for why there is less sufficiently dense ($n \gtrsim n_{\rm SSh}$) gas at large radii in our haloes than is implied by the observations. The dense neutral hydrogen containing gas may reside in very small clumps ($\ell \lesssim 10$pc), as suggested by observations (e.g. Prochaska & Hennawi, 2009; Hennawi et al., 2015; Stern et al., 2016). These small clumps may have formed as result of rapid cooling of galactic wind shocked material (e.g. Thompson et al., 2016a), or as a result of pressure confinement after condensing out of a hotter, thermally unstable background (e.g. McCourt et al., 2012). These small clumps would be unresolved in our simulations, so the gas would not be able to reach the large densities necessary to explain the large observed H I columns. Alternatively, the H I may be due to substructure in the dark matter halo, which is not included in our simulations. Satellite galaxies could provide the necessary binding energy to hold dense clouds together when pressure confinement is insufficient, and their winds could inject more dense gas into the CGM. Finally, if the large scale accretion proceeds along filaments the density of the inflowing gas may be high enough for there to be an appreciable amount of H I. Note, however, that this cannot explain the ~1 covering fraction of H I absorbers with $N_{\rm H\,I} > 10^{15}{\rm cm}^{-2}$ (Tumlinson et al., 2013). It is likely that all of these effects (and more), which are not included in our simulations, come into play in setting the amount of H I in real haloes. It is important to stress that our idealized calculations are able to roughly reproduce the observed properties of C IV and O VI absorbers, suggesting that these ions may be better than H I as probes of the overall impact of star formation feedback on the CGM.

The physical properties of the haloes we simulated were chosen to represent haloes in the $z = 0$ universe, which allows us to compare to COS observations. However, our results are applicable to higher redshifts as well because of the weak redshift dependence of $t_{\rm cool}/t_{\rm ff}$ at the virial shock (Dekel & Birnboim, 2006). This ratio determines whether a virial shock will remain hot and grow or cool rapidly and collapse. We have verified this argument by carrying out a suite of $z = 2$ simulations, which showed the same qualitative behavior as their $z = 0$ counterparts, for a given set of feedback parameters. Of course, it may well be that the efficiency of stellar and/or AGN feedback vary with redshift, due to changing gas fractions, black hole masses, metallicities, and other physical characteristics of the galaxies and haloes. If so, the CGM properties would vary as well. Although the redshift-independence of our results implies that for a given mass our results are valid for a range of redshifts, the numerical setup we adopted for this paper neglects to account for the growth of the underlying dark matter potential. Moreover our simulations use only the mean cosmic accretion rate and do not account for any scatter or evolution of this rate, which could have potentially important implications for the CGM structure (McCourt et al., 2013) and for galaxy properties (Feldmann et al., 2016). In a future study we plan to include an evolving potential and explore variations to the accretion rate at fixed halo mass.

In a similar vein, our simulations neglect large scale filamentary accretion, which is the norm

in galaxy formation. Nelson et al. (2013) argued that the long standing cold-mode–hot-mode dichotomy (e.g., Kereš et al., 2005) is partially a numerical artifact arising from deficiencies in smooth-particle hydrodynamics (SPH) codes that lead to thinner, denser filaments, and heating due to spurious dissipation of turbulent motions at large scales. The lack of filaments in our current simulations precludes us from addressing this concern. However, the controlled environment our setup affords is ideal for studying how the properties of gaseous haloes vary with filament properties and stellar feedback. This is particularly important given the numerical subtleties involved in capturing mixing via the Kelvin-Helmholtz instability (Lecoanet et al., 2015) and its supersonic variants (Belyaev & Rafikov, 2012). In a future study we plan to repeat a similar set of simulations as those in this paper, but with filamentary accretion. Magnetic fields, anisotropic conduction, and cosmic rays may also play an important role in the evolution and phase structure of the CGM (e.g., Booth et al., 2013; McCourt et al., 2015).

# Acknowledgements

We thank Claude-André Faucher-Giguère, Freeke van de Voort, Robert Feldmann, Joe Hennawi, Prateek Sharma, Joel Bregman, Zachary Hafen, and Jonathan Stern for useful conversations. Additionally, we thank Freeke van de Voort for providing the CLOUDY results on O VI fractions in PIE used in Figures 2.14 and 2.15.This work was supported in part by NASA ATP grant 12-APT12-0183 and a Simons Investigator award from the Simons Foundation to EQ. DF was supported by the NSF GRFP under Grant # DGE 1106400. MM was supported by NASA grant # NNX15AK81G. TAT is supported by NSF Grant #1516967. TAT and EQ thank the Simons Foundation and organizers Juna Kollmeier and Andrew Benson for support for the *Galactic Winds: Beyond Phenomenology* symposium series, where this work germinated. This research used the Savio computational cluster resource provided by the Berkeley Research Computing program at the University of California, Berkeley (supported by the UC Berkeley Chancellor, Vice Chancellor of Research, and Office of the CIO). In addition, this work used the Extreme Science and Engineering Discovery Environment (XSEDE), which is supported by National Science Foundation grant number ACI-1053575. Much of our analysis was performed using the publicly available data analysis software package `yt` (Turk et al., 2011).

# Appendix

## 2.A Resolution study

We test the numerical convergence of our results with two separate tests. In the primary test we vary the number of levels of mesh refinements of two of our simulations, which allows us to assess how the properties of the halo cores vary with resolution. The fiducial resolution of our simulations is achieved using three, nested $256^3$ levels (base grid, and two nested refined levels). This gives a central spatial resolution of 228 cells per $r_{\rm vir}$, or $\Delta x = 1.4$ kpc $(\rm M_{halo}/10^{12} M_\odot)^{1/3}$. We re-simulated the low $\eta$ $10^{12}$ $\rm M_\odot$ and high $\eta$ $10^{11.5}$ $\rm M_\odot$ haloes using two and four levels, which halved and doubled the central resolution, respectively.

Figure 2.A.1 shows the number density and pressure profiles of gas in three distinct temperature regimes of these two haloes (compare with Figure 2.10). The profiles of the cold gas ($T < T_{\rm vir}/4$) are in blue, the warm, virialized gas ($T_{\rm vir}/2 < T < 2T_{\rm vir}$) in gold, and the hot gas ($T > 4T_{\rm vir}$) in red. The agreement between the profiles for the different resolution simulations of the high $\eta$ $10^{11.5}$ $\rm M_\odot$ halo (top two panels) is very good in the cold and warm gas. However, the central densities and pressures of the hot gas in the high resolution (solid lines) simulations exceeds that of the fiducial resolution (dashed lines) and low resolution (dot-dashed lines) simulations. Reassuringly, the differences between the high and fiducial resolution simulations are much smaller than the differences between the fiducial and low resolution simulations, indicating that our simulations are approaching convergence in this hottest phase. This hot gas in the center of these haloes is heated by shocks between the wind material and the ambient/inflowing material.

The temperature dependence of the resolution sensitivity is reversed in the low $\eta$ $10^{12}$ $\rm M_\odot$ halo (bottom two panels). In this case, with different resolutions the hot and warm gas profiles agree very well, while the cold gas pressures and densities increase with resolution. Again, however, the differences decrease as resolution increases. The gas in this cold temperature range is primarily in small pressure confined clumps (e.g. Figure 2.12). The size of these clumps should be determined either by thermal conduction, which would require resolving the Field length ($\lambda_F \lesssim 0.1$ pc $\ll \Delta x$ for $10^{-2}$ $\rm cm^{-3}$ gas at $10^4$ K), or should be roughly the size where the sound crossing time equals the cooling time ($\sim c_s t_{\rm cool} \lesssim 3$pc). These clumps are therefore unlikely to be resolved in our simulations (or any other full halo simulations).

Figure 2.A.2 shows a convergence plot for the evolution of the ratio of the cooling time $t_{\rm cool}$ of the hot gas at $3r_{\rm gal} = 0.075r_{\rm vir}$ to its free fall time $t_{\rm ff}$ along with the cold and hot gas content of the inner $0.2r_{\rm vir}$ for the low $\eta$ $10^{12}$ $\rm M_\odot$ halo at different resolutions (the middle panel is the same as the

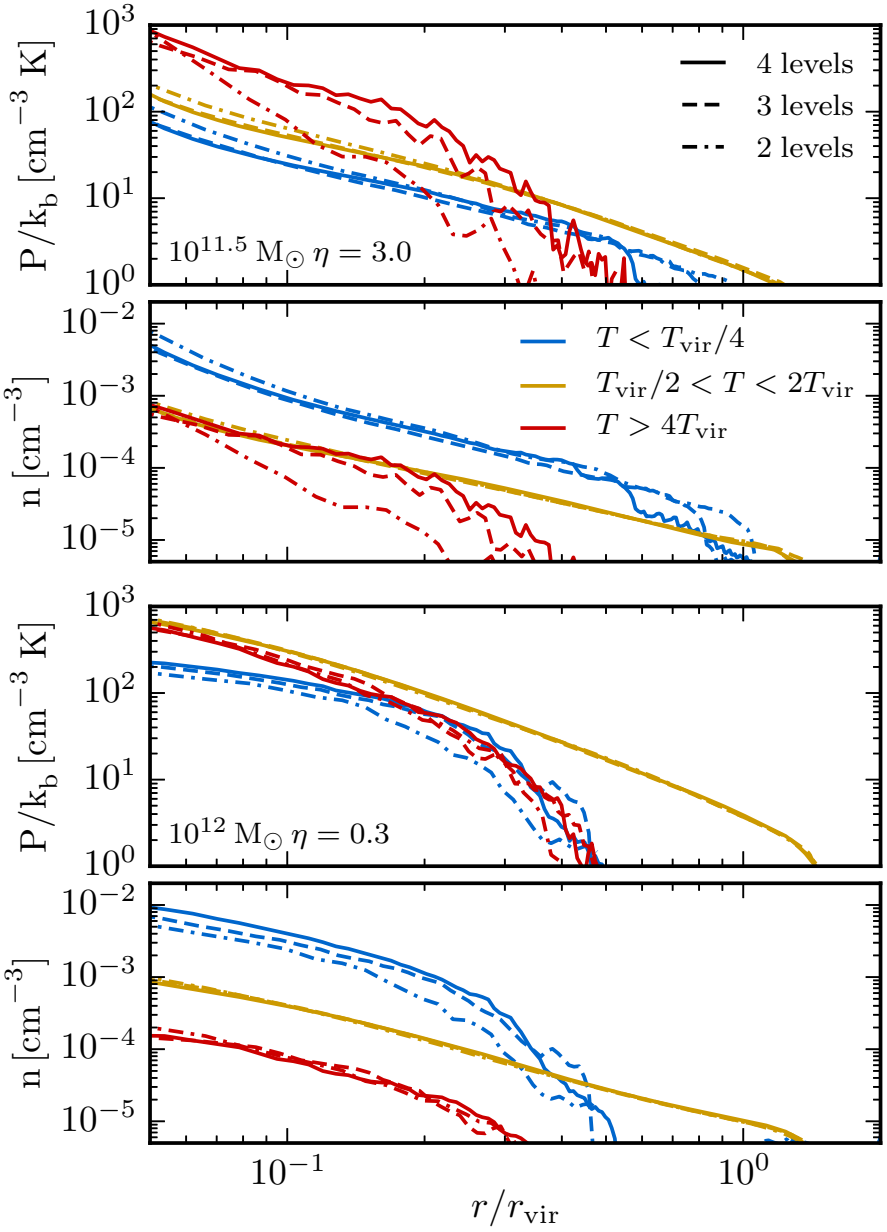


Figure 2.A.1: The time averaged (from 3 to 9 Gyr) pressure and number density profiles of gas in three temperature bins that are delineated relative to the haloes' virial temperatures, for the high $\eta$ $10^{11.5}$ M$_\odot$ (top) and low $\eta$ $10^{12}$ M$_\odot$ haloes (bottom). The hot gas with $T > 4T_{\rm vir}$, virial gas with $T_{\rm vir}/2 < T < 2T_{\rm vir}$, and cold gas with $T < T_{\rm vir}/4$ are shown in red, gold, and blue, respectively. We show the profiles from the four mesh refinement level (solid lines), fiducial resolution, three mesh refinement level (dashed lines), and low resolution, two mesh refinement level (dot-dashed lines) simulations. The profiles change from low to fiducial resolution, but are similar at fiducial and high resolution, indicating that our simulations are close to converged.

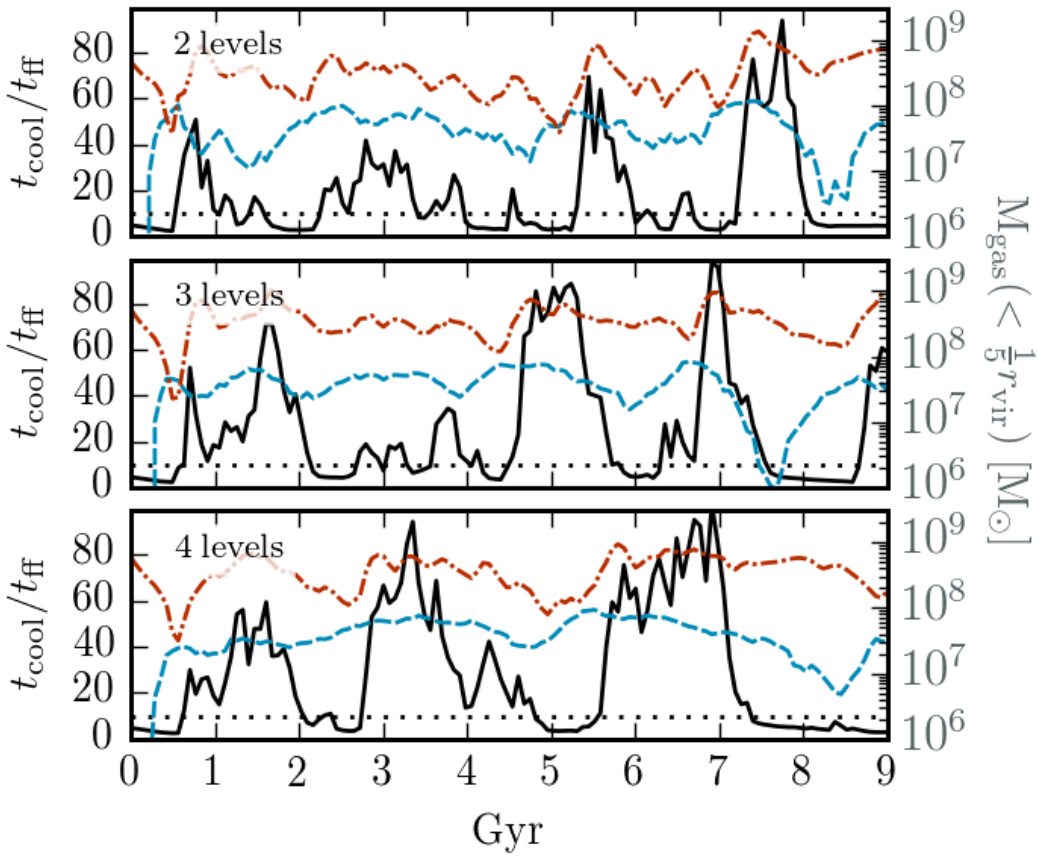


Figure 2.A.2: Spherical shell averaged $t_{\rm cool}/t_{\rm ff}$ evolution at $r = 3r_{\rm gal} = 0.075r_{\rm vir}$ (left vertical axis) relative to the cold ($T < 10^{4.5}$K; blue dashed line) and hot ($T > 10^{6}$K; red dot-dashed line) gas mass contained within 0.2 $r_{\rm vir}$ (right vertical axis) for the low $\eta$ $10^{12}$ $M_\odot$ halo simulation with resolution increasing from top to bottom. A thin dotted line is drawn at $t_{\rm cool}/t_{\rm ff} = 10$, the value below which hot halo gas is predicted to generate significant multiphase gas via thermal instability. The increase of cold gas mass when $t_{\rm cool}/t_{\rm ff} < 10$ is a strong indication of thermal instability. The thermal instability cycles are qualitatively similar, but quantitatively different because of the difficulty in resolving the small dense blobs created by thermal instability (e.g., Figure 2.12).

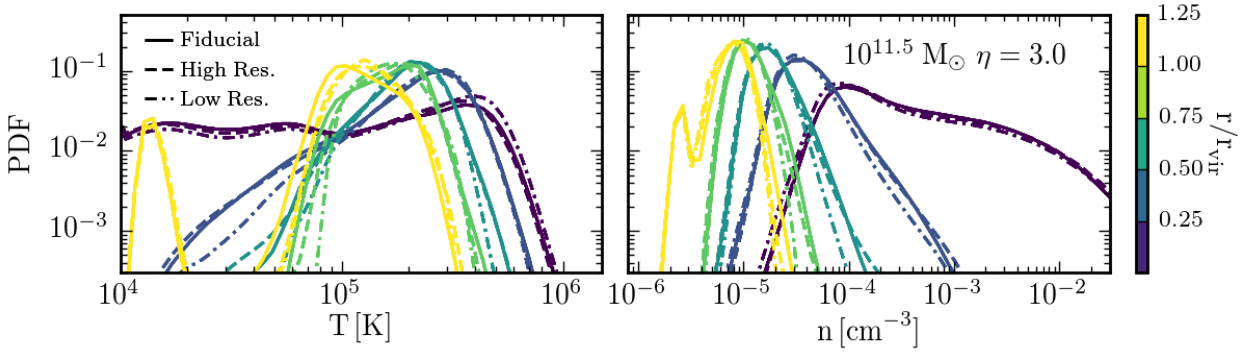


Figure 2.A.3: Mass weighted probability distribution as a function of temperature (left) and number density (right) for the high $\eta$ $10^{11.5}$ M$_\odot$ halo. The different colors correspond to different spherical annuli ranging from the center (excluding the galaxy) to 1.25 $r_{\rm vir}$ in steps of 0.25 $r_{\rm vir}$. The structure of the haloes in the high resolution (two level $512^3$) simulation agrees very well with the structure from the fiducial resolution (three level $256^3$) and the low resolution (four level $128^3$) simulations.

top panel of Figure 2.13). The increase of cold gas only when $t_{\rm cool}/t_{\rm ff} < 10$ and the corresponding increase in hot gas mass and $t_{\rm cool}/t_{\rm ff}$ immediately after is a strong indicator of thermal instability triggered feedback regulation. As resolution increases there are fewer of these cycles over a fixed length of time. Additionally, at low resolution the increases in the cold gas mass are more abrupt and the duration of the $t_{\rm cool}/t_{\rm ff} > 10$ phase is shorter than in the higher resolution simulations. Although the precise details of this regulation and its indicators change with resolution, the overall behavior is similar at the resolutions we considered.

The second numerical convergence test we performed was aimed at assessing how our results depend on the resolution at large radii ($\gtrsim 0.5 r_{\rm vir}$). To do so we simulated the low $\eta$ $10^{11}$ M$_\odot$, high $\eta$ $10^{11.5}$ M$_\odot$, and low $\eta$ $10^{12}$ M$_\odot$ haloes with the same central resolution but differing base grid resolution. For these tests the high resolution simulations have two nested $512^3$ grids and the low resolution simulations have four nested $128^3$ grids, compared to the three nested $256^3$ grids used in our fiducial resolution simulations.

Figure 2.A.3 shows the mass-weighted probability distribution as a function of temperature and number density in five radial bins for the high $\eta$ $10^{11.5}$ M$_\odot$ halo. The low $\eta$ $10^{11}$ M$_\odot$ and low $\eta$ $10^{12}$ M$_\odot$ haloes show a similar degree of convergence so they are not shown. At all three halo masses the agreement, especially at large radii, is very good, which demonstrates that the large scale properties of our haloes are well resolved in our simulations.

# Chapter 3

# How Supernovae Launch Galactic Winds

An earlier version of this article was previously published as Fielding D., Quataert E., Martizzi D., and Faucher-Giguère C.-A., 2017, MNRAS, 470, L39

## 3.1 Abstract

We use idealized three-dimensional hydrodynamic simulations of global galactic discs to study the launching of galactic winds by supernovae (SNe). The simulations resolve the cooling radii of the majority of supernova remnants (SNRs) and thus self-consistently capture how SNe drive galactic winds. We find that SNe launch highly supersonic winds with properties that agree reasonably well with expectations from analytic models. The energy loading ($\eta_{\rm E} = \dot{E}_{\rm wind}/\dot{E}_{\rm SN}$) of the winds in our simulations are well converged with spatial resolution while the wind mass loading ($\eta_{\rm M} = \dot{M}_{\rm wind}/\dot{M}_{\star}$) decreases with resolution at the resolutions we achieve. We present a simple analytic model based on the concept that SNRs with cooling radii greater than the local scale height breakout of the disc and power the wind. This model successfully explains the dependence (or lack thereof) of $\eta_{\rm E}$ (and by extension $\eta_{\rm M}$) on the gas surface density, star formation efficiency, disc radius, and the clustering of SNe. The winds in the majority of our simulations are weaker than expected in reality, likely due to the fact that we seed SNe preferentially at density peaks. Clustering SNe in time and space substantially increases the wind power.

## 3.2 Introduction

Galactic winds help limit the efficiency with which galaxies turn gas into stars by expelling material from the ISM and by halting gas inflow into galaxies (e.g., Dekel & Silk, 1986; Springel & Hernquist, 2003; Faucher-Giguère et al., 2011). They are also responsible for enriching and heating the CGM (e.g., Aguirre et al., 2001; Oppenheimer & Davé, 2006a; Hummels et al., 2013; Fielding et al., 2017a). As a result galactic winds are at the heart of many of the cornerstone relationships of modern astronomy such as the stellar mass function, stellar mass to halo mass relation, and

the mass-metallicity relation. Many processes are capable of launching galactic winds, but in star forming galaxies energy deposition by SNe is often thought to be a key driver.

Constraints on the nature of star formation powered galactic winds come from numerous sources. First, extensive observations have directly measured the energy and mass loading of galactic winds in different environments (e.g., Heckman et al., 1990; Veilleux et al., 2005b; Chisholm et al., 2017). Second, analytic considerations predict the density, temperature, and velocity profiles of a galactic wind for a given energy and mass loading (e.g., Chevalier & Clegg 1985 hereafter CC85, Thompson et al. 2016a). Third, cosmological simulations demonstrate that winds with a particular range of efficiencies are required to reproduce many observations (e.g., Finlator & Davé, 2008; Somerville & Davé, 2015; Muratov et al., 2015). Given all we know about galactic winds there is nonetheless a surprising degree of disagreement on if/how SNe are capable of launching winds that meet all the necessary constraints.

Numerical simulations of isolated galaxies inform how SNe drive winds—commonly using local stratified box simulations (e.g., Joung & Mac Low, 2006; Creasey et al., 2013; Girichidis et al., 2016a; Li et al., 2016; Kim & Ostriker, 2016). These stratified box simulations generally predict winds that are subsonic, which may be a result of the geometry, namely the lack of a well-defined escape speed and free-space for the wind to expand into (Martizzi et al. 2016a hereafter M16). To more faithfully address how SNe launch galactic winds we designed a new suite of simulations that adopts a global geometry, capturing an entire gaseous galactic disc while resolving most SNRs. Because we neglect self-gravity, molecular line cooling, and other important physics these are not the final word on the true energy and mass loading of SNe-driven winds. But they do significantly sharpen our understanding of the origin and properties of such winds.

## 3.3 Method

We ran a series of simulations designed to study the launching of galactic winds by SNe in a global geometry using the Eulerian hydrodynamics code ATHENA (Stone et al., 2008). We evolve a gaseous galactic disc that is stratified by an external potential—representing the gravitational field from baryons and dark matter—in which intermittent, discrete SNe go off at a given rate. The setup of the numerical experiment is simple and provides a useful counterpoint to analogous experiments that differ essentially only in their use of local Cartesian simulation domains; we compare primarily to our earlier work (M16). The simulations evolve an ideal fluid in three dimensions with cooling and without self-gravity. The gas has solar metallicity everywhere and cooling proceeds assuming collisional ionization equilibrium. Cooling below $10^4$ K and photoelectric heating are not included. The gas is initialized in a rotating, $10^4$ K disc that is in radial centripetal balance and vertical hydrostatic equilibrium with the background gravitational potential that is given by a Hernquist profile, $\Phi(r) = -GM_\circ/(r + a)$, where $r$ is the spherical radius ($R$ represents the cylindrical radius) (Hernquist, 1990). The disc initially has an exponentially declining surface density profile characterized by a central surface density $\Sigma_g$ and a scale length $R_d$ that is set to match the characteristic radius of the gravitational potential $a$.

The simulation parameters are listed in Table 3.1. In all simulations the parameters are chosen

| $M_\circ[\mathrm{M}_\odot]$ | $R_d$[pc] | $\Sigma_\mathrm{g}[\mathrm{M}_\odot\,\mathrm{pc}^{-2}]$ | $f_\mathrm{cl}$ | $f_\star/100$ |
|---|---|---|---|---|
| $1.0\times10^9$ | 100 | 10, 30, 50 | 1 | 0.3, 1, 3 |
| $2.8\times10^9$ | **300** | **10, 30, 100, 300** | **1**, 3, 10, 30 | 0.3, **1**, 3 |
| $9.2\times10^9$ | 1000 | 10, 30 | 1 | 1 |

Table 3.1: Full range of simulation parameters. Not all combinations are discussed in the text. The fiducial models are in bold. $M_\circ$ is the mass of the external gravitational potential. $R_d$ is the characteristic radius of the gravitational potential and the scale length of the exponential gas disc. $\Sigma_\mathrm{g}$ is central gas surface density. The parameter $f_\mathrm{cl}$ is the clustering factor of SNe: the total energy per SNR is equal to $f_\mathrm{cl}\times10^{51}$ ergs while the SN rate $\propto f_\mathrm{cl}^{-1}$. The efficiency of star formation is encapsulated in $f_\star = t_\star/t_\mathrm{dyn}$, such that a lower $f_\star$ yields more star formation.

so that $v_\mathrm{circ}(r = a = R_d) = \sqrt{GM(r)/r} = 100$ km s$^{-1}$. For our fiducial simulations we adopt the relatively small disc scale length of $R_d = 300$ pc, although we study the differences resulting from using a $\sim3\times$ smaller and larger disc. Our disc sizes and $v_\mathrm{circ}$ are similar to those in M82 and NGC 253, but our $\Sigma_\mathrm{g}$ are not quite as high.

The major drawback of running global rather than local simulations is the computational expense of resolving the SNR injection when we are primarily interested in the large-scale structure and wind dynamics. This partially motivates the smaller disc scale-lengths considered here, so that SNR evolution can be resolved. To further this goal, we use five levels of static-mesh-refinement. We space our cubical $256^3$ grids logarithmically, enabling us to use a domain side length of $L_\mathrm{box} \gtrsim 40R_d$ and have high resolution (3 pc) in the disc mid-plane where most of the mass resides (the highest resolution region is $L_\mathrm{HR} \gtrsim 2R_d$ on a side).

We seed and inject SNRs in our simulations as in the "SC" model used by M16, so we refer the reader there for more details. In short, the probability of a SN being set off is proportional to the local gas density and inversely proportional to the local star formation timescale, which is chosen to be proportional to the dynamical time, so that

$$P(\mathrm{SN\ in\ cell}) = \frac{M_\mathrm{cell}}{100\mathrm{M}_\odot}\frac{dt_\mathrm{hydro}}{t_\star} \propto \frac{n_\mathrm{cell}}{t_\star} = \frac{n_\mathrm{cell}}{f_\star t_\mathrm{dyn}}. \tag{3.1}$$

This assumes that for every 100 $\mathrm{M}_\odot$ of stars that form there is one SN. Our fiducial choice of $f_\star$ is 100, which corresponds to a 1% star formation efficiency and results in star formation rate surface densities $\dot{\Sigma}_\star$ that are similar to observations.

SNRs are injected using the subgrid model developed by Martizzi et al. (2015a), which accounts for subgrid cooling and injects both kinetic and thermal energy at a value calibrated to high resolution single SNR simulations. Additionally, 3 $\mathrm{M}_\odot$ of ejecta is added to the SNR per SN, so the ISM mass loading ($\dot{M}_\mathrm{ej}/\dot{M}_\star$) is 0.03. One of the primary aims of this study is to determine wind mass and energy loss rates when the SNRs' cooling radii ($r_\mathrm{cool}$) are explicitly resolved, so we chose parameters to ensure that this occurs for our higher resolution simulations. In this limit our SNe injection model corresponds to $2.9\times10^{50}$ ergs of kinetic energy and $7.1\times10^{50}$ ergs of thermal energy. One new feature we added to the injection scheme relative to M16 is a somewhat crude

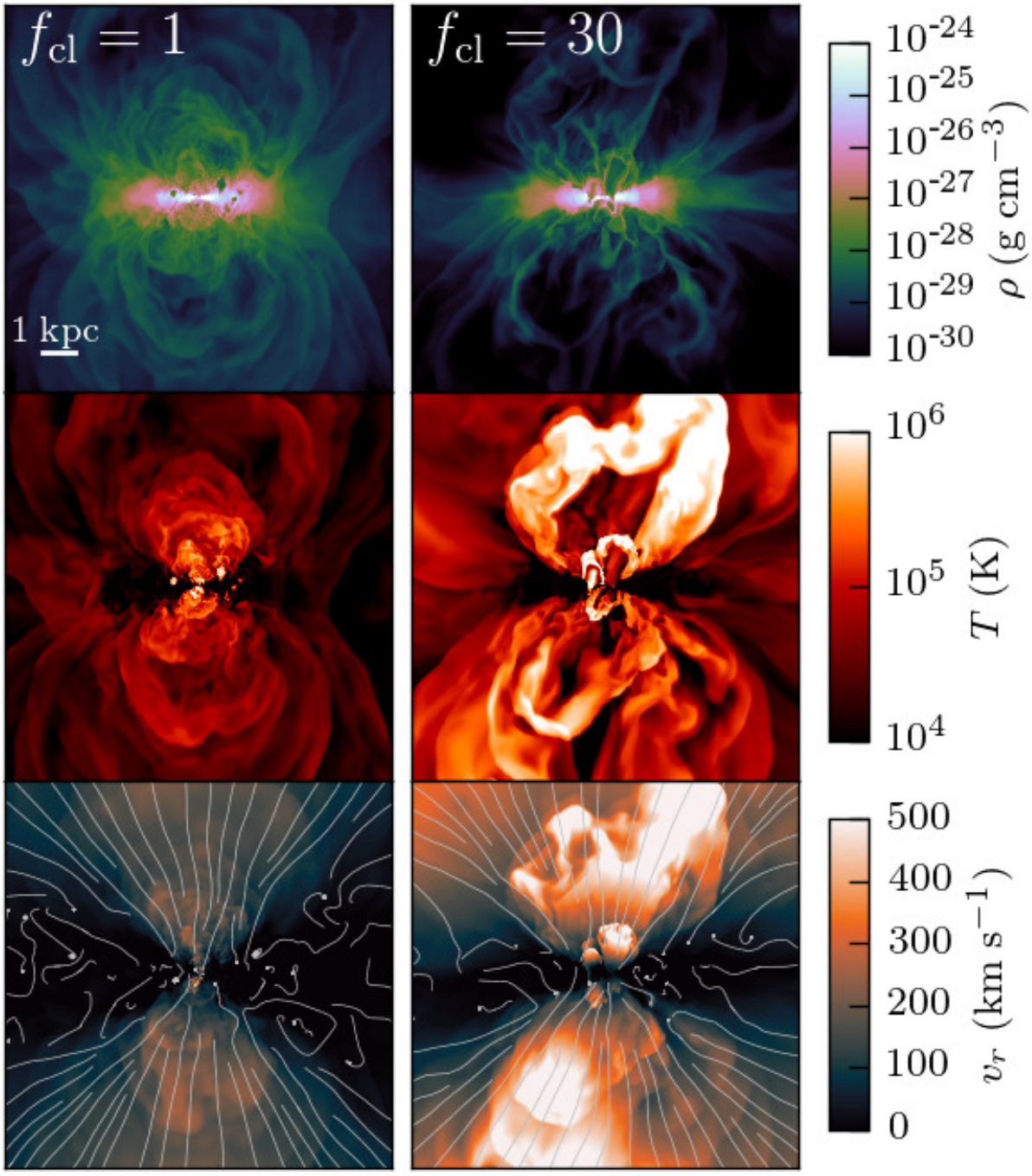


Figure 3.1: Slices along the disc rotation axis showing the density, temperature, spherical radial velocity for the $R_d = 300$ pc and $\Sigma_{\rm g} = 10\ {\rm M}_\odot\ {\rm pc}^{-2}$ simulations with $f_\star = 100$ and $f_{\rm cl} = 1$ (left column), and $f_{\rm cl} = 30$ (right column). Each image spans the entire computational domain and is 12.3 kpc across. In several places a SNR can be seen breaking out of the disc and powering the wind. The streamlines in the velocity plot trace the flow direction and highlight the nearly straight radial outflow in the central biconical region, turbulence in the disc, and shearing and fountain flow between the two. Clustering the SNe ($f_{\rm cl} = 30$; see §3.3) significantly increases the wind velocity, temperature, and mass and energy outflow rates.

model for the clustering of SNe in space and time (future work will expand this feature). We allow the injected energy per SN to be scaled up by an integer clustering factor $f_{\rm cl}$, which represents multiple SNe going off simultaneously (the SN rate is correspondingly reduced by $f_{\rm cl}$, so that the total injected energy by SNe is unchanged). The cooling radius and other radii in the Martizzi et al. (2015a) fits for subgrid injection are scaled up by $f_{\rm cl}^{2/7}$ in accordance with analytic expectations (Cioffi et al., 1988).

## 3.4 Results

We begin our presentation of the simulation results with a qualitative description to ground the readers' intuitions. In Fig. 3.1 we show density, temperature, and spherical radial velocity images from simulations with $R_d = 300$ pc, $\Sigma_{\rm g} = 10\ {\rm M}_\odot\ {\rm pc}^{-2}$, $f_\star = 100$ and both $f_{\rm cl} = 1$ and $f_{\rm cl} = 30$, after 300 Myr of evolution ($\sim$16 $t_{\rm orb}$). These images are slices through the computational domain along the rotation axis of the disc. Clearly shown are the strong biconical outflows driven by the SN. Along the rotation axis of the disc densities are low, temperatures are high, and velocities reach upwards of 300 km s$^{-1}$ ($\sim$ 500 km s$^{-1}$ in the clustered model). In the midplane of the disc densities remain high, the temperature remains at roughly $10^4$ K, and the gas is turbulent with a mass-weighted velocity of $\sim$10s km s$^{-1}$. These images show several supernova remnants breaking out of the disc. These breakout events carve out a region of the disc and dump thermal energy into the low density wind region, thereby powering the wind. The discrete breakouts lead to an inhomogeneous outflow composed of a series of hot, dense, and fast fronts of material that are trailed by gas which has expanded, cooled, and slowed down. This is reminiscent of what is observed in the M82 wind.

In Fig. 3.1 we show the time averaged radial profiles of $T$, $n$, $v_r$, $c_s$, $\eta_{\rm E}$, and $\eta_{\rm M}$ for the fiducial $\Sigma_{\rm g}$=10 ${\rm M}_\odot\ {\rm pc}^{-2}$ simulation. The averages are volume-weighted and computed in a biconical region centered on the disc rotation axis with a half opening angle of 45°. Several features are immediately apparent. The outflow is supersonic. The mass and energy outflow rates are roughly independent of radius beyond a certain point, indicating that we have a steady state outflow. The density of the wind material falls off rapidly, and the temperature decreases with radius slower than expected for just adiabatic expansion, which predicts $T \propto r^{-4/3}$. We have omitted the profiles from simulations with other parameters because they are all sufficiently similar and show the same trends.

Comparing the profiles in Fig. 3.1 to those from local Cartesian box simulations demonstrates the simulation geometry's effect on the wind structure. For example, Fig. 4 of M16 shows that the sound speed and velocity of the wind are roughly independent of height beyond the scale height of the disc and the flow is always subsonic. Additionally, Fig. 9 and B1 of M16 show that $\eta_{\rm M}$ decreases dramatically with distance from the disc whereas we find $\eta_{\rm M}$ to be roughly constant with radius. It is, therefore, the ratio of wind thermal to kinetic energy and the fraction of wind material that escapes that are primarily affected by the simulation geometry (important quantities for galactic winds!).

Standard theoretical arguments for the structure of a galactic wind of a given $\eta_{\rm E}$, $\eta_{\rm M}$, and $\dot{\Sigma}_\star$ assume spherical symmetry and a uniform injection of energy and mass (e.g., CC85, Thompson

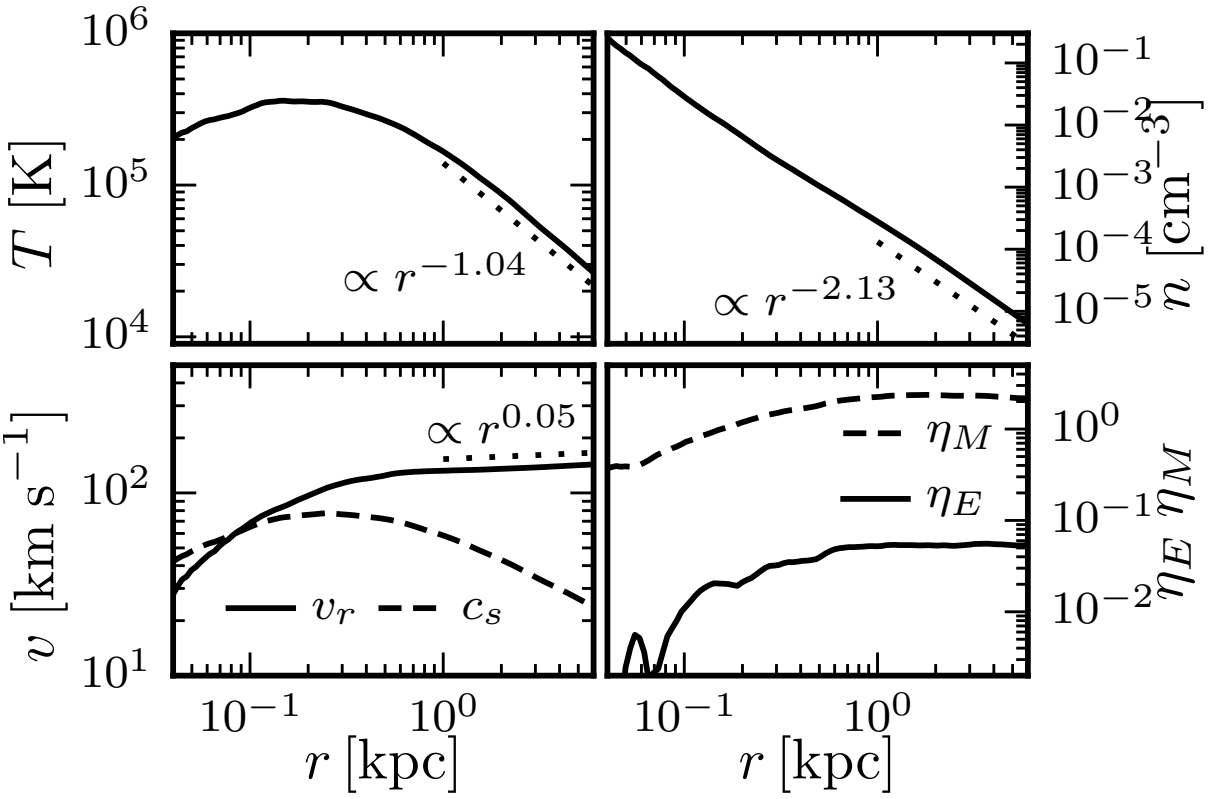


Figure 3.1: Time averaged radial profiles of $T$, $n$, $v_r$, $c_s$, $\eta_{\rm E}$, and $\eta_{\rm M}$ for the fiducial $\Sigma_{\rm g} = 10\ {\rm M}_\odot\,{\rm pc}^{-2}$ simulation. The averages are volume-weighted and computed in a biconical region with a 45° half-opening angle. The best fit power-law slope between 1 and 6 kpc is shown for $T$, $n$, and $v_r$. The outflow properties are reasonably consistent with analytic models (CC85).

et al. 2016a). Nevertheless, a comparison to the analytic work is instructive. A generic prediction of these models is that the wind will be supersonic beyond a sonic point that is approximately the radius of the star forming region (unless cooling is too strong). Our simulations agree with this prediction very well as can be seen in Fig. 3.1 where the sonic point is at $\sim R_d/3$. CC85 predict the asymptotic velocity to be $v_\infty \approx 10^3$ km s$^{-1}$ $(\eta_{\rm E}/\eta_{\rm M})^{1/2}$ and the temperature at the sonic point to be $T \approx 2\times10^7{\rm K}\,\eta_{\rm E}/\eta_{\rm M}$, which agrees strikingly well with our simulations. We indicate the best fit power law slope for the $T$, $n$, and $v_r$ profiles at large radii in Fig. 3.1 for comparison to observations and analytic models. Interestingly, $T$ falls off slower with distance than is expected for adiabatic expansion ($T \propto r^{-4/3}$), which could be due to cooling at small radii, additional heating beyond $R_d$ either by the rare (but effective) distant SNe, or by internal shocks. The biconical $n$ profile falls off roughly as $r^{-2}$ as expected for a freely expanding constant $\dot{M}$ wind. When averaging over a spherical region the $n$ profile falls off much more quickly as $r^{-\alpha}$ with $\alpha$~4-5 for different simulations. The steeper fall off of the spherically averaged profile indicates there may be some

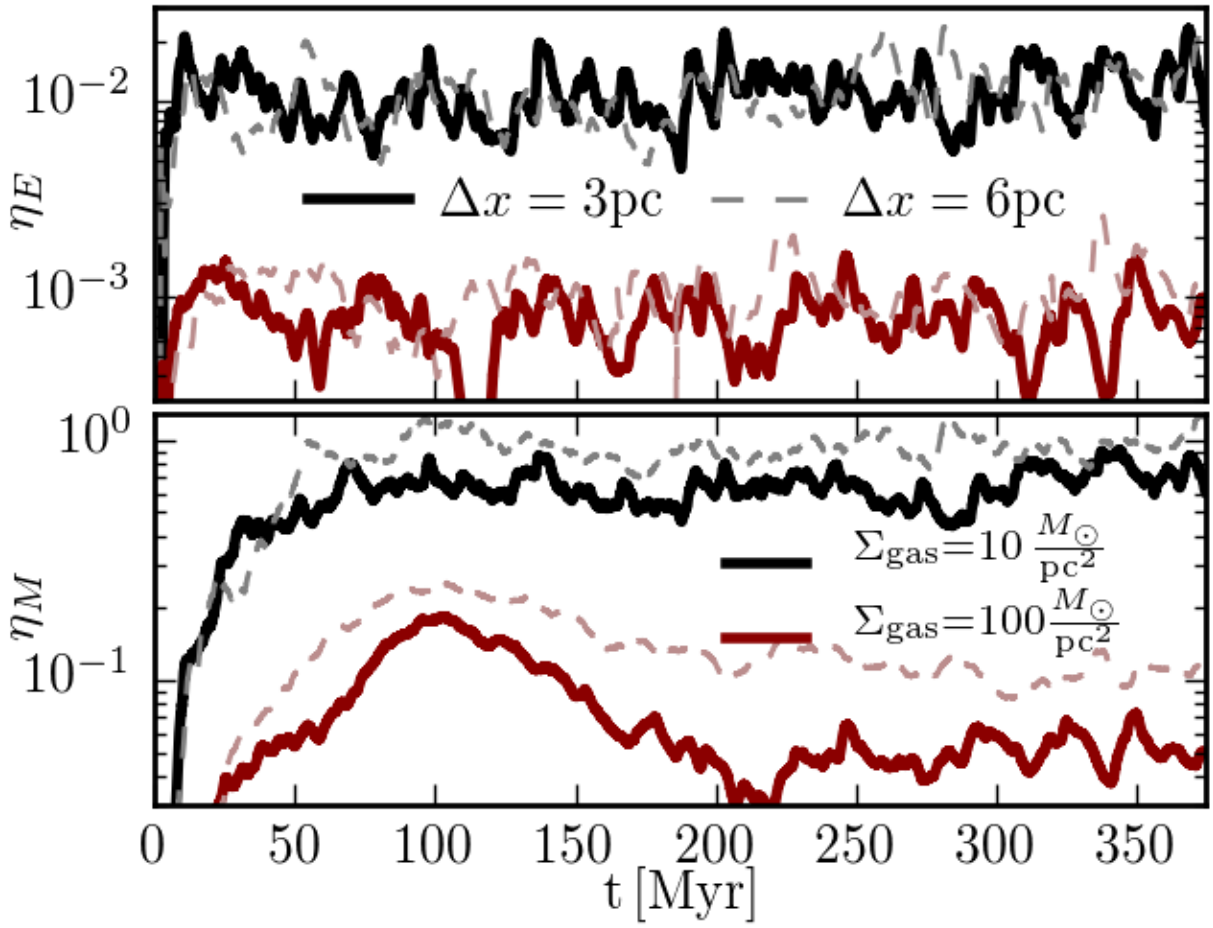


Figure 3.2: Time evolution of the energy outflow rate through a 4 kpc sphere normalized by SNe energy injection rate ($\eta_{\rm E}$), and the mass outflow rate through a 4 kpc sphere normalized to the star formation rate ($\eta_{\rm M}$) for the fiducial $\Sigma_{\rm g}$ = 10 and 100 $\rm M_\odot\,pc^{-2}$ simulations, shown in black and red, respectively. Identical simulations with half the resolution are shown with the thin dashed lines demonstrating the convergence of $\eta_{\rm E}$, but not $\eta_{\rm M}$.

fall back of wind material on the side of the biconical outflows creating a fountain flow (see Fig. 3.1). This steeper slope is also consistent with the values inferred for local starburst galaxy M 82 (Leroy et al., 2015).

In Fig. 3.2 we show the time evolution of $\eta_{\rm E}$ and $\eta_{\rm M}$ for the fiducial $\Sigma_{\rm g}$=10 and 100 $\rm M_\odot\,pc^{-2}$ simulations at the highest and half the highest central spatial resolution. The energy and mass outflow rates of the wind are measured at 4 kpc. After the initial transient the outflow settles into a steady state (quite different from local Cartesian box simulations; e.g., M16 Fig. 9 and B1). We performed extensive resolution testing on our simulations and found that with even half the resolution $\eta_{\rm E}$ is converged. However, as we increased the resolution $\eta_{\rm M}$ continued to decrease. This is

likely due to more mixing from unresolved shear layers with worse resolution, and more efficient venting at high resolution. The convergence of $\eta_{\rm E}$ does not depend sensitively on the degree to which we resolve the SNRs' $r_{\rm cool}$. In our calculations, a resolved SNR has $r_{\rm cool}$>$r_{\rm inj}$=2$\Delta x$. In the fiducial $\Sigma_{\rm g} = 10$ M$_\odot$ pc$^{-2}$ simulation with $\Delta x = 3$,6, and 12 pc 97.3, 73.5, and 31.8 per cent of the SNR are resolved, respectively, and yet $\eta_{\rm E}$ is the same. In the fiducial $\Sigma_{\rm g} = 100$ M$_\odot$ pc$^{-2}$ simulation with $\Delta x = 3$,6, and 12 pc 49.0, 12.1, and 1.4 per cent of the SNRs are resolved, respectively. In these higher surface density simulations $\eta_{\rm E}$ is roughly the same for the two higher resolution cases, but at $\Delta x = 12$ pc, $\eta_{\rm E}$ drops by a factor of ∼2. Overall, because $\eta_{\rm M}$ measured at large radii depends sensitively on the structure of the disc and the properties of the surrounding circumgalactic medium swept up by the wind (Sarkar et al., 2015) we consider $\eta_{\rm M}$ of secondary importance relative to $\eta_{\rm E}$. Nevertheless, the lack of $\eta_{\rm M}$ convergence is something that should be considered whenever simulations similar to ours are compared to observations.

A standard physical picture of models such as CC85 is that winds are launched when the volume filling fraction of hot gas in the disc is large enough so that the number of SNe per cooling time and cooling volume—known as the porosity $Q_c$ (McKee & Ostriker, 1977)—is greater than 1. Martizzi et al. (2015a) found that $r_{\rm cool} \approx 20.8$ pc ${n_H}^{-2/5}$ $f_{\rm cl}^{2/7}$, and $t_{\rm cool} \approx 2.9 \times 10^4$ yrs ${n_H}^{-0.54}$. Therefore, the porosity of the disc is $Q_c = (4\pi/3) r_{\rm cool}^3 t_{\rm cool} \dot{n}_{SN} = 6 \times 10^{-5} (n_H/100\ {\rm cm}^{-3})^{-4/5} (100/f_\star)(10^6\ {\rm yrs}/t_{\rm dyn})$. In all of the simulations carried out here $Q_c \ll 1$. As can be seen in Fig. 3.1, the SNe that contribute to the launching of the wind are the (rare) ones whose SNRs are able to breakout of the disc before radiating away their energy. Working under the assumption that SNRs that breakout satisfy $r_{\rm cool} \gtrsim h$, where $h$ is the local scale height of the gaseous disc, we now provide a simple argument for the expected scaling of the wind properties with the disc and injection properties. There is a critical hydrogen number density $n_{\rm crit} = (h/20.8\ {\rm pc})^{-5/2} f_{\rm cl}^{5/7}$ cm$^{-3}$ that satisfies $r_{\rm cool} = h$. Since, by design, the SN rate is proportional to the local density, the fraction of SNe that satisfy $n_H \leq n_{\rm crit}$ should be roughly equal to the ratio of $n_{\rm crit}$ to the midplane density $n_{\rm mid} \sim \Sigma_{\rm g}/2hm_p$ (this need not be true for models with different SN seeding schemes or that account for additional physics). Neglecting further radiative loses post breakout, the fraction of the injected energy that goes into the wind should be equal to the same ratio, which yields

$$\eta_{\rm E} = \frac{\dot{E}_{\rm wind}}{\dot{E}_{\rm SN}} \sim \frac{n_{\rm crit}}{n_{\rm mid}} \propto h^{-3/2}\, f_{\rm cl}^{5/7}\, \Sigma_{\rm g}^{-1}. \tag{3.2}$$

The total energy injection rate is $\dot{E}_{\rm SN}$=$10^{51}$ ergs $\pi R_d^2 \Sigma_{\rm g}/(t_\star\, 100{\rm M}_\odot)$, which follows from the definition of $t_\star$ and our model's assumption that there are $10^{51}$ ergs released per SN and there is one SN per 100M$_\odot$ of stars formed. Combining this expression with equation (3.2) we find that $\dot{E}_{\rm wind} = \eta_{\rm E} \dot{E}_{\rm SN} \propto R_d^2\, f_{\rm cl}^{5/7}/(h^{3/2}\, t_\star)$. One particularly interesting feature of this expression is the lack of any dependence on $\Sigma_{\rm g}$. Finally, the ratio of the scale height to the disc radius is approximately equal the ratio of the velocity dispersion to the circular velocity $h/R_d \sim \delta v/v_{\rm circ}$, which is ∼ 0.1 in our model. With this assumption in hand we end up with the following expected scalings

for the wind energetics

$$\eta_{\rm E} \propto R_d^{-3/2} \left( \frac{\delta v}{v_{\rm circ}} \right)^{-3/2} f_{\rm cl}^{5/7} \, \Sigma_{\rm g}^{-1}. \tag{3.3}$$

The scalings above have been derived for $\eta_{\rm E}$ because the condition $r_{\rm cool} \gtrsim h$ is explicitly a statement about energetics, but similar reasoning can be applied to mass-loading. Assuming that each SNR that breaks out contributes to the wind all of the mass it swept up prior breakout, $M_{\rm swept} = (4\pi/3) r_{\rm cool}^3 \rho \approx 1200 \, {\rm M}_\odot \, n_{\rm crit}^{-1/5}$, yields $\eta_{\rm M} \approx (n_{\rm crit}/n_{\rm mid})(M_{\rm swept} \, \dot{N}_{\rm SN}/\dot{M}_\star) = 12 \, \eta_{\rm E} \, n_{\rm crit}^{-1/5}$. Therefore, we expect $\eta_{\rm M}$ to scale similarly to $\eta_{\rm E}$ and to be one to two orders of magnitude larger than $\eta_{\rm E}$.

The top panel of Fig. 3.3 demonstrates that, for all other properties being equal, $\eta_{\rm E}$ is inversely dependent on $\Sigma_{\rm g}$ exactly as predicted by equation (3.3). Increasing the star formation efficiency by decreasing $f_\star$ leads to an increase in $\dot{E}_{\rm wind}$, but no appreciable change in $\eta_{\rm E}$ as expected. Likewise, equation (3.3) captures roughly the correct behavior for the scaling of $\eta_{\rm E}$ with $R_d$ seen in Fig. 3.3, which demonstrates that more compact systems launch more powerful winds.

The bottom panel of Fig. 3.3 shows how $\eta_{\rm E}$ and $\eta_{\rm M}$ scale with $f_{\rm cl}$ for $R_d = 300$ pc discs with $\Sigma_{\rm g} = 10$ and 30 ${\rm M}_\odot \, {\rm pc}^{-2}$. In these simulations $\eta_{\rm E}$ increases roughly linearly with $f_{\rm cl}$—somewhat more strongly than predicted in equation (3.2). Regardless of the exact scaling, the strong $f_{\rm cl}$ dependence of $\eta_{\rm E}$ may be critical for understanding the launching of real galactic winds that are powerful enough to match observations and satisfy the requirements from cosmological simulations. This is because stars—massive stars in particular—are expected to form in clusters and it is likely that their SNRs will be nested or overlap rather than being spatially and temporally separated as in our $f_{\rm cl} = 1$ simulations. Although $\eta_{\rm M}$ also increases with $f_{\rm cl}$, the measured scaling is less robust due to the lack of $\dot{M}_{\rm wind}$ convergence. Nevertheless, it is worth noting that for nearly all cases $\eta_{\rm M}$ surpasses 0.03—the value corresponding to all wind material coming from SNe ejecta.

## 3.5 Discussion & Conclusion

Using idealized global galactic disc simulations we have quantified the properties of galactic winds driven solely by SNe for a range of disc and star formation properties. We have focused on small discs (~0.1−1 kpc in size) in order to ensure that the cooling radii of most of the SNRs in our simulations can be resolved. Our simulations roughly reproduce the supersonic wind structure expected from analytic models (e.g., CC85). Previous simulations that attempted to study galactic winds launched by SNe in a stratified medium often adopted local Cartesian domains (with periodic and outflow boundary conditions in the disc plane and perpendicular to it, respectively) and found subsonic outflows with outflow rates that depend on box height (e.g., Martizzi et al., 2016a; Girichidis et al., 2016a; Kim & Ostriker, 2016). The more physical global geometry we adopt allows the winds to adiabatically expand causing them accelerate to supersonic velocities, and the gravitational potential with a well-defined escape velocity leads to outflows with radially constant $\dot{M}_{\rm wind}$ and $\dot{E}_{\rm wind}$ (Fig. 3.2). Other numerical models for studying galactic winds inject a fixed $\dot{E}$ uniformly in a given volume (Strickland & Heckman, 2009b; Sarkar et al., 2015). Our calculations compliment these by addressing the key question of how discrete SNe collectively drive a wind.

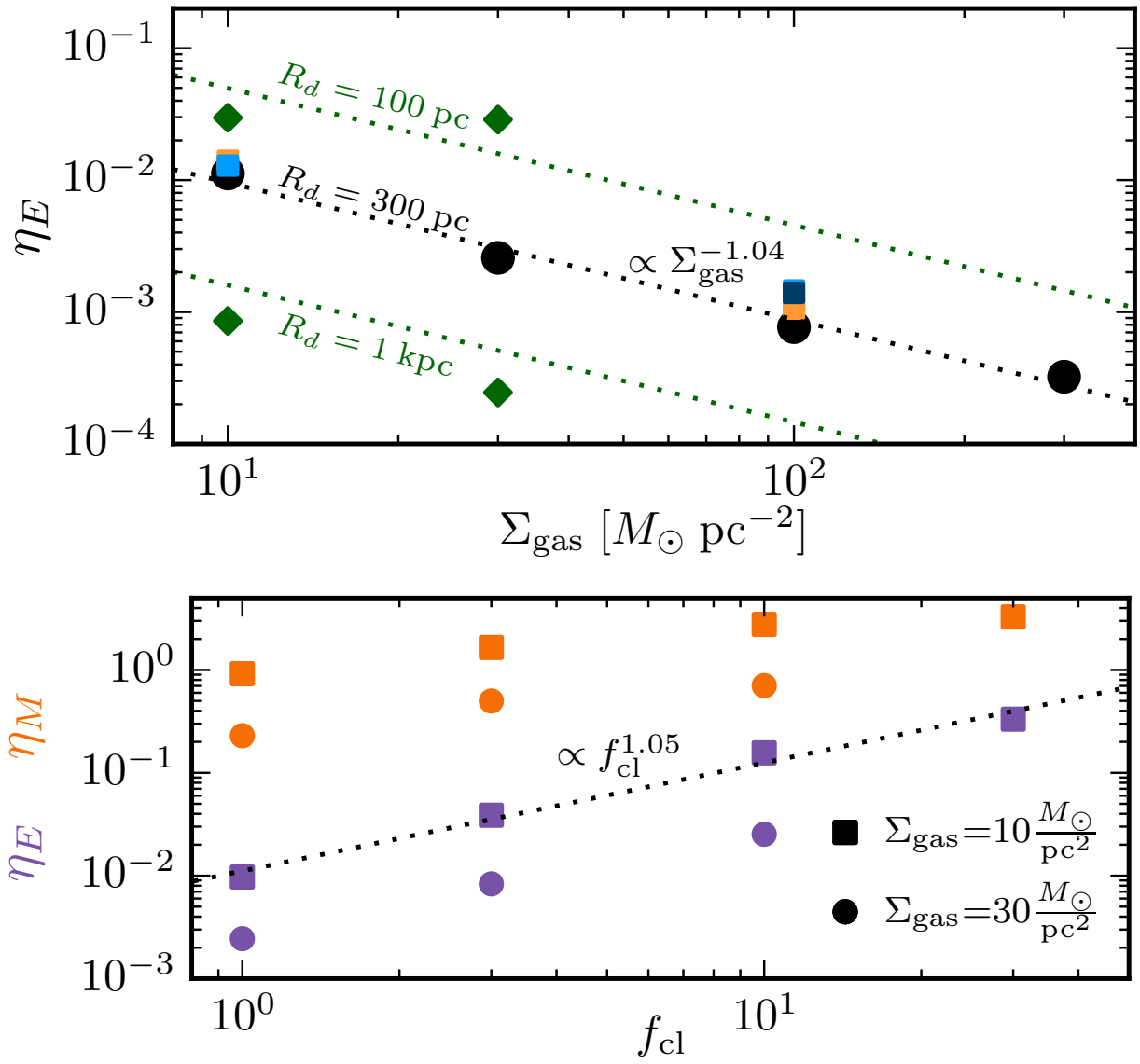


Figure 3.3: (Top) The time averaged energy loading $\eta_{\rm E}$ versus $\Sigma_{\rm g}$. The black circles correspond to simulations with $f_\star = 100$ and $f_{\rm cl} = 1$, colored squares correspond to different $f_\star$, which controls the star formation rate (orange is higher SFR, blue is lower), and the green diamonds show $\eta_{\rm E}$ for different disc sizes. The black dotted line shows the best fit to the fiducial models and the green dotted lines show the predicted $\eta_{\rm E}$ for different $R_d$ from our analytic model in which the wind properties are set by the SNe that breakout of the galactic disc (eq. 3.3). (Bottom) The dependence of the time averaged $\eta_{\rm E}$ (purple) and $\eta_{\rm M}$ (orange) through a 4 kpc sphere on the degree of clustering $f_{\rm cl}$ (§3.3) for $\Sigma_{\rm g} = 10$ and $30\,{\rm M}_\odot\,{\rm pc}^{-2}$ shown with squares and circles, respectively. Clustering the SNe significantly boosts the wind energy and mass loss rates.

In analytic galactic wind models the mass ($\eta_{\rm M}$) and energy ($\eta_{\rm E}$) loading of the wind are free parameters. Our simulations determine these wind properties as a function of the underlying disc structure (e.g., $\Sigma_{\rm g}$ and $R_d$) and the SN seeding model (e.g., degree of clustering $f_{\rm cl}$). In our simulations the winds are driven by SNe that go off in low density regions where the cooling radius $r_{\rm cool}$ is larger than the local scale height $h$; this enables SNRs to drive the wind without radiative losses sapping their energy. In general only a small fraction of the SNe satisfy this constraint because at the disc midplane $r_{\rm cool} \ll h$. We present a simple model based on this concept (see eq. 3.3) that predicts, among other things, that $\dot{E}_{\rm wind}$ should be independent of $\Sigma_{\rm g}$, increase with the degree of SNe clustering $f_{\rm cl}$ and the star formation efficiency $f_\star$, and decrease with increasing disc size. This simple model successfully explains many of the trends we find in our simulations (Fig. 3.3). Although this analytic model and the numerical scaling of wind efficiency with disc and SNe parameters are likely to be somewhat modified with different SNe seeding schemes, we expect that the general trends found here are likely to be more robust—in particular the simple criterion that $r_{\rm cool} \gtrsim h$ for the SNe that drive the wind.

The mass and energy loading of the galactic winds driven by SNe we find are likely lower than suggested by observations. This may be due to the fact that our SNe are set off preferentially at density peaks and that the ISM is relatively homogeneous. A more realistic (or a spatially random) SNe seeding scheme that separates the SN locations from density peaks and/or clustering the SNe would increase the efficiency of the outflows (e.g., Sharma et al., 2014a; Girichidis et al., 2016a; Kim & Ostriker, 2016; Gentry et al., 2017a). Indeed, in our calculations, we implemented a simple model of clustering in which each SNR's energy is increased by a factor of $f_{\rm cl}$, and the SN rate decreased by the same factor, leaving the total energy input rate the same. The resulting galactic wind energy loss rate increases roughly linearly with $f_{\rm cl}$ (Fig. 3.3). The wind power might well be further increased if additional physics were included such as molecular line cooling (Li et al., 2016) and stronger ISM turbulence possibly enhanced by self-gravity and/or galactic inflows (Sur et al., 2016). These would result in larger density inhomogeneities, causing more of the ISM volume to be filled with low density gas, and thereby allowing more SNe to go off in low density regions and breakout of the disc.

# Acknowledgements

We thank Prateek Sharma for useful conversations during the development of this work. This work was supported in part by NASA ATP grant 12-APT12-0183 and a Simons Investigator award from the Simons Foundation to EQ. DF was supported by the NSF GRFP under Grant # DGE 1106400. CAFG was supported by NSF through grants AST-1412836 and AST-1517491, and by NASA through grant NNX15AB22G. DM was supported by the Swiss National Science Foundation as an Advanced Postdoc Mobility Fellow until Nov. 2016; grant number P300P2_161062. This research used the Savio computational cluster resource provided by the Berkeley Research Computing program at UC, Berkeley (supported by the UC Berkeley Chancellor, Vice Chancellor of Research, and Office of the CIO). In addition, this work used the Extreme Science and Engineering Discovery Environment (XSEDE), which is supported by National Science Foundation grant

number ACI-1053575, via grant number TG-AST160020.

# Chapter 4

# Clustered Supernovae Drive Powerful Galactic Winds after Super-Bubble Breakout

An earlier version of this article has been submitted for publication to MNRAS.

## 4.1 Abstract

We use three-dimensional hydrodynamic simulations of vertically stratified patches of galactic discs to study how the spatio-temporal clustering of supernovae (SNe) enhances the power of galactic winds. SNe that are randomly distributed throughout a galactic disc drive inefficient galactic winds because most supernova remnants lose their energy radiatively before breaking out of the disc. Accounting for the fact that most star formation is clustered alleviates this problem. Super-bubbles driven by the combined effects of clustered SNe propagate rapidly enough to break out of galactic discs well before the clusters' SNe stop going off. The radiative losses post-breakout are reduced dramatically and a large fraction ($\gtrsim 0.2$) of the energy released by SNe vents into the halo powering a strong galactic wind. These energetic winds are capable of providing strong preventative feedback and eject substantial mass from the galaxy with outflow rates on the order of the star formation rate. This conclusion holds for a range of galaxy properties, both in the local Universe (e.g., M82) and at high redshift (e.g., $z \sim 2$ star forming galaxies). We further show that if the efficiency of forming star clusters increases with increasing gas surface density, as suggested by theoretical arguments, the condition for star cluster-driven super-bubbles to break out of galactic discs corresponds to a threshold star formation rate surface density for the onset of galactic winds $\sim 0.03\,M_{\odot}\,\mathrm{yr}^{-1}\,\mathrm{kpc}^{-2}$, of order that observed.

## 4.2 Introduction

Galactic winds are seen to emanate from galaxies across the star forming sequence with outflow rates and velocities correlated with star formation rate (Rubin et al., 2014). These galactic winds are typically invoked to explain the small baryon fraction in low mass galaxies (e.g., Guo et al., 2010), the observed mass-metallicity relationship of galaxies (e.g., Tremonti et al., 2004), and the enrichment and heating of the circumgalactic and intergalactic media (CGM and IGM) (e.g., Oppenheimer & Davé, 2006b; Fielding et al., 2017b). The energy injected by supernovae (SNe) – as well as other forms of stellar feedback such as HII regions, stellar winds, radiation pressure, and/or cosmic rays generated by SNe – plays a key role in unbinding gas from low-mass galaxies and powering galactic winds (e.g., Martin, 1999b).

Winds have been observed extensively at a many wavelengths probing gas at a broad range of temperatures. The hottest component ($T \gtrsim 10^7$ K) of the winds are measured using their X-ray emission (e.g., Strickland & Heckman, 2009a), intermediate temperature wind material is observed in UV absorption studies (e.g., Chisholm et al., 2016), and molecular gas is used to map out the coldest phases ($T \lesssim 10^2$ K) (e.g., Walter et al., 2002). However, there is large uncertainty inherent in inferring the amount of mass and energy carried by galactic winds from observations. In general, mass-loading factors (the ratio of the mass outflow rate to the star formation rate) ranging from $\sim 0.1 - 10$ (see Veilleux et al. 2005b for review) and order unity energy-loading factors (the ratio of the energy outflow rate to the SN energy injection rate; Chevalier & Clegg 1985; Strickland & Heckman 2009a) are expected.

Cosmological simulations have further demonstrated the critical importance of galactic winds for reproducing the properties of galaxies. Without feedback associated with star formation, or with inefficient feedback, cosmological simulations over-predict the stellar masses of lower mass galaxies. Feedback brings the predicted stellar masses and star formation rates into agreement with observations (e.g., Hopkins et al., 2014). These winds must carry a large fraction of the energy injected by SNe in order to prevent excessive accretion onto galaxies, eject interstellar gas, and thereby affect galactic evolution.

Numerous numerical studies have sought to understand in detail exactly if/how galactic winds are driven by SNe. In particular, in recent years many groups have adopted a similar approach in which SNe are set off in a stratified medium meant to represent a patch of a galaxy's ISM. These simulations span a wide range in the degree of realism and have been used to address many topics, such as how the galactic wind properties depend on gas surface density (e.g., Creasey et al., 2013) and on the relative scale height of gas and SNe (e.g., Li et al., 2016), to name just a few. The most realistic of the simulations of this type include magnetic fields, self-gravity, gravitational collapse induced star-formation, and differential rotation, among other features (Kim & Ostriker, 2018; Gatto et al., 2017). These simulations have focused on roughly Milky Way like conditions with $\Sigma_g = 10\ M_\odot\ pc^{-2}$ and have been used to study the equilibrium state of the ISM. More idealized/controlled simulations, such as those presented in this paper, complement the more realistic simulations, by allowing for different aspects of the problem to be isolated and studied in detail. The aggregate results of all of these recent simulations can be summarized as follows: SNe alone (i.e., without also adding cosmic rays and/or radiation pressure) can launch powerful

galactic winds (with, say, $\gtrsim$ 10 per cent of the SNe energy in a wind) if the SNe go off in low density regions, which can be achieved by having a highly inhomogeneous ISM due to cooling to $T \lesssim 100$ K, having the SNe go off above the gaseous scale height, and/or by having overlapping SN remnants.

It is now well-established that the efficiency of SNe feedback depends sensitively on how they are distributed in time and space, with, for example, SNe distributed randomly in space producing stronger turbulence and winds than SNe correlated with the local density peaks (e.g., Gatto et al. 2015; Martizzi et al. 2016b). Tightly clustering SNe both spatially and temporally in star clusters further enhances their efficiency in driving turbulence and powering galactic winds (e.g., Sharma et al. 2014b; Fielding et al. 2017c). Significant clustering is expected since the massive stars that eventually become core-collapse SNe predominantly form in clusters (e.g., de Wit et al., 2005) that disperse on $\gtrsim$ 100 Myr time scales (e.g., Portegies Zwart et al., 2010), which is significantly longer than the $\lesssim$ 10 Myr lifetime of these stars (e.g., Leitherer et al., 1999). Recent simulations have investigated the evolution of the bubbles blown by clustered SNe (referred to as 'super-bubbles') to assess the net momentum injection into the ISM and how much energy remains after radiative losses to power a wind (Gentry et al., 2017b; Kim et al., 2017; Yadav et al., 2017). Although these works disagree on several important fronts, they all indicate that under many conditions the cluster-drive super-bubble will have sufficient time to reach the vertical boundary of the disc in which it is embedded and breakout. These works, however, did not include gravity and a vertically stratified disc and so could not capture the breakout process and post-breakout dynamics. In this paper we extend this line of inquiry by studying both the pre- and post-breakout evolution, and find crucial differences in the energetics that support the picture of clustered SNe driving powerful galactic winds.

Throughout we focus our attention primarily on the energy carried by the winds as opposed to the wind mass flux. This is because the energy flux of a wind is much closer to a conserved quantity as the wind propagates into the CGM. The mass flux, by contrast, tends to increase as the wind sweeps up the inner CGM.

To start we provide analytic arguments suggesting that, for a wide range of galaxy properties, realistic clustering of SNe in star clusters can lead to a large fraction of the energy produced by SNe venting out into the halo in galactic winds. We first explain why randomly distributed SNe do not drive strong galactic winds (§4.3.1) and then study the critical role of clustering of SNe for producing powerful galactic winds (§4.3.2).

After setting the analytic framework we introduce a series of numerical experiments that probe the conditions under which a sizable fraction of the energy liberated by SNe can escape the disc to power galactic winds (§4.5). We focus our attention on the relatively high gas surface density regime, $\Sigma_g = 30 - 300\,M_\odot\,pc^{-2}$, appropriate for vigorously star forming galaxies that are seen to launch powerful winds, but also the regime where cooling losses have the potential to dramatically sap the wind potency. To start, we study how the super-bubble driven by the collective effect of numerous SNe propagates through the ISM while confined within the disc (§4.5.1). In the cases where the super-bubble reaches the scale height of the disc and can breakout we measure the dramatic decrease in radiative losses and the amount of mass and energy that are carried by the resulting wind (§4.5.2). In these experiments we detonate spatio-temporally clustered SNe in

discs of varying surface densities, which are either stratified or unstratified and have either no cooling below $10^4$ K making the ISM homogeneous, or inhomogeneous and multiphase with cooling down to $10^2$ K plus turbulent motions driven externally with $\delta v \approx 10$ km/s. The homogeneous and unstratified simulations are less realistic but allow for clearer analysis and provide a useful benchmark in comparison to the more realistic turbulent and stratified simulations in terms of the dynamics and numerical convergence. In §4.6, we summarize our findings, and discuss their observation implications, how they compare to existing works, and how they might be affected by missing physics. Finally, in a series of Appendices, we investigate the dependence of our results on spatial resolution (App. 4.A) and changes to the turbulent realization (App. 4.B).

## 4.3 Analytic Expectations

### 4.3.1 Uniformly Distributed SNe Do Not Drive Strong Galactic Winds

We begin by explaining analytically why SNe that are relatively uniformly distributed throughout a galaxy do not drive efficient winds. To do so, we consider a gas disc with surface density $\Sigma_{\rm g}$ and scale-height $h$. The Kenicutt-Schmidt relation implies a star formation rate surface density of $\dot{\Sigma}_* \simeq 0.07 \left(\Sigma_{\rm g}/100\,{\rm M_\odot\,pc^{-2}}\right)^2 M_\odot\,{\rm yr^{-1}\,kpc^{-2}}$ (Ostriker & Shetty, 2011). We assume that for each 100 $M_\odot$ stars formed ($\equiv m_*$) there is a core-collapse SNe. The resulting SNe rate per unit volume is thus

$$\dot{n}_{\rm SNe} \simeq 3\times10^{-3}\left(\frac{\Sigma_g}{100\,{\rm M_\odot\,pc^{-2}}}\right)^2\left(\frac{100\,{\rm pc}}{h}\right)\frac{\rm SNe}{\rm yr\,kpc^3}. \tag{4.1}$$

The ability of the SN remnants to overlap before cooling saps their energy is determined by the porosity $Q_{\rm cool} = 4/3\pi r_{\rm cool}^3 t_{\rm cool}\dot{n}_{\rm SNe}$ where $r_{\rm cool} \sim 21 n^{-0.42}$ pc and $t_{\rm cool} \sim 3\times10^4 n^{-0.54}$ yr are the cooling radius and cooling time of a SN remnant (e.g., Martizzi et al. 2015b), respectively, and $n$ is the ambient gas density in cm$^{-3}$ that a typical SNe goes off in. This will be less than the mean density of the ISM $\langle n\rangle$ because the ISM is inhomogeneous. For example, in a medium with a log-normal density distribution, as is typical of super-sonic turbulence in the ISM, half the volume is occupied by gas below a density $\sim 0.06\langle n\rangle(\mathcal{M}/30)^{-1.2}$ where $\mathcal{M} \gg 1$ is the assumed Mach number of the turbulence (Faucher-Giguère et al., 2013). We will thus take $n \equiv 0.1\,{\rm f_{V,0.1}}\,\langle {\rm n}\rangle$ as a typical value. Writing $\langle n\rangle = \Sigma_g/2hm_p$ we can combine the above results to estimate that

$$Q_{\rm cool} \sim 10^{-3}\left(\frac{\Sigma_g}{100\,{\rm M_\odot\,pc^{-2}}}\right)^{0.2}\left(\frac{h}{100\,{\rm pc}}\right)^{0.8}{\rm f_{V,0.1}^{-1.8}}. \tag{4.2}$$

Equation 4.2 shows that for conditions typical of galactic discs, SNe that are relatively uniformly distributed fail to overlap prior to the onset of radiative cooling. Most of the SNe energy is thus lost radiatively and SNe cannot collectively drive an energetically efficient wind of the kind envisioned in canonical SNe-driven wind models (e.g., Chevalier & Clegg 1985). Fielding et al. (2017c) showed this explicitly using global simulations of galactic discs that resolve the majority of the SN remnants in the disc. They found that the fraction of the SNe energy powering a wind

could be explained by an analytic model that considers only SNe going off sufficiently far above the disc midplane that the density has dropped to the point where $r_{\rm cool} \gtrsim h$; these are the supernova remnants that break out of the disc prior to the onset of strong radiative cooling. The resulting wind energy flux relative to the SNe energy injection rate, known as the energy loading $\eta_{\rm E}$, is given by (their eq. 3 & Fig. 4)

$$\frac{\dot{E}_{\rm wind}}{\dot{E}_{\rm SN}} \sim 2 \times 10^{-4} \left(\frac{h}{100\,{\rm pc}}\right)^{-3/2} \left(\frac{\Sigma_g}{100\,{\rm M_\odot\,pc^{-2}}}\right)^{-1}. \tag{4.3}$$

Equation 4.3 is inconsistent (by orders of magnitude) with observational estimates of the energy flux in galactic winds (including the hot gas portion of the wind in M82, for which Chandra observations suggest $\dot{E}_{\rm wind} \sim 0.3 - 1\,\dot{E}_{\rm SNe}$; Strickland & Heckman 2009a) and the wind powers needed to explain the inefficiency of low mass galaxy formation. In the remainder of this paper, we argue analytically and numerically that these problems can be rectified by accounting for the fact that star formation is highly clustered.

### 4.3.2 Clustered SNe

Most massive stars form in massive star clusters that in turn form in massive giant molecular clouds (GMCs) (de Wit et al., 2005). Observations and theory suggest that to first approximation massive GMCs and star clusters dominate the star formation rate in galaxies (e.g., Murray & Rahman 2010). This is because the GMC mass function (e.g., Solomon et al. 1987) and star cluster mass function (e.g., McKee & Williams 1997; McCrady & Graham 2007) are generally somewhat flatter than $\propto M^{-2}$, and so the most massive systems contain most of the mass/stars. Moreover, more massive GMCs probably turn a larger fraction of their mass into stars (because it is harder for feedback to disrupt more massive GMCs; e.g., Murray et al. 2010; Grudić et al. 2018). This strong clustering of massive stars and hence SNe can greatly enhance the efficacy of SNe feedback, leading to much stronger winds than suggested by equation 4.3.

#### 4.3.2.1 Star Cluster Properties

A plausible model of star clusters relates their mass to that of large-scale gravitationally unstable perturbations in the galactic disc in which they reside. In this case, star clusters have a characteristic mass

$$\begin{aligned} {\rm M_{cl}} &\simeq \epsilon_* {\rm M_{GMC}} \simeq \epsilon_* \pi {\rm h}^2 \Sigma_{\rm g} \\ &\simeq 10^5\,{\rm M_\odot} \left(\frac{\epsilon_*}{0.01}\right) \left(\frac{h}{100\,{\rm pc}}\right)^2 \left(\frac{\Sigma_g}{300\,{\rm M_\odot\,pc^{-2}}}\right), \end{aligned} \tag{4.4}$$

where ${\rm M_{GMC}} \simeq \pi {\rm h}^2 \Sigma_{\rm g}$ is the Toomre mass of self-gravitating clumps in a galactic disc and $\epsilon_*$ is the star cluster formation efficiency. In more detail, GMCs are expected to have a power-law distribution of masses with the Toomre mass representing the characteristic maximum mass of the distribution.

We assume that star clusters have a typical size of $R_{cl} \sim 10$ pc, although our results are not sensitive to this choice. We further assume that the star cluster can be modeled as a simple stellar population so that the SNe rate is roughly constant for $t \lesssim t_{SN} \equiv 30$ Myr (Leitherer et al., 1999). As a result the SNe rate per unit volume associated with (or bound to) a single star cluster is

$$\dot{n}_{SNe} \simeq \frac{3\,M_{cl}}{4\pi m_* t_{SN} R_{cl}^3} \simeq 8 \left(\frac{M_{cl}}{10^5\,M_\odot}\right)\left(\frac{R_{cl}}{10\,pc}\right)^{-3} \frac{SNe}{yr\,kpc^3} \tag{4.5}$$

The enhanced efficiency of SNe feedback is evident comparing equations 4.1 and 4.5: the SNe rate per unit volume is larger in the location of a star cluster by a factor of $\sim 2 \times 10^3$!

#### 4.3.2.2 Overlap of SNRs

For sufficiently massive clusters the SNe associated with an individual star cluster generically overlap and thus collectively power a coherent 'wind bubble' from the cluster. To see this, we note that for an individual SNR, the timescale over which the SNR reaches pressure equilibrium and/or mixes with the ambient ISM is $t_{PE} \sim 2 \times 10^6\, n^{-0.4}\, (\delta v/10\text{ km s}^{-1})^{-1.4}$ yrs and the radius of the SNR at that time is $R_{PE} \sim 70\, n^{-0.12} (\delta v/10\text{ km s}^{-1})^{-1.4}$ pc (Cioffi et al., 1988), where the ambient medium pressure is assumed to be $P = \rho \delta v^2$. We assume that because the ISM is turbulent, the timescale $\sim t_{PE}$ is of order the timescale on which the ambient ISM conditions revert to what they were prior to the SNe. For comparison, the time between SNe in a given cluster is $\Delta t_{SN} = t_{SN}(m_*/M_{cl})$. The cluster's SNe can only drive a coherent bubble if $\Delta t_{SN} \ll t_{PE}$, which requires

$$M_{cl} \gg 1500\, n^{0.4} \left(\frac{\delta v}{10\text{ km s}^{-1}}\right)^{1.4} M_\odot. \tag{4.6}$$

When equation 4.6 is not satisifed, each individual SNR is effectively isolated and the results of §4.3.1 are likely to be applicable. By contrast, when equation 4.6 is satisfied each SNe produced by the cluster goes off in a medium whose properties are set by the cluster's previous SNe. Moreover, so long as $R_{cl} \ll R_{PE}$, which is easily satisfied, the exact size of the star cluster is not that important to the subsequent dynamics. In this regime, the star cluster feedback should be modeled as a coherent 'wind bubble' driven by the cluster's SNe (§4.3.3). In fact, because $R_{PE}$ is significantly larger than the size of massive star clusters, many of the SNe within the GMC that formed at the same time as the cluster likely contribute to driving the bubble, not just those associated with the most massive cluster.

### 4.3.3 Cluster-driven Super-Bubbles

The preceding section shows that for a wide range of cluster properties, a cluster's SNe drive a coherent bubble into the ISM. Here we review analytically some of the expected properties of these bubbles (e.g., Weaver et al. 1977; McCray & Kafatos 1987), approximating the multiple SNe as a constant source of mass and energy. We numerically model the bubble evolution in §4.5.

We assume that $\dot{N}_{\rm SNe} = {\rm M_{cl}}/({\rm m_* t_{SN}})$, so that

$$\dot{M} = \beta {\rm M_{ej}} \dot{\rm N}_{\rm SNe} = \beta {\rm M_{ej}} \frac{\rm M_{cl}}{\rm m_* t_{SN}} \tag{4.7}$$

$$\dot{E}_{\rm SN} = {\rm E_{SN}} \dot{\rm N}_{\rm SNe} = \frac{\rm E_{SN} M_{cl}}{\rm t_{SN} m_*} \tag{4.8}$$

The parameter $\beta \gtrsim 1$ characterizes mixing of ambient ISM gas into the hot, shocked SNe ejecta.

One model for the collective effect of the cluster's SNe is the steady state wind model of Chevalier & Clegg (1985), in which the SNe thermalize their energy and drive a steady wind into the ISM, which is in turn the source driving the super-bubble considered here. Sharma et al. (2014b) showed that for the steady wind model to be applicable the free expansion radius of an individual SNR must be smaller than the termination shock of the Chevalier & Clegg (1985) wind model. This only occurs for massive clusters $\gtrsim 10^6 n^{3/13} {\rm M_\odot}$. Nonetheless, so long as equation 4.6 is satisfied, the properties of the cluster-driven super-bubble are not strongly affected by whether or not a steady wind is established. The reason is that the sound crossing time inside the super-bubble is much shorter than the expansion time of the bubble as a whole and so the density and temperature approach roughly constant values inside the bubble, set by the mass and energy supplied by the SNe, but relatively independent of exactly where the SNe ejecta thermalize their energy.

#### 4.3.3.1 Cooling of SNe-Driven Super-Bubbles

In the absence of radiative losses in the SNe ejecta, the radius of the forward shock associated with the super-bubble propagating into a medium of density $\rho$ is given by $R_s \propto (\dot{E}/\rho)^{1/5} t^{3/5}$. Including the constants,

$$R_s \simeq 760\, A_E \left(\frac{t}{\rm t_{SN}}\right)^{3/5} \ {\rm pc} \ \ ({\rm t} < {\rm t_{SN}}) \tag{4.9}$$

$$\text{where } A_E \equiv \left(\frac{\rm M_{cl}}{10^5\, {\rm M_\odot}}\right)^{1/5} \left(\frac{n}{\rm cm^{-3}}\right)^{-1/5}.$$

The super-bubble is driven by the pressure of the hot SNe ejecta. It is the cooling of this ejecta, not the forward shock driven into the ISM, that determines whether the non-radiative evolution assumed in equation 4.9 is applicable. Estimating the cooling of the hot SNe ejecta we find that

$$\frac{t_{\rm cool}}{t_{\rm exp}} \simeq \frac{2\times 10^3}{\beta^{3/2}\, n^{2/3}} \left(\frac{\rm M_{cl}}{10^5\, {\rm M_\odot}}\right)^{-1/3} \left(\frac{R_s}{100\, {\rm pc}}\right)^{-1/3} \tag{4.10}$$

where we have assumed free-free cooling dominates. Equation 4.10 shows that the cooling of the super-bubble is negligible even for densities as high as $n \sim 10^3 {\rm cm^{-3}}$ unless there is efficient mixing of the hot SNe ejecta with the surrounding ambient ISM (parameterized here by $\beta \gtrsim 1$ which is larger for higher mass loading of the SNe ejecta).

The above estimate of $t_{\rm cool}$ in the SNe ejecta assumes that the electron and proton temperatures are equal. Observations of SNe shocks show, however, that this is not the case for high

speed shocks (Ghavamian et al., 2007). The electron-proton Coulomb collision time $t_{\rm ep}$ is actually quite long and may be the rate limiting step in setting the cooling of the shocked SNe ejecta (see Faucher-Giguère & Quataert 2012 for similar physics in the context of bubbles driven by black hole feedback). We find

$$\frac{t_{\rm ep}}{t_{\rm exp}} \simeq \frac{6000\, f_e^{3/2}}{\beta^{5/2} n^{2/3}} \left(\frac{\rm M_{cl}}{10^5\,\rm M_\odot}\right)^{-1/3} \left(\frac{R_s}{100\,\rm pc}\right)^{-1/3}, \tag{4.11}$$

where we have assumed $T_e = f_e T_p = 1.3\times10^9 f_e/\beta$ K. So long as $t_{\rm ep} \gtrsim t_{\rm exp}$, most of the thermal energy of the bubble will remain locked in the protons which cannot radiate efficiently. Equation 4.11 demonstrates that if SNe-driven super-bubbles undergo a significant energy conserving phase, properly modeling the cooling of that phase requires taking into account $T_e \neq T_p$ at SNe shocks. However, since $t_{\rm ep}$ (eq. 4.11) $\lesssim t_{\rm cool}$ (eq. 4.10) for all realizable parameters ($f_e \lesssim 1$ and $\beta \gtrsim 1$), and they scale the same with $n$ and $R_s$, it is unlikely that electron-proton thermalization will change the bubble cooling by more than order unity. It is thus unlikely to be dynamically important even though the absence of electron-proton equilibration is important for interpreting observations of young SNe remnants. Moreover, as with free-free cooling, the Coulomb coupling timescale is very sensitive to the mixing of the SNe ejecta with the ambient ISM, with $t_{\rm ep}/t_{\rm exp} \propto \beta^{-5/2}$.

There are two potential mechanisms that generate mixing between the SNe ejecta and the ambient medium: the Rayleigh-Taylor instability and the fact that the ambient medium is inhomogeneous. The contact discontinuity between the (denser) shocked ambient medium and the (less dense) shocked SNe ejecta is formally Rayleigh-Taylor stable as the bubble shock and contact discontinuity decelerate into the surrounding ISM. However, each individual SNR goes through a Rayleigh-Taylor unstable phase as it transitions from free-expansion to the Sedov-Taylor phase. To model the mixing induced by the Rayleigh-Taylor instability it is thus critical to separately resolve each individual SNR, rather than treat the SNe as a source of uniform energy and mass injection as is often done.

Independent of the Rayleigh-Taylor instability, a second source of mixing is determined by the multiphase structure of the ambient ISM, i.e., the extent to which dense clouds from the ISM penetrate into the SNe ejecta (e.g., Kim et al. 2017). To quantify the importance of mixing increasing the density and cooling rate of the SNe ejecta, we note that the rate at which the ambient medium is swept-up by the forward shock is $\dot{M}_s = 4\pi R_s^2 \rho v_s$. If we assume that a fraction $\rm f_{mix} \leq 1$ of this becomes mixed into the SNe ejecta via the combined action of the Rayleigh-Taylor instability and the inhomogeneous ambient medium, we find that the effective $\beta$ of the ejecta is

$$\beta_{\rm mix} \simeq 1.7\times10^3\, \rm f_{mix}\, n^{2/3} \left(\frac{\rm M_{cl}}{10^5\,\rm M_\odot}\right)^{-2/3} \left(\frac{\rm R_s}{100\,\rm pc}\right)^{4/3}. \tag{4.12}$$

For $\rm f_{mix} \sim 1$, this is enormous and is sufficient to increase the density and decrease the temperature of the SNe ejecta to $\sim 10^6$ K at which point Coulomb coupling and radiative cooling are far more efficient. Re-evaluating the cooling of the ejecta given this new density and temperature we find

$$\frac{t_{\rm cool}}{t_{\rm exp}} \simeq 10^{-2}\, \frac{\rm f_{mix}^{-2} n^{-2}}{\Lambda_{-22}} \left(\frac{\rm M_{cl}}{10^5\,\rm M_\odot}\right) \left(\frac{R_s}{100\,\rm pc}\right)^{-3} \tag{4.13}$$

where the cooling function is given by $\Lambda = 10^{-22}\Lambda_{-22}$ ergs cm$^3$ s$^{-1}$. Kim et al. (2017)'s simulations of super-bubble evolution in a multiphase ISM with $\langle n \rangle \sim 0.1 - 10$ cm$^{-3}$ suggest that mixing of the SNe ejecta with ambient ISM gas is relatively efficient, so that the rapid cooling implied by equation 4.13 is probably appropriate regime. We find the same in our simulations in the early phase of bubble evolution, prior to the bubble breaking out of the galactic disc (see §4.5.1). As we shall show, however, radiative losses become much less significant after breakout (see §4.5.2).

#### 4.3.3.2 Momentum Conserving Bubbles

When radiative cooling saps the bubble of much of its energy, we can approximate the bubble evolution as momentum conserving, with $R_s \propto (\dot{P}/n)^{1/4} t^{1/2}$ where $\dot{P}$ is the momentum per unit time supplied by the star cluster. This implies

$$R_s \simeq 650\, A_P \left(\frac{t}{\mathrm{t_{SN}}}\right)^{1/2} \mathrm{pc} \quad (\mathrm{t} < \mathrm{t_{SN}}) \tag{4.14}$$
$$\text{where } A_P \equiv \left(\frac{\mathrm{M_{cl}}}{10^5\,\mathrm{M_\odot}} \frac{\mathrm{P_{SN}}}{3\times10^5\,\mathrm{km\,s^{-1}\,M_\odot}}\right)^{1/4} \left(\frac{n}{\mathrm{cm^{-3}}}\right)^{-1/4}$$

and $\mathrm{P_{SN}}$ is the momentum of a typical SNe at the end of the Sedov-Taylor phase, which is only a weak function $\propto n^{-1/7}$ of the density of the medium into which the SNe goes off (e.g., Cioffi et al. 1988). Equation 4.14 also implies that the speed of the forward shock is

$$v_s \simeq 70\, n^{-1/2} \left(\frac{\mathrm{M_{cl}}}{10^5\,\mathrm{M_\odot}}\right)^{1/2} \left(\frac{R_s}{100\,\mathrm{pc}}\right)^{-1} \times \left(\frac{\mathrm{P_{SN}}}{3\times10^5\,\mathrm{km\,s^{-1}\,M_\odot}}\right)^{1/2} \mathrm{km\ s^{-1}}. \tag{4.15}$$

### 4.3.4 Application to Galactic discs

We now evaluate the previous results in the context of galactic discs to determine when the bubble driven by the star cluster will breakout of the disc, potentially contributing to a galaxy-scale outflow. We define breakout to be satisfied if the bubble reaches $R_s \sim h$ with $v_s \gtrsim \delta v$ for $t < \mathrm{t_{SN}}$ (e.g., McCray & Kafatos 1987; Koo & McKee 1992). If this is the case the majority of the cluster's SNe go off after the bubble has broken out of the disc. This removes the pressure confining the late-time SNe and they are likely to freely expand out into the halo, contributing a large fraction of their energy to a galactic wind. In §4.5.2 we demonstrate explicitly using numerical simulations that $\dot{E}_{\mathrm{wind}} \sim \dot{E}_{\mathrm{SNe}}$ post breakout because most of the cluster's SNe can vent into the halo. Thus determining whether or not star cluster driven bubbles can breakout out of galactic discs is critical for understanding the efficiency of galactic winds driven by SNe.

We consider a gas disc of surface density $\Sigma_{\mathrm{g}}$ in a spherical potential with circular velocity $v_c$. The scale-height of the disc is given by $h/r \sim \delta v/v_c$, i.e.,

$$h \sim 100\, \delta v_{10}\, \mathrm{t_{d,7}\ pc} \tag{4.16}$$

where we have defined $\delta v_{10} = \delta v/10\,\mathrm{km\ s^{-1}}$ and $t_{d,7} = (r/v_c)/(10^7 \mathrm{yr})$. We assume that the interstellar medium has density

$$n = f_V \langle n \rangle \simeq 20 \left(\frac{f_V}{\delta v_{10}\, t_{d,7}}\right) \left(\frac{\Sigma_g}{100\,M_\odot\,\mathrm{pc}^{-2}}\right) \mathrm{cm}^{-3}. \tag{4.17}$$

In contrast to §4.3.1, we do not necessarily assume $f_V \ll 1$ in what follows, even though this is appropriate for the median conditions in the ISM. The reason is that the mass mixed into the SNe ejecta (and thus the bulk of the overlying ISM) must itself be removed in order for the hot gas produced by later SNe to vent.

To quantify the likelihood of breakout, we assume momentum conserving evolution prior to breakout, evaluate $M_{cl}$ using equation 4.4 (scaling $\epsilon_* = 0.1\epsilon_{*,0.1}$), $h$ using equation 4.16, and $n$ using equation 4.17, to find

$$\frac{R_s(t = t_{SN})}{h} \simeq 4\, \epsilon_{*,0.1}^{1/4}\, f_V^{-1/4}\, \delta v_{10}^{-1/4}\, t_{d,7}^{-1/4} \tag{4.18}$$

$$v_s(R_s = h) \simeq 30\, \epsilon_{*,0.1}^{1/2}\, f_V^{-1/2}\, \delta v_{10}^{1/2}\, t_{d,7}^{1/2}\ \mathrm{km\ s^{-1}}. \tag{4.19}$$

Equations 4.18 and 4.19 show that the most stringent constraint is typically whether the bubble reaches pressure equilibrium with $v_s \sim \delta v$ prior to breakout. The condition $R_s(t = t_{SN}) \gtrsim h$ is comparatively easy to satisfy. Put another way, if star-cluster driven bubbles breakout of galactic discs, they do so quickly, on a timescale $\ll t_{SN}$, so that most of the SNe associated with the cluster vent at late times contributing their energy to a galactic wind.

The above results can be derived even more simply by asking at what time $t_{breakout}$ and speed can a thrust $\dot{P}$ move the ambient ISM mass of $\pi \Sigma_g h^2$, neglecting gravity or pressure confinement. The results can be expressed in terms of two basic velocities in the problem. The first is $h/t_{SN} \sim 3\,(h/100\mathrm{pc})$ km s$^{-1}$, the speed to move a distance of order the scale-height before the cessation of the cluster's SNe. The second is $\epsilon_* P_{SN}/m_* \sim 300\,\epsilon_{*,0.1}$ km s$^{-1}$, the speed set by the terminal momentum of SNe, scaled by the cluster formation efficiency. Expressed in these terms, we find

$$\frac{t_{breakout}}{t_{SN}} \simeq \left(\frac{h}{t_{SN}}\,\frac{m_*}{\epsilon_* P_{SN}}\right)^{1/2} \quad \text{and} \tag{4.20}$$

$$v_s(R_s = h) \simeq \left(\frac{\epsilon_*\, P_{SN}}{m_*}\,\frac{h}{t_{SN}}\right)^{1/2}, \tag{4.21}$$

which is valuable because it also reveals more directly the dependence on the SNe/IMF properties $P_{SN}$, $t_{SN}$, and $m_*$.

## 4.4 Numerical Simulations

The analytic arguments in the preceding section demonstrate that sufficiently clustered SNe can inflate a bubble 100s of pc in size well before $t_{SN}$, even in the conservative, momentum-driven

limit. This means that in many cases the bubble will be able to reach $h$, the scale height of the galactic disc and breakout. Post-breakout the dynamics and energetics can change dramatically, which will have major implications for the properties of the resulting galactic wind.

We performed a set of controlled simulations to test the conditions under which a large fraction of the SNe energy can escape the disc to power galactic winds. We specifically look at the change in energetics prior to and following breakout, which in turn determines the degree of mass and energy loading of the wind. Our simulations are performed with the Eulerian hydrodynamics code ATHENA++ (White et al., 2016), which is a recent rewrite of ATHENA (Stone et al., 2008). We adopt an adiabatic equation of state and evolve the standard hydrodynamics equations with source terms to include optically thin cooling and photoelectric heating, energy and momentum injection from SNe and from externally driven turbulence. We do not add any explicit thermal or viscous diffusion.

We study the bubble evolution and breakout process with four types of simulations that are either homogeneous or turbulent, and vertically stratified or unstratified (including an external gravitational potential or not). The turbulent stratified simulations are the most realistic and are our main focus. The homogeneous simulations have no radiative cooling below $10^4$ K and no photoelectric heating, so, with the exception of the bubble material, the ISM is single phase. On the other hand, in the turbulent simulations we allow the gas to cool down to $10^2$ K and include photoelectric heating. The turbulent energy injected prevents the ambient ISM from forming a razor thin disc when gravity is included.

## 4.4.1 Numerical Method

### 4.4.1.1 Cooling and Heating

The energy source term – the net change in energy per unit time per unit volume – is $\dot{E}_{\rm cool-heat} = -n_H^2\Lambda(T)+n_H\Gamma$. The cooling curve $\Lambda(T)$ we use was made by combining the $T > 10^4$ K collisional ionization equilibrium cooling curve provided by Oppenheimer & Schaye (2013) with the $T < 10^4$ K cooling curve developed by Koyama & Inutsuka (2002). We adopt a photoelectric heating rate $\Gamma = 10^{-26}$erg/s $(\langle n_H\rangle/{\rm cm}^{-3})$, which scales with the average density as a means to crudely approximate the increase in photoelectric heating in higher density regions where the star formation rates are higher. We explicitly modeled our cooling and heating implementation on what was used by Kim et al. (2017) to facilitate comparisons between our results. All of the gas in our simulations has fixed solar metallicity. In keeping with the idealized nature of our simulations we also keep the mean molecular mass $\mu$ fixed at the value appropriate for a fully ionized plasma at solar metallicity, which means that the temperature of neutral and partially ionized gas ($T \lesssim 10^4$ K) is $\lesssim 2$ factor of two lower than it would've been with a variable $\mu$ – this has a negligible effect on the dynamics.

We impose a cooling time constraint on the hydrodynamics time step so that $dt_{\rm hydro}$ is less than or equal to one quarter of the shortest cooling time $t_{\rm cool}$ in the entire domain. This rather stringent requirement ensures that the operator split implementation of cooling and heating properly captures the dynamics. Comparison simulations run only using the standard CFL constraint on $dt_{\rm hydro}$ yielded qualitatively different results.

#### 4.4.1.2 Supernovae Injection

We inject SNe using the method developed by Martizzi et al. (2015b) that determines the amount of thermal and kinetic energy to inject given the spatial resolution and ambient gas properties. This implementation accounts for the cooling and expansion of the SN remnant below the grid scale and is derived from high resolution simulations of individual SN remnants. In practice this sub-grid model works by first calculating the average properties within a small sphere of radius $r_{\rm inj} = 3\Delta x$ centered on the location of the upcoming SN, then setting all of the state variables within that sphere to their average value plus the additional mass, energy, and momentum from the SNe. We have used this SNe injection method in studies of the effect of SNe on an unstratified ISM patch (Martizzi et al., 2015b), a stratified ISM patch (Martizzi et al., 2016b), and on launching winds from global galactic discs (Fielding et al., 2017c). In our current simulations the SNe are seeded at random locations within the cluster radius $R_{\rm cl} = 10$ pc. Their temporal spacing is set by the cluster mass $\Delta {\rm t_{SN}} = {\rm t_{SN}}/({\rm M_{cl}}/{\rm m_\star})$. Because the SNe are tightly clustered in space and time all but the first few SNe go off within the hot, dilute remnant of a previous SN (so long as $\Delta t_{\rm SN} < t_{\rm PE}$; see §4.3.2.2), so the cooling radii are at least an order of magnitude larger than the injection radius $r_{\rm inj}$. The very large cooling radii relative to the spatial resolution ensures that essentially all of $E_{\rm SN} \equiv 10^{51}$ erg is deposited in the surrounding gas.

#### 4.4.1.3 Turbulence and ISM inhomogeneities

In the turbulent simulations velocities are driven on large scales such that the mass-weighted velocity dispersion $\delta v = \langle v^2 \rangle_M^{1/2} = 10$ km/s – consistent with observed ISM velocity dispersions and roughly equal to the sound speed of $10^4$ K gas. The turbulent kinetic energy injection rate is given by $\dot{E}_{\rm turb} \approx \rho L_{\rm box}^2 \delta v^3$, where $L_{\rm box}$ is the horizontal box width. The turbulence is driven on large scales with power equally distributed between wave numbers of 1 to 4 in units of $2\pi/L_{\rm box}$. The velocity forcing is restricted spatially to focus the driving to be within $h$. The relative energy input follows $1 + \tanh((h - |z|)/0.5\,h)$. A new realization of the driving pattern is generated every $5 \times 10^{-3}$ crossing-times and they are time correlated by an Ornstein-Uhlenbeck process with a correlation time of 1/2 crossing-time (Lynn et al., 2012). The smoothly changing driving pattern ensures that the turbulence does not develop any unphysical standing patterns or outbursts from impulsive changes.[1] The turbulence, heating, and cooling in the turbulent simulations lead to a multiphase medium that is closer to what is expected in reality although additional processes such as self-gravity, magnetic fields, viscosity and conduction would likely change the details of the phase structure.

The initial conditions for the turbulent simulations are generated by allowing the turbulence and cooling to proceed for 60 Myr – many turbulent crossing times and cooling times – prior to the onset of SN explosions.

[1] Interestingly the driving alone is capable of launching a weak wind from the ISM as was studied by Sur et al. (2016).

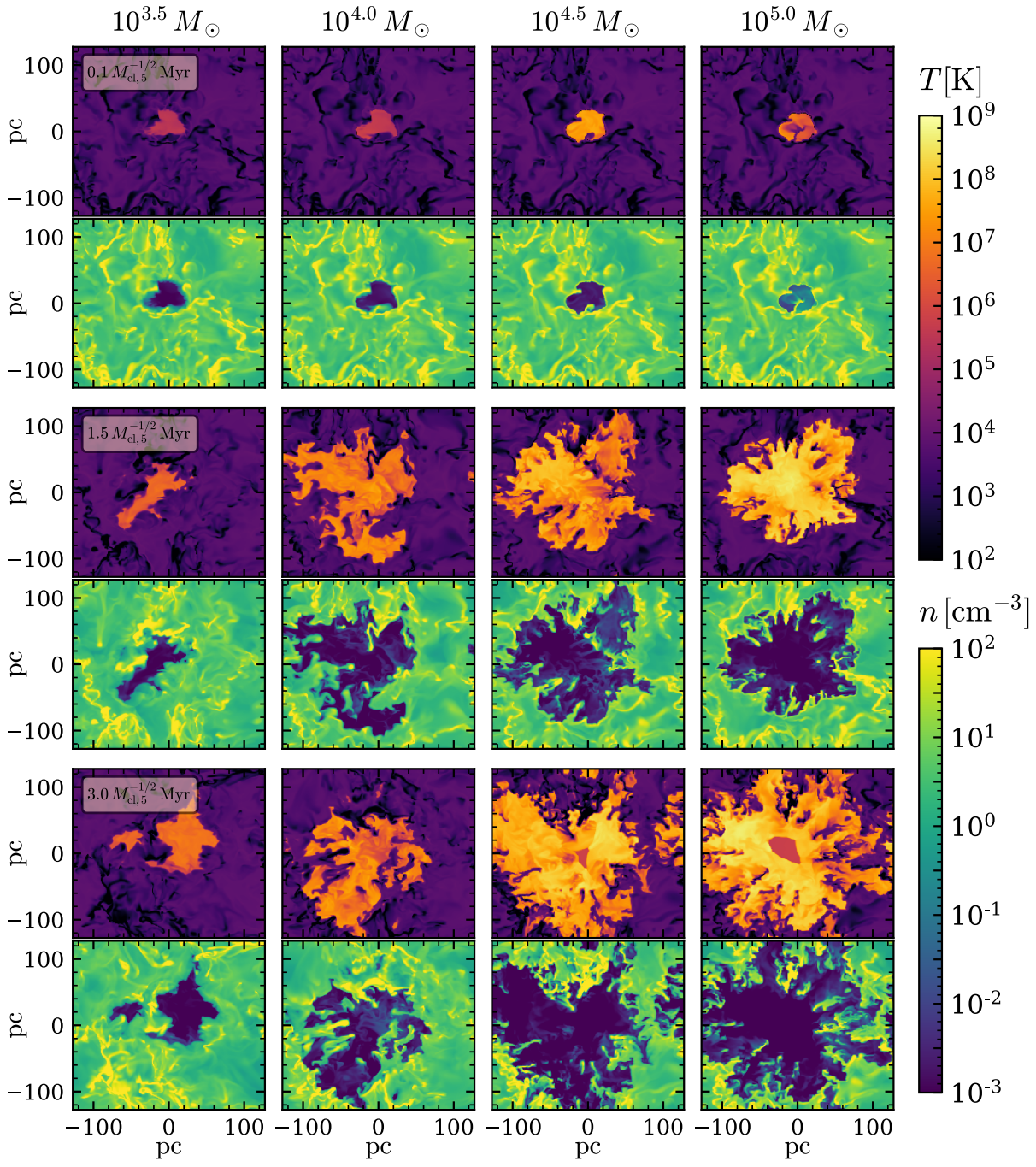


Figure 4.1: Temperature and number density slices through the turbulent unstratified simulations that have a mean density $\langle n \rangle = 13.87\,\mathrm{cm}^{-3}$. Each column shows the bubble evolution for cluster masses increasing from left to right. Each row shows a snapshot at $t = 0.33, 1.5$ and 3 $\mathrm{M_{cl,5}}^{-1/2}$ Myr, respectively. The times are scaled with $\mathrm{M_{cl}^{-1/2}}$ to account for the fact that $r_{\rm sh} \propto t^{1/4}\mathrm{M_{cl}^{1/2}}$ (see eq. 4.14). The bubbles expand more rapidly in the low density regions causing them to be highly asymmetric. Over dense regions in the ISM penetrate the expanding bubbles and the strong shear forces lead to significant mixing of the ISM and bubble material.

Table 4.1: Key simulation properties

| | |
|---|---|
| ISM structure | turbulent or homogeneous, and stratified (gravity) or unstratified |
| mean gas densities (midplane) | $\langle n \rangle = 13.9,\ 139\ \mathrm{cm}^{-3}$ |
| median gas densities (turbulent sims.) | $n_{\mathrm{median}} = 3.6,\ 32\ \mathrm{cm}^{-3}$ |
| gas surface density (stratified sims.) | $\Sigma_{\mathrm{g}} = 30,\ 300\ \mathrm{M}_{\odot}\ \mathrm{pc}^{-2}$ |
| escape speed to top of box (stratified sims.) | $94\ \mathrm{km\ s}^{-1}$ |
| star cluster masses | $\mathrm{M}_{\mathrm{cl}} = 10^4 - 10^6\ \mathrm{M}_{\odot}$ |
| $\epsilon_{\star} \equiv \mathrm{M}_{\mathrm{cl}}/\pi \mathrm{h}^2 \Sigma_{\mathrm{g}}$ | $\sim 0.003 - 0.1$ |

#### 4.4.1.4 External Gravity

By including an external gravitational potential we can study the evolution of bubbles in a vertically stratified medium and what happens after a super-bubble reaches the scale height and breaks out of the disc. In our stratified simulations we adopt a simple gravitational potential that depends only on the height $z$ and represents the vertical component of a spherical potential with circular velocity $v_c$ at a distance of $r$, so $\Phi = \frac{1}{2}(v_c^2/r^2)z^2$. We adopt $v_c = 175$ km/s and $r = 1$ kpc. We neglect the self gravity of the gas $\sim 2\pi G \Sigma_{\mathrm{gas}} z$, which is sub-dominant at most heights up to a gas surface density of $\sim 1000\, M_{\odot}/\mathrm{pc}^2$. Although less realistic, studying the super-bubble evolution without gravity and stratification has the advantage of allowing us to cleanly isolate the pre-breakout phase, so we also present simulations with no external gravity. This has the added benefit of allowing us to connect to the existing numerical simulations of bubble evolution in an unstratified ISM, both inhomogeneous (Kim et al., 2017), and homogeneous (Yadav et al., 2017; Gentry et al., 2017b, 2018).

### 4.4.2 Simulation Suite

For each of our four types of simulations – either turbulent or homogeneous, and stratified or unstratified – we adopted two surface densities, $\Sigma_{\mathrm{g}} = 30$ and $300\ \mathrm{M}_{\odot}\ \mathrm{pc}^{-2}$ (really volume densities $\langle n \rangle \approx 13.9$ and $139\ \mathrm{cm}^{-3}$ for the unstratified simulations). For each surface density we simulated four different cluster masses corresponding to a range in cluster formation efficiencies of $\epsilon_* = 0.003 - 0.1$. The key properties of the simulations are summarized in Table 4.1.

The surface densities we adopt are appropriate for many star forming galaxies and begin to approach the levels seen in the starburst galaxies that launch the most vigorous and readily observable winds. The high surface densities also allow us to study the evolution of the bubbles in the regime where cooling losses have the potential to dramatically reduce their potency. In the unstratified simulations, when we refer to $\Sigma_{\mathrm{g}}$ we mean that the average density of the simulation is equal

to the midplane density of the corresponding stratified simulation, namely of a disc with that $\Sigma_g$ and a scale height $h = 100\,\mathrm{pc}$. The $\Sigma_g = 30$ and $300\,\mathrm{M_\odot\,pc^{-2}}$ simulations have mean (midplane) densities of $\langle n \rangle = 13.9$ and $139\,\mathrm{cm^{-3}}$, respectively. However, the possibly more relevant density for the turbulent simulations is the median density, or the density of the volume-filling material, since the expanding bubble will follow the path of least resistance. The $\Sigma_g = 30$ and $300\,\mathrm{M_\odot\,pc^{-2}}$ unstratified turbulent simulations have median densities $n_{\mathrm{median}} \approx 3.6$ and $32\,\mathrm{cm^{-3}}$, respectively, and average warm gas (above 5000 K) densities of $\langle n_{\mathrm{warm}} \rangle \approx 2.6$ and $30.6\,\mathrm{cm^{-3}}$.

For the unstratified simulations we adopt a periodic cubical domain that is 256 pc on a side, while the stratified simulations are 512 pc on a side in the horizontal direction and 1080 pc in the vertical direction. The stratified simulations are periodic in the horizontal direction and have modified outflow boundary conditions in the vertical direction that prevent artificial inflows that can arise from a non-zero gravitational acceleration at the boundary.

Our fiducial spatial resolution is $\Delta x = 2\,\mathrm{pc}$ for the stratified simulations and 1 pc for the unstratified simulations. In Appendices 4.A.1, 4.A.2, and 4.A.3, we present higher resolution simulations as well and demonstrate that this resolution is sufficient to achieve converged results in most of the quantities of interest.

## 4.5 Simulation Results

We begin by focusing on the evolution of the super-bubble prior to breakout – paying close attention to the bubble growth and the degree of cooling and mixing in the bubble (§4.5.1). This allows us to demonstrate that failure to break out is due to stalling rather than the bubble not having enough time to breakout prior to the cessation of SNe at $t = t_{\mathrm{SN}}$ (Kim et al., 2017). Next, we present the results of the post-breakout evolution, showing, in particular, that once a vent through the ISM is opened the amount of energy lost to cooling drops dramatically and the resulting winds have much higher mass and energy loadings – on the order of $\sim 0.1 - 1$ – than contained in the pre-breakout bubble (§4.5.2). For reference, Table 4.1 lists and defines the main quantities we focus on in our analysis.

### 4.5.1 Super-Bubble Evolution Within the ISM: Stall or Breakout?

In this section we restrict our attention to the evolution of the super-bubble prior to breakout. To isolate this phase of the evolution we use our unstratified simulations that have no external gravitational potential. The primary quantity we are interested in is the super-bubble radius $r_{\mathrm{bubble}}$ to connect to the above analytic predictions and to assess under what conditions the super-bubble reaches the disc scale height $h$ and can breakout of the disc. We also present the energy and hot gas mass of the bubble as it expands into and mixes with the surrounding ISM. However, as we will show in the next section these quantities are of secondary importance because after breakout the cooling and mixing change dramatically.

Fig. 4.1 shows temperature and number density slices through the middle of the $\langle n \rangle = 13.9\,\mathrm{cm^{-3}}$ turbulent simulations with cluster masses ranging from $10^{3.5}$ to $10^5\,\mathrm{M_\odot}$ at three times. The time

| Mass | Energy | Momentum |
|---|---|---|
| $\dot{M}_\star$ [c] $= m_* \dot{N}_{\rm SNe} = \frac{m_*}{\Delta t_{\rm SN}} = \frac{M_{\rm cl}}{t_{\rm SN}}$ | $\dot{E}_{\rm SN}$ [d] $= E_{\rm SN}\dot{N}_{\rm SNe} = \frac{E_{\rm SN} M_{\rm cl}}{t_{\rm SN} m_*} = \frac{E_{\rm SN}}{\Delta t_{\rm SN}}$ | $\dot{P}_{\rm SN}$ [e] $= M_{\rm ej}\, v_{\rm ej}\, \dot{N}_{\rm SNe}$ |
| $\dot{M}_{\rm wind} = \int \rho\,(\vec{v}\cdot\hat{z})dA$ | $\dot{E}_{\rm wind} = \int \rho\,(\vec{v}\cdot\hat{z})\left(\frac{1}{2}v^2 + \frac{\gamma}{\gamma-1}\frac{P}{\rho} - \frac{1}{2}v_{\rm esc}^2\right) dA$ | $\dot{P}_{\rm wind} = \int \rho\,(\vec{v}\cdot\hat{z})^2 dA$ |
| $\eta_{\rm M}$ [a] $= \frac{\dot{M}_{\rm wind}}{\dot{M}_\star}$ | $\eta_{\rm E}$ [b] $= \frac{\dot{E}_{\rm wind}}{\dot{E}_{\rm SN}}$ | $\eta_{\rm P} = \frac{\dot{P}_{\rm wind}}{\dot{P}_{\rm SN}}$ |
| $\hat{M}_{\rm hot}$ [a] $= \frac{\sum_{T>10^5\,{\rm K}} m_{\rm cell}}{N_{\rm SN}\, m_*}$ | $\hat{E}_{\rm hot}$ [b] $= \frac{\sum_{T>10^5\,{\rm K}} E_{\rm cell}}{N_{\rm SN}\, E_{\rm SN}}$ | |
| | $\eta_{\rm cool}$ [b] $= \frac{\dot{E}_{\rm SN} + \dot{E}_{\rm turb} - \dot{E}_{\rm cool}}{\dot{E}_{\rm SN}}$ | |

Table 4.1: Definitions of primary quantities used in analysis. [a] $\hat{M}_{\rm hot}$ is calculated in the unstratified simulations as a proxy for $\eta_{\rm M}$ in the stratified simulations. [b] $\hat{E}_{\rm hot}$ is calculated in the unstratified simulations as a proxy for $\eta_{\rm E}$ in the stratified simulations, and both are compared to $\eta_{\rm cool}$, the normalized energy that remains after cooling. [c] Star formation rate that corresponds to the cluster mass where $m_* = 100\,{\rm M}_\odot$, and $t_{\rm SN} = 30\,{\rm Myr}$. [d] SN energy injection rate where $E_{\rm SN} = 10^{51}$ ergs. [e] Momentum injection rate by SN where $M_{\rm ej} = 3\,{\rm M}_\odot$, and $v_{\rm ej} = 2.6\times10^3$ km s$^{-1}$. The momentum per SN is the value injected by our SN model not the asymptotic momentum of an isolated SN in an unstratified medium, which can be $\sim 20-40$ times larger due to work done in the Sedov-Taylor phase.

interval is scaled with $M_{\rm cl}^{-1/2}$ to match the expected scaling of a momentum driven bubble (see eq. 4.14). It only takes the bubble from the most massive cluster a few Myr to reach $\sim 100\,{\rm pc}$. On the other hand, the least massive cluster's super-bubble is only a few tens of pc in size at this time and has reached pressure equilibrium with the ISM and stalled. The super-bubbles expand more rapidly in the low density regions of the ISM and end up enveloping the over dense clumps. These dense clumps experience strong shear forces, which leads to significant mixing. As shown in §4.3.3.1, the degree of mixing is critical for the bubble evolution since an order unity $f_{\rm mix}$ can cause the bubble material to cool very rapidly.

Before looking at the bubble radius evolution we must first define how we identify it. There are several possible choices for measuring the size of the bubble. In the homogeneous ISM simulations it is straightforward to separate the swept up ISM material from the unperturbed ISM material with a velocity cut since the unperturbed ISM is initially at rest (see Kim et al. 2017 in which the ISM was inhomogeneous but static, and Yadav et al. 2017; Gentry et al. 2018 whose simulations adopted a purely homogeneous static ISM). However, in the turbulent simulations the ISM is not static so we instead adopt a temperature cut. We classify all gas with $T > 10^5$ K as bubble material[2] and

[2] Absent the bubble material no gas is in this temperature range.

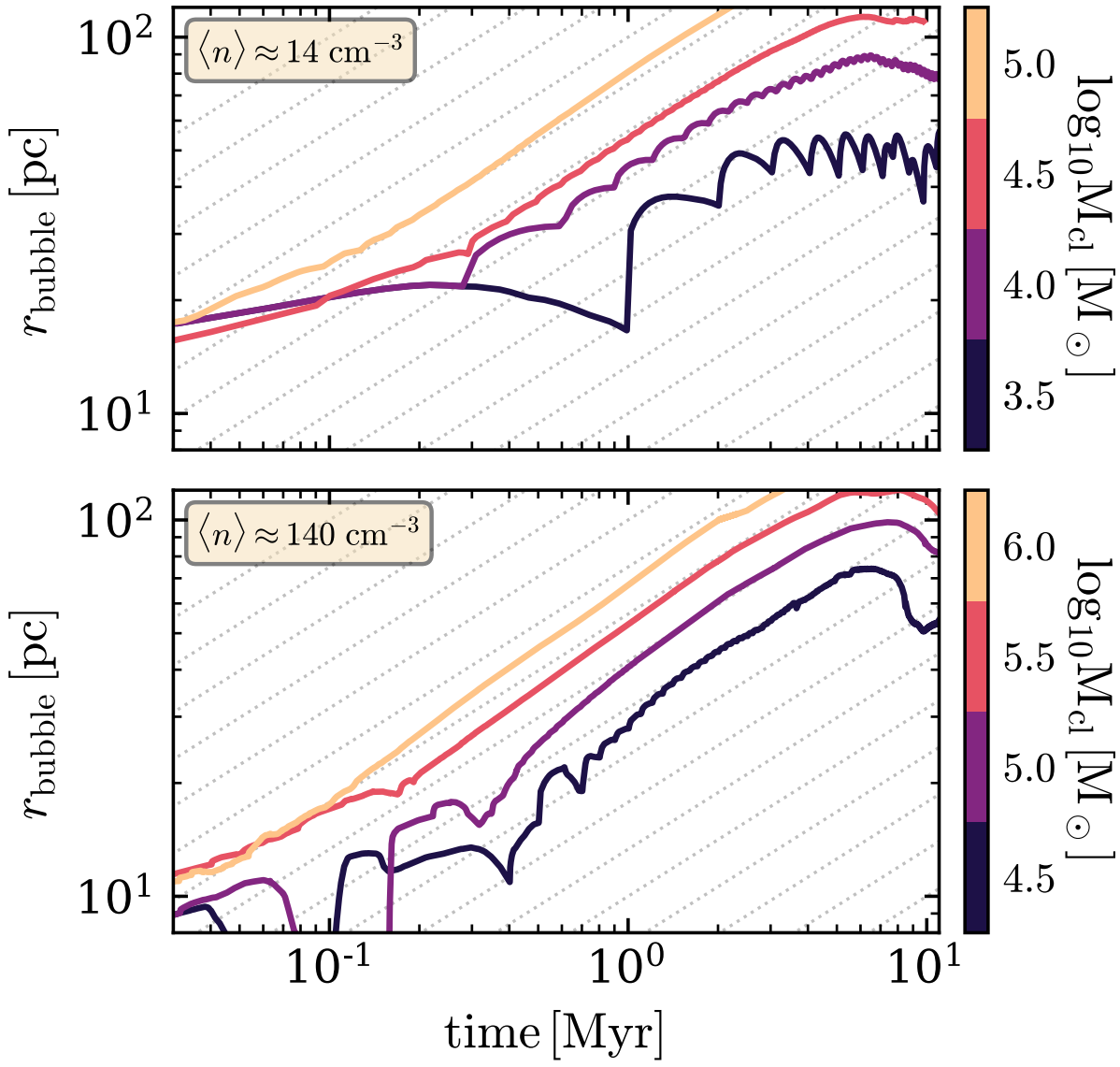


Figure 4.1: The bubble radius evolution in the unstratified turbulent simulations for a range of cluster masses. The top and bottom rows are for the simulations with mean densities $\langle n \rangle = 13.9$ and $139\,\mathrm{cm}^{-3}$, respectively. These correspond to a midplane density appropriate for a galactic disc with $h = 100\,\mathrm{pc}$ and $\Sigma_g = 30\,\mathrm{M}_\odot\,\mathrm{pc}^{-2}$, and the bottom $\Sigma_g = 300\,\mathrm{M}_\odot\,\mathrm{pc}^{-2}$. The dotted grey lines trace $t^{1/2}$. In the more massive cluster simulations that succeed in overcoming the ISM pressure and blow significant bubbles the radius increases as $t^{1/2}$ indicating that the momentum driven limit applies (see equation 4.14). The bubbles in lower cluster mass simulations stop growing and stall at some $t < \mathrm{t_{SN}}$.

define an effective bubble radius to be

$$r_{\rm bubble} = \left( \frac{3}{4\pi} \sum_{T>10^5\,{\rm K}} \Delta x^3 \right)^{1/3} . \quad (4.22)$$

The analytic predictions for the bubble radius evolution presented in §4.3 are technically for the forward shock (shocked interstellar material), so eq. 4.22 has the potential to miss regions of the ISM that have been swept up and shock heated, but then cooled back down below $10^5$ K. However, the thickness of the cooled swept up shell will be very small compared to the radius, so the error this introduces will be minimal.

Fig. 4.1 shows the growth of the bubble radius in the turbulent simulations for both densities and the full range of cluster masses (star cluster formation efficiencies $\epsilon_*$). Since the shock radius scales with $M_{\rm cl}/n$ to the 1/5 or 1/4 power in either the energy- or momentum-driven limits (equations 4.9 and 4.14), and $M_{\rm cl}$ scales linearly with $n$ (equation 4.4) we do not expect at fixed $\epsilon_*$ for there to be a significant dependence on $\Sigma_{\rm g}$. This is indeed born out in fig. 4.1 when comparing different surface densities. The temporal scaling of super-bubble radius shown in Fig. 4.1 gives us a clue into whether the bubbles are being driven by energy or momentum. Momentum-driven bubbles evolve with $t^{1/2}$ while energy-driven bubbles evolve with $t^{3/5}$. Although the difference in slope is minor, the bubbles predominantly follow the $t^{1/2}$ scaling quite closely (shown with the thin grey lines). This agrees with the findings of Kim et al. (2017) in their similar unstratified inhomogeneous simulations.

In the context of powering galactic winds the key result in Fig. 4.1 is that under a broad range of conditions clustered SNe driven super-bubbles can reach the disc scale height $h$ – generally on the order of 100 pc – prior to the cessation of energy injection by SNe at $t_{\rm SN}$. This is true for star cluster formation efficiencies $\epsilon_* \gtrsim 0.03$ (which corresponds to $M_{\rm cl} \gtrsim 10^{4.5}$ and $10^{5.5}\,M_\odot$ for $\Sigma_{\rm g} = 30$ and $300\,M_\odot\,{\rm pc}^{-2}$, respectively). For both ISM densities the bubbles driven by the highest $M_{\rm cl}$ ($\epsilon_* = 0.1$) reach 100 pc in $\sim 2$ Myr and fill the computational volume prior to stalling (we halt the simulations when $r_{\rm bubble} \approx L_{\rm box}/2$ or $t = t_{\rm SN}$, which ever comes first). The second highest cluster masses ($\epsilon_* = 0.03$) reach 100 pc by $\sim 3-4$ Myr, and stall soon after. The bubbles powered by the lowest two cluster masses never reach 100 pc, but instead reach pressure equilibrium and stall at $\sim 80$ and 50 pc for $\epsilon_* = 0.01$ and 0.003, respectively. In all of the simulations it is stalling rather than running out of time that sets the maximum extend of the hot bubble.

The critical $\epsilon_*$ that determines whether a bubble will make it to $h$ prior to stalling can be found by equating the shock velocity at the scale height with the turbulent velocity dispersion (see eq. 4.21). This critical value is given by

$$\epsilon_{\star,{\rm crit}} = 0.03 \left(\frac{f_V}{0.1}\right)^{-1/2} \left(\frac{\delta v}{10\,{\rm km\ s^{-1}}}\right)^2 \left(\frac{h}{100{\rm pc}}\right)^{-1} \left(\frac{P_{\rm SN}}{10^5 M_\odot\ {\rm km\ s^{-1}}}\right)^{-1} . \quad (4.23)$$

Below this $\epsilon_{\star,{\rm crit}}$ the bubble will never breakout and will instead reach pressure equilibrium with the ISM and stall. This analytic prediction is in close agreement with the numerical results. There

is, however, a factor of roughly 3 uncertainty in the appropriate value to adopt for the momentum injected per SNe $P_{SN}$ at the time of breakout (Kim et al., 2017).

The amount of energy and mass contained within the bubble at the time of breakout has been used a proxy for the resulting wind's energy and mass loadings (Kim et al., 2017). These quantities encode how much mixing of the ISM and bubble material has occurred and how much energy has been lost to cooling. Following Kim et al. (2017) we define the following normalized bubble energy and mass:

$$\hat{E}_{\rm hot} = \frac{\sum\limits_{T>10^5\,{\rm K}} E_{\rm cell}}{N_{\rm SN}\, E_{\rm SN}} \quad \text{and} \quad \hat{M}_{\rm hot} = \frac{\sum\limits_{T>10^5\,{\rm K}} m_{\rm cell}}{N_{\rm SN}\, m_{\star}}, \tag{4.24}$$

where $N_{\rm SN}$ is the number of SNe that have gone off thus far. These quantities are analogous to the standard energy and mass loading of the wind – the outflow rates normalized by the injection rates – that we define to be

$$\eta_{\rm E} = \frac{\dot{E}_{\rm wind}}{\dot{E}_{\rm SN}} = \frac{\dot{M}_{\rm wind}}{\dot{E}_{\rm SN}} \left( \frac{1}{2} v^2 + \frac{\gamma}{\gamma - 1} \frac{P}{\rho} - \frac{1}{2} v_{\rm esc}^2 \right) \qquad \eta_{\rm M} = \frac{\dot{M}_{\rm wind}}{\dot{M}_{\star}} \tag{4.25}$$

with $\dot{M}_{\star} = m_{*} \dot{N}_{\rm SNe}$. Eq. 4.24 is appropriate for the unstratified simulations in which there is no wind.

Figs. 4.2 and 4.3 show the evolution of $\hat{E}_{\rm hot}$ and $\hat{M}_{\rm hot}$ for the same simulations in Fig. 4.1. Except at very early times well before the bubble can breakout $\hat{E}_{\rm hot}$ is less that 0.1 and may be as small as 0.01, even for the most massive clusters. Likewise, $\hat{M}_{\rm hot}$ is rarely larger than 0.2. As we discuss in Appendix 4.A.2 $\hat{E}_{\rm hot}$ and $\hat{M}_{\rm hot}$ are also below 0.1 in the unstratified homogeneous simulations indicating that there is non-negligible mixing even without the large inhomogeneities in the ISM. This degree of mixing is significantly more than found by Gentry et al. (2017b) who used a spherically symmetric Lagrangian code capable of resolving the contact discontinuity better than is possible with the Eulerian code and Cartesian grid we used for these simulations. It is, therefore, reasonable to worry that the mixing in our case may be artificial and owing to numerical errors. However, as we show in Appendices 4.A.1 and 4.A.2 we find that our both our homogeneous and turbulent simulations are very well converged in $\hat{E}_{\rm hot}$ and $\hat{M}_{\rm hot}$ down to a resolution of $\Delta x = 0.25\,{\rm pc}$. We, therefore, believe that to a large extent the ISM-bubble mixing in both the homogeneous and turbulent simulations is real. One possible source of mixing not captured in 1D codes is that the SNe in our simulations are set off at locations distributed within 10 pc of each other which leads to complex internal bubble dynamics and asymmetrical acceleration of the shock. Additional mixing can arise because the energy injection within the bubble is not continuous, so the boundary of the bubble experiences impulsive accelerations after each SNe. These accelerations push the less dense bubble material into the more dense shell leading to the development of Rayleigh-Taylor instability, which we discuss in more detail in Appendix 4.A.2.1. Finally, in the turbulent simulations the cold clumps that penetrate the bubble are ablated due to the strong shear forces they experience. It is important to note that all of these mixing processes are hard to model numerically. Although in Appendix 4.A.1 we show that our results are well converged and do not depend sensitively on our resolution, we caution against over interpreting our findings on these highly mixing dependent quantities to more than a factor of a few level. This is highlighted

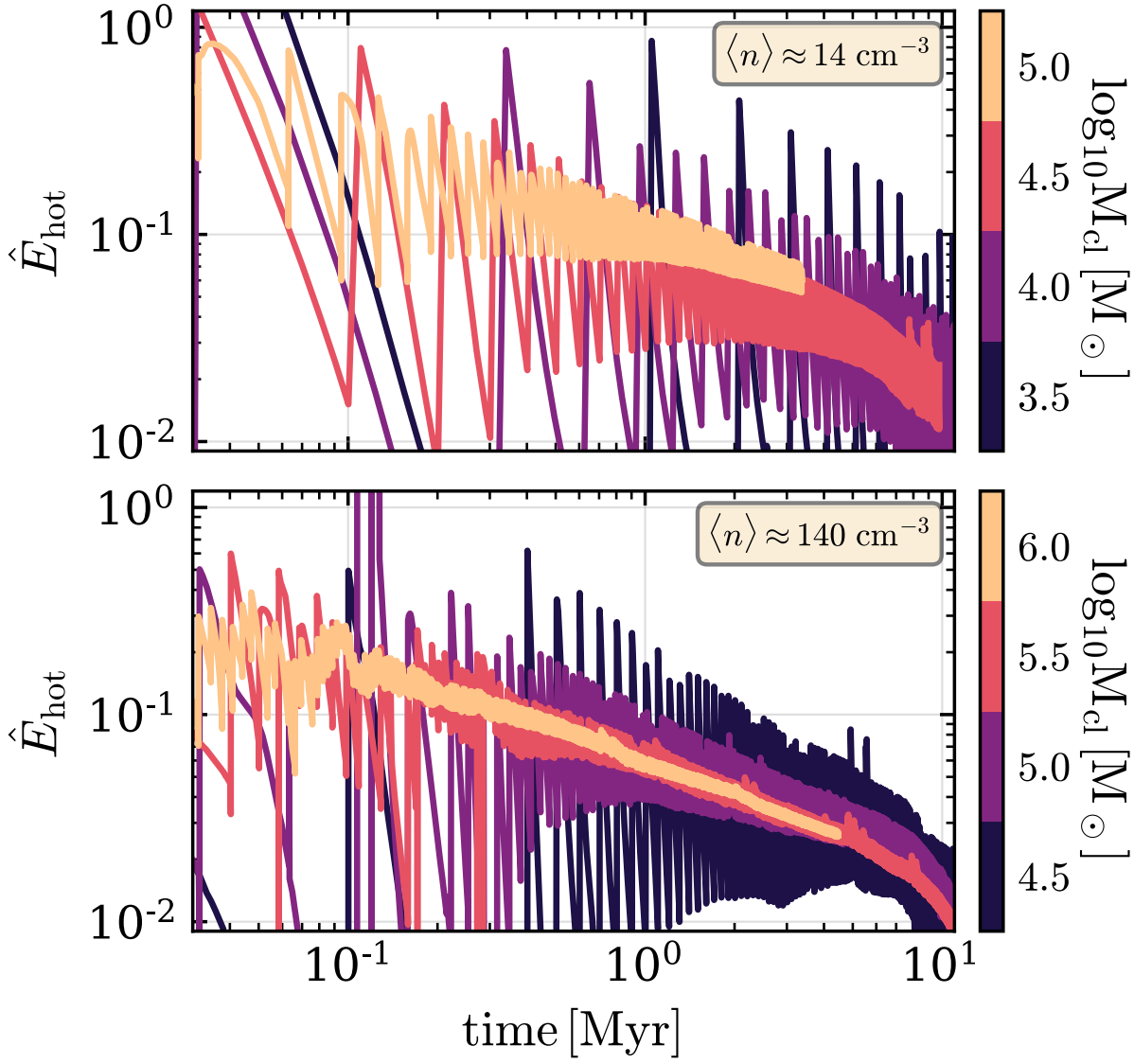


Figure 4.2: $\hat{E}_{\rm hot}$ evolution for the unstratified turbulent simulations for a range of cluster masses. $\hat{E}_{\rm hot}$ quantifies the fraction of the SNe energy retained as thermal energy of the bubble (eq. 4.24), and is a proxy for the wind energy loading. The top and bottom rows are for the simulations with mean densities $\langle n \rangle = 13.9$ and $139\,{\rm cm}^{-3}$, similar to the $\Sigma_{\rm g} = 30$ and $\Sigma_{\rm g} = 300\,{\rm M}_\odot\,{\rm pc}^{-2}$ stratified simulations, respectively.

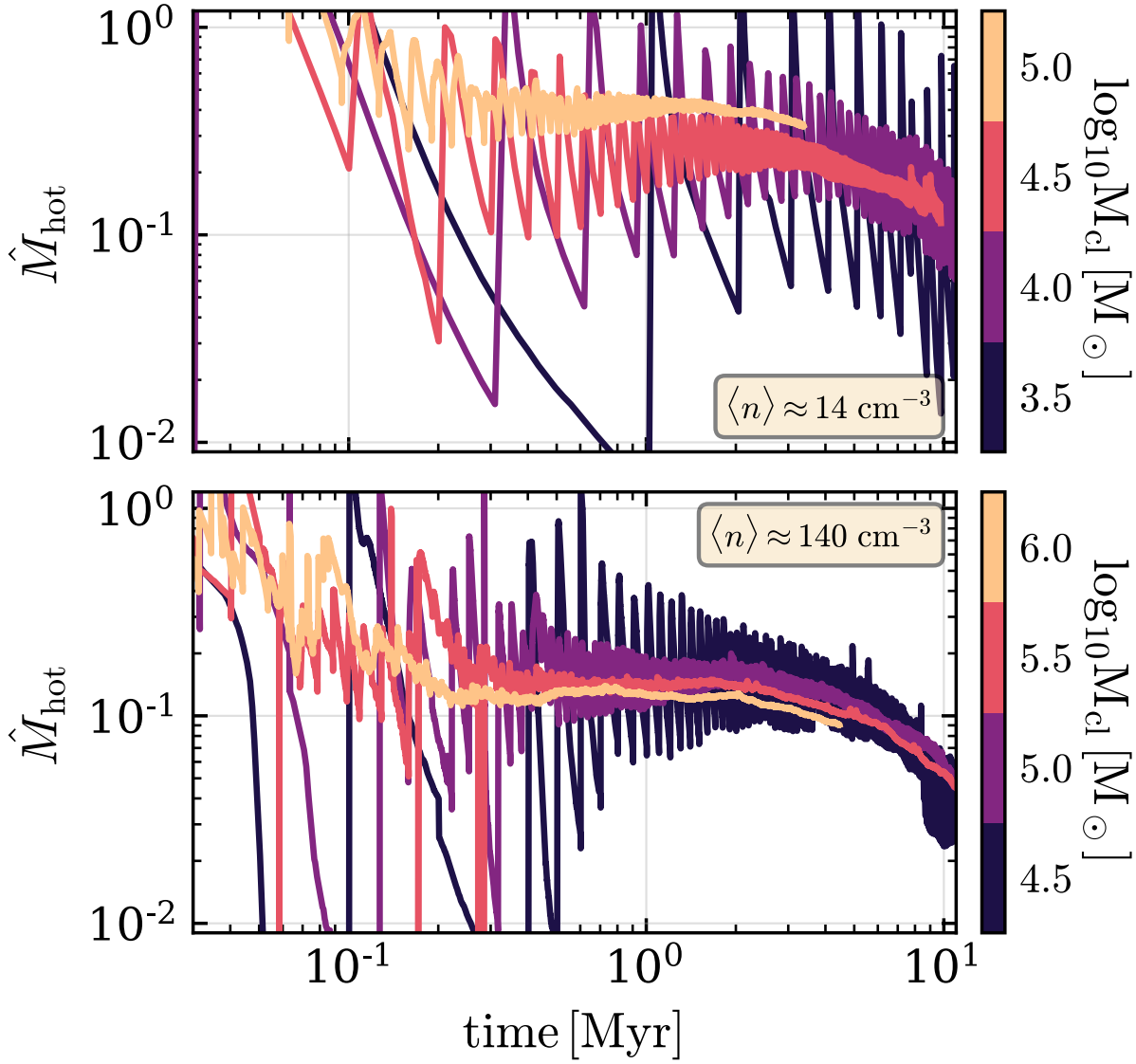


Figure 4.3: $\hat{M}_{\rm hot}$ evolution for the unstratified turbulent simulations for a range of cluster masses. $\hat{M}_{\rm hot}$ is the amount of hot gas relative to the amount of stars formed (eq. 4.24), and is a proxy for the wind mass loading. The top and bottom rows are for the simulations with mean densities $\langle n \rangle = 13.9$ and $139\,{\rm cm}^{-3}$, similar to the $\Sigma_{\rm g} = 30$ and $\Sigma_{\rm g} = 300\,{\rm M}_\odot\,{\rm pc}^{-2}$ stratified simulations, respectively.

by the fact that Kim et al. (2017) performed a similar set of numerical experiments using a similar method (albeit with a static inhomogeneous ISM compared to our turbulent ISM, different SNe injection model and equation of state, and different Riemann solvers and reconstruction methods) and found $\sim 3$ times lower values of $\hat{E}_{\rm hot}$ and $\hat{M}_{\rm hot}$. Suffice it to say that at the time of breakout $\hat{E}_{\rm hot}$ and $\hat{M}_{\rm hot}$ are both likely no more than $10^{-1}$ and may be as small as $\lesssim 10^{-2}$.

It has been argued that $\hat{E}_{\rm hot}$ and $\hat{M}_{\rm hot}$ are representative of the energy and mass loading ($\eta_{\rm E}$ and $\eta_{\rm M}$) of the galactic winds that would result once the bubble breaks out of the disc (Kim et al., 2017). We now show, however, that the post breakout winds are in fact much more powerful than suggested by Figs. 4.2 and 4.3.

### 4.5.2 Post-breakout Super-Bubble evolution: Wind properties

In the previous section we looked at the properties of super-bubbles blown by the collective effect of a star cluster's numerous SNe while confined within the ISM, prior to reaching the scale height of the disc. We now focus our attention on what happens once the super-bubble pushes its way through the disc and is able to breakout into the surrounding medium. Therefore in this section we primarily focus on the stratified simulations. We begin with a qualitative look at the properties of the super-bubble and post-breakout wind. Then we show that the pre-breakout energetics have little bearing on the post-breakout energetics, thus alleviating the concerns raised by the unstratified simulations – although not obviating their utility in understanding the bubble dynamics while confined within the disc. Finally, we discuss the wind mass and energy loading for different choices of $\Sigma_{\rm g}$ and $\rm M_{cl}$ – highlighting the temperature dependence of the wind loading.

Fig. 4.4 shows the state of the $\Sigma_{\rm g} = 30\,\rm M_\odot\,pc^{-2}$, $\rm M_{cl} = 10^{4.5}\,M_\odot$ simulation at $t = 3$ (top row) and 23 Myr (middle and bottom rows). From left to right the columns show slices of the temperature $T$, number density $n$, outward velocity $v_{\rm out} \equiv \vec{v}\cdot\hat{z}$, and $\dot{E}_{\rm cool-heat}$, respectively. At $t = 3$ Myr the bubble is still confined within the disc and there is a large amount of cooling on the boundary of the bubble. At these early times the stratified and unstratified simulations are qualitatively similar. However, post-breakout the properties are entirely different as shown in the $t = 23$ Myr panels. Upon reaching the scale height of the disc ($h \approx 100\,\rm pc$) the super-bubble loses the confining pressure in the vertical direction and is able to open a wide 'chimney' in the ISM through which it can vent into the surrounding medium without suffering appreciable cooling losses. In the horizontal direction the cavity is continually pressed upon by the thermal and ram pressure of the turbulent ISM. Dense ISM clumps are able to penetrate the cavity wall where they are immediately buffeted, shredded, and/or entrained by the wind. These clumps are responsible for much of the mass loading of the wind and can be seen in different stages of their shredding/entrainment in Fig. 4.4 as the cold dense clumps above and below the disc. This shredding and entraining process can be seen in better detail in the zoom-in panels in the bottom row. In some cases, as these clouds are accelerated they grow due to the enhanced cooling of the hot medium in their wakes (Gronke & Oh, 2018).

However, even without the dense clumps the wind would still be appreciably mass loaded, since in the homogeneous ISM stratified simulations (not shown here) the mass loading is greater than pure SNe ejecta loading would imply ($\rm M_{ej}/m_* = 0.03$ in our case). In the homogeneous

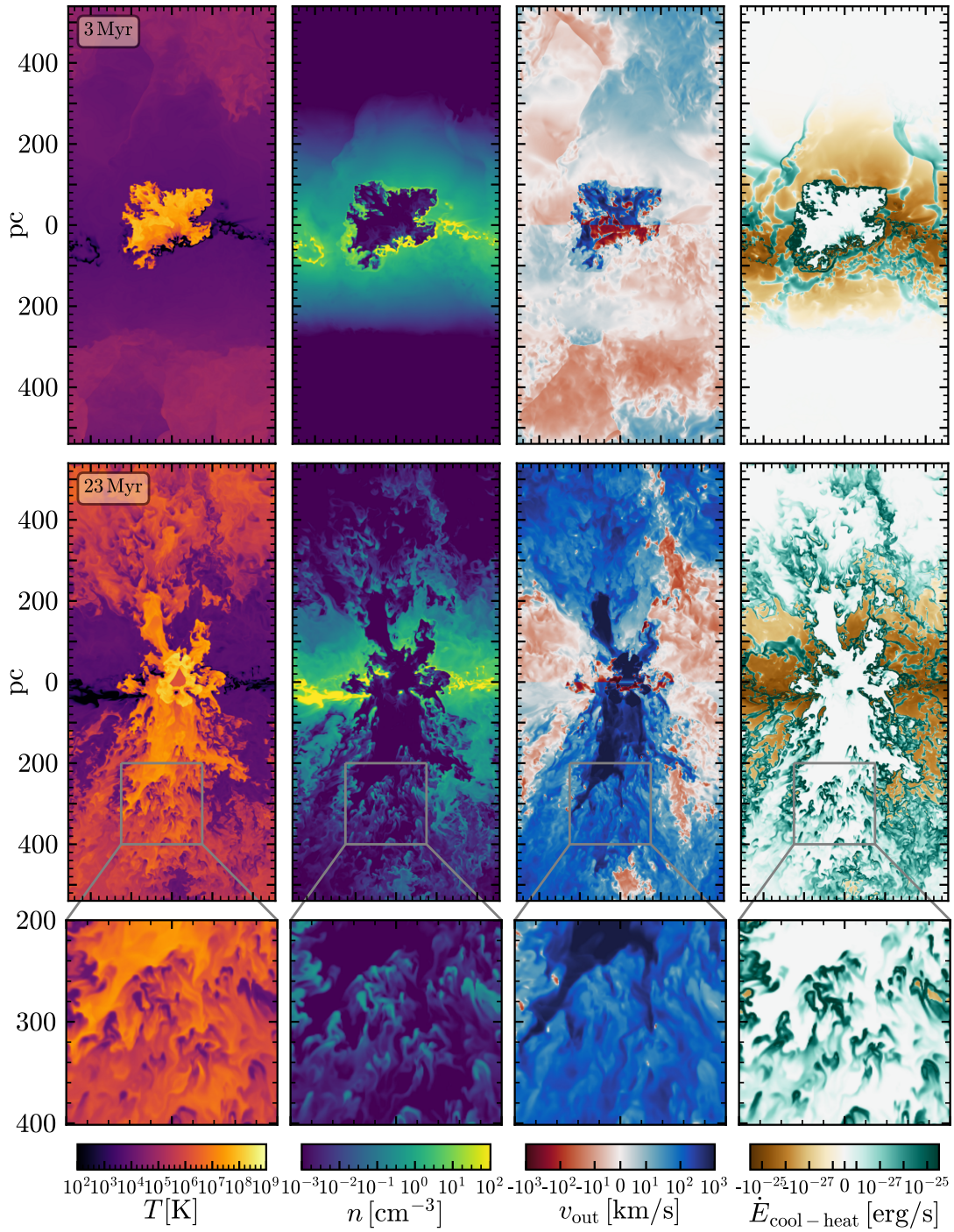


Figure 4.4: Vertical slices through the $\Sigma_{\rm g} = 30\,{\rm M}_\odot\,{\rm pc}^{-2}$, $M_{\rm cl} = 10^{4.5}\,{\rm M}_\odot$, $\Delta x = 1$ pc turbulent stratified simulation showing from left to right the temperature, number density, outflowing velocity ($\vec{v}\cdot\hat{z}$, positive means leaving the box), and the cooling/heating rate (positive means losing energy) at $t = 3$ Myr, prior to breakout, and near $t_{\rm SN}$ at $t = 23$ Myr, well past the initial breakout, in the top and middle rows, respectively. The bottom rows show zoomed-in patches on a region above the disc that exhibits significant cold cloud entrainment – these clouds are also growing due to cooling of the enhanced cooling of the hotter medium in their wakes.

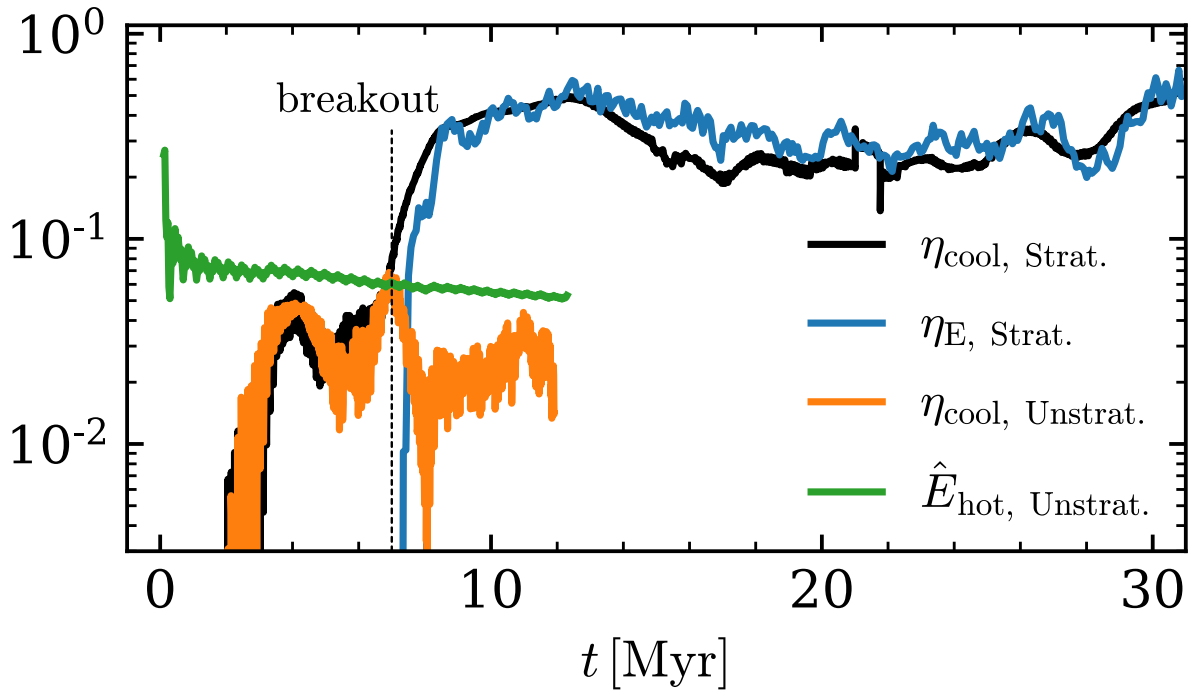


Figure 4.5: Time evolution of $\eta_{\rm cool}$ for the stratified (black) and unstratified (orange) $\Sigma_{\rm g} = 30\,{\rm M}_\odot\,{\rm pc}^{-2}$, ${\rm M}_{\rm cl} = 10^{4.5}\,{\rm M}_\odot$ homogeneous simulations, compared with $\eta_{\rm E}$ leaving the top and bottom of the stratified simulations domain (blue line), and $\hat{E}_{\rm hot}$ from the unstratified simulation (green line). The correspondence between the $\eta_{\rm cool}$ and $\hat{E}_{\rm hot}$ or $\eta_{\rm E}$ for the unstratified and stratified simulations respectively, indicates that the injected energy not radiated away goes into the energy of the bubble and the wind. The vertical dashed line at 7 Myr demarcates when the bubble breaks out in the stratified simulations. After this time the $\eta_{\rm cool}$ of the stratified and unstratified simulations differ by an order of magnitude demonstrating that once a channel through the ISM has been opened the energy is able to vent into the lower density surroundings where it experiences significantly less cooling. Most of the SNe go off at $t > 7$ Myr leading to a time average energy loading of $\eta_{\rm E} \gtrsim 0.2$.

simulations the ISM mixing results from the asymmetrical SNe distribution and the strong shear flows on the cavity walls that lead to Kelvin-Helmholtz instabilities. Thus, a combination of effects work in concert to continually mass load the winds. The mass loading can come at a cost to the wind energy. The shredded clouds increase the wind density and decrease the wind temperature, which increases the wind cooling rate – shown clearly in the middle and lower right panels of fig. 4.4.

We now quantify how much of the energy injected into the ISM is lost to radiative cooling. We demonstrated in the previous section that while the bubble is confined within the disc on the

order of 90 to more than 99 per cent of the energy injected by SNe was lost to cooling. We can assess this in the stratified case by measuring the difference between the energy injected and the energy lost to cooling relative to the injected energy SNe energy. We call this quantity $\eta_{\rm cool}$ and it represents the energy that is leftover to power the wind and is defined to be

$$\eta_{\rm cool} = \frac{\dot{E}_{\rm SN} + \dot{E}_{\rm turb} - \dot{E}_{\rm cool}}{\dot{E}_{\rm SN}} = 1 + \frac{\dot{E}_{\rm turb}}{\dot{E}_{\rm SN}} - \frac{\dot{E}_{\rm cool}}{\dot{E}_{\rm SN}}. \tag{4.26}$$

Recall from equation 4.8 that $\dot{E}_{\rm SN} \propto \Sigma_{\rm g}\epsilon_*$ and that $\dot{E}_{\rm turb} \propto \Sigma_{\rm g}$, so for the fiducial choice of parameters $\dot{E}_{\rm turb}/\dot{E}_{\rm SN} \approx (\epsilon_*/0.01)^{-1}/3$ and is independent of $\Sigma_{\rm g}$.

Fig. 4.5 shows the time evolution of $\eta_{\rm cool}$ for the homogeneous $\Sigma_{\rm g} = 30\,{\rm M}_\odot\,{\rm pc}^{-2}$, $M_{\rm cl} = 10^{4.5}\,{\rm M}_\odot$ simulation. For comparison the energy loading at the top and bottom of the box $\eta_{\rm E}$ is also shown (eq. 4.25), as well as $\hat{E}_{\rm hot}$ and $\eta_{\rm cool}$ for the matching unstratified simulation. For the first $\sim$ 7 Myrs $\eta_{\rm cool}$ is similar in both the stratified and unstratified simulations, but once the first fingers of bubble material reach the disc's edge and begin to expand freely into in the low density medium above and below the disc the amount of energy lost to cooling drop dramatically and the energetics of the stratified and unstratified simulations differ significantly. The energy that is not radiated away in the unstratified simulation goes into expanding and heating the super-bubble, albeit with diminishing efficiency, as reflected by $\hat{E}_{\rm hot}$. However, in the stratified simulations up to 50 per cent of the energy from SNe is not radiated away and is instead carried away by the wind and ends up leaving the domain. This can be seen by the close correspondence of $\eta_{\rm cool}$ and $\eta_{\rm E}$.

Fig. 4.6 shows the same quantities as Fig. 4.5 shows but for the turbulent $\Sigma_{\rm g} = 30\,{\rm M}_\odot\,{\rm pc}^{-2}$, $M_{\rm cl} = 10^{4.5}\,{\rm M}_\odot$ and $\Sigma_{\rm g} = 300\,{\rm M}_\odot\,{\rm pc}^{-2}$, $M_{\rm cl} = 10^{5.5}\,{\rm M}_\odot$ simulations. The same finding holds in the turbulent simulations as in the homogeneous simulations that pre-breakout the energetics of the stratified and unstratified simulations are similar while post-breakout they differ dramatically. Relative to the homogeneous simulations the turbulent simulations breakout sooner owing to their lower median densities. Additionally they exhibit more variability in $\eta_{\rm cool}$ and $\eta_{\rm E}$ post-breakout. This variability is due to the fact that the massive cold ($T = 10^2$ K) clumps in the turbulent simulations – absent in the homogeneous simulations – are able to partially, or sometimes completely, re-seal the vent through the ISM that the cluster has carved out. When this occurs the energy released by the cluster is spent on shredding the clump and carving a new vent out of the ISM. This process is inherently sensitive to the properties of the turbulent ISM since that is what sets the flux of cold clumps into the bubble/vent region. We explore in Appendix 4.B how our results vary with different turbulent driving realizations. Four otherwise identical simulations with different turbulent realizations yielded a range of $\eta_{\rm E}$ and $\eta_{\rm cool}$ on the order of a factor of $\sim$3. The case shown in the top panel of Fig. 4.6 lies in the middle of the spread.

The exact value of $\eta_{\rm E}$ driven by clustered SNe varies somewhat across the range in $\Sigma_{\rm g}$ and $M_{\rm cl}$ that we explored, but it is ubiquitously true that when the bubble is able to breakout (even if only for a short time while the turbulent fluctuations are favorable) the radiative losses are diminished and the winds carry an appreciable faction of the injected energy ($\eta_{\rm E} \gtrsim 0.1$). Fig. 4.7 shows the time evolution of $\eta_{\rm E}$ measured at the top and bottom of the domain, $\pm$540 pc from the disc midplane, for the full range of turbulent stratified simulations. For both surface densities the more massive the

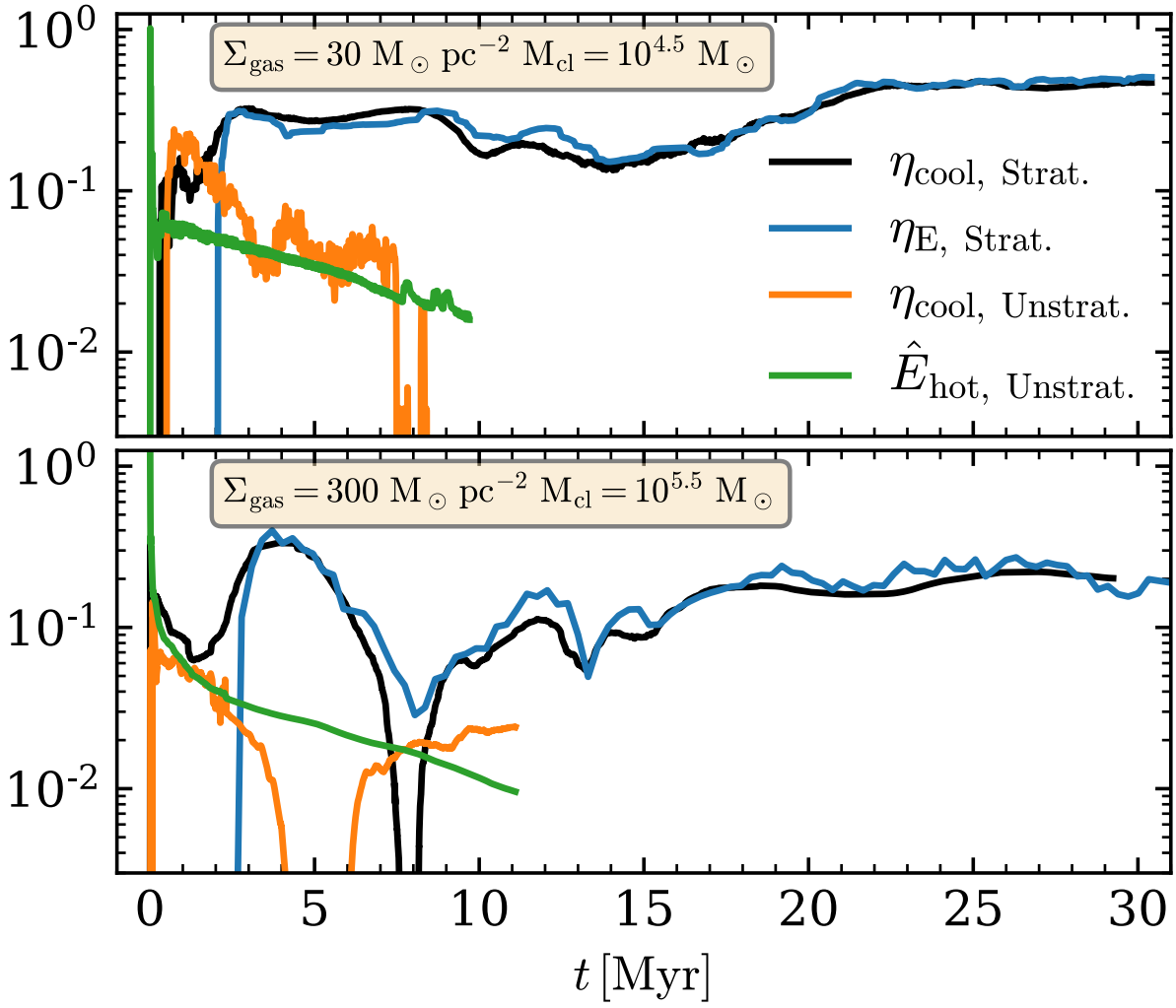


Figure 4.6: Time evolution of $\eta_{\rm cool}$ for the stratified (black) and unstratified (orange) turbulent simulations, compared with $\eta_{\rm E}$ leaving the top and bottom of the stratified simulations domain (blue line), and $\hat{E}_{\rm hot}$ from the unstratified simulation (green line). The top panel shows the $\Sigma_{\rm g} = 30\,{\rm M}_\odot\,{\rm pc}^{-2}$, ${\rm M}_{\rm cl} = 10^{4.5}\,{\rm M}_\odot$ simulation and the bottom panel shows the $\Sigma_{\rm g} = 300\,{\rm M}_\odot\,{\rm pc}^{-2}$, ${\rm M}_{\rm cl} = 10^{5.5}\,{\rm M}_\odot$ simulation (both correspond to $\epsilon_* = 0.03$). $\hat{E}_{\rm hot}$ and $\eta_{\rm E}$ trace $\eta_{\rm cool}$ because the injected energy not radiated away goes into the energy of the bubble and the wind. The striking divergence of the stratified and unstratified simulations' $\eta_{\rm cool}$ after $\sim 3$ Myr when the bubble breaks out demonstrates the efficient venting of SNe energy once a channel through the ISM has been cleared.

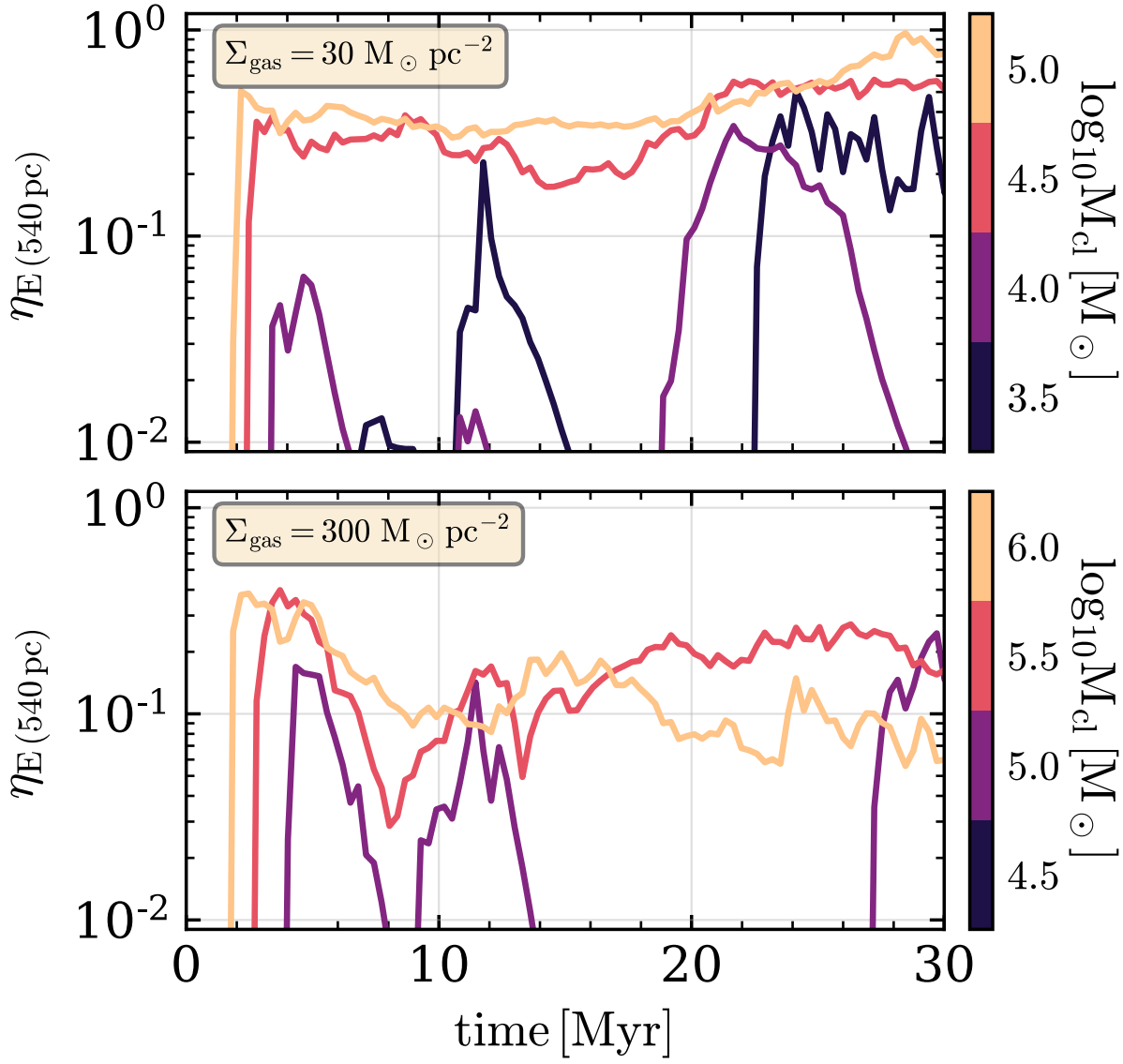


Figure 4.7: Time evolution of the wind energy loading, $\eta_{\rm E}$, measured 540 pc from the disc mid-plane – the edge of computational domain – for $\Sigma_{\rm g}$ = 30 (top) and 300 $\rm M_\odot\,pc^{-2}$ (bottom) simulations. At each surface density clusters with masses corresponding to $\epsilon_* = 10^{-2.5}$, $10^{-2}$, $10^{-1.5}$, and $10^{-1}$ are shown. For $\epsilon_* \gtrsim 10^{-1.5}$, which corresponds to $\rm M_{cl} = 10^{4.5}$ and $10^{5.5}$ $\rm M_\odot$ for $\Sigma_{\rm g}$ = 30 and 300 $\rm M_\odot\,pc^{-2}$ respectively, $\eta_{\rm E} \gtrsim 0.1$ after the initial breakout of the bubble. At lower $\epsilon_*$ the bubbles are only able to breakout for short periods of time when the turbulent fluctuations are favorable leading to much lower values of $\eta_{\rm E}$. Additionally, the occasional weak outflow events driven by the turbulence alone contributes appreciably to the $\eta_{\rm E}$ from the lowest cluster masses.

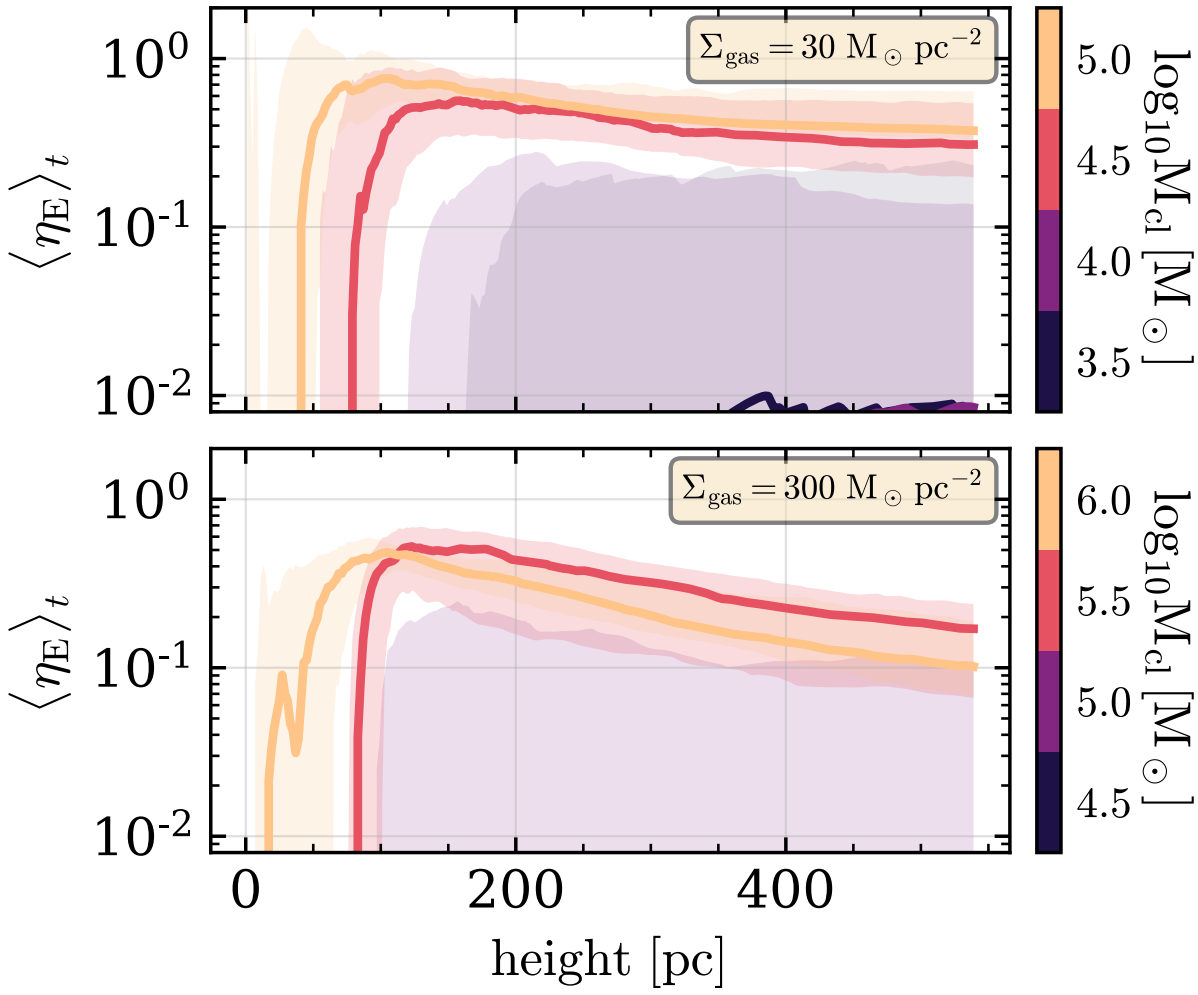


Figure 4.8: Vertical profiles of the time average energy loading $\eta_{\rm E}$ of the $\Sigma_{\rm g} = 30$ (top) and 300 $\rm M_\odot\ pc^{-2}$ (bottom) simulations. The shaded region denotes the one sigma range of scatter over time. For the sake of clarity we show only the energy loading of outflowing material because within the disc, $|z| < h$, the turbulent motions lead to large variations, and beyond the disc, $|z| > h$ the energy of the outflow is indistinguishable from that of the total. For $\epsilon_* \gtrsim 10^{-1.5}$, which corresponds to $\rm M_{cl} = 10^{4.5}$ and $10^{5.5}\ \rm M_\odot$ for $\Sigma_{\rm g} = 30$ and 300 $\rm M_\odot\ pc^{-2}$ respectively, $\eta_{\rm E}$ is large, $\gtrsim 0.1$, and falls by at most a factor of 3 from $h \approx 100$ pc to the top of the box at 540 pc, where as for $\epsilon_* \lesssim 10^{-2.0}$ $\eta_{\rm E}$ is small, $\lesssim 10^{-2}$ most of the time.

cluster the sooner it breaks out of the disc and for all cluster masses they reach a maximum $\eta_E$ of around 0.5. There are fluctuations in the outflow rate due to changes in the turbulent surroundings. This is most apparent in the lowest $M_{cl}$ simulations that only break out for short periods when there happens to be a lower ambient density.

Fig. 4.8 shows the time averaged vertical $\eta_E$ profile for the stratified turbulent simulations. The shaded regions show the one sigma temporal variation in the outflow rates. The lowest mass clusters only occasionally power enough of an outflow for its shaded region to make it into the plotted range and its mean is down around $\eta_E \lesssim 10^{-2}$. In the winds driven by the more massive clusters the value of $\eta_E$ drops by $\lesssim 2$ from the edge of disc at 100 pc to the top of the box at 540 pc. This is decrease with height is due to mixing and cooling of the material stripped off entrained clouds. However, there can be artificially enhanced cooling due to the geometry of the numerical setup, as was pointed out by Martizzi et al. (2016b) and verified by Fielding et al. (2017c). The periodic boundary conditions in the horizontal directions can limit the expansion and adiabatic cooling of the wind, which in turn can prevent the acceleration of the wind and keep it too hot and slow. That being said, the wind temperatures produced by the clustered SNe are much higher than the wind temperatures produced by the randomly distributed SN studied by Martizzi et al. (2016b) and as such cooling is much less efficient.

For galaxy formation and the chemical evolution of galaxies it is important to know not just the energy carried by galactic winds but the potentially sizable mass removed rates from the ISM out into the CGM. The solid lines in Fig. 4.9 show the time averaged $\eta_M$ vertical profiles across the full range of $\Sigma_g$ and $M_{cl}$. The $\eta_M$s are not plotted in the midplane ($|z| < 100$ pc) to remove confusion caused by the turbulent motions within the disc. Interpreting the $\eta_M$ values is further complicated by 'fountain' flows where gas is lifted out of the disc but falls back before leaving the domain. To account for this, we focus on the highest energy phase of the wind. Specifically we use the fact that the Bernoulli parameter is constant along flow lines (neglecting cooling) to define a 'Bernoulli velocity,'

$$v_{\mathcal{B}} = \sqrt{2\left(\frac{1}{2}v^2 + \frac{\gamma}{\gamma-1}\frac{P}{\rho}\right)}, \tag{4.27}$$

that when compared to the escape velocity will give an estimate for how far the material can go. The dashed lines in fig. 4.9 show the portion of $\eta_M$ that has $v_{\mathcal{B}} > 300$ km s$^{-1}$, which is the portion of the wind that has the potential to make it far out in the halo and beyond. The high $v_{\mathcal{B}}$ component actually increases with radius. This is due to the mixing of low $v_{\mathcal{B}}$ (mostly cold) material into the high $v_{\mathcal{B}}$ (mostly hot) material. In some cases $\eta_M$ of the high $v_{\mathcal{B}}$ component is larger than the $\eta_M$ of all of the material due to fall back of lower $v_{\mathcal{B}}$ material. For the higher mass clusters with $\epsilon_* \gtrsim 0.03$ ($M_{cl} \gtrsim 10^{4.5}$, $10^{5.5}$ $M_\odot$ for $\Sigma_g = 30$, 300 $M_\odot$ pc$^{-2}$, respectively), by a height of 300 to 400 pc the majority of the outflowing material has $v_{\mathcal{B}} > 300$ km s$^{-1}$ and the profiles of total and high $v_{\mathcal{B}}$ components have mostly leveled off. The winds from these higher mass clusters have $\eta_M \sim 0.3 - 1$.

In addition to mass and energy the wind carries significant momentum. Analogous to the

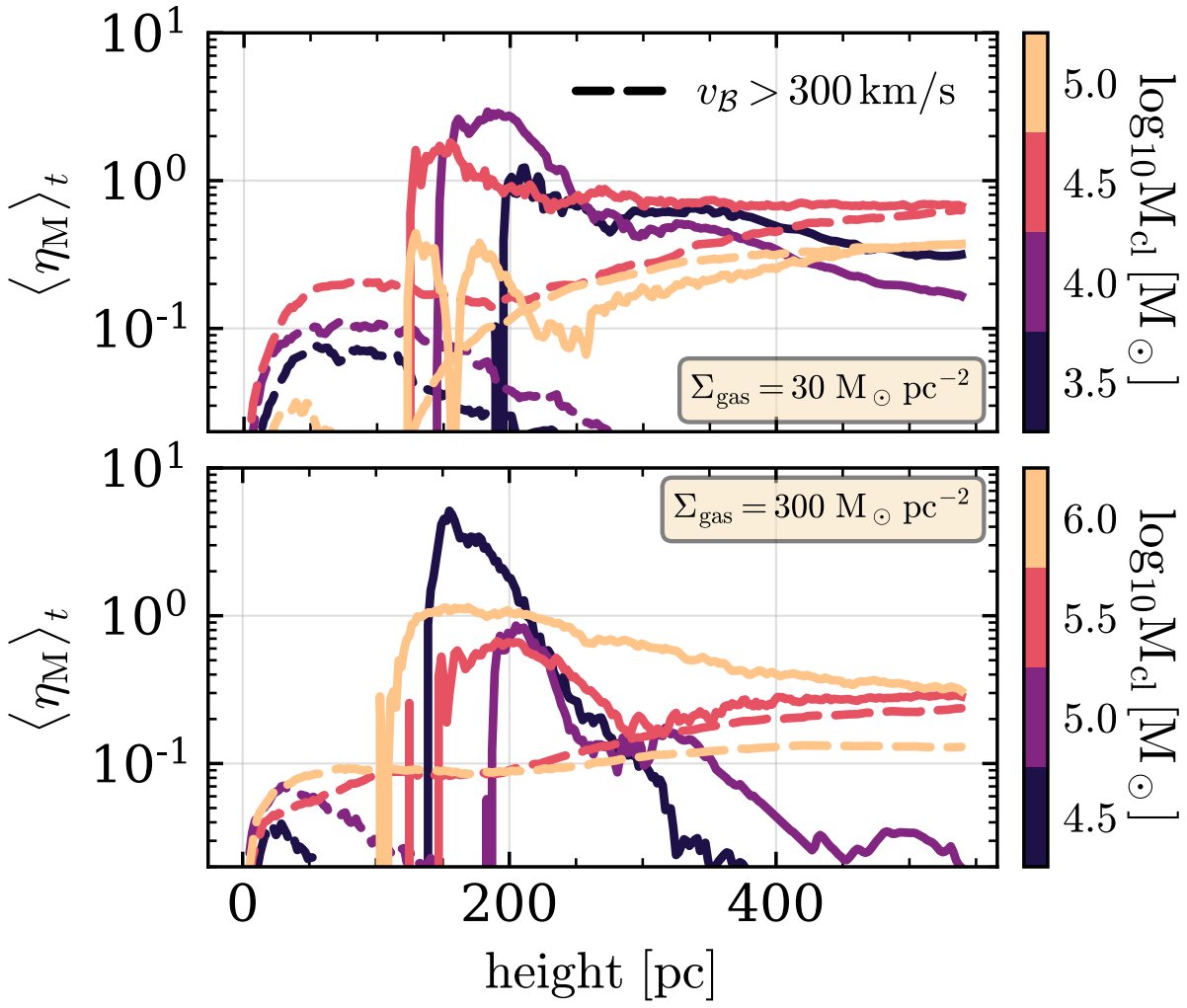


Figure 4.9: Vertical profiles of the time average mass loading $\eta_M$ of the $\Sigma_g = 30$ (top) and 300 $M_\odot$ pc$^{-2}$ (bottom) simulations. The solid lines show the net (outflowing minus inflowing) mass flux for all of the gas and the dashed lines correspond to only material with $v_{\mathcal{B}} > 300$ km s$^{-1}$. The total $\eta_M$ is not shown within the disc ($|z| < 100$ pc) since the turbulent motions dominate there. The higher $v_{\mathcal{B}}$ material would be able to reach well out into the halo or beyond. In some cases $\eta_M$ above the given $v_{\mathcal{B}}$ increases with height due to mixing of low density high energy material with higher density lower energy material as cold clouds are shredded/entrained.

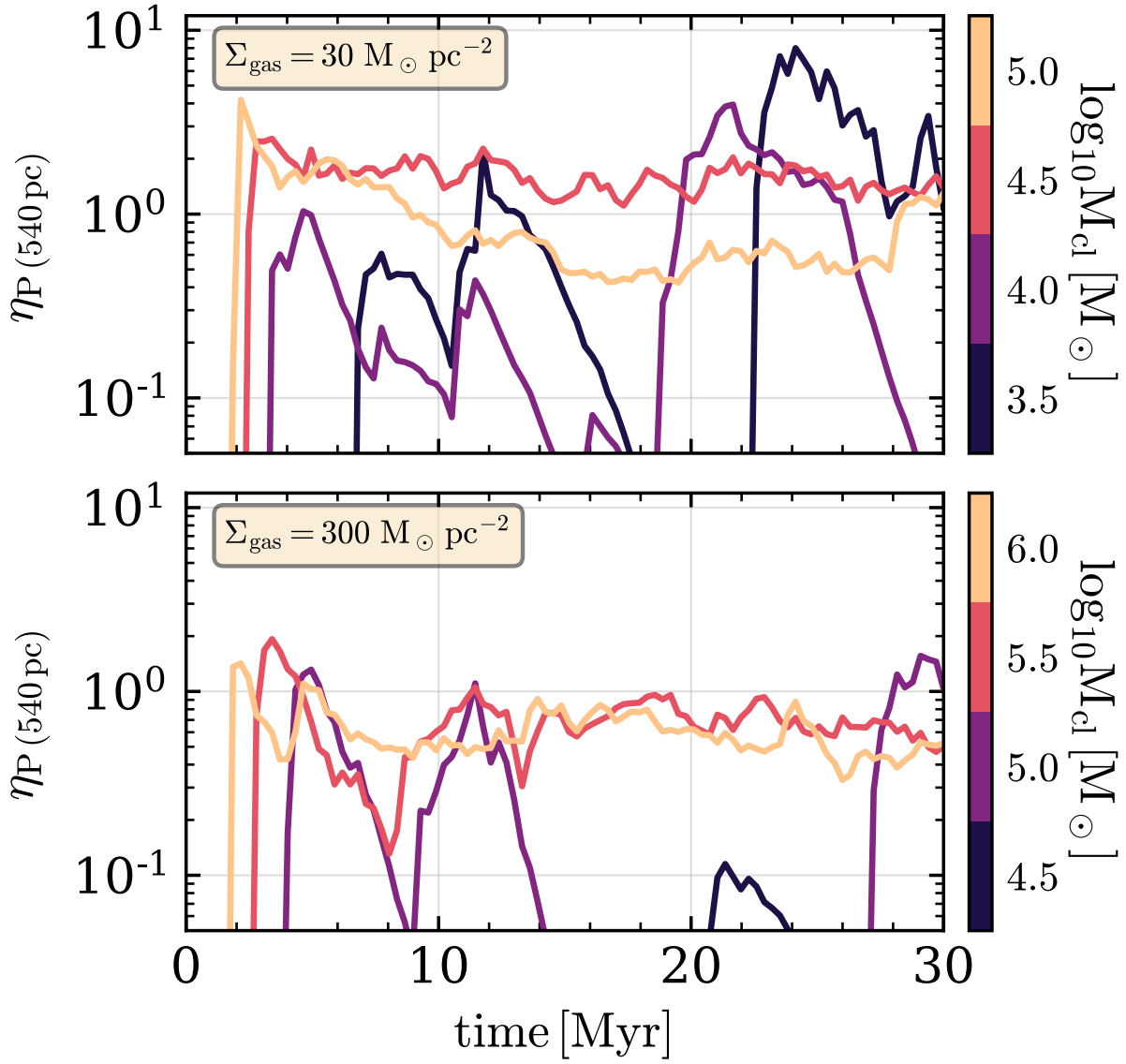


Figure 4.10: Time evolution of the wind momentum loading, $\eta_{\rm P}$, measured 540 pc from the disc midplane – the edge of computational domain – for $\Sigma_{\rm g}$ = 30 (top) and 300 $\rm M_\odot\,pc^{-2}$ (bottom) simulations. At each surface density clusters with masses corresponding to $\epsilon_*$ = 0.003, 0.01, 0.03, and 0.1 are shown. For $\epsilon_* \gtrsim 0.03$, which corresponds to $\rm M_{cl} = 10^{4.5}$ and $10^{5.5}$ $\rm M_\odot$ for $\Sigma_{\rm g}$ = 30 and 300 $\rm M_\odot\,pc^{-2}$ respectively, $\eta_{\rm P} \sim 1$ after the initial breakout of the bubble. At lower $\epsilon_*$ the bubbles are only able to breakout for short periods of time when the turbulent fluctuations are favorable leading to lower values of $\eta_{\rm P}$.

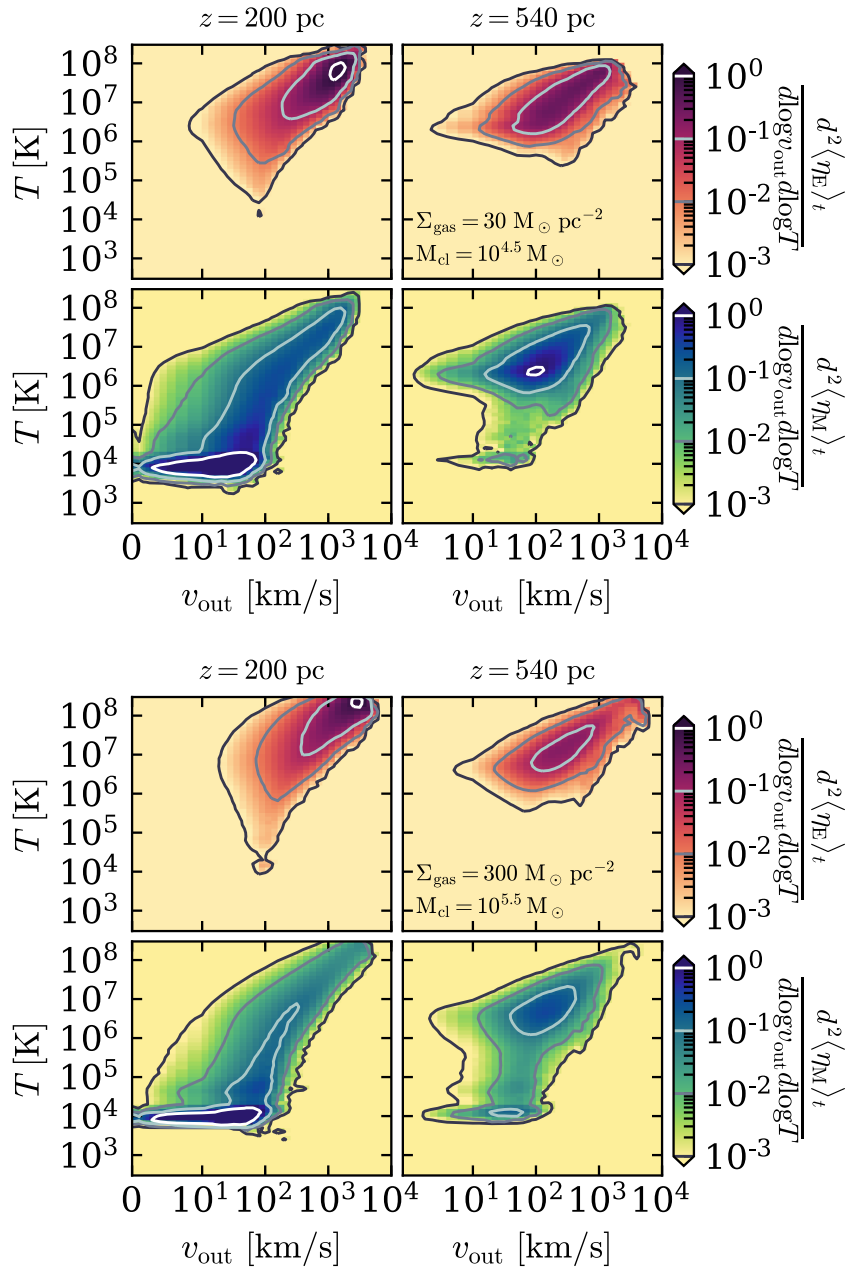


Figure 4.11: Time averaged $\eta_{\rm E}$ (top row) and $\eta_{\rm M}$ (bottom row) per two dimensional logarithmic bin in temperature and outward velocity just above the disc at 200 pc (left column) and at 540 pc, the edge of the computational domain (right column) in the $\Sigma_{\rm g} = 30\,{\rm M}_\odot\,{\rm pc}^{-2}$ ${\rm M_{cl}} = 10^{4.5}\,{\rm M}_\odot$ (top) and $\Sigma_{\rm g} = 300\,{\rm M}_\odot\,{\rm pc}^{-2}$ ${\rm M_{cl}} = 10^{5.5}\,{\rm M}_\odot$ (bottom) ($\epsilon_* = 0.03$) simulations. The contour lines are added to guide the eye and are separated by a factor of 10. The energy flux is dominated by the fast hot component at all heights. The mass flux is dominated by the cooler slower phase close the disc, which mostly drops out or is mixed into the hotter phase so that by the top of the box most of the mass is in the fast hot phase. In the $\Sigma_{\rm g} = 300\,{\rm M}_\odot\,{\rm pc}^{-2}$ simulation there is also a notable $T = 10^4$ K component of the wind at 540 pc with $v_{\rm out} \gtrsim 30\,{\rm km\ s}^{-1}$ that carries a mass flux of $\eta_{\rm M} \sim 0.02$.

energy and mass loading we can define a momentum loading

$$\eta_{\rm P} = \frac{\dot{P}_{\rm wind}}{\dot{P}_{\rm SN}} = \frac{\dot{P}_{\rm wind}}{{\rm M_{ej}\, v_{ej}\, \dot{N}_{SNe}}}, \tag{4.28}$$

where $\rm M_{ej} = 3\,M_\odot$ is the mass ejected with each SNe, and $\rm v_{ej} \approx 2.6 \times 10^3$ km s$^{-1}$ is the average velocity of the SN ejecta in our simulations. Fig. 4.10 show the time evolution of $\eta_{\rm P}$ for all of the turbulent stratified simulations. As with $\eta_{\rm E}$ and $\eta_{\rm M}$, massive clusters with $\epsilon_* \gtrsim 0.03$, which are able to breakout, drive winds with significant momentum loading $\eta_{\rm P} \sim 1$, whereas the winds driven by lower mass clusters carry significantly less momentum. There are, however, times when the momentum flux from the lowest $\rm M_{cl}$ simulations is high, which occurs intermittently when the conditions in the turbulent ISM are favorable for breakout. For comparison, an individual SN remnant in an unstratified ISM effectively has $\eta_{\rm P} \sim 20 - 40$ due to work done in the Sedov-Taylor phase. The fact that post-breakout $\eta_{\rm P} \sim 1$ highlights that the energy of the SNe is not going into accelerating ISM material but instead escapes out into the halo. This is particularly important because it means the energy is available to accelerate the inner CGM material and potentially prevent accretion onto the galaxy.

An observationally important question is how much of the wind is hot (hard to observe) or cold (easier to observe). The majority of galactic wind observations are of ionic species that trace cold gas. Likewise, the most readily observable species in the CGM trace cold gas. Understanding how the mass and energy are partitioned between the phases may allow us to better understand the unobserved phases of galactic winds (and the CGM) from observations of a given phase. Fig. 4.11 demonstrates how the mass and energy fluxes are distributed in temperature and velocity space, showing the amount of $\eta_{\rm E}$ and $\eta_{\rm M}$ per two dimensional logarithmic bins in temperature and outward velocity $v_{\rm out}$ at two heights for the $\epsilon_* = 0.03$ turbulent stratified simulations. These distributions are representative of most of the winds in our simulations albeit with minor quantitative variations. Just above the disc (left columns) and at the edge of the box (right columns) the majority of the energy is carried by hot ($T > 10^6$ K), fast moving ($v_{\rm out} > 100$ km s$^{-1}$) gas that has a high enough $v_{\mathcal{B}}$ to escape far out into the halo. Between 200 and 540 pc there is a shift to lower temperature and velocities due to mixing, cooling, and gravity. On the other hand, near the disc (200pc) the mass loading is dominated by much cooler gas ($\sim 10^4$ K) moving outward at $\sim 30$ km s$^{-1}$. By 540 pc this cooler phase of the wind has mostly fallen back or mixed into the hotter phase. There is, however, a non-zero cold component of the outflow that is moving at nearly the same speed as the hot phase – more so in the $\Sigma_{\rm g} = 300\,\rm M_\odot\,pc^{-2}$ simulation than in the $\Sigma_{\rm g} = 30\,\rm M_\odot\,pc^{-2}$ simulation. This cold component may further out in the halo as the hot medium cools in the wake of the cold clouds (e.g., Thompson et al., 2016b; Schneider et al., 2018; Gronke & Oh, 2018).

## 4.6 Discussion and Conclusion

### 4.6.1 Summary

The energy injected by SNe into the ISM is one of the most promising candidates for driving galactic winds. Galactic winds are observed to emanate from a wide range of galaxies and play a critical role in explaining many global galaxy scaling relations such as the stellar-mass to halo-mass relation and the mass-metallicity relation. In this paper we have used numerical simulations, motivated by analytic arguments (see §4.3), to study how spatially and temporally clustered SNe inflate hot super-bubbles in the ISM that can, under a range of conditions, breakout of the disc, vent a large fraction of the injected SNe energy, and drive powerful winds.

Our numerical simulations targeted gas surface densities of $\Sigma_g = 30$ and $300\ M_\odot\ pc^{-2}$ that are appropriate for vigorously star forming galaxies. At each surface density we studied how changes to the number of SNe in a cluster (parameterized by the cluster mass $M_{cl}$ or equivalently the cluster formation efficiency $\epsilon_*$; see Table 4.1), which sets the time between successive SNe $\Delta t_{SN}$, changed the evolution of the bubble and its ability to breakout. We ran simulations both with and without an external gravitational potential. The simulations without the external potential and the resulting stratification enabled us to isolate the pre-breakout evolution, while the stratified simulations allowed us to study the breakout process and the post-breakout evolution. Similarly, we adopted two choices for the phase structure of the ISM: a homogeneous $10^4$ K ISM, and a more realistic turbulent, multi-phase ISM. The homogeneous simulations help guide physical intuition because of their straightforward interpretation, while the turbulent simulations enabled us to capture the evolution in a more realistic environment including the interaction of the hot super-bubble/wind fluid with cold dense clouds in the ambient ISM.

There are two possible conditions that determine whether SNe driven bubbles can breakout of a galactic disc. The first is whether the bubble can reach a size of order the disc scale height before reaching pressure equilibrium. The second is whether the bubble can do so prior to the cessation of SNe at $t_{SN} \sim 30$ Myr. Using the unstratified subset of simulations we confirmed analytic expectations (eq. 4.18 - 4.21) that the first of these conditions is more stringent (Fig. 4.1) and that there is a critical cluster formation efficiency $\epsilon_* \sim 0.03$ (or, equivalently, a critical $M_{cl}$ or $\Delta t_{SN}$) that determines whether a super-bubble will breakout. While the super-bubble is confined within the ISM radiative losses remove between 90 and 99 per cent of the injected energy and leave a hot gas mass of only $\lesssim 10$ per cent of the mass of stars formed (see Figs. 4.2 and 4.3). This efficient cooling seems to argue against the ability of clustered SNe to drive powerful winds (Kim et al., 2017).

Our stratified simulations, however, uncovered a crucial change in cooling once the super-bubble breaks out and the wind can expand more unimpeded. When the cluster is massive enough for its super-bubble to breakout it blows a 'chimney' through the ISM that enables a large fraction ($\sim 0.1 - 0.6$) of the energy injected by the cluster's SNe to vent into the region above the disc and out into the CGM. During this venting phase cooling is much less effective. This qualitative difference in the energetics of the stratified simulations relative to the unstratified simulations strongly supports clustered SNe as a primary driver of galactic winds (see Figs. 4.5 and 4.6). The efficient

venting is also reflected in the momentum of the wind, which carries roughly the same amount of momentum as is injected by the SNe ($\eta_{\rm P} \sim 1$; see Fig. 4.10). Whereas in unstratified simulations that cannot vent significant work is done by the SNe and the momentum is boosted by $\sim 30-300$ (e.g., Gentry et al., 2017b; Kim et al., 2017). In addition to the large energy and momentum flux the winds are also significantly mass loaded with $\eta_{\rm M} \sim 0.5-1$. Importantly, a large fraction of the mass and energy carried by the wind has the potential to escape far out into the halo (as quantified by having Bernoulli parameters corresponding to speeds $> 300$ km s$^{-1}$; see Fig. 4.9).

### 4.6.2 Implications and Application to Observations

Although our simulations predict the energy, momentum, and mass loading of galactic winds ($\eta_{\rm E}, \eta_{\rm P}, \& \, \eta_{\rm M}$ in Figures 4.7-4.10; see Table 4.1), we believe that the energy and momentum content of the wind are more robust and more useful in diagnosing the importance of winds for galaxy formation. The primary reason for this is that as the wind propagates into the CGM, $\eta_E$ ($\eta_P$) will be the key conserved quantity if radiative cooling is not (is) important as the wind interacts with the inner regions of the CGM (see, e.g., Lochhaas et al. 2018). By contrast, $\eta_M$ is not a conserved quantity since the wind sweeps up mass as it propagates out into the halo. In particular, there is sometimes confusion regarding the interpretation of the very large mass loadings $\eta_M \gg 1$ required to explain the low masses of dwarf galaxies in cosmological simulations and semi-analytic models. To a large extent these large mass-loadings are halo scale quantities, not galaxy scale quantities. This distinction is related to the distinction between preventive and ejective feedback often discussed in the literature (e.g., Davé et al., 2012). In low mass galaxies, winds with $\eta_E \sim 1$ and $\eta_M \sim 1$ on galaxy scales (due to efficient venting of SNe like that found here) can prevent accretion of the CGM onto the galaxy, thus explaining the low stellar mass to halo mass of low mass galaxies. This can effectively correspond to $\eta_M \gg 1$ averaged over the halo. In fact, X-ray observations of galactic winds rule out $\eta_M \gg 1$ on galaxy scales in actively star forming galaxies (Zhang et al., 2014), strongly supporting a physical picture like that advocated here. That being said, some consequences of galactic winds for galaxy formation are sensitive to $\eta_M$ on galaxy scales. This includes, in particular, the chemical evolution of galaxies and the mass-metallicity relation, which depend on the fraction of mass and metals ejected from galaxies.

One key question we do not address in this paper is the fraction of star formation that occurs sufficiently clustered in space and time for SNe to breakout of galactic disks and drive powerful winds. Convolving this fraction with our results on wind strength as a function of cluster mass $M_{\rm cl}$ (or, equivalently, $\epsilon_*$) would determine the overall wind strength from a given galaxy. It is worth stressing that the clustering required to enhance the strength of galactic winds does not imply that the star formation must occur in bound clusters. All SNe that are correlated in time on timescales $\lesssim t_{\rm SN} \sim 30$ Myrs and space on lengthscales $\lesssim$ the disc scale-height can overlap, thus enhancing the efficacy of wind driving.

We now consider the application of our results to the prototypical local starburst M82 and $z \sim 2$ star forming disc galaxies. M82 has $\Sigma_g \simeq 3000\,{\rm M}_\odot\,{\rm pc}^{-2}$, $t_d \sim 2\times10^6$ yrs, and $\delta v \sim 20\,{\rm km\ s}^{-1}$ (Kennicutt, 1998; Greco et al., 2012). Equations 4.18 and 4.21 thus imply $R_s(t = {\rm t_{SN}}) \simeq 5{\rm h}$ and $v_s(R_s = h) \sim 20\,{\rm km\ s}^{-1}$, such that breakout at $t \ll {\rm t_{SN}}$ is plausible, but only for our fiducial

$\epsilon_* = 0.03 - 0.1$. The latter corresponds to $M_{cl} \sim 0.5 - 1.5 \times 10^6\,M_\odot$ for our assumed M82 conditions, consistent with the star cluster masses in M82 (McCrady & Graham, 2007). Thus our model argues that clusters like those observed can indeed account for the large energy in the hot wind in M82 inferred from Chandra observations by Strickland & Heckman (2009a). For $z \sim 2$ star forming discs, $\Sigma_g \sim 10^{2-3}\,M_\odot\,pc^{-2}$, $\delta v \sim 30 - 50\,km\ s^{-1}$, and $t_d \sim 3 \times 10^7$ yrs (Tacconi et al., 2013). Equations 4.18 and 4.21 thus imply $R_s(t = t_{SN}) \simeq 2h$ and $v_s(R_s = h) \sim 100\ km\ s^{-1} \gg \delta v$; thus breakout is again likely satisfied, leading to efficient venting of late-time SNe associated with star clusters. These comparisons support a key role for clustered SNe in driving powerful galactic winds in a wide range of star forming galaxies.

#### 4.6.2.1 A Minimum Star Formation Rate Surface Density for Galactic Winds

To further expand on the implications of these results, we suggest here that the role of clustered SNe in driving galactic winds may set a minimum star formation rate surface density $\dot{\Sigma}_*$ for galactic winds.

Theoretical models of GMC disruption by star clusters find that GMCs are harder to disrupt in higher surface density environments (Murray et al., 2010). This suggest that $\epsilon_*$ will be a increasing function of increasing surface density $\Sigma_g$. For concreteness, consider $\epsilon_* = \epsilon_0 \Sigma_g / \Sigma_{max}$ for $\Sigma_g \lesssim \Sigma_{max}$, with $\epsilon_0 \sim 1$ and $\Sigma_{max} \equiv 3000\,\Sigma_{3000} M_\odot\,pc^{-2}$ (Grudić et al., 2016); the exact functional form assumed here is not critical for what follows. Using the analytic scalings from §4.3, we then find that breakout $v_s(R_s = h) \gtrsim \delta v$ only occurs if

$$\Sigma_g \gg \Sigma_{crit,1} \simeq 40\,f_V \epsilon_0^{-1}\,t_{d,7}^{-1}\,\delta v_{10}\,\Sigma_{3000}\,M_\odot\,pc^{-2} \tag{4.29}$$

It is also useful to rewrite equation 4.6 using equation 4.4, 4.17, and $\epsilon_*(\Sigma_g)$, which yields

$$\Sigma_g \gg \Sigma_{crit,2} \simeq 20\,f_V^{1/4} \left(\frac{\Sigma_{3000}}{\epsilon_0\,\delta v_{10}}\right)^{0.6} t_{d,7}^{-1.5}\,M_\odot\,pc^{-2} \tag{4.30}$$

Equations 4.29 and 4.30 show that i) the SNe associated with star clusters only coherently drive bubbles and ii) the resulting bubbles only breakout out of the galactic disc if the gas surface density of the disc is sufficently large. The surface density thresholds in equations 4.29 and 4.30 correspond, via the Kenicutt-Schmidt relation, to a condition on the star formation rate per unit area of the disc required to drive a strong galaxy-scale wind, roughly $\dot{\Sigma}_* \gg 0.03\,M_\odot\ yr^{-1}\,kpc^{-2}$. This is comparable to the observational threshold described by Heckman (2002). We predict that it is a correlation between star cluster properties and gas surface density that ultimately produces a star formation surface density threshold for galactic winds.

### 4.6.3 Comparison to Related Work

We now discuss our findings in the context of related numerical work. The relevant related work covers a wide range, so we will restrict our discussion only to the most similar work. First,

we compare to other simulations of clustered SNe in unstratified media, followed by a comparison to simulations of winds launched by (not necessarily clustered) SNe in a stratified medium.

The three dimensional inhomogeneous unstratified simulations of Kim et al. (2017) are the most directly comparable to our unstratified turbulent simulations. Kim et al. (2017) focused on somewhat lower mean ISM densities, ranging from $n = 0.1$ to $10\,\mathrm{cm}^{-3}$, than we have. When comparing our most similar simulations the $\hat{M}_{\rm hot}$ and $\hat{E}_{\rm hot}$ in our simulations are roughly $\sim 3$ and 10 times higher, respectively, than in theirs. Reassuringly the bubble radii in both of our simulations grow as $t^{1/2}$ appropriate for the momentum-driven regime and have similar normalizations. Nevertheless, it is worthwhile to consider possible explanations for why the values of $\hat{M}_{\rm hot}$ and $\hat{E}_{\rm hot}$ differ. Although our simulations are similar there are differences in the details of how our cooling, photoelectric heating, and SN injection are implemented, and although in both cases the ISM is inhomogeneous in our simulations it is turbulent while theirs is static. Moreover, from a purely computational fluid dynamics standpoint the differences could be due to differences in choice of Riemann solver, reconstruction, or integration scheme (we used the HLLC Riemann solver, with plm reconstruction and a Van Leer integrator), all of which can change the properties of cooling and mixing (e.g., Martizzi et al., 2018; Grønnow et al., 2018). All told it is not that surprising that the quantities most sensitive to mixing differ depending on simulation details.

Separately, both 1D and 3D unstratified homogeneous ISM simulations have provided valuable insight into the numerical challenges in obtaining converged results for SNe-driven super-bubble evolution (Yadav et al., 2017; Gentry et al., 2017b, 2018). The root of this challenge can be traced to how thin the forward shock is once it has cooled. Gentry et al. (2017b) showed that the radial momentum per SNe is well converged when using a 1D moving mesh code that can resolve the thin shell with many cells, but when the grid was fixed, even with sub-pc resolution the radial momentum per SNe was an order of magnitude smaller, and not converged with resolution (see their fig. 15). This striking difference may, however, be artificial though due to mixing processes not captured in 1D simulations. This includes the Rayleigh-Taylor instability, which we find is important even for a homogeneous ambient medium (see Appendix 4.A.2.1).

The 3D homogeneous ISM simulations presented by Yadav et al. (2017) and Gentry et al. (2018) also stress the difficulty in obtaining converged results. Although these simulations are able to capture physical multi-dimensional mixing, the concerns may not be relevant since the lack of convergence only appears at late times $t \sim t_{\rm SN}$ when the super-bubble would have already broken out of the galactic disc. Moreover, the real ISM is highly inhomogeneous and the mixing is dominated by the cold clumps that are enveloped by/penetrate the expanding super-bubble. In Appendix 4.A we look in detail at the super-bubble properties' dependence on resolution for both the homogeneous and inhomogeneous simulations over the few Myr timescale before a bubble would break out of the galactic disc. We find the results to be well converged, with the inhomogeneous simulations showing more of a resolution dependence, as well as enhanced mixing and cooling relative to the homogeneous simulations.

In addition to the work on clustered SNe in an unstratified medium, much work has gone into simulating the winds launched by SNe in a stratified medium. Girichidis et al. (2016a) performed a related study, measuring the difference between detonating SNe at density peaks, randomly distributed in the ISM, or clustered. They found significantly higher $\eta_{\rm M}$ than we have, but there are

numerous differences in our methods that can account for this. Notably, their disc, which had $\Sigma_g = 10\ M_\odot\ pc^{-2}$ was thinner with a gas scale height of 30 pc and as shown in eq. 4.21 thinner discs are easier to breakout of. Moreover the ISM turbulence required to support this scale height was not driven externally but instead generated by the SNe themselves. Without initial turbulence the disc initially becomes even thinner. Fielding et al. (2017c) also studied how clustering SNe increases their ability to drive powerful winds relative to most distributed SNe. By systematically increasing the degree of clustering they showed that in cases where randomly distributed SNe launch effectively no wind at all clustered SNe can drive powerful ($\eta_E \sim 0.5$ and $\eta_M \sim$ few) winds. The winds in the more physically realistic simulations of SNe in a stratified medium of Kim & Ostriker (2018) are comparable, albeit a factor of a few lower in $\eta_E$ and $\eta_M$, to what we found here. Their star formation and subsequent SN locations are handled self-consistently, so clustering can arise naturally. However, their simulations probe lower surface density discs with $\Sigma_g = 10\ M_\odot\ pc^{-2}$.

### 4.6.4 Missing Physics

There are numerous complex physical processes at play in the ISM that together determine the properties of its different phases and contribute to setting the properties of galactic winds. In keeping with the idealized nature of our numerical simulations we have limited ourselves to a restricted set of these processes. This enabled us to keep the problem tractable and the interpretation of the results relatively straightforward. There are, however, several processes that we have not considered here that may have an important impact on the galactic winds driven by clustered SNe, in particular, magnetic fields, thermal conduction, self-gravity, and additional feedback processes.

The inclusion of magnetic fields may change the winds driven by clustered SNe by changing the pre-breakout evolution and the shear-flow mixing. Within the Milky Way's ISM magnetic fields are observed to be in rough equipartition with the thermal pressure. This large additional energy density in the ISM can change the early evolution of a bubble while it is still confined within the disc. Gentry et al. (2018) demonstrated that magnetic tension forces can drain momentum from an expanding bubble. Moreover, magnetic fields can suppress mixing by stabilizing shear instabilities. During the pre-breakout phase this is relevant when cold clouds are enveloped by the hot bubble and during the development of the Rayleigh-Taylor instability (Stone & Gardiner, 2007). Magnetic fields are also likely important with regards to the shredding and entraining of cold clouds by the wind post-breakout. As seen in Fig. 4.11 only a small fraction of the mass carried by the wind is at low temperature, but many observations of galactic winds show a sizable cold component. Magnetic fields can dramatically prolong the lifetime of a cold cloud in a hot wind (McCourt et al., 2015). Furthermore, suppressed mixing in the wind may reduce the degree of radiative losses the wind suffers.

The problem at hand inherently has many regions with steep temperature gradients, which would lead to large conductive fluxes. Conduction could impact both the phase structure of the ISM and therefore the expansion of the super-bubble as well as the mixing of the cold clouds as they are entrained and shredded. Moreover, Yadav et al. (2017) showed that only when including

explicit thermal conduction did they achieve numerical convergence in homogeneous ISM SNe-driven bubble simulations.

Including self-gravity would cause the dense structures in the ISM to be more tightly bound and may impact their survival when interacting with the bubble/wind material. Moreover, by including self-gravity, star formation would be tied to gravitational collapse, thereby giving a self-consistent relation between a clusters location and the ISM density and velocity field. This may be important because the proximity of the cluster to massive cold clouds can have a sizable impact on the evolution of the bubble and strength of the wind (see Appendix 4.B).

In recent years much work has gone into understanding the role of cosmic rays in launching galactic winds. Cosmic rays introduce an appreciable pressure gradient which can lift material above the disc where it can be more easily unbound by SNe (e.g., Salem & Bryan, 2014; Girichidis et al., 2016b; Butsky & Quinn, 2018). Therefore the combined effect of SNe and cosmic rays may further increase the strength of galactic winds. Likewise, other feedback processes, such as photoionization, radiation pressure, and stellar winds, might clear gas out around star clusters prior to the onset of SNe. This would effectively increase $\epsilon_*$ by decreasing $\Sigma_g$ around a given cluster, making breakout and strong winds more likely.

As stressed in this section, there are many effects that may play a role in determining the detailed properties of galactic winds. However, there is no reason to think that the processes we have omitted from this current study would qualitatively change our primary finding that post-breakout cooling is significantly reduced and clustered SNe can drive powerful winds by efficiently venting a large fraction of their energy out of the ISM. That said, the quantitative details of the wind properties are likely subject to change and our results should be considered instructive guides rather than the final word on the subject.

# Appendix

## 4.A Spatial Resolution Convergence

Previous studies have reached conflicting conclusions regarding the numerical convergence of bubble evolution. This is most likely due to differences in the convergence of 1D versus 3D simulations and differences in numerical techniques. Groups that investigated the evolution of cluster-driven super-bubbles in a homogeneous ISM found that as they decreased the cell size the amount of energy lost to cooling decreased (Yadav et al., 2017; Gentry et al., 2017b). Alternatively, Kim et al. (2017) simulated the evolution of cluster-driven super-bubbles in an inhomogeneous ISM and found their results to be well converged with spatial resolution. In Appendices 4.A.1 and 4.A.2 we investigate the resolution dependence of our results for the unstratified turbulent and homogenous simulations, respectively. In both cases we find our results to be very well converged and discuss briefly why previous homogeneous ISM simulations may have over estimated the resolution dependence.

In Appendix 4.A.3 we look at the convergence of the turbulent stratified simulations, focusing on the post-breakout energetics and wind properties. The results at different resolutions agree well – on the tens of per cent level.

### 4.A.1 Turbulent Unstratified Simulations

To test the spatial resolution sensitivity of our turbulent unstratified simulations we ran otherwise identical $\Sigma_g = 30\,M_\odot\,pc^{-2}$ $M_{cl} = 10^{4.5}\,M_\odot$ simulations with spatial resolutions of $\Delta x = 0.5$, 1 and 2 pc. The initial conditions of the higher resolution simulations were generated by refining the lowest resolution simulation. This guaranteed that any variations we see are not caused by different ISM properties. That being said the subsequent turbulent driving did not use the same random numbers so minor differences may arise at late times because of this.

Fig. 4.A.1 shows $r_{bubble}$ (top), $\hat{E}_{hot}$ (middle), and $\hat{M}_{hot}$ (bottom) for these simulations. The agreement is excellent. The highest resolution simulation has marginally higher $\hat{M}_{hot}$ and lower $r_{bubble}$ and $\hat{E}_{hot}$, at the level of ten per cent or less. This indicates that there is slightly more mixing at higher resolution. Previous studies with inhomogeneous ISMs found similar convergence (Kim et al., 2017).

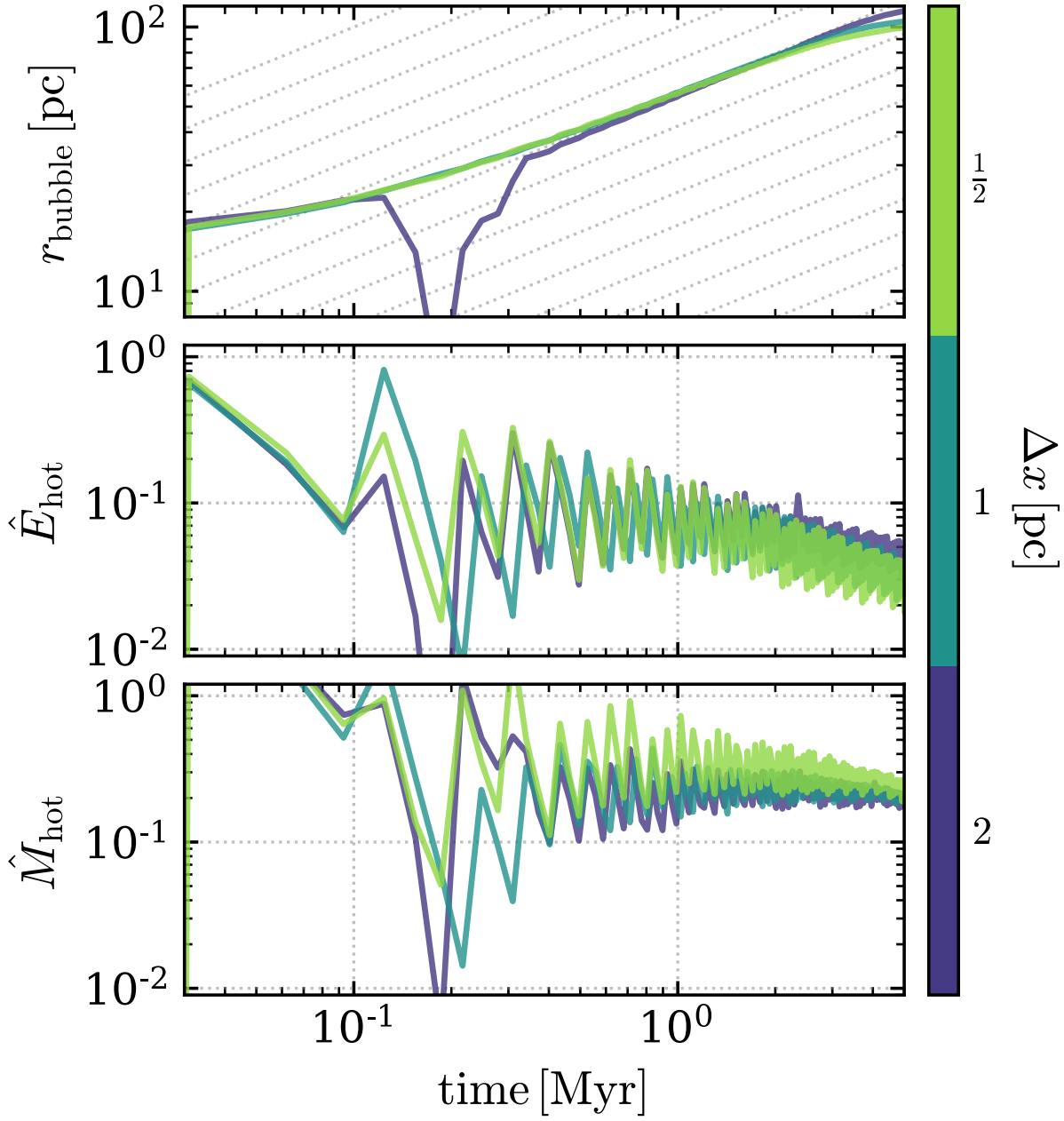


Figure 4.A.1: Resolution dependence of the evolution of $r_{\rm bubble}$ (top), $\hat{E}_{\rm hot}$ (middle), and $\hat{M}_{\rm hot}$ (bottom) in the turbulent unstratified $\Sigma_{\rm g} = 30\,{\rm M}_\odot\,{\rm pc}^{-2}$ $M_{\rm cl} = 10^{4.5}\,{\rm M}_\odot$ simulations. Throughout the 5 Myr duration of this test the quantities agree extremely well and are (at worst) within a few tens of per cent of each other. The highest resolution simulation has slightly lower $r_{\rm bubble}$ and $\hat{E}_{\rm hot}$ and higher $\hat{M}_{\rm hot}$ as a result of slightly enhanced mixing and subsequent cooling.

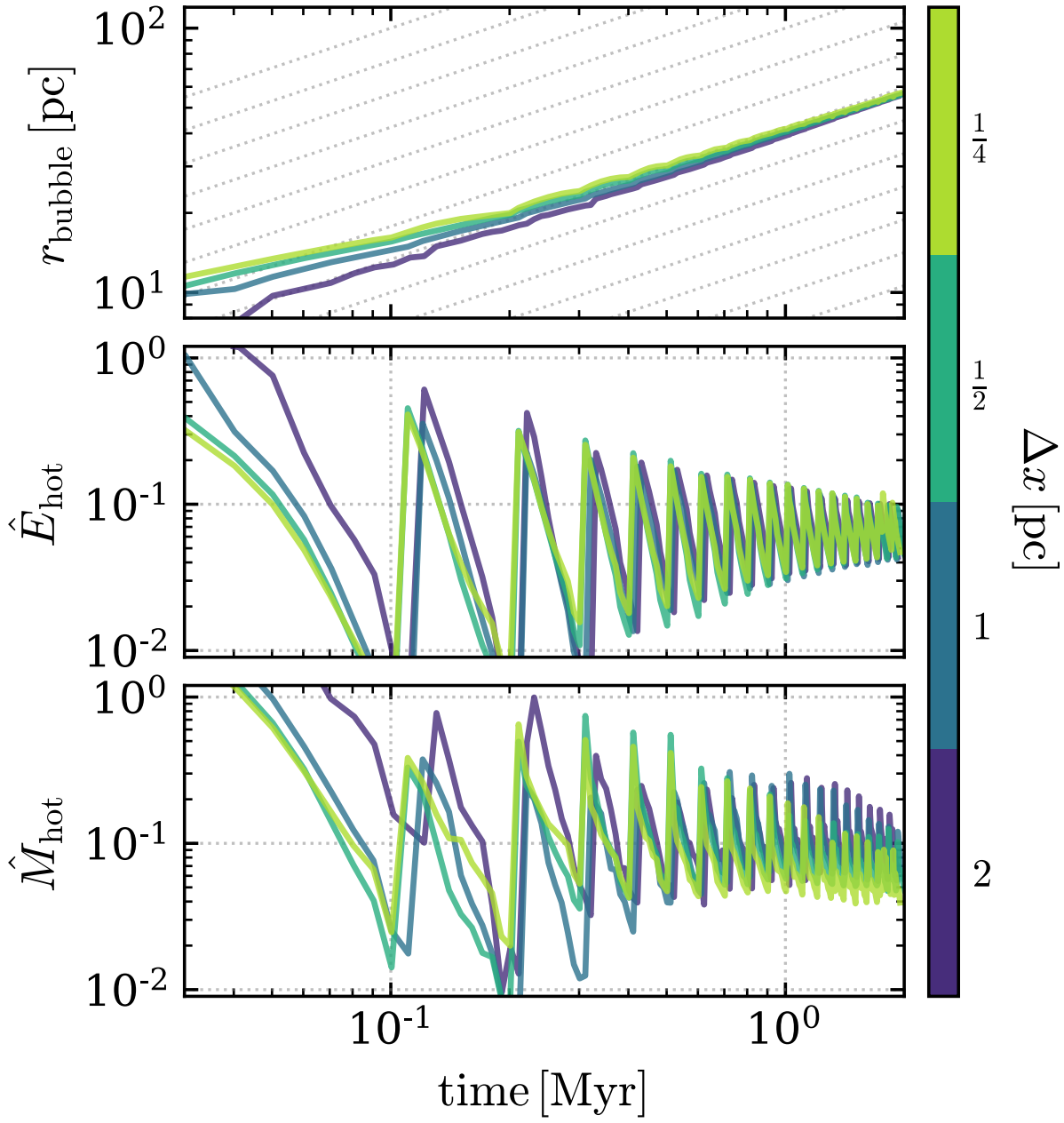


Figure 4.A.2: The evolution of $r_{\rm bubble}$ (top), $\hat{E}_{\rm hot}$ (middle), and $\hat{M}_{\rm hot}$ (bottom) in homogeneous unstratified $\Sigma_{\rm g} = 30\,{\rm M}_\odot\,{\rm pc}^{-2}$ $M_{\rm cl} = 10^{4.5}\,{\rm M}_\odot$ simulations with spatial resolutions ranging from $\Delta x = 0.25$ to 2 pc. These simulations were run in a box 128 pc on a side, so they were stopped after 2 Myr once the bubble had reached the edge of the domain. The agreement of these quantities is excellent across a factor of 8 in resolution.

### 4.A.2 Homogeneous Unstratified Simulations

Our unstratified homogeneous simulations enable us to compare with turbulent simulations to understand what is mediating mixing between the ISM and the super-bubble. Previous work that adopted a homogeneous ISM found that their results were not converged (Yadav et al., 2017; Gentry et al., 2017b), which has raised questions about the robustness of simulations with an inhomogeneous ISM.

Fig. 4.A.2 shows $r_{\rm bubble}$ (top), $\hat{E}_{\rm hot}$ (middle), and $\hat{M}_{\rm hot}$ (bottom) for $\Sigma_{\rm g} = 30\,{\rm M}_\odot\,{\rm pc}^{-2}$ $M_{\rm cl} = 10^{4.5}\,{\rm M}_\odot$ simulations with $\Delta x$ ranging from 0.25 to 2 pc. These simulations were run in a 128 pc box and were stopped prior to when the bubble reached the boundaries at 2 Myr. All three quantities agree exceptionally well. At higher resolution the bubble evolves somewhat faster for the first few tenths of a Myr. However, across a factor of 8 in resolution these quantities vary by at most a few per cent. Therefore even 2 pc resolution is sufficient to capture the initial expansion of the bubble.

Yadav et al. (2017) ran similar three-dimensional homogeneous unstratified simulations and found that at higher resolution the cooling decreased. They, however, focused at late times $t \sim {\rm t_{SN}}$ well after the super-bubble would have broken out of a galactic disc. Their Fig. 18 also shows clearly that the resolution dependence is decreasing with increasing resolution in their three-dimensional simulations, which indicates they are approaching convergence by $\Delta x = 1$ pc. Moreover they adopt a ten times larger cluster radius of 100 pc, so it takes much longer for the SNRs to overlap. We thus believe our convergence results are reasonably consistent.

However, one dimensional homogeneous unstratified ISM simulations are inconsistent with our results (Yadav et al., 2017; Gentry et al., 2017b). As we show in the next section this is due in large part to their inability to capture multi-dimensional instabilities that arise in the contact discontinuity separating the bubble and ISM.

#### 4.A.2.1 Rayleigh-Taylor

The one dimensional homogeneous unstratified ISM simulations performed by Yadav et al. (2017) and Gentry et al. (2017b) showed clearly that as the resolution was improved the amount of energy lost to cooling decreased. One dimensional simulations are able to achieve far higher resolution than three dimensional simulations, but they are unable to capture multi-dimensional instabilities. In particular, in this case, the ability capture the Rayleigh Taylor (RT) instability is crucial to accurately model the mixing of the bubble and ISM. As the bubble expands it sweeps up material and forms a thin dense shell. Weaver et al. (1977) demonstrated that in the limit of constant energy and mass injection the contact discontinuity separating the shell and the bubble is stable to RT. However, because the supernovae inject energy sporadically not continuously the shell experiences impulsive pushes after each explosion. These explosions accelerate the less dense bubble material into the more dense shell material – the density gradient and the pressure gradient have opposite signs – setting up the conditions for the RT.

Clear signs of development of RT can be seen in Fig. 4.A.3, which shows density slices immediately after the first, second and sixth SNe in the 0.25 pc resolution homogeneous unstratified

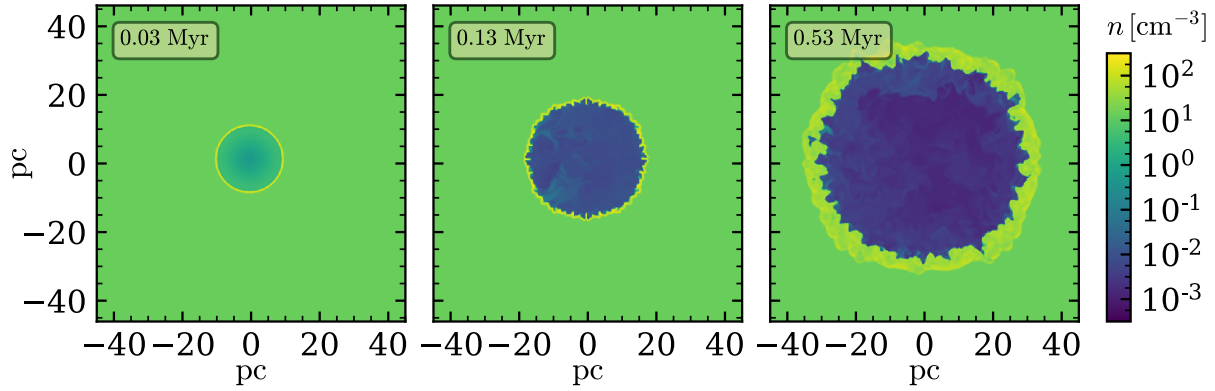


Figure 4.A.3: Slices showing the number density 0.03 Myr after the first, second, and sixth SNe in a homogeneous unstratified $\Sigma_{\rm g} = 30\,{\rm M}_\odot\,{\rm pc}^{-2}$ $\mathrm{M_{cl}} = 10^{4.5}\,{\rm M}_\odot$ simulation with $\Delta x = 0.25$ pc. After the first SN the contact discontinuity separating the bubble and ISM is nearly perfectly spherical. However, after the second SN and all subsequent SNe the contact discontinuity is no longer symmetric but instead is significantly corrugated. The disruption of the contact discontinuity develops due to Rayleigh-Taylor instability.This generates physical mixing between the shocked ISM and the SNe ejecta, and makes the simulations converge much better than the analogous one dimensional simulations.

simulation. After the first SN the shell is nearly perfectly spherical and is stable to RT because the shell is decelerating. On the other hand, after all subsequent SNe there are clear signs of disruption to the contact discontinuity due to the growth of RT. The disruption of the contact discontinuity and subsequent mixing is a real physical effect that is not captured in the one-dimensional simulations, which are therefore prone to underestimating the mixing and cooling. This was also confirmed by Gentry et al. (2018). Although in the simulations shown in Fig. 4.A.3 grid scale noise seeds the growth of the instability, in the turbulent simulations and in the real universe inhomogeneities in ISM are unavoidable and the instability will have ample perturbations to amplify.

### 4.A.3 Turbulent Stratified Simulations

We now shift our attention to the numerical convergence of the stratified turbulent simulations. In the previous section we assessed the convergence of the pre-breakout dynamics and energetics and showed that 2 pc resolution is sufficient to accurately capture the bubble evolution. Here instead we focus on the post-breakout evolution convergence, looking at the cooling loses, energy and mass loading, and the phase distribution of the wind. Capturing the shredding and entrainment of cold clumps by a hot wind is well known to be fraught with numerical difficulties, and cloud crushing simulations have shown that with higher resolution cold clouds are shredded more quickly (e.g., Schneider & Robertson, 2017). Much of the mass-loading of the winds launched in our simulations comes from the shredding of cold clouds, so this resolution dependence could

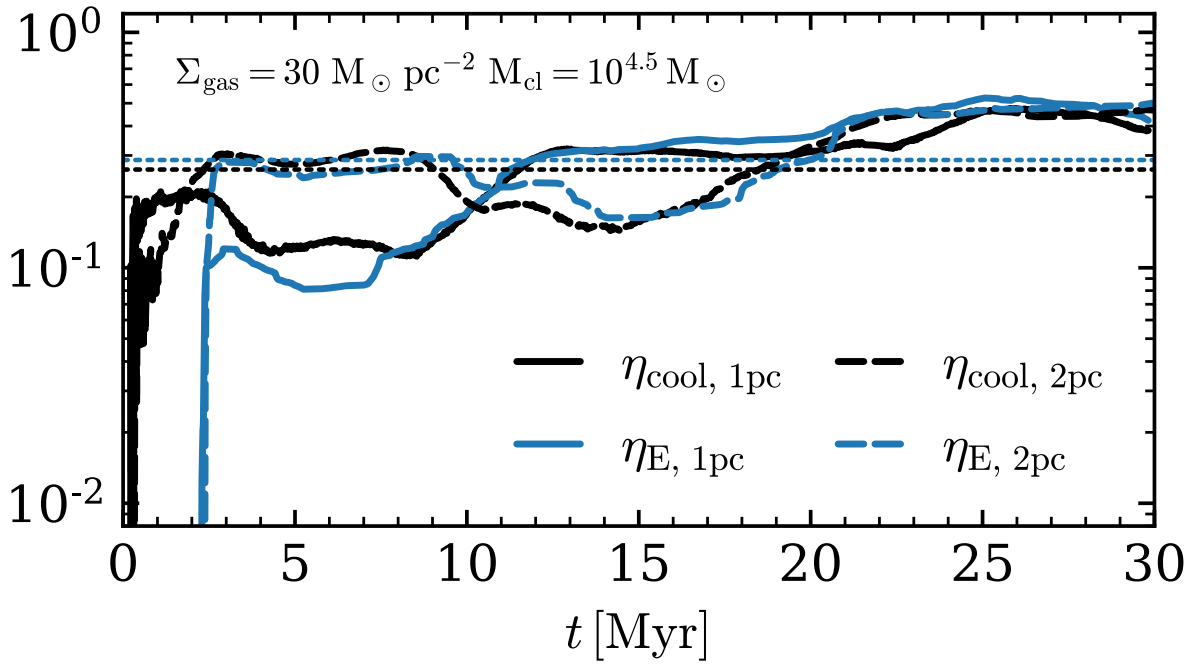


Figure 4.A.4: The time evolution of $\eta_{\rm cool}$ (black) and $\eta_{\rm E}$ (blue) measured at 540 pc for $\Sigma_{\rm g} = 30\,{\rm M}_\odot\,{\rm pc}^{-2}$ ${\rm M}_{\rm cl} = 10^{4.5}\,{\rm M}_\odot$ turbulent stratified simulations with $\Delta x = 1$ pc (solid lines) and 2 pc (dashed lines). Initially the 1 pc simulation has $\sim 2$ more cooling, but during the middle of the simulations this is reversed, and by the end the two have nearly identical $\eta_{\rm E}$ and $\eta_{\rm cool}$. The thin dotted lines show the time average $\eta_{\rm E}$. The close agreement indicates that the post-breakout evolution of our simulations is reasonably well converged.

potentially impact our findings. Moreover, changes to the mass loading can potentially change the degree of radiative cooling in the wind.

To test the dependence of post-breakout dynamics on resolution we re-simulated the $\Sigma_{\rm g} = 30\,{\rm M}_\odot\,{\rm pc}^{-2}$ ${\rm M}_{\rm cl} = 10^{4.5}\,{\rm M}_\odot$ turbulent stratified simulation with twice the spatial resolution, pushing $\Delta x$ down to 1 pc. The initial conditions for the higher resolution simulation were generated by refining the initial conditions of the fiducial resolution simulation. Although the subsequent driving is different, the matched initial conditions ensures that the ISM structures and dynamics are similar.

Fig. 4.A.4 shows $\eta_{\rm cool}$ and $\eta_{\rm E}$ for the $\Delta x = 1$ and 2 pc stratified turbulent simulations. The 1 pc simulation initially cools more and drives a weaker wind by a factor of $\sim 2$, but after about 10 Myr this trend flips and the 1 pc simulation cools less than the 2 pc simulation. For the final 10 Myr of the simulations the two resolutions cool at essentially the same rate and drive comparable winds. The time averaged $\eta_{\rm E}$ and $\eta_{\rm cool}$ between these two simulations agree well – with $\eta_{\rm E} \approx \eta_{\rm cool} = 0.26$ and 0.29 for the 1pc and 2pc simulations, respectively (shown with the dotted lines).

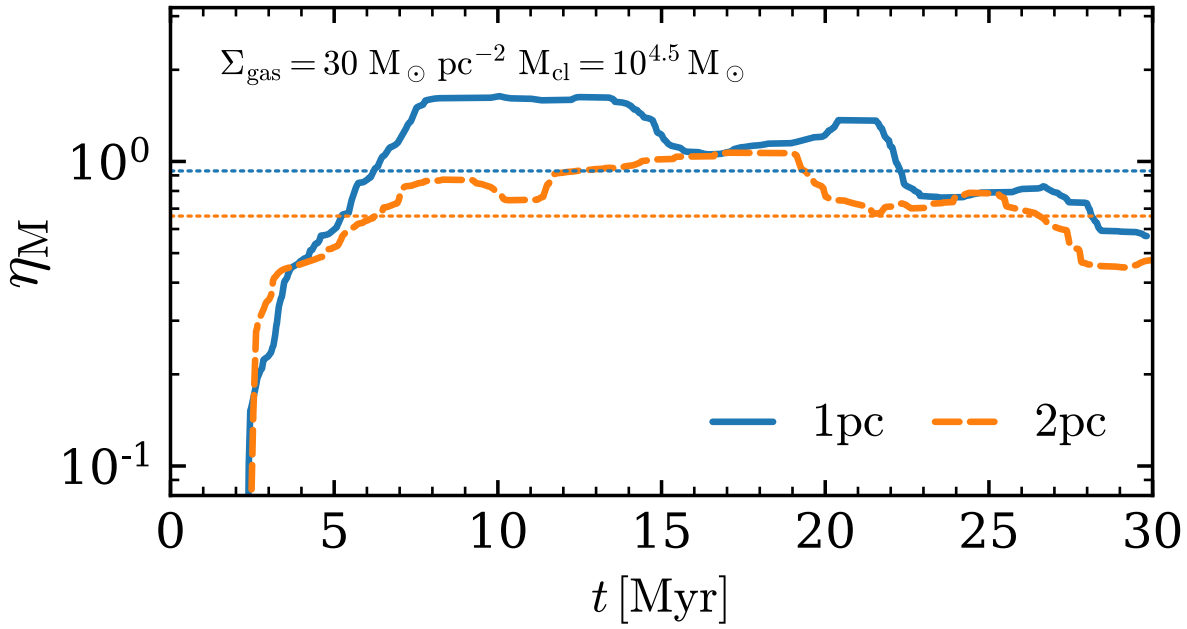


Figure 4.A.5: The time evolution of $\eta_{\rm M}$ measured at 540 pc for the $\Sigma_{\rm g} = 30\,{\rm M}_\odot\,{\rm pc}^{-2}$ $\rm M_{cl} = 10^{4.5}\,M_\odot$ turbulent stratified simulation with $\Delta x = 1$ pc (blue solid line) and 2 pc (orange dashed line). The dotted lines show the time average. The mass loading of the higher resolution simulation is systematically higher than the lower resolution simulation by a few tens of per cent. This is likely due to enhanced entrainment of material shredded off of cold clumps that is better captured with higher resolution. Nevertheless the differences are relatively minor and our conclusions are qualitatively unchanged.

Given the degree of numerical complications inherent to this problem this the level of agreement is encouraging and supports our primary finding that the energetics change dramatically post-breakout.

The mass-loading of the winds, on the other hand, shows a slightly larger dependence on the resolution. Fig. 4.A.5 shows the time evolution of $\eta_{\rm M}$ measured at 540 pc for the two resolution simulations. Cold clumps in the higher resolution simulation are shredded more efficiently which enhances the mass flux out of the domain. The dotted lines show the time averaged value of $\eta_{\rm M}$, which drops from 0.9 to 0.7 when going from 1 pc to 2 pc resolution.

Fig. 4.A.6 shows the distributions of $\eta_{\rm E}$ and $\eta_{\rm M}$ in $T - v_{\rm out}$ space for the two resolutions at two heights above the disc. For both quantities and at both heights the distributions are at systematically higher temperatures in the lower resolution simulation. This is due to enhanced mixing of cold and hot phases with better resolution that decreases the temperature. This enhanced mixing, however, has minimal effect on the energy loading because the post-mixing temperature of the majority of the wind is still $T \gtrsim$ few $\times 10^6$ K where radiative cooling is inefficient. Notably, the $\eta_{\rm M}$ distribution

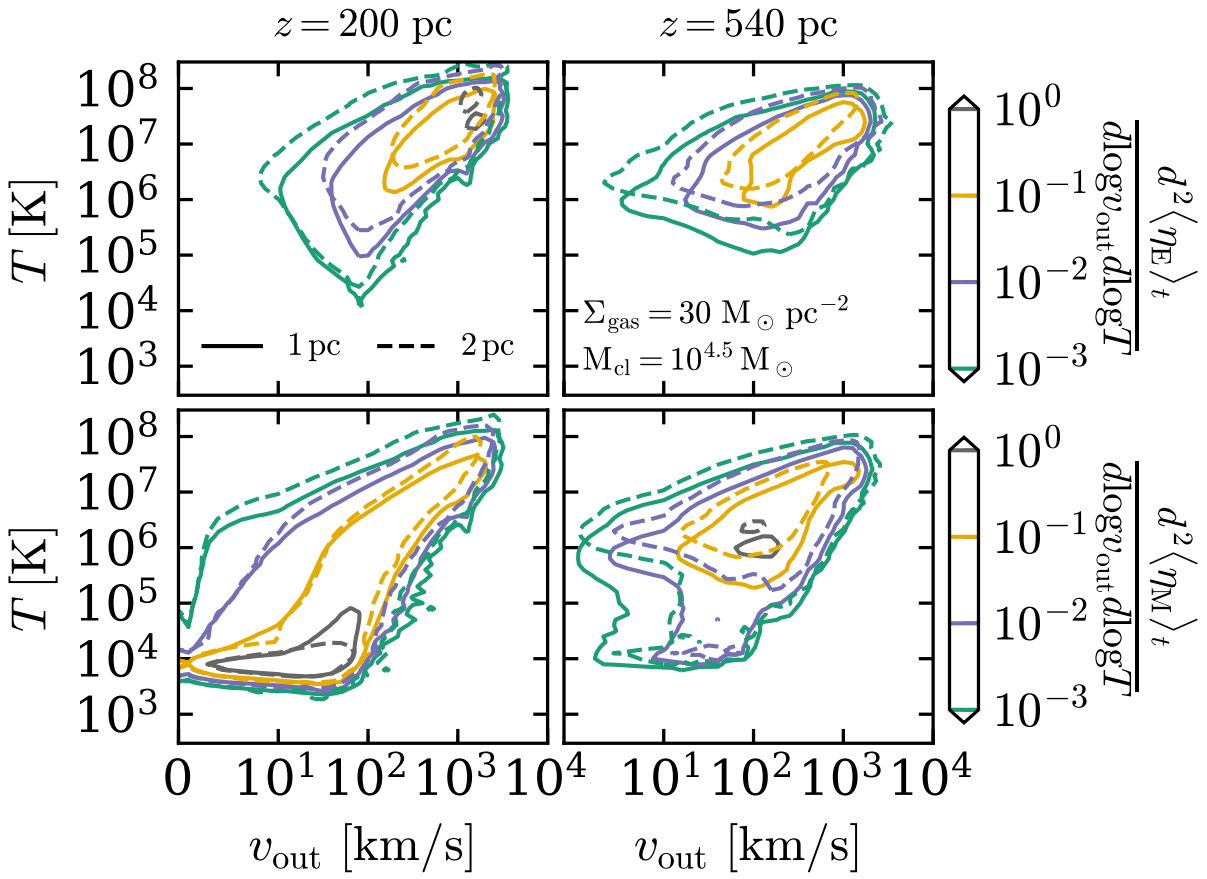


Figure 4.A.6: The amount of the time averaged $\eta_{\rm E}$ (top row) and $\eta_{\rm M}$ (bottom row) per two dimensional logarithmic bin in temperature and outward velocity just above the disc at 200 pc (left column) and at 540 pc, the edge of the computational domain (right column) in $\Sigma_{\rm g} = 30\,{\rm M}_\odot\,{\rm pc}^{-2}$ ${\rm M}_{\rm cl} = 10^{4.5}\,{\rm M}_\odot$ turbulent stratified simulations with $\Delta x = 1$ pc (solid contours) and 2 pc (dashed contours). At both heights the energy and mass in the higher resolution simulation is carried by systematically cooler gas due to enhanced mixing.

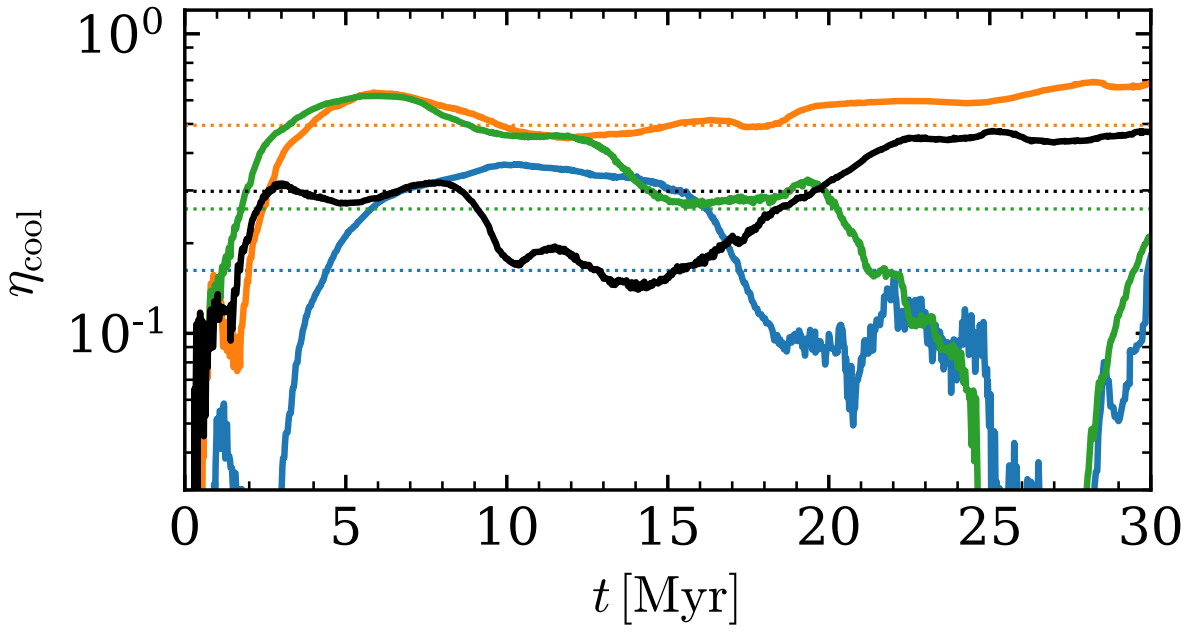


Figure 4.B.1: The time evolution of $\eta_{\rm cool}$ for four different $\Sigma_{\rm g} = 30\,{\rm M}_\odot\,{\rm pc}^{-2}$ $M_{\rm cl} = 10^{4.5}\,{\rm M}_\odot$ turbulent stratified simulations with $\Delta x = 2$ pc that differ only in turbulent driving realizations. The thin dotted lines show the time average value. The black line is the fiducial simulation discussed throughout the paper. Once the bubble breaks out in the simulation traced by the orange line the cluster efficiently vents without having to carve out a new vent. Alternatively, the clusters in the simulations traced by the blue and green simulations are impinged on by cold dense clouds that force the bubble to re-breakout. The differences in turbulent ISM properties leads to a factor of $\sim 3$ range in the average amount of cooling over the whole simulation.

in the 1 pc simulation has a tail that extends down to between $T = 10^4$ and $10^5$ K and $v_{\rm out} = 10$ and 100 km s$^{-1}$ that carries roughly $\eta_{\rm M} \sim 0.01$. This absent in the 2 pc resolution simulation. Although this mass flux is only a small fraction of the total outflow it is indicative that with higher resolution, and/or additional physical processes there may be a larger cold component of the wind.

## 4.B Turbulence Realizations

The proximity of the cluster to massive cold clouds in the ISM has a large impact on the subsequent wind dynamics. These cold clouds carry a large amount of mass and momentum and when one drifts near the cluster an appreciable fraction of the cluster's energy is spent pushing and ablating the cloud. When this happens the energy remaining to power a wind is diminished. Because of this our simulations are sensitive to the properties of the turbulent ISM. Moreover, since the turbulence in our simulation is driven by hand and the location of the cluster is not tied to

the local ISM properties it is likely that a given simulation may experience more or less favorable wind launching conditions (lower or higher frequency of interacting with cold clouds). To test the sensitivity of our results to the properties of the ISM we re-simulated the $\Sigma_g = 30\,M_\odot\,pc^{-2}$ $M_{cl} = 10^{4.5}\,M_\odot$ turbulent stratified simulation three additional times with different random number seeds and therefore different realizations of the turbulent ISM. Fig. 4.B.1 shows the evolution of $\eta_{cool}$ for these four simulations. Not surprisingly there is a large degree of variability. The simulation shown with the orange line breaks out once and then is able to efficiently vent its energy virtually unimpeded for the duration of $t_{SN}$. On the other hand, the clusters in the simulations shown with the blue and green lines have far more difficulty keeping a channel clear for efficient venting and are nearly completely bottled up for several Myr around 20 Myr. The black line shows the fiducial simulation which lies in the middle of the range. The time average $\eta_{cool}$ ranges from 0.15 to 0.5. This factor of $\sim 3$ spread in the cooling loses and accordingly the wind energy loading points to the sensitivity of wind launching to ISM properties. Simulations with self-consistently driven ISM turbulence and star formation tied to the ISM density/velocity field (e.g., gravitational collapse) will be able to assess if this degree of wind strength variation is intrinsic to the problem or a result of our idealized setup. Nevertheless, our primary finding that post-breakout cooling saps much less of the energy injected by SNe is valid regardless of the sensitivity to turbulent properties, although a given cluster may have to breakout more than once over its lifetime if ISM flows conspire to refill the cavity it excavated.

# Bibliography


Aguirre A., Hernquist L., Schaye J., Katz N., Weinberg D. H., Gardner J., 2001, ApJ, 561, 521

Anderson M. E., Bregman J. N., 2011, ApJ, 737, 22

Balbus S. A., 2001, ApJ, 562, 909

Behroozi P. S., Conroy C., Wechsler R. H., 2010, ApJ, 717, 379

Behroozi P. S., Wechsler R. H., Conroy C., 2013, ApJ, 770, 57

Belyaev M. A., Rafikov R. R., 2012, ApJ, 752, 115

Bett P. E., Frenk C. S., 2012, MNRAS, 420, 3324

Bigiel F., et al., 2011, ApJL, 730, L13

Binney J., 1977, ApJ, 215, 483

Birnboim Y., Dekel A., 2003, MNRAS, 345, 349

Book L. G., Brooks A., Peter A. H. G., Benson A. J., Governato F., 2011, MNRAS, 411, 1963

Booth C. M., Agertz O., Kravtsov A. V., Gnedin N. Y., 2013, ApJL, 777, L16

Bordoloi R., et al., 2014, ApJ, 796, 136

Borthakur S., et al., 2015, ApJ, 813, 46

Butsky I., Quinn T. R., 2018, preprint, (arXiv:1803.06345)

Chen H.-W., Lanzetta K. M., Webb J. K., Barcons X., 1998, ApJ, 498, 77

Chevalier R. A., Clegg A. W., 1985, Nature, 317, 44

Chisholm J., Tremonti Christy A., Leitherer C., Chen Y., 2016, MNRAS, 463, 541

Chisholm J., Tremonti C. A., Leitherer C., Chen Y., 2017, arXiv.org

Cioffi D. F., McKee C. F., Bertschinger E., 1988, ApJ, 334, 252

Crain R. A., et al., 2015, MNRAS, 450, 1937

Creasey P., Theuns T., Bower R. G., 2013, MNRAS, 429, 1922

Danforth C. W., et al., 2016, ApJ, 817, 111

Davé R., Finlator K., Oppenheimer B. D., 2012, MNRAS, 421, 98

Dekel A., Birnboim Y., 2006, MNRAS, 368, 2

Dekel A., Silk J., 1986, ApJ, 303, 39

Dekel A., et al., 2009, Nature, 457, 451

Fang T., Bullock J., Boylan-Kolchin M., 2013, ApJ, 762, 20

Faucher-Giguère C.-A., Quataert E., 2012, MNRAS, 425, 605

Faucher-Giguère C.-A., Kereš D., Ma C.-P., 2011, MNRAS, 417, 2982

Faucher-Giguère C.-A., Quataert E., Hopkins P. F., 2013, MNRAS, 433, 1970

Faucher-Giguère C.-A., Hopkins P. F., Kereš D., Muratov A. L., Quataert E., Murray N., 2015, MNRAS, 449, 987

Faucher-Giguère C.-A., Feldmann R., Quataert E., Keres D., Hopkins P. F., Murray N., 2016, preprint, (arXiv:1601.07188)

Feldmann R., Hopkins P. F., Quataert E., Faucher-Giguere C.-A., Keres D., 2016, preprint, (arXiv:1601.04704)

Ferland G. J., Korista K. T., Verner D. A., Ferguson J. W., Kingdon J. B., Verner E. M., 1998, PASP, 110, 761

Fielding D. B., McKee C. F., Socrates A., Cunningham A. J., Klein R. I., 2015, MNRAS, 450, 3306

Fielding D., Quataert E., McCourt M., Thompson T. A., 2017a, MNRAS, 466, 3810

Fielding D., Quataert E., McCourt M., Thompson T. A., 2017b, MNRAS, 466, 3810

Fielding D., Quataert E., Martizzi D., Faucher-Giguère C.-A., 2017c, MNRAS, 470, L39

Finlator K., Davé R., 2008, MNRAS, 385, 2181

Ford A. B., Oppenheimer B. D., Davé R., Katz N., Kollmeier J. A., Weinberg D. H., 2013, MNRAS, 432, 89

Ford A. B., et al., 2015, preprint, (arXiv:1503.02084)

Forman W., Jones C., Tucker W., 1985, ApJ, 293, 102

Gardiner T. A., Stone J. M., 2008, Journal of Computational Physics, 227, 4123

Gaspari M., Ruszkowski M., Sharma P., 2012, ApJ, 746, 94

Gatto A., Walch S., Low M.-M. M., Naab T., Girichidis P., Glover S. C. O., Wünsch R., Klessen R. S. e. a., 2015, MNRAS, 449, 1057

Gatto A., et al., 2017, MNRAS, 466, 1903

Gentry E. S., Krumholz M. R., Dekel A., Madau P., 2017a, MNRAS, 465, 2471

Gentry E. S., Krumholz M. R., Dekel A., Madau P., 2017b, MNRAS, 465, 2471

Gentry E. S., Krumholz M. R., Madau P., Lupi A., 2018, preprint, (arXiv:1802.06860)

Genzel R., et al., 2015, ApJ, 800, 20

Ghavamian P., Laming J. M., Rakowski C. E., 2007, ApJL, 654, L69

Girichidis P., et al., 2016a, MNRAS, 456, 3432

Girichidis P., et al., 2016b, ApJL, 816, L19

Greco J. P., Martini P., Thompson T. A., 2012, ApJ, 757, 24

Gronke M., Oh S. P., 2018, preprint, (arXiv:1806.02728)

Grønnow A., Tepper-García T., Bland-Hawthorn J., 2018, preprint, (arXiv:1805.03903)

Grudić M. Y., Hopkins P. F., Faucher-Giguère C.-A., Quataert E., Murray N., Kereš D., 2016, preprint, (arXiv:1612.05635)

Grudić M. Y., Hopkins P. F., Faucher-Giguère C.-A., Quataert E., Murray N., Kereš D., 2018, MNRAS, 475, 3511

Guo Q., White S., Li C., Boylan-Kolchin M., 2010, MNRAS, 404, 1111

Gupta A., Mathur S., Krongold Y., Nicastro F., Galeazzi M., 2012, ApJL, 756, L8

Haardt F., Madau P., 2001, in Neumann D. M., Tran J. T. V., eds, Clusters of Galaxies and the High Redshift Universe Observed in X-rays. (arXiv:astro-ph/0106018)

Hayes M., Melinder J., Östlin G., Scarlata C., Lehnert M. D., Mannerström-Jansson G., 2016, ApJ, 828, 49

Heckman T. M., 2002, in Mulchaey J. S., Stocke J. T., eds, Astronomical Society of the Pacific Conference Series Vol. 254, Extragalactic Gas at Low Redshift. p. 292 (arXiv:astro-ph/0107438)

Heckman T. M., Armus L., Miley G. K., 1990, ApJS, 74, 833

Heckman T. M., Lehnert M. D., Strickland D. K., Armus L., 2000, ApJs, 129, 493

Heckman T. M., Alexandroff R. M., Borthakur S., Overzier R., Leitherer C., 2015, ApJ, 809, 147

Hennawi J. F., Prochaska J. X., Cantalupo S., Arrigoni-Battaia F., 2015, Science, 348, 779

Hernquist L., 1990, ApJ, 356, 359

Hopkins P. F., Kereš D., Oñorbe J., Faucher-Giguère C.-A., Quataert E., Murray N., Bullock J. S., 2014, MNRAS, 445, 581

Hummels C. B., Bryan G. L., Smith B. D., Turk M. J., 2013, MNRAS, 430, 1548

Joung M. K. R., Mac Low M.-M., 2006, ApJ, 653, 1266

Kennicutt Jr. R. C., 1998, ApJ, 498, 541

Kereš D., Katz N., Weinberg D. H., Davé R., 2005, MNRAS, 363, 2

Kereš D., Vogelsberger M., Sijacki D., Springel V., Hernquist L., 2012, MNRAS, 425, 2027

Kim C.-G., Ostriker E. C., 2016, arXiv.org

Kim C.-G., Ostriker E. C., 2018, ApJ, 853, 173

Kim C.-G., Ostriker E. C., Raileanu R., 2017, ApJ, 834, 25

Koo B.-C., McKee C. F., 1992, ApJ, 388, 93

Koyama H., Inutsuka S.-i., 2002, ApJL, 564, L97

Kunz M. W., 2011, MNRAS, 417, 602

Lecoanet D., et al., 2015, preprint (arXiv:1509.03630)

Leitherer C., et al., 1999, ApJs, 123, 3

Leroy A. K., et al., 2015, ApJ, 814, 83

Li Y., Bryan G. L., Ruszkowski M., Voit G. M., O'Shea B. W., Donahue M., 2015, ApJ, 811, 73

Li M., Bryan G. L., Ostriker J. P., 2016, preprint, (arXiv:1610.08971)

Lochhaas C., Thompson T. A., Quataert E., Weinberg D. H., 2018, preprint, (arXiv:1804.00741)

Lynn J. W., Parrish I. J., Quataert E., Chandran B. D. G., 2012, ApJ, 758, 78

Maller A. H., Bullock J. S., 2004, MNRAS, 355, 694

Martin C. L., 1999a, ApJ, 513, 156

Martin C. L., 1999b, ApJ, 513, 156

Martin C. L., 2005, ApJ, 621, 227

Martin C., Moore A., Morrissey P., Matuszewski M., Rahman S., Adkins S., Epps H., 2010, in Ground-based and Airborne Instrumentation for Astronomy III. p. 77350M, doi:10.1117/12.858227

Martizzi D., Faucher-Giguère C.-A., Quataert E., 2015a, MNRAS, 450, 504

Martizzi D., Faucher-Giguère C.-A., Quataert E., 2015b, MNRAS, 450, 504

Martizzi D., Fielding D., Faucher-Giguère C.-A., Quataert E., 2016a, MNRAS, 459, 2311

Martizzi D., Fielding D., Faucher-Giguère C.-A., Quataert E., 2016b, MNRAS, 459, 2311

Martizzi D., Quataert E., Faucher-Giguere C.-A., Fielding D., 2018, preprint, (arXiv:1805.06461)

McBride J., Fakhouri O., Ma C.-P., 2009, MNRAS, 398, 1858

McCourt M., Parrish I. J., Sharma P., Quataert E., 2011, MNRAS, 413, 1295

McCourt M., Sharma P., Quataert E., Parrish I. J., 2012, MNRAS, 419, 3319

McCourt M., Quataert E., Parrish I. J., 2013, Monthly Notices of the Royal Astronomical Society, 432, 404

McCourt M., O'Leary R. M., Madigan A.-M., Quataert E., 2015, MNRAS, 449, 2

McCrady N., Graham J. R., 2007, ApJ, 663, 844

McCray R., Kafatos M., 1987, ApJ, 317, 190

McGaugh S. S., 2012, AJ, 143, 40

McKee C. F., Ostriker J. P., 1977, ApJ, 218, 148

McKee C. F., Williams J. P., 1997, ApJ, 476, 144

McNamara B. R., Nulsen P. E. J., 2007, AR&A, 45, 117

McQuinn M., Werk J. K., 2018, ApJ, 852, 33

Miller M. J., Bregman J. N., 2015, ApJ, 800, 14

Miller M. J., Hodges-Kluck E. J., Bregman J. N., 2016, ApJ, 818, 112

Mo H. J., Mao S., White S. D. M., 1998, MNRAS, 295, 319

Mulchaey J. S., Jeltema T. E., 2010, ApJL, 715, L1

Muratov A. L., Kereš D., Faucher-Giguère C.-A., Hopkins P. F., Quataert E., Murray N., 2015, MNRAS, 454, 2691

Murray N., Rahman M., 2010, ApJ, 709, 424

Murray N., Quataert E., Thompson T. A., 2010, ApJ, 709, 191

Navarro J. F., Frenk C. S., White S. D. M., 1997, ApJ, 490, 493

Nelson D., Vogelsberger M., Genel S., Sijacki D., Kereš D., Springel V., Hernquist L., 2013, MNRAS, 429, 3353

Nelson D., Genel S., Vogelsberger M., Springel V., Sijacki D., Torrey P., Hernquist L., 2015, MNRAS, 448, 59

O'Sullivan E., Forbes D. A., Ponman T. J., 2001, MNRAS, 328, 461

Oppenheimer B. D., Davé R., 2006a, MNRAS, 373, 1265

Oppenheimer B. D., Davé R., 2006b, MNRAS, 373, 1265

Oppenheimer B. D., Schaye J., 2013, MNRAS, 434, 1043

Oppenheimer B. D., et al., 2016, preprint, (arXiv:1603.05984)

Ostriker E. C., Shetty R., 2011, ApJ, 731, 41

Parker E. N., 1965, Space Sci. Rev., 4, 666

Parrish I. J., Quataert E., Sharma P., 2010, ApJL, 712, L194

Parrish I. J., McCourt M., Quataert E., Sharma P., 2012, MNRAS, 422, 704

Planck Collaboration et al., 2016, A&A, 594, A13

Portegies Zwart S. F., McMillan S. L. W., Gieles M., 2010, ARA&A, 48, 431

Prochaska J. X., Hennawi J. F., 2009, ApJ, 690, 1558

Prochaska J. X., Weiner B., Chen H.-W., Mulchaey J., Cooksey K., 2011, ApJ, 740, 91

Prochaska J. X., et al., 2017, ApJ, 837, 169

Quataert E., 2008, ApJ, 673, 758

Rahmati A., Pawlik A. H., Raicevic M., Schaye J., 2013, MNRAS, 430, 2427

Rees M. J., Ostriker J. P., 1977, MNRAS, 179, 541

Rubin K. H. R., Prochaska J. X., Ménard B., Murray N., Kasen D., Koo D. C., Phillips A. C., 2011, ApJ, 728, 55

Rubin K. H. R., Prochaska J. X., Koo D. C., Phillips A. C., Martin C. L., Winstrom L. O., 2014, ApJ, 794, 156

Rudie G. C., et al., 2012, ApJ, 750, 67

Ruszkowski M., Oh S. P., 2010, ApJ, 713, 1332

Salem M., Bryan G. L., 2014, MNRAS, 437, 3312

Salem M., Bryan G. L., Corlies L., 2016, MNRAS, 456, 582

Sarkar K. C., Nath B. B., Sharma P., Shchekinov Y., 2015, MNRAS, 448, 328

Schaye J., et al., 2010, MNRAS, 402, 1536

Schneider E. E., Robertson B. E., 2017, ApJ, 834, 144

Schneider E. E., Robertson B. E., Thompson T. A., 2018, preprint, (arXiv:1803.01005)

Sharma P., McCourt M., Quataert E., Parrish I. J., 2012a, Monthly Notices of the Royal Astronomical Society, 420, 3174

Sharma P., McCourt M., Parrish I. J., Quataert E., 2012b, Monthly Notices of the Royal Astronomical Society, 427, 1219

Sharma P., Roy A., Nath B. B., Shchekinov Y., 2014a, MNRAS, 443, 3463

Sharma P., Roy A., Nath B. B., Shchekinov Y., 2014b, MNRAS, 443, 3463

Shen S., Madau P., Guedes J., Mayer L., Prochaska J. X., Wadsley J., 2013, ApJ, 765, 89

Silk J., 1977, ApJ, 211, 638

Solomon P. M., Rivolo A. R., Barrett J., Yahil A., 1987, ApJ, 319, 730

Somerville R. S., Davé R., 2015, ARA&A, 53, 51

Springel V., Hernquist L., 2003, MNRAS, 339, 312

Springel V., et al., 2005, Nature, 435, 629

Steidel C. C., Erb D. K., Shapley A. E., Pettini M., Reddy N., Bogosavljević M., Rudie G. C., Rakic O., 2010, ApJ, 717, 289

Stern J., Hennawi J. F., Prochaska J. X., Werk J. K., 2016, preprint, (arXiv:1604.02168)

Stone J. M., Gardiner T., 2007, ApJ, 671, 1726

Stone J. M., Gardiner T. A., Teuben P., Hawley J. F., Simon J. B., 2008, ApJs, 178, 137

Strickland D. K., Heckman T. M., 2009a, ApJ, 697, 2030

Strickland D. K., Heckman T. M., 2009b, ApJ, 697, 2030

Sur S., Scannapieco E., Ostriker E. C., 2016, ApJ, 818, 28

Suresh J., Rubin K. H. R., Kannan R., Werk J. K., Hernquist L., Vogelsberger M., 2015, preprint, (arXiv:1511.00687)

Sutherland R. S., Dopita M. A., 1993, ApJs, 88, 253

Tacconi L. J., et al., 2013, ApJ, 768, 74

Tacconi L. J., et al., 2018, ApJ, 853, 179

Tepper-García T., Richter P., Schaye J., Booth C. M., Dalla Vecchia C., Theuns T., Wiersma R. P. C., 2011, MNRAS, 413, 190

Thom C., et al., 2012, ApJL, 758, L41

Thompson T. A., Quataert E., Zhang D., Weinberg D. H., 2016a, MNRAS, 455, 1830

Thompson T. A., Quataert E., Zhang D., Weinberg D. H., 2016b, MNRAS, 455, 1830

Tremonti C. A., et al., 2004, ApJ, 613, 898

Tumlinson J., et al., 2011, Science, 334, 948

Tumlinson J., et al., 2013, ApJ, 777, 59

Turk M. J., Smith B. D., Oishi J. S., Skory S., Skillman S. W., Abel T., Norman M. L., 2011, ApJs, 192, 9

Veilleux S., Cecil G., Bland-Hawthorn J., 2005a, AR&A, 43, 769

Veilleux S., Cecil G., Bland-Hawthorn J., 2005b, ARA&A, 43, 769

Vogelsberger M., et al., 2014, MNRAS, 444, 1518

Voit G. M., Donahue M., 2015, The Astrophysical Journal Letters, 799, L1

Voit G. M., Bryan G. L., O'Shea B. W., Donahue M., 2015, ApJL, 808, L30

Walter F., Weiss A., Scoville N., 2002, ApJL, 580, L21

Weaver R., McCray R., Castor J., Shapiro P., Moore R., 1977, ApJ, 218, 377

Weiner B. J., et al., 2009, ApJ, 692, 187

Werk J. K., et al., 2014, ApJ, 792, 8

White C. J., Stone J. M., Gammie C. F., 2016, ApJS, 225, 22

Wiersma R. P. C., Schaye J., Smith B. D., 2009, MNRAS, 393, 99

Yadav N., Mukherjee D., Sharma P., Nath B. B., 2017, MNRAS, 465, 1720

Yang X., Mo H. J., van den Bosch F. C., 2009, ApJ, 695, 900

Zhang D., Thompson T. A., Murray N., Quataert E., 2014, ApJ, 784, 93

de Wit W. J., Testi L., Palla F., Zinnecker H., 2005, A&A, 437, 247

van de Voort F., Schaye J., 2012, MNRAS, 423, 2991

van de Voort F., Quataert E., Hopkins P. F., Faucher-Giguère C.-A., Feldmann R., Kereš D., Chan T. K., Hafen Z. H., 2016, preprint, (arXiv:1604.01397)